Silicon rich nitride for silicon based laser devices

by

Jae Hyung Yi

B. S., Inorganic Materials Science and Engineering (1995), with Highest Honors
Seoul National University

M. S., Inorganic Materials Science and Engineering (1997)
Seoul National University

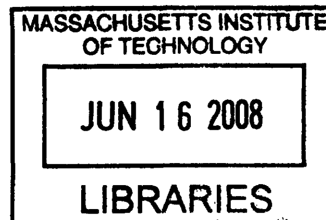

ARCHIVES

Submitted to the Department of Materials Science and Engineering
in partial fulfillment of the requirements for the degree of

Doctor of Philosophy in Electronic, Photonic and Magnetic Materials
at the
MASSACHUSETTS INSTITUTE OF TECHNOLOGY

June 6th, 2008

© Massachusetts Institute of Technology 2008. All rights reserved

Author..
Department of Materials Science and Engineering
February 22nd, 2008

Certified by ....
Lionel C. Kimerling
Thomas Lord Professor of Materials Science and Engineering
Thesis Supervisor

Accepted by ....
Samuel M. Allen
POSCO Professor of Physical Metallurgy
Chair, Departmental Committee on Graduate Students

Silicon rich nitride for silicon based laser devices

by

Jae Hyung Yi

Submitted to the Department of Materials Science and Engineering
on February 22nd, 2008 in partial fulfillment of the requirements for the degree of

Doctor of Philosophy in Electronic, Photonic and Magnetic Materials

Abstract

Silicon based light sources, especially laser devices, are the key components required to achieve a complete integrated silicon photonics system. However, the fundamental physical limitation of the silicon material as light emitter and the limited understanding of the excitation mechanism of Er in dielectric media by optical and electrical pumping methods impedes the progress of the research activities in this area. Silicon rich nitride (SRN) has been investigated as a strong candidate for silicon based laser devices. SRN has many advantages over other Si-based materials systems. These advantages include a high electrical injection level at low voltages, a low annealing temperature for Si nanocluster (Si-nc) formation and a large refractive index for strong optical confinement. Strong light emission from localized states in Si-nc embedded in SRN was demonstrated with a PLQE (Photoluminescence Quantum Efficiency) of 7%. This effect was confirmed through several experiments and first principle calculations. Thue Morse aperiodic structures were fabricated with light emitting SRN and SiO_2 materials, for the first time. Through the resonance phenomena achieved using this approach an emission enhancement of a factor of 6 was demonstrated experimentally. A sequential annealing technique was investigated to enhance the light emission from the Si-nc based light emitter. Electrical injection was greatly improved with annealing treatments of SRN based devices. In particular, bipolar electrical injection into SRN led to electroluminescence which was comparable to photoluminescence in peak shape and spectral position. Er doped SRN (Er:SRN) was fabricated through a co-sputter technique to achieve light emission at the wavelength of 1.54 μm. Energy transfer from SRN to Er was confirmed and shown to have a strong dependence on Si content. Si racetrack resonator structures with a low loss value of 2.5 dB/cm were fabricated through a Local Oxide (LOCOS) process and coupled with an Er:SRN layer to investigate gain behavior. Electrical injection properties into the Er:SRN layer were investigated and the electroluminescent device was fabricated. A detailed discussion on optical and electrical excitation of Er is provided to clarify the difference of the Er excitation mechanisms. A comparison of key simulation parameters used within the two level equations for optical and electrical excitation of Er atoms is provided to explain how the parameters contribute to each excitation mechanism. The most significant differences between the parameters and excitation mechanisms are also explained. Finally a summary of important factors to achieve a silicon based laser is provided and discussed for

future investigation based on the experimental data and the investigation presented in this work.

Thesis Advisor: Professor Lionel C. Kimerling
Title: Thomas Lord Professor of Materials Science and Engineering

Acknowledgement

I would like to express my gratitude to so many people around me for their support during my Ph.D. course and their contributions that made this research work possible.

First, Prof. Lionel C. Kimerling has been a great educator and researcher. From him I learned what it means to be the expert and big guru in the field of scientific research. I benefited from his deep insight and learned how to draw a big picture under his guidance. His talent of analyzing problems and breaking them down into fundamental key parameters has always been very impressive to me. It was a great opportunity for me to be a member of his research group and to be trained and educated by a person with such a talent. Thank you for your advising role and endless care for me, Kim.

During my Ph.D. period I met another precious advisor and mentor, Prof. Luca Dal Negro. He was a postdoctoral fellow in our group for more than two years. During his tenure in EMAT we shared an office. I was amazed by his deep and fundamental knowledge of topics related to photonics and by his endless enthusiasm and passion for research. We have worked hard even into the late night ordering pizza for dinner. The pizza menu is still attached to his desk in the office. I strongly believe he will be a great scholar in his field and I am happy to see that the establishment of his lab. in Boston Univ. is progressing well.

I also want to thank Prof. Harry Tuller and Prof. Eugene Fitzgerald for their guidance during my thesis research and presentation. By providing their insight, knowledge and very precious comments for conducting research, they raised the standard of this work.

I have been helped a lot by so many EMAT members. It was a great pleasure and honor for me to share my life and time with such talented people in the world. Dr. Jurgen Michel is very knowledgeable of science and lab skills. He was very kind and always tried to give me good direction. He helped me many times and was ready to help me personally at any time. Dr. Xiaoman Duan contributed to our research by performing TEM analysis. She also encouraged and helped me a lot. I am very grateful to Dr. Ching-yin Hong for her kind discussion and assistance with process related issues. She has been a good friend also in personal discussions as a colleague since we are the same age. Dr. Kazumi Wada, who is a professor in Japan, provided very insightful discussions. He personally helped me during my thesis. Dr. Anu Agarwal always helped me in every aspect. Dr. Anat Eshed was great resource of information regarding vacuum processes and fabrication equipment. On the topic of photonic device simulation I have had many discussions with Dr. Ning-Ning Feng and Dr. Winnie Ye. On the topic of the Er silicate research I worked and discussed with Dr. Xiaoxin Wang. I received help from not only staff members but also all the student members who had a strong influence on my development during my thesis. Among them are Dr. Jifeng Liu, Dr. Mike Stolfi, Dr. Sajan Saini, Dr. Daniel Sparacin, Dr. David Danielson, Dr. Lirong Zeng, Dr. Samerkhae Jongthammanurak, Dr. Donghwan Ahn, Dr. Victor Nguyen, Dr. Shoji Akiyama, Dr. Douglas Cannon, Dr. Wojtek Giziewicz, Dr. Jessica Sandland, Dr. Yasha Yi, Trisha Motalbo, Rong Sun, Juejun Hu, Xiaochen Sun, Kevin McComber, Jing Cheng, Sarah Bernardis, Jinfei Wang, and many others who are

currently working in our group. I also thank Mindy Baughman, Ellen Weene, and Lisa Page for their support and administration. It was very helpful for me.

To all the collaborators for my Ph.D. work I would like to express deep gratitude for sharing access to their facilities, their time and their knowledge. To Dr. Sebastien Hamel, Dr. Andrew Williamson, and Dr. Giulia Galli in Lawrence Livermore Nat'l Lab for performing the first principle calculations on the SRN and SRO microstructure which was correlated to the experimental data collected during this thesis. To Dr. Tung-Wah Frederick Chang, Vlad Sukhovatkin, and Dr. Edward Sargent in Univ. of Toronto for excitation/emission lifetime and efficiency measurements and also the experiment of energy transfer from SRN to PbS QD. To Maria Hiltunen in VTT Electronics for her simulation of Thue Morse waveguide structure. To all MURI members on the silicon laser project. Finally to all Pirelli members on the integrated photonic device project.

I am deeply grateful for the proofreading by Dr. Daewon Hong, Dr. Mike Stolfi, Dr. Victor Nguyen, Dr. Winne Ye, Dan Gutmann, and Meekyung Kim. Their comments made my thesis more complete.

I learned not only by performing experiments but also from the work of others. It has been great honor to have served as a reviewer for Applied Physics Letters and Journal of Applied Physics on papers in the topics of silicon nanocrystals and GaN. I learned a lot during my review processes.

In addition to the people I met from the research side I met so many good people through other avenues during my Ph.D. period. KGSA (Korean Graduate Student Association) and KGMSE ('KG'SA in the department of Materials Science and Engineering) members have made my life at MIT more enjoyable even with the somewhat stressful experience of performing research. Especially during my presidency periods of KGSA and KGMSE I met so many people (including high level managers from highly reputable Korean companies, journalists, and producers) not only at MIT but also in Korea. I have collected more than 300 business cards mostly during those periods. I learned personally how to serve people, organize and contribute to make the society better and more enjoyable. Especially for the colleagues I studied with for the core courses and for the qualifying exams, I am really grateful. Eastgate and Westgate members and their spouses were all good people to our family during our stay. I was also involved in SNUAANE (Seoul National University Alumni Association, New England) and KSEANE (Korean-American Scientists and Engineers Association, New England), as an executive committee member, where I met highly talented and good mannered people from whom I could learn a lot. Especially Dr. Sangrae Yoon and Dr. Hong Kyun Choi have helped me so much in person. I also enjoyed so many gatherings with SNUCHOIR OB members in Boston chapter even though we could sing together only several times. Highly intellectual discussion with MENSA and ULTRANET members always stimulated my mind. Especially many members in Mega foundation let me enjoy intellectual discussion a lot. Thank you, Dr. Gina LoSasso. My church colleagues, seniors and pastors in the CKPC (Cambridge Korean Presbyterian Church) cheered me up a lot and they always prayed for me and for my family. 72 ttorae friends in SaRang Community Church in Korea, especially RNA members, supported me so much. I am very proud of their endless service with loving care to patients for more than 10 years. I do love you guys. '91 classmates of the dept. of inorganic materials science and

engineering in SNU are always my mental supporters. Dr. Ji-Jon Sit was my MIT mentor and he cared for me a lot.

For me to come to MIT there were so many people who helped me in person. Prof. Euijoon Yoon, as my master advisor, supported a lot. He kindly wrote me a recommendation letter for me to be a recipient of a national scholarship. He supported and helped me in person even during my Ph.D. period. Prof. Hyeong Joon Kim and Prof. Hyoun-Ee Kim supported me by writing recommendation letters. I do appreciate your support. All the people I have known during my work period at LG Electronics Institute of Technology for more than 5 years have been always a great memory. I met many of them even in person during MRS conference periods in Boston every year. I learned a lot personally from the late Dr. Min Hong Kim in so many aspects. I also met many LG members during my Ph.D. course and they always cheered my work here and made me proud of being an LG alumnus.

During my Ph.D. course at MIT I also enjoyed the Sloan (MBA school at MIT) courses that I took for my minor program (Management and Business Administration). I also enjoyed the courses in economics department such as macroeconomics and microeconomics. From these experiences I learned what kind of classes MBA students take and how they are different from those in the engineering school. I will not forget these experiences in my life; they will be great asset for a long time.

Dr. Deo Shenai at Rohm and Haas graciously supported my completion of Ph.D. work. Dr. Jeff Calvert and Dr. Sarah Reybuck also understood some delay in the completion schedule and provided their highest support for me.

I would like to thank all my family members for always being supportive of my studies and activities. Many thanks especially to my wife, Eun Hie Kim, who always supported my study despite the fact that she has endured a difficult period for such a long time. I deeply feel sorry about that and want to express my best gratitude from deep in my heart to her. My daughter, Michelle Yi, is always lovely and cute. Even though she does not understand what I have in mind and how challenging my life has been, she was a great relief for me. My parents, my sister and her husband have wished my success always. My parents in law, sisters in law and their husbands always supported and cheered my family a lot. I feel thankful deeply for that.

Finally I want to acknowledge my funding sources: the Ministry of Information and Communication in Korea (National Scholarship), Pirelli in Italy, and the Department of Defense's MURI (Multidisciplinary University Research Initiative) program.

Table of Contents

1. Introduction......11
1.1. Si photonics......11
1.2. Silicon-based light emitter......14
1.3. Why a silicon laser?......18
1.4. SRN and Er:SRN......19
1.5. Energy transfer......20
1.6. Aperiodic photonic structures......23
1.7. Racetrack resonator and others......26
1.8. References......26

2. Silicon rich nitride......29
2.1. Light emission from silicon-rich nitride nanostructures......29
2.1.1. Introduction......30
2.1.2. Fabrication and analysis......31
2.1.3. Experimental results......32
2.1.4. First principle calculation......34
2.1.5. Conclusion......41
2.1.6. References......41
2.2. Light emission efficiency and dynamics in silicon-rich nitride films......43
2.2.1. Introduction......43
2.2.2. Fabrication and analysis......45
2.2.3. Experimental results and discussion......46
2.2.4. Conclusion......53
2.2.5. References......54

3. Emission enhancement from silicon rich nitride......57
3.1. One dimensional Thue-Morse aperiodic light emitting structure......58
3.1.1. Introduction......59
3.1.2. Fabrication......60
3.1.3. Experimental results......61
3.1.4. Conclusion......68
3.1.5. References......69
3.2. Aperiodic waveguide structures......70
3.2.1. Introduction......70
3.2.2. Concept of aperiodic waveguide and discussion......70
3.2.3. Fabrication results and the related issues......73
3.2.4. Conclusion......76
3.2.5. References......77
3.3. Sequential annealing technique for light enhancement......77
3.3.1. Introduction......77
3.3.2. Nucleation of the silicon nanocrystals......77

3.3.3. Emission enhancement from Si nanocrystals..........................78
3.3.4. Experimental results and discussion....................................80
3.3.4.1. Concept of sequential annealing...............................80
3.3.4.2. Behavior with varied Si contents...............................84
3.3.5. Conclusion..87
3.3.6. References..88

4. Electrical properties and electroluminescence of SRN 89
4.1. Introduction..89
4.2. Electrical injection improvement..90
4.3. Light emitting device and electroluminescence.............................97
4.4. Conclusion...101
4.5. References...101

5. Optical properties of Er:SRN...103
5.1. Introduction...103
5.2. Fabrication and analysis...104
5.2.1. Investigation on the process conditions..............................106
5.3. Optical properties of Er:SRN...108
5.3.1. Luminescence optimization..108
5.3.2. Non-resonant pumping, excitation cross section, and upconversion.........113
5.3.3. The relationship between SRN emission and Er emission..........122
5.4. Er sensitization with varied Si content..................................125
5.5. Discussion on gain related parameters with optical pumping..................127
5.5.1. Effect of sensitizer density...130
5.5.2. Dependency on coupling coefficient................................131
5.5.3. Effect of sensitizer excitation cross section.........................133
5.6. Energy transfer to lead sulphide (PbS) quantum dots............................134
5.6.1. Introduction..135
5.6.2. Materials preparation...136
5.6.3. Experimental results and discussion..................................137
5.7. Conclusion...141
5.8. References...142

6. Si racetrack resonator...145
6.1. Introduction...145
6.2. Device design..146
6.2.1. Waveguide dimension for single mode...............................146
6.2.2. Bending radius...147
6.2.3. Coupling length...148
6.2.4. Resonance..151
6.2.5. Quality factor...152
6.3. Fabrication process and related issues...152

6.3.1. Thermal oxidation....155
6.3.2. Gap narrowing with thermal oxidation....156
6.3.3. Nitride and oxide removal....158
6.3.4. Wet treatment for smoothening....161
6.3.5. Oxide deposition and selective removal....162
6.3.6. Er:SRN deposition....164
6.4. Optical measurement....165
6.4.1. Loss measurement....167
6.4.2. Observation of resonance....168
6.4.3. Gain measurement....171
6.5. Conclusion....172
6.6. References....173

7. Optical and electrical excitation of Er....175
7.1. Introduction....175
7.2. Electrical properties of Er:SRN....175
7.3. Electrically injected light emitting device and electroluminescence....177
7.4. Detailed comparison and analysis of optical and electrical excitation of Er..179
7.5. Alternative approach for Er excitation by electrical injection....185
7.6. Discussion on gain related parameters with electrical pumping....190
7.6.1. Effect of loss....192
7.6.2. Dependence on Er concentration....193
7.6.3. Importance of upconversion coefficient....195
7.6.4. Effect of coupling....196
7.6.5. Excitation cross section....198
7.7. Conclusion....201
7.8. References....203

8. Conclusion and future work....205
8.1. Conclusion....205
8.2. Important factors....209
8.3. Future work....210

Chapter 1. Introduction

1.1. Si photonics

The microelectronics industry has followed the general trend of Moore's law where performance enhancement is achieved through shrinking the gate width and packing the gates densely on a chip. However, as the cell size is reduced, the gate delay is no longer the limiting factor. As the gate width becomes less than 0.1 μm, due to closely packed transistors and the increased length of metal interconnect, the limiting factor in delay is from interconnect delay rather than gate delay [1, 2]. As the device interconnection becomes more complex and the number of metal levels increases, the total length of metal interconnects increases dramatically (Fig. 1.1) [3]. As shown in fig. 1.2, the interconnect delay dominates the total delay as the gate width shrinks [4]. The long length of interconnects in the chip results in huge RC delay and causes power dissipation issues. Fig. 1.3 shows the magnitude of power density increase for each calendar year. As the computing power increases, the power density approaches that of a nuclear reactor and a rocket nozzle [5]. This situation will only get worse as the cell size decreases. As a result, several researchers are investigating novel approaches to solve the RC delay and power dissipation issues. One of the strongest candidates is the monolithic integration of Si photonics and electronics due to its low heat dissipation, low cross-talk, and lack of latency issues. Si photonics utilizes light transmitted through optical interconnects to exchange signals between transistors. If successful, this approach will lead to a dramatic change in information carrying capacity of device interconnects. Fig. 1.4 shows the increase in telecommunications information carrying capacity versus time. It is clear to see how optical communication outperforms other previous communication systems in terms of information carrying capacity. III-V semiconductors, despite possessing superior optical properties compared to Si, form devices that are difficult to manufacture and assemble. Furthermore, hybrid integration of III-V based devices on Si integrated circuits is very challenging because it requires very precise alignment between the optics and electronics. To achieve monolithic integration of Si photonics and electronics at the chip level several components

are required such as a light source, a modulator, a waveguide, and a detector. Among these components the light source is the most important but its fabrication is difficult due to the intrinsic limitation of Si as a light emitter. Due to the indirect bandgap of Si, light emission from this material occurs through low probability phonon mediated processes that are inhibited by fast Auger recombination, and free carrier absorption [6]. Despite this discouraging situation, if efficient light emission using CMOS compatible materials such as Si, SiO_2 and Si_3N_4 is achieved, that result will further stimulate optical interconnect research and more quickly lead to the demonstration of monolithic integration of Si photonics and electronics. Recently it was demonstrated that Si-nanocrystals are efficient sensitizers of the emission of rare earth materials, specifically Er aroms that producing 1.54 μm emission which is the lowest absorption wavelength of SiO_2 based optical fibers. The phenomenon of emission sensitization is related to the efficient energy transfer from Si-nanocrystals to Er atoms [7-12]. Investigation of efficient energy transfer phenomena is highly interesting since, through this approach, we can combine other more efficient light emitters with Si-based materials provided we can control the energy transfer phenomena in a smart way. In addition to the importance of light emission, light control by using aperiodic complex photonic structure can not be disregarded since light can be greatly enhanced with multi-wavelength characteristics within these structures.

A detailed review of Si-based light emission is provided in the following sections.

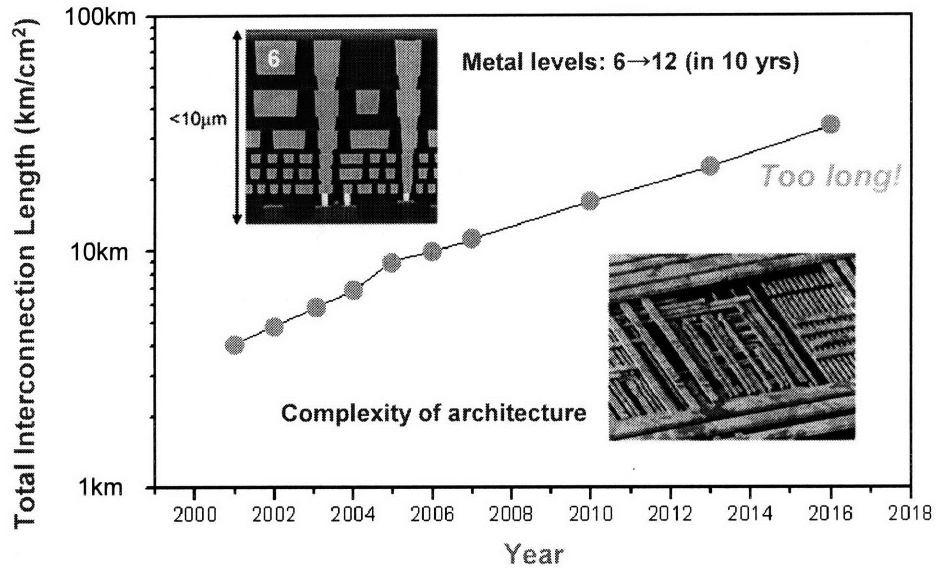

Figure 1.1. Total interconnection length with calendar year. Insets show the complexity of architecture and metal levels.

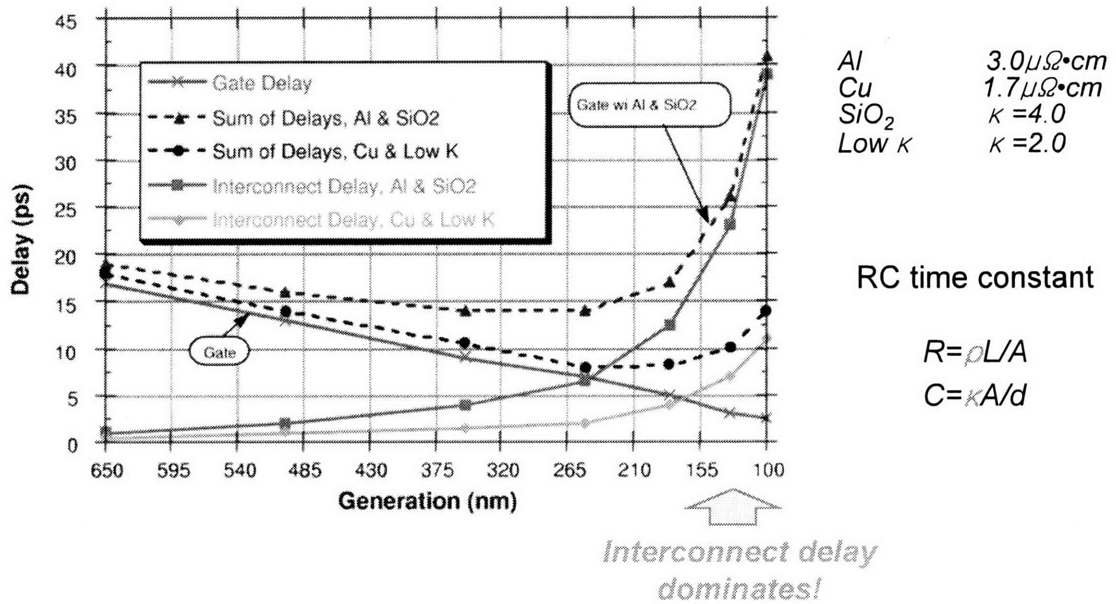

Figure 1.2. Total delay combining interconnect delay and gate delay for various interconnect and dielectric materials.

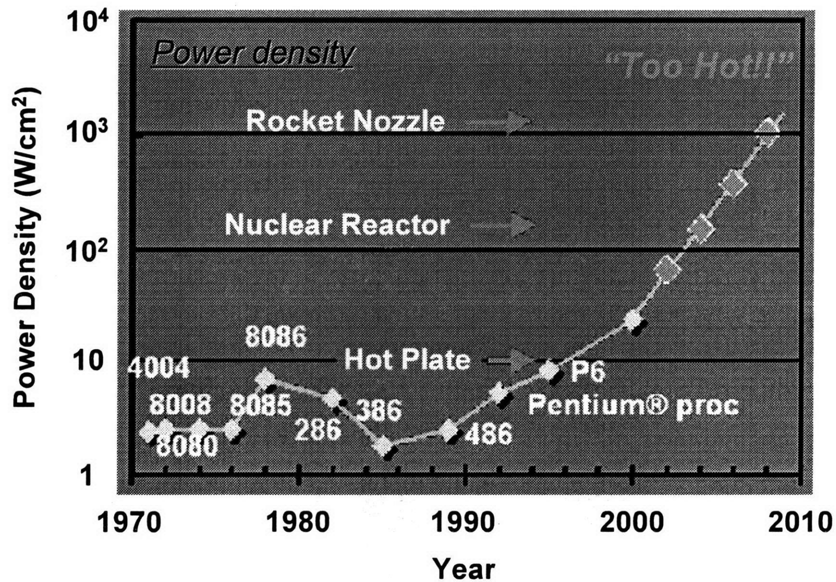

Figure 1.3. Power density with calendar year. As the computing power increases, power density approaches that of a nuclear reactor and rocket nozzle.

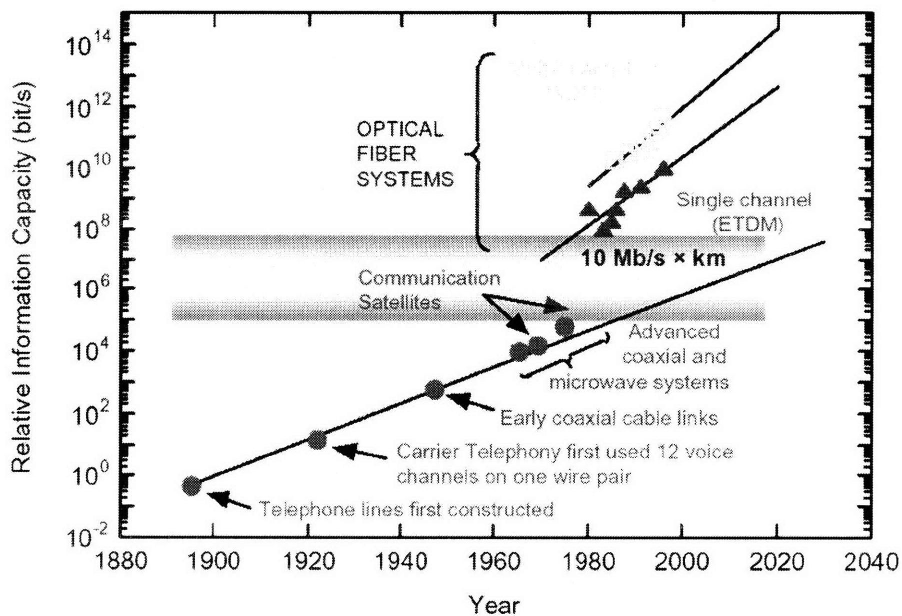

Figure 1.4. Increase in the information carrying capacity versus time [1].

1.2. Silicon-based light emitter

(1) Fundamental limitation of light emission from silicon

Silicon is an indirect bandgap material which has a very long radiative lifetime. Since Si has a very long radiative lifetime, excited free carriers have a high probability of finding non-radiative recombination centers. Additionally, in Si, Auger recombination is very efficient and free carrier absorption is high [6]. Due to the combination of these factors, achieving light emission from silicon is not an easy task. Fig. 1.5 shows a schematic of these competing processes.

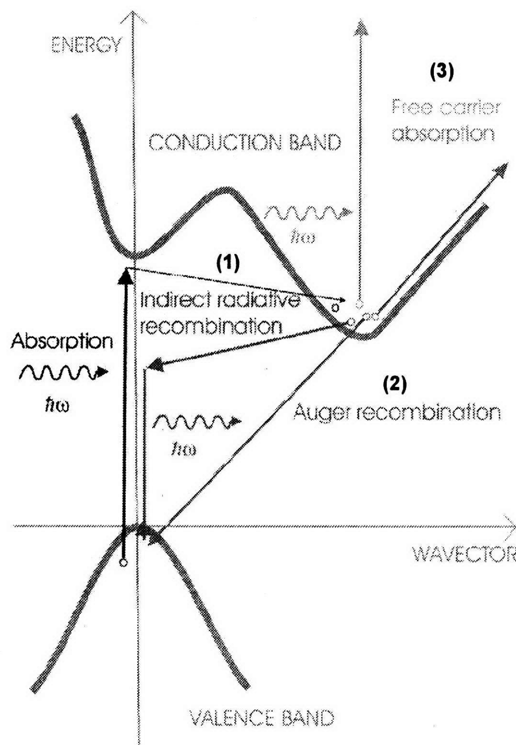

Figure 1.5. Three main reasons why silicon is poor light emitter. (1) Silicon is an indirect band-gap material (2) Auger recombination is very efficient (3) Free carrier absorption is high [6].

(2) Approaches to overcome the intrinsic limitations of Si

Several approaches have been suggested to overcome the intrinsic phenomena that limit light emission from bulk silicon. Ultra-pure silicon, with a surface passivated by native oxide that acts as a carrier recombination site which increases the probability of radiative recombination, was investigated. This technique was used in combination with

surface textures to enhance the light extraction efficiency [13]. However, this approach has fundamental limitations since using ultra-pure silicon and surface texture is not compatible with standard CMOS processing. The modulation speed of the device is also limited by a long radiative lifetime.

Another approach of applying dislocation engineering in bulk Si was suggested. This technique uses strain from localized dislocation loops to reduce non-radiative recombination channels [14]. However, this approach does not eliminate Auger recombination and free carrier absorption which are harmful for population inversion.

Low dimensionality is considered as a strong solution to enhance emission efficiency by increasing the radiative probability through the quantum confinement effect. To achieve low dimensionality in Si, researchers used electrochemical etching with a dilute HF solution to create porous Si, a sponge-like network structure with nanometer scale joint parts connected to each other through nanowire structures [15]. Through the quantum confinement effect and by reducing the probability that free carriers reach nonradiative recombination centers the light emission efficiency was greatly increased and bright visible luminescence was achieved at room temperature. External quantum efficiencies in porous Si of up to 23% have been achieved through a high pressure water vapor technique [16]. Porous Si also reduces the effective refractive index of the Si making the light extraction much easier. However, due to the fragile and weak network structure, aging and uncontrollable performance of the device was observed which is a serious fundamental limitation of this approach.

Many other approaches have been widely used to overcome the intrinsic problems of porous Si. After deposition of a sub-stoichiometric silicon oxide (SRO, silicon rich oxide) film, high temperature annealing was performed to induce Si nanocrystal formation through phase separation of silicon and silicon dioxide from the SRO [17-21]. The size and density of the Si nanocrystals can be controlled by changing the annealing temperature and time. Compared to the porous Si structure, the structure of Si nanocrystals embedded in SRO is very stable with time. Optical gain, recently demonstrated in Si nanocrystals

embedded in SiO_2 matrices, has opened the race towards the fabrication of an integrated, fully Si-based laser [22-27].

Even with the advantages of the SRO system, stoichiometric oxide provides a high barrier for current injection into the Si nanocrystal preventing the easy flow of current into Si nanocrystal devices. Therefore, we should consider other materials systems for inducing Si nanocrystal formation through phase separation that have matrices with smaller barriers for current injection.

(3) Physics of light emission from silicon in reduced scale

a. Quantum confinement effect

High luminescence quantum efficiency can be obtained through quantum confinement since spatial confinement of the free carriers prevents them from reaching nonradiative recombination centers and thus increases the radiative recombination probability. According to the quantum confinement model, the band gap decreases as the nanocrystal size is reduced [28]. It has been demonstrated that this correlation of band gap to nanocrystal size is true up to a certain size of nanocrystals. Below that certain size surface passivation plays an important role and influences the emission energy of the nanocrystals.

b. Surface state effect

The surface to volume ratio increases as the nanocrystal size is reduced. In particular, researchers have observed that Si=O bonds at the interface between the Si nanocrystal and the SiO_2 matrix has a crucial role in light emission mechanism of this materials system, especially for the case of small sized nanocrystals [29-32]. Light emission from this localized state at the interface, combined with the quantum confinement model, should also be considered as a plausible mechanism for light emission of nanocrystals.

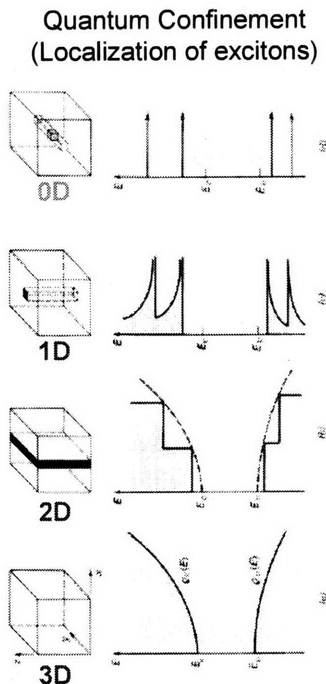

Quantum confinement effects

- Electron density of state modifications
- Carrier localization/wavefunction overlapping
- Bandstructure modifications

Surface chemistry effects

- Localized states
- Electron density of state modifications
- Carrier localization/wavefunction overlapping
- Bandstructure modifications

Nanoscale structures with size comparable to the exciton Bohr radius

d = 1~3nm

Figure 1.6. Chart explaining the physics of light emission from silicon in reduced scale.

1.3. Why a silicon laser?

As discussed in the previous sections, silicon has a fundamental physical limitation preventing it from achieving efficient light emission. Researchers in the field of silicon photonics have solved many issues impacting other devices in the photonics system and have demonstrated the silicon (and germanium, which is also CMOS compatible) based modulator and detector as well as Si compatible waveguides. Despite these advances an efficient light source using silicon compatible materials has not been demonstrated. As a result external light sources have been considered. Integration of any discrete laser device requires delicate and precise alignment which is painstaking, causes high fabrication costs, leads to unavoidably very low yield and, ultimately, causes the final price of the product to increase dramatically. This has stimulated a strong and diverse quest to achieve a silicon laser. This is especially true in the pursuit of the electrically injected silicon laser because the alternative, a silicon laser pumped by an external optical source, can not meet the requirement of complete integration with Si electronics. If an electrically injected silicon

laser is achieved, the optical communication and silicon photonics technologies can be applied to increase the bandwidth of integrated circuits and allow Moore's law to continue. Combined with the low processing cost of the mature silicon technology this approach will provide higher computing power for PC's, servers and personal devices that use microprocessors for the benefit of the general public, not only professionals. Even with these immense benefits the fundamental work required for demonstrating an electrically injected silicon laser are far from completion.

1.4. SRN and Er:SRN

Researchers have tried to overcome the fundamental physical limitation of bulk silicon as a light emitter by fabricating Si structures with low dimensionality as discussed in section 1.2. This pursuit finally led to the discovery of the widely investigated material system, Si-nanocrystals (Si-nc) nucleated from a Si-rich oxide film (SRO), which exhibits efficient room temperature light emission under optical pumping and the possibility of achieving light amplification and sizable optical gain [4, 10-16]. However, the huge electrical barrier mismatch between Si and SiO_2, observed for Si-nc embedded in SiO_2 matrices, prevents the fabrication of stable and efficient electrically-driven devices. Moreover, the achievement of high emission efficiency is severely impeded by the slow radiative lifetime of Si-nc in SiO_2 (approx. 10 to 100 μs) which competes with the much faster non-radiative channels (Auger recombination, in particular). Therefore, there is a need to investigate alternative CMOS-compatible approaches that can yield intense and fast light emission in nanostructured silicon systems that are also suitable for efficient electrical excitation. An intriguing possibility is the nucleation of Si-nc in dielectric environments with smaller band-gaps than SiO_2. SRN provides a much smaller electrical barrier to injected carriers and is expected to have a lower current density. Furthermore, Er:SRN can also serve as a light emitting material with the emission wavelength of 1.54 μm for telecommunication since it utilizes the advantages of emission sensitization previously demonstrated in Er:SRO systems with the additional benefit of a lower current density. A detailed background of these phenomena will be also provided in chapter 5. Even with the

many advantages of SRN and Er:SRN mentioned above, an extensive investigation of this material system, especially focusing on the optical properties, electrical properties, electroluminescent behavior, and the difference in the mechanism of Er excitation by optical and electrical pumping has not been completed. The detailed information and discussion regarding these properties and phenomena that is provided in later chapters will shed light onto the way to achieve an electrically injected silicon based laser device.

1.5. Energy transfer

Energy transfer is a very important phenomenon which is used to explain the efficient excitation of Er atoms via the Si nanocrystal embedded SiO_x matrix, Er:SRO [7-11]. The Si nanocrystal has a two or three orders of magnitude higher absorption cross-section than the Er atom. Therefore, understanding the detailed phenomena governing energy transfer in the Er:SRO system is important for further and extreme utilization of the Er atom for light emission. The following discussion will provide the basic background for a better understanding of these phenomena which can then be applied to the case of Er atoms in an SRN matrix. We will also provide a more detailed introduction with the discussion of our experiments, including the energy transfer from SRN to colloidal PbS quantum dots, in chapter 5.

a. Resonant energy transfer

This section is basically a recapitulation of what J. Heitmann *et al.* described for resonant energy transfer [33].

We can consider at least four different resonant energy transfer mechanisms for the system: the Forster transfer process, the re-absorption process, a transfer due to the formation of complexes, and the energy transfer due to collisions [34]. This description does not consider bio or polymer related systems. The collision-related process requires the transport of the donor and the acceptor and is only achieved in liquids or gases. The formation of complexes requires molecular contact between donor and acceptor. The re-

absorption process involves a photon emitted by the donor which is re-absorbed by the acceptor.

In the Er doped SRO system the excitonic Si nanocrystal lifetime is decreased and the emission and absorption spectra are nearly unchanged. These observations indicate that the Förster process is the fundamental mechanism of the energy transfer [33].

Förster developed the theory of energy transfer through a dipole-dipole interaction between an excited donor and an acceptor [35]. A short summary of the mechanism will be given here to provide a better understanding of the theory. The simple classical theory of the electric field implies that the field of the oscillating dipole (donor) can be represented for r (distance from the donor) up to the r^{-3} term. The r^{-3} term basically represents the Förster energy transfer which is dominant for the near field case where r is small while the electric field is dominated by the term with an r^{-1} dependence for larger r. The range where the field is regarded as near one is within the sphere of a radius $0.1 \times b$ with:

$$b = \frac{\lambda}{2\pi n} \tag{1}$$

where λ is the wavelength of the donor luminescence, and n is the refractive index of the matrix (SRO). b can be estimated to be below 100 nm for λ of 600 ~ 1000 nm and n of 1.4 ~ 1.6. Therefore, the volume with a radius of 10 nm around the donor (Si-nc) can be regarded as the Förster zone. If acceptors, such as Er^{3+} ions, reside within this range, and there is spectral overlap between the donor and acceptor states, Förster transfer is possible. The schematic diagram in fig. 1.7 shows the transfer process. Even though the diagram does not show the resonant character clearly, it explains the process kinetics well. The transfer efficiency of the energy transfer E_T is given by the percentage of all absorbed photons which are transferred nonradiatively from the donor to the acceptor:

$$E_T = \frac{k_T}{k_T + k_D + k_{Di}} \tag{2}$$

where k_D, k_{Di}, k_T are the decay rates as introduced in fig. 1.7.

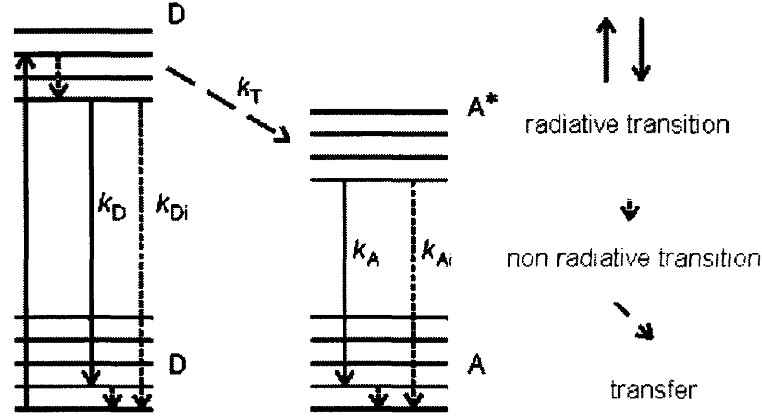

Figure 1.7. Simplified energy schema of a resonant energy transfer adapted from [34]. D represents the donor and A the acceptor. The star indicates the excited states. The symbol *k* represent the transition rates for the different processes (D: donor, A: acceptor, T: transfer). The nonradiative transfer rates are assigned with *i*.

We can also determine the transfer efficiency E_T by using the lifetime of the donor in the absence of an acceptor (τ_D) and in the presence of an acceptor (τ_{DA}).

$$E_T = 1 - \frac{\tau_{DA}}{\tau_D} \qquad (3)$$

$$\text{where } \tau_D = \frac{1}{k_D + k_{Di}} \text{ and } \tau_{DA} = \frac{1}{k_T + k_D + k_{Di}} \qquad (4)$$

The transfer efficiency can also be expressed using the Förster distance R_0, where the transfer probability is 50% of all possible processes. In other words, at the Förster distance, the decay rates for processes within the donor and for the energy transfer to the acceptor are the same ($k_T = k_D + k_{Di}$).

$$E_T = \frac{R_0^{\,6}}{R_0^{\,6} + r^6} \qquad (5)$$

The Förster distance R_0 scales with:

$$R_0^{\,6} \propto \frac{\kappa^2 Q_D J}{n^4} \qquad (6)$$

where κ is the orientation of the donor-acceptor dipole, Q_D is the quantum efficiency of the donor, J *is* the overlapping integral of the donor emission and acceptor

absorption spectra, and n is the refractive index of the matrix. We clearly see from these expressions that at a given k and n the transfer efficiency E_T increases with increasing quantum efficiency of the donor and with increasing overlap of the donor and acceptor spectra.

b. Non-resonant energy transfer

According to the theory by Miyakawa and Dexter, the probability of the energy transfer W is [36]

$$W = W_0 \exp(-\beta \Delta E), \tag{1}$$

where ΔE is the energy mismatch (the difference between the transition energies of a donor and an acceptor), β is a constant which depends on the nature of the phonons in the host lattice and the strength of the electron-phonon coupling, and W_0 is the probability for a ΔE of zero. The probability also depends on the number of excited phonons. At a temperature T the probability of energy transfer is expressed, analogous to the multiphonon relaxation process, as follows:

$$W(T) = W(\overline{n}_i + 1)^N \tag{2}$$

for energy transfer involving the emission of N phonons, and

$$W(T) = W(\overline{n}_i)^N \tag{3}$$

for the absorption of N phonons, where $\overline{n}_i$ is the average occupation number of the ith vibrational mode which is given as

$$\overline{n}_i = \frac{1}{\exp(\frac{h\nu_i}{kt}) - 1} \tag{4}$$

1.6. Aperiodic photonic structures

For laser operation three key ingredients are necessary typically, such as active material with low loss, pumping source for energy supply, finally optical cavity or other feedback mechanism for positive optical feedback (Fig. 1.8).

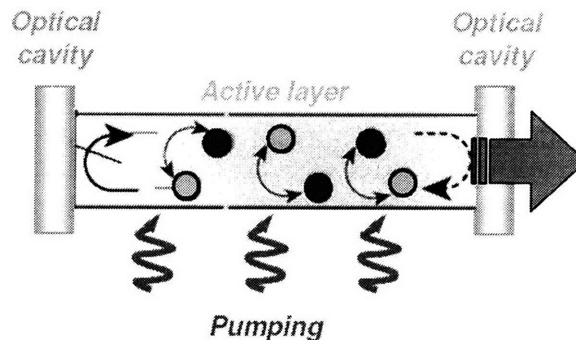

Figure 1.8. Schematic diagram showing typical laser structure with key ingredients such active layer with low loss, pumping source, and optical cavity.

Typically laser action occurs when the single pass gain equals the total loss within the optical cavity. The optical cavity is formed using periodic Bragg gratings or multilayer optical coatings and provides optical feedback required to achieve lasing. As shown in fig. 1.9, various approaches for optical feedback can be considered. Well known periodic structure leads to regularly spaced resonance peaks in wavelength. Random cavity results in resonance peak in random wavelength from multiple scattering with coherent feedback. However, aperiodic photonic structure such as Thue-Morse photonic structure can provide multi-wavelength peaks fixed by deterministic generation rule. Its characteristic is intermediate between random structure and periodic structure. The almost random dielectric matrix of the aperiodic photonic structure causes multiple light scatterings and the diffusion of light waves is localized following a power law (weak localization). Strong field enhancement at specific wavelengths corresponding to resonant transmission states also occurs.

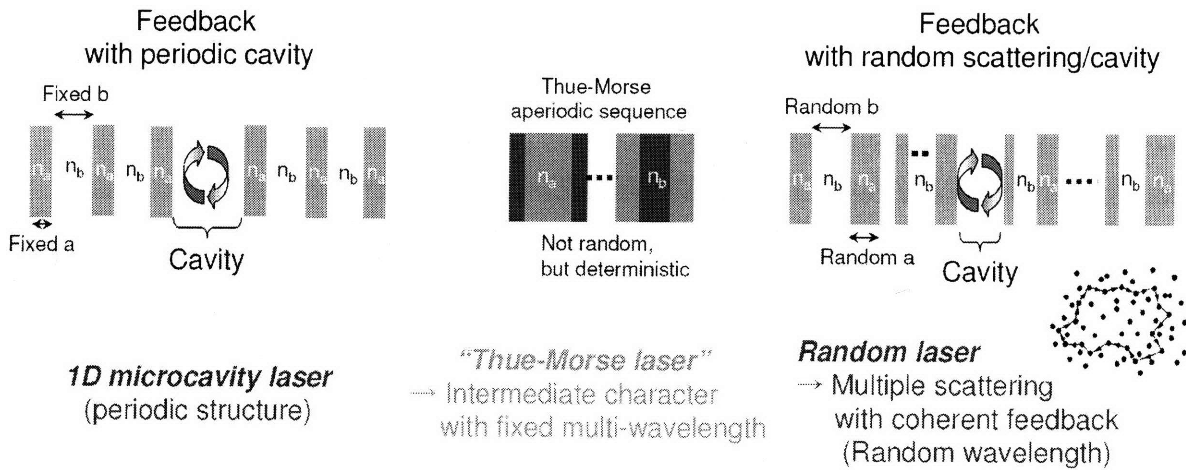

Figure 1.9. Various approaches for optical feedback: Periodic optical cavity, Aperiodic photonic structure, and random cavity.

Aperiodic photonic structures are deterministically generated structures with a non-periodic refractive index modulation. Aperiodic photonic structures show characteristics that are intermediate between periodic [37-39] and random structures [40-43]. Aperiodic photonic structures show unique physical properties such as the formation of multiple frequency gap regions called pseudo bandgaps [44, 45], the presence of fractal transmission resonances with local field enhancement [46, 47] and the occurrence of "critically" localized states [48, 49]. This thesis focused on the Thue-Morse sequence [50-52]. The generation rule for the Thue-Morse sequence is $\sigma_{T\text{-}M}$: A→AB, B→BA [53]. The lower order Thue-Morse sequences are given by the strings: S_0=A, S_1=AB, S_2=ABBA, S_3=ABBABAAB, etc. Recently optical Thue-Morse photonic structures were experimentally demonstrated for the case of A=SiO_2 and B=Si [54]. If the Si layer is replaced with light emitting Si-rich nitride (SRN), the emitted light from SRN can be enhanced by the Thue-Morse structure [55]. This structure and concept can be applied to waveguide structures ranging from on-chip light amplification and lasing, to optical bio-sensing and dense optical wavelength division multiplexing (WDM). More detailed information regarding one dimensional aperiodic structures and the aperiodic waveguide structure will be provided in chapter 3.

1.7. Racetrack resonator and others

A racetrack resonator (or ring resonator) is one of the important building blocks for a photonics system with complex functionality. Applications of the racetrack resonator include as a WDM device, as an optical modulator and as a laser. Resonant devices are appropriate for high index contrast photonics systems since for high index contrasts 1) the interaction distance between the ring and bus waveguides is small, 2) small bending radii can be achieved with low loss, and 3) the evanescent field from the waveguide decays fast. These features allow the photonic system to be composed of small resonators with weak coupling leading to high performance.

Several other topics, including sequential annealing, will be introduced in the first part of each section.

1.8. References

[1] L.C. Kimerling, Appl. Surf. Sci. **159-160**, 8 (2000).

[2] L. Pavesi, J. Phys.: Condens. Matter **15**, R1169 (2003).

[3] www.intel.com/research/silicon/CMIC_2002_Jose_Maiz.htm

[4] www.amanogawa.com/epep2000/files/jose1.pdf

[5] www.science.unitn.it/~semicon/

[6] Mater. Today, 1, Jan. 2002.

[7] A. J. Kenyon, P. F. Trwoga, M. Federighi, and C. W. Pitt, J. Phys. Condens. Matter **6**, L319 (1994).

[8] M. Fujii, M. Yoshida, Y. Kanzawa, S. Hayashi, and K. Yamamoto, Appl. Phys. Lett. **71**, 1198 (1997).

[9] G. Franzò, F. Iacona, V. Vinciguerra, and F. Priolo, Mater. Sci. Eng. B, **69/70**, 338 (1999).

[10] P. G. Kik, M. L. Brongersma, and A. Polman, Appl. Phys. Lett. **76**, 2325 (2000).

[11] F. Priolo, G. Franzò, F. Iacona, D. Pacifici, and V. Vinciguerra, Mater. Sci. Eng. B, **81**, 9 (2001).

[12] J. H. Shin, M.-J. Kim, S.-Y. Seo, and C. Lee, Appl. Phys. Lett. **72**, 1092 (1998).

[13] M. A. Green, J. Zhao, A. Wang, P. J. Reece, and M. Gal, Nature **412**, 805 (2001).

[14] W. L. Ng, M. A. Lourenço, R. M. Gwilliam, S. Ledain, G. Shao, and K. P. Homewood, Nature **410**, 192 (2001).

[15] L. T. Canham, Appl. Phys. Lett. **57**, 1046 (1990).

[16] B. Gelloz, A. Kojima, and N. Koshida, Appl. Phys. Lett. **87**, 031107 (2005).

[17] T. Shimizu-Iwayama, K. Fujita, S. Nakao, K. Saitoh, T. Fujita, and N. Itoh, J. Appl. Phys. **75**, 7779 (1993).

[18] K. S. Min, K. V. Shcheglov, C. M. Yang, H. A. Atwater, M. L. Brongersma, and A. Polman, Appl. Phys. Lett. **69**, 2033 (1996).
[19] F. Iacona, G. Franzò, and C. Spinella, J. Appl. Phys. **87**, 1295 (2000).
[20] S. Hayashi, T. Nagareda, Y. Kzawa, and K. Yamamoto, Jpn. J. Appl. Phys. **32**, 3840 (1993).
[21] U. Kahler and H. Hoffmeister, Opt. Mater. **17**, 83 (2001).
[22] L. Pavesi, L. Dal Negro, C. Mazzoleni, G. Franzò, and F. Priolo, Nature **408**, 440 (2000).
[23] L. Khriachtchev, M. Rasanen, S. Novikov, and J. Sinkkonen, Appl. Phys. Lett. **79**, 1249 (2001).
[24] L. Dal Negro, M. Cazzanelli, L. Pavesi, S. Ossicini, D. Pacifici, G. Franzò, F. Priolo, and F. Iacona, Appl. Phys. Lett. **82**, 4636 (2003).
[25] J. Ruan, P. M. Fauchet, L. Dal Negro, M. Cazzanelli, and L. Pavesi, Appl. Phys. Lett. **83**, 5479 (2003).
[26] L. Dal Negro, M. Cazzanelli, B. Danese, L. Pavesi, F. Iacona, G. Franzò, and F. Priolo, J. Appl. Phys. **96**, 5747 (2004).
[27] M. Cazzanelli, D. Kovalev, L. Dal Negro, Z. Gaurro, and L. Pavesi, Phys. Rev. Lett. **93**, 207402 (2004).
[28] N. M. Park, C. J. Choi, T. Y. Seong, and S. J. Park, Phys. Rev. Lett. **86**, 1355 (2001).
[29] M. V. Wolkin, J. Jorne, P. M. Fauchet, G. Allan, and C. Delerue, Phys. Rev. Lett. **82**, 197 (1999).
[30] A. J. Williamson, J. C. Grossman, R. Q. Hood, A. Puzder, and G. Galli, Phys. Rev. Lett. **89**, 196803 (2002).
[31] A. Puzder, A. J. Williamson, J. C. Grossman, and G. Galli, J. Chem. Phys. **117**, 6721 (2002).
[32] E. Degoli, G. Cantele, E. Luppi, R. Magri, D. Ninno, O. Bisi, and S. Ossicini, Phys. Rev. B **69**, 155411 (2004).
[33] J. Heitmann, M. Schmidt, M. Zacharias, V. Yu. Timoshenko, M. G. Lisachenko, and P. K. Kashkarov, Mater. Sci. Eng. B **105**, 214 (2003).
[34] B. Wieb Van Der Meer, G. Coker, and S. –Y. Simon Chen, *"Resonance Energy Transfer – Theory and Data"*, VCH Publisher, New York (1994).
[35] Th. Förster, Ann. Phys. **6**, 55 (1948).
[36] Eichi Okamoto, Hiromitsu Masui, Katsutoshi Muto, and Kenzo Awazu, J. Appl. Phys. **43**, 2122 (1972).
[37] E. Yablonovitch, Phys. Rev. Lett. **58**, 2059 (1987).
[38] S. John, Phys. Rev. Lett. **58** , 2486 (1987).
[39] J. D. Joannopoulos, P. R. Villeneuve, and S. Fan, Nature **386**, 143 (1997).
[40] P. W. Anderson, Philos. Mag. **52**, 505 (1985).
[41] S. John, Phys. Rev. Lett. **53**, 2169 (1984).
[42] M. P. van Albada and A. Lagendijk, Phys. Rev. Lett. **55**, 2692 (1985).
[43] D. S. Wiersma, P. Bartolini, A. Lagendijk, and R. Righini, Nature **390**, 671 (1997).
[44] F. Nori and J. P. Rodriguez, Phys. Rev. B **34**, 2207 (1986).
[45] R. B. Capaz, B. Koiller, and S. L. A. de Queiroz, Phys. Rev. B **42**, 6402 (1990).
[46] T. Fujiwara, M. Kohmoto, and T. Kokihiro, Phys. Rev. B **40**, 7413 (1989).

[47] C. M. Soukoulis and E. N. Economou, Phys. Rev. Lett. **48**, 1043 (1982).
[48] M. Kohmoto, B. Southerland, and C. Tang, Phys. Rev. B **35**, 1020 (1987).
[49] E. Maciá, Phys. Rev. B **60**, 10032 (1999).
[50] Z. M. Cheng, R. Savit, and R. Merlin, Phys. Rev. B **37**, 4375 (1988).
[51] M. Queffélec, "*Substitution Dynamical Systems-Spectral Analysis, Lecture Notes in Mathematics*", 1294, Springer, Berlin (1987).
[52] F. Axel, J. P. Allouche, M. Kleman, M. Mendès-France, and J. Peyrière, J. Phys. (Paris), Colloq. **47**, C3-181 (1986).
[53] N.-H. Liu, Phys. Rev. B **55**, 3543 (1997).
[54] L. Dal Negro, M. Stolfi, Y. Yi, J. Michel, X. Duan, L. C. Kimerling, J. LeBlanc, and J. Haavisto, Appl. Phys. Lett. **84**, 5186 (2004).
[55] L. Dal Negro, J. H. Yi, V. Nguyen, Y. Yi, J. Michel, and L. C. Kimerling, Appl. Phys. Lett. **86**, 261905 (2005).
[56] L. Dal Negro, J. H. Yi, J. Michel, L. C. Kimerling, T.-W. F. Chang, V. Sukhovatkin, and E. H. Sargent, Appl. Phys. Lett. **88**, 233109, (2006).
[57] L. Dal Negro, J. H. Yi, L. C. Kimerling, S. Hamel, A. Williamson, and G. Galli, Appl. Phys. Lett. **88**, 183103 (2006).
[58] I. H. Campbell and P. M. Fauchet, Solid State Comm. **58**, 739 (1986).
[59] P. Mishra and K. P. Jain, Phys. Rev. B, **64**, 073304 (2001).
[60] Luca Dal Negro, Jae Hyung Yi, Lionel C. Kimerling, Sebastien Hamel, Andrew Williamson, and Giulia Galli, IEEE J. Select. Topics Quantum Electron. **12**, 1628 (2006).
[61] L. Dal Negro, J. H. Yi, M. Hiltunen, J. Michel, L. C. Kimerling, S. Hamel, A. Williamson, G. Galli, T. F. Chang, V. Sukhovatkin, and E. H. Sargent, J. Exper. Nanoscience **1**, 29 (2006).
[62] The Photon Design *FimmWave* software was used for optimization of the modal overlap in the waveguide sub-units and the *FimmProp* framework code was used to simulate the mode propagation.

Chapter 2. Silicon rich nitride

As discussed in chapter 1, getting light from the silicon based material is not an easy task due to fundamental physical limitation. By adopting low dimensionality of the silicon based material, especially silicon nanocrystal in SiO_2 matrix, light emission has been reported. However, even with many advantages including, but not limited to, better electrical injection properties, low annealing temperature for nanocrystal formation, and high refractive index for flexible design of photonic device structure, limited number of researches have been performed regarding silicon nitride based matrix.

In this chapter the light emission properties of silicon rich nitride films by PECVD will be provided and discussed. With the first principles simulations we provided how the nitrogen incorporation changes HOMO-LUMO localization behavior and also the microstructure showing the closest agreement with our experimental measurements. Light emission efficiency measurement result and comparison with optimized SRO samples were provided. Low temperature photoluminescence behavior and recombination dynamics were also investigated. The lack of emission tuneability, the PL temperature behavior, and its emission dynamics suggest that the light emission originates from strongly localized radiative states introduced by nitrogen groups that passivate the surface of small Si-nc's, rather than from the core of Si-nc's.

2.1. Light emission from silicon-rich nitride nanostructures

Light-emitting Si-rich nitride films (SRN) were fabricated by PECVD deposition

followed by low temperature (500~900°C) thermal annealing. The optical properties of SRN films were studied by micro-Raman and photoluminescence spectroscopy and indicate the presence of small Si-clusters characterized by broad near-infrared emission, large absorption/emission Stokes shift and nanosecond recombination. Our results are supported by first-principles simulations indicating that nitrogen atoms bonded to the surface of nanometer-sized silicon clusters play a crucial role in the emission mechanism of SRN films. Light emission from SRN systems can provide alternative routes towards the fabrication of optically active CMOS-devices.

2.1.1. Introduction

Light emission from silicon (Si), to date the undisputed material in the microelectronics market, originates from low probability phonon-mediated transitions that unfavourably compete with fast non-radiative de-excitation paths. The lack of practical silicon light emission severely limits the feasibility of a monolithically integrated Si optoelectronics that aims to combine electronic and optical functions on inexpensive integrated Si chips. However, several strategies have been recently developed to turn Si into an efficient light-emitting material [1-5]. The traditional approach is to reduce the Si dimensionality to nanometer scales, where both quantum confinement and surface chemistry effects improve the efficiency of light generation [6-9]. The widely investigated material system, Si-nanocrystals (Si-nc) nucleated from a Si-rich oxide film (SRO), shows efficient room temperature light emission under optical pumping and the possibility to achieve sizable optical gain and light amplification has been recently demonstrated by

several groups [4, 10-16]. However, Si-nc embedded in SiO_2 matrices prevents the fabrication of stable and efficient electrically-driven devices due to a huge barrier mismatch between Si and SiO_2. Moreover, the achievement of high emission efficiency is severely impeded by the slow radiative lifetime of Si-nc in SiO_2 (approx. 10 to 100 μs) which competes with much faster non-radiative channels (Auger recombination in particular). Therefore, there is a need to investigate alternative CMOS-compatible approaches that can yield intense and fast light emission in nanostructured silicon systems that are also suitable for efficient electrical excitation. An intriguing possibility is the nucleation of Si-nc in dielectric environments with smaller band-gaps than SiO_2. Tuneable room temperature visible light emission from Si-nc embedded in silicon nitride matrices and efficient electroluminescence have been recently demonstrated [17-19].

2.1.2. Fabrication and analysis

In this chapter we report on the observations of fast (nanosecond) and intense broad band near-infrared light emission from Si-rich silicon nitride films (SRN) obtained by Plasma Enhanced Chemical Vapor Deposition (PECVD) deposition followed by low temperature (500-900°C) thermal annealing. In addition, we present a microscopic interpretation of our results based on first principles theoretical studies. The samples were fabricated on transparent fused silica substrates through PECVD using an Applied Materials Centura DxZ chamber. The silicon nitride layer was deposited using SiH_4 and N_2 as precursors and the substrate temperature during deposition was 400˚C. Micro-Raman measurements were performed at 514 nm using Kaiser Optical Systems Raman

spectrometer with confocal microprobe. Optical transmission experiments were performed using a commercial Cary 5E double beam spectrophotometer equipped with a PbS detector (for the near infrared range) or a Hamamatsu photomultiplier tube (for the visible range). Room temperature photoluminescence (PL) experiments were performed using a 488 nm Ar pump laser and the radiation was collected by a single grating monochromator coupled to a nitrogen cooled InGaAs phototube. Photoluminescence time decay measurements were obtained using the 457 nm line of a nitrogen-laser pumped dye laser (pulse width ~ 1ns, repetition rate 10 Hz). The light emission was detected using a commercial PTI Time Master system under the collaboration with Prof. Edward Sargent group in Univ. of Toronto.

2.1.3. Experimental results

In fig. 2.1 (a1) we show typical photoluminescence spectra of SRN films annealed for 10 minutes at different temperatures ranging between 500°C and 900°C. The emission lineshape consists of an intense and broad band centred at 1.4 eV, with a large absorption/emission Stokes-shift with respect to the falling-edge of the measured transmission spectrum (Fig. 2.1 (a2)). Figure 2.1 (b1) and (b2) summarizes our study of the effects of post-deposition annealing conditions on the integrated PL intensity trends in SRN films. We found that, at a given temperature (i.e. 700°C) the PL intensity increases rapidly with annealing time (Fig. 2.1 (b2)) while at a fixed annealing time (i.e. 10 min.) the PL intensity is maximized at a temperature around 700°C (Fig. 2.1 (b1)). The observed PL trends are compatible with a SRN light emission mechanism that is controlled, analogously to the SRO case [20], by thermally induced Si diffusion and subsequent cluster nucleation.

In order to confirm this hypothesis we performed micro- Raman analysis

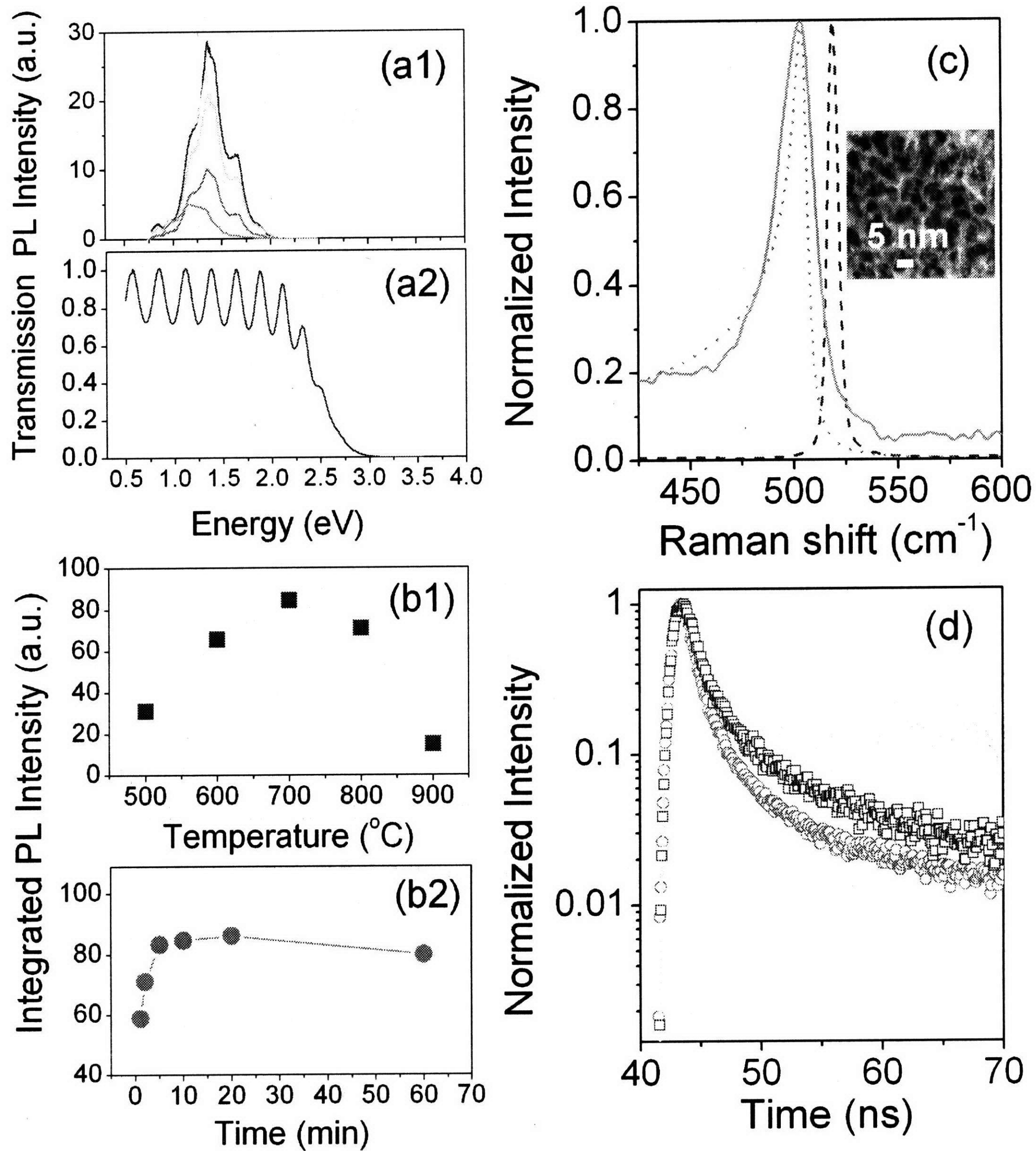

Figure 2.1. (a1) Room temperature photoluminescence (PL) spectra of SRN samples annealed for 10 min. at different temperatures ranging between 500°C (second from the bottom) and 900 °C (first from the bottom). The spectra at intermediate temperatures scale as in panel b1. (a2) Typical transmission spectrum of SRN sample annealed at 700°C. The oscillations in the spectrum originate from wave interference due to the sample thickness (700 nm). (b1) Integrated PL intensity versus annealing temperatures. Annealing time was

10 min. (b2) Integrated PL intensity versus annealing time. Annealing temperature was 700°C. (c) Micro-Raman spectrum of bulk Si (dash line). Micro-Raman spectrum of the SRN sample annealed at 700°C (solid line) Phonon confinement model simulation (dot line). Inset: Transmission Electron Microscopy cross section image of the SRN sample annealed at 700°C (d) Normalized PL decay traces of the SRN sample annealed at 700°C detected at 810 nm (squares) and 710 nm (circles) respectively. Double exponential fitting curves (solid lines).

on samples deposited on SiO_2 substrates. In fig. 2.1 (c) we show the reference Raman signal of a bulk Si sample (dash line) along with the signal from the 700°C annealed SRN sample (solid line). The broad and asymmetric SRN Raman signal is attributed to the formation of small Si clusters (average size ~ 1-2 nm) embedded in the SRN film, as confirmed by transmission electron microscopy (TEM) analysis (Fig. 2.1 (c), inset). We independently estimated the average size of the Si clusters by fitting (dot line) the SRN Raman signal with a one-phonon confinement model that has been successfully applied to Si-nc in SiO_2 [21-23]. Assuming the Si LO phonon dispersion relation as in ref. 22, 23 we estimated a cluster radius of approximately 1 nm, compatible with the TEM data shown in the inset of fig. 2.1 (c). The photoluminescence emission lifetime of 700°C annealed SRN films is shown, for two different detection wavelengths, in fig. 2.1 (d). The decay traces were accurately fitted with a double exponential model characterized by a faster decay constant of approximately 1 ns (resolution limited), and a longer decay component, in the range of 5 to 10 ns depending on the observation energy.

2.1.4. First principle calculation

Understanding the interaction between a Si nanocluster and the surrounding SRN

matrix is extremely complex due to the unknown structure of the cluster and the various types of Si-N bonds that may be present at the interface between the cluster and the matrix. To investigate how the structure of the cluster and bonds at the interface can influence the optical properties of SRN materials, we performed a series of density functional theory (DFT) calculations [27], with the local density approximation (LDA), of the structural, electronic and optical properties of silicon nanoclusters under the collaboration with Lawrence Livermore National Lab. Based on the cluster size estimated in fig. 2.1 (c) we consider 1 nm clusters with both crystalline and amorphous core structures whose surfaces are terminated with hydrogen and various nitrogen containing groups. A description of each cluster can be found in the caption of fig. 2.2. Structures (a)-(g) have a diamond crystalline core. Structures (h)-(i) have an amorphous core generated using *ab initio* molecular dynamics simulations [31]. For each cluster, the atomic coordinates were relaxed to their closest lowest energy configuration and then the opto-electronic properties were calculated for the relaxed structure.

The properties we computed to determine which structure(s) are most likely to be responsible for luminescence observed in SRN are the DFT-LDA calculated energy gap between the Highest Occupied Molecular Orbital (HOMO), and Lowest Unoccupied Molecular Orbital (LUMO) and the radiative lifetime for the HOMO-LUMO transition. As the HOMO and LUMO orbitals will be shown localized around nitrogen atoms on the surface of the nanoclusters (see fig. 2.2), we expect that the calculated qualitative trends between the gaps and radiative lifetimes of the different structures will be insensitive to the exact size of the clusters and the nature of the surrounding SRN matrix. This effect was

observed in nanoclusters terminated with oxygen [8], where the localized nature of

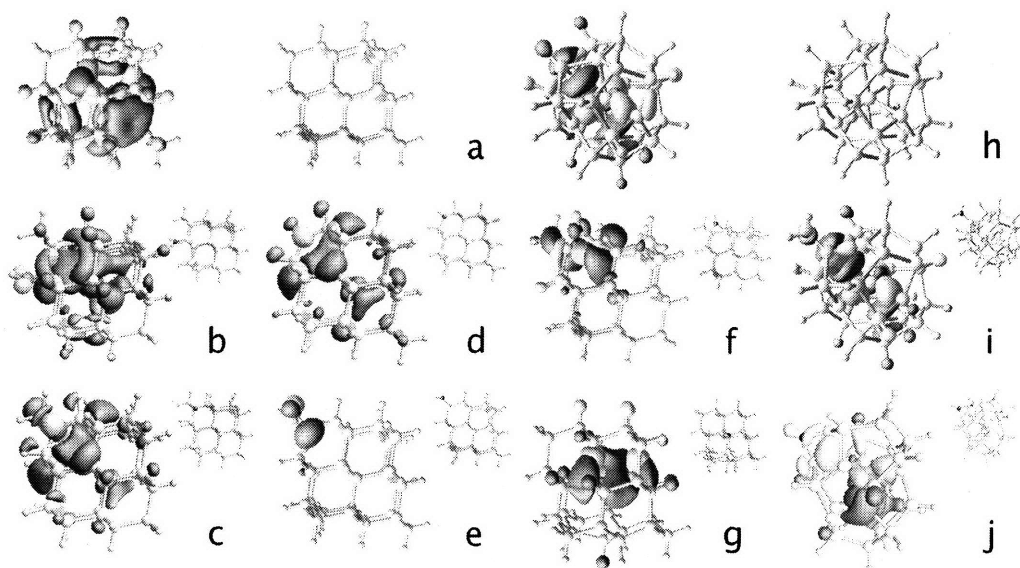

Figure 2.2. Isosurface plots of the density of the highest occupied molecular orbital (HOMO) in cyan and lowest unoccupied molecular orbital (LUMO) in magenta. Silicon atoms are yellow, nitrogen atoms are blue and hydrogen atoms are light grey. The isosurfaces contain 30% of an electron charge. (a), $Si_{35}H_{36}$, is the reference structure. In (b) a H is replaced by an amine. In (c) an SiH is replaced by a N. In (d) an SiH_2 is replaced with an NH. In (e), the N of an NH group is double bonded to the Si of a SiH_2 site, in (f) an NH is bonded to two neighboring silicon atoms, forming a Si-NH-Si bridge. In (g) a Si atom in the core of the cluster is replaced with a N. Structure (h) is our reference hydrogen terminated amorphous silicon cluster, $Si_{30}H_{20}$. In (i), a H atom is replaced with an amine. (j) is the amorphous version of the Si-NH-Si bridged structure (f).

the HOMO and LUMO orbital gave rise to a weak size dependence of the gap. In addition, as the measured luminescence is bright and weakly temperature dependent, we believe that comparing the calculated radiative lifetimes of different structures with measured values can provide additional data for discriminating between candidate structures.

The DFT-LDA calculated energy gaps between the Highest Occupied Molecular

Orbital (HOMO) and Lowest Unoccupied Molecular Orbital (LUMO) of each structure are summarized in Table 2.1. Previous calculations [8] have shown that it is not possible to directly compare DFT-LDA calculated gaps of doped silicon nanoclusters with experimental gaps for two reasons; (i) DFT calculated gaps of Si nanoclusters may underestimate the true optical gap, (ii) gaps calculated with a single surface dopant, typically overestimate the gap compared to clusters covered with multiple surface dopants. However, studies of oxygen terminated Si nanoclusters [8] showed that the qualitative changes in the gap of nanoclusters with different surface dopant structures are well reproduced by DFT calculations. In fig. 2.1 the measured onset of absorption is determined to be approximately 2 eV. This is considerably lower than the 3.4 eV DFT-LDA absorption gap of our reference crystalline structure, $Si_{35}H_{36}$, and also slightly lower than the 2.2 eV DFT-LDA absorption gap of the hydrogen terminated amorphous structure. As we expect the calculated DFT-LDA gaps to be underestimates of experimental values, it is unlikely that the absorption in SRN materials is occurring in the cores of either crystalline or amorphous, pure silicon clusters.

However, for both the crystalline and amorphous clusters, addition of N significantly lowers the calculated gaps and the smallest gaps are found when N is added on the surface of the cluster. This suggests that absorption and emission may originate at the interface between the Si cluster and the SRN matrix rather than from the core of the nanoclusters. The HOMO and LUMO orbital densities of each cluster are shown in fig. 2.2. In our reference crystalline and amorphous clusters, (a) and (h), both the HOMO and LUMO

Table 2.1. Calculated LDA optical gaps, and radiative lifetimes corresponding to different Si nanoclusters. *In (d), the HOMO-LUMO transition is forbidden and we quote the lifetime of the HOMO-LUMO+1 transition at 2.9 eV.

Structure	LDA Gap (eV)	Lifetimes (ns)
(a) $Si_{35}H_{36}$ – reference crystalline structure	3.4	10^2
(b) $Si_{35}H_{35}NH_2$ – NH_2 substituting H	3.0	10^3
(c) $Si_{34}H_{35}N$ – N substituting SiH	2.8	10^2
(d) $Si_{34}H_{34}NH$ – NH substituting SiH_2	2.7, 2.9	forbidden*, 10^3
(e) $Si_{35}H_{34}NH$ – NH substituting 2H	2.4	10^2
(f) $Si_{35}H_{34}NH$ – Si-NH-Si bridge	2.2	10^1
(g) $Si_{34}H_{37}NH$ – N in the core of the cluster	2.7	10^2
(h) a-$Si_{30}H_{22}$ – reference amorphous structure	2.2	10^2
(i) a-$Si_{30}H_{21}NH_2$ – NH_2 substituting H	2.1	10^2
(j) a-$Si_{30}H_{20}NH$ – Si-NH-Si bridge	1.8	10^4

orbitals are delocalized throughout the core of the cluster. Upon addition of nitrogen, the HOMO orbital becomes localized around the nitrogen atom and exhibits a *p* character. Analysis of the individual HOMO and LUMO eigenvalues shows that the gap of these clusters is reduced because the nitrogen localized HOMO states are higher in energy than the HOMO of the reference hydrogen terminated clusters.

It is interesting to compare these calculations of N terminated clusters with previous calculations [8] of structurally similar Si clusters with oxygen on their surface. Structure (b) is similar to $Si_{35}H_{35}OH$, where surface hydrogen is replaced with either an NH_2 or an OH group. Neither of these singly bonded groups significantly reduces the gap of the cluster.

NH_2 reduces the gap from 3.4 to 3.0 eV while OH reduces it to 3.3 eV. Structure (e), which has a surface Si=NH double bond can be compared with $Si_{35}H_{34}O$, which has a double bonded surface Si=O group. Both these structures have gaps considerably lower than the undoped reference structure (2.4 and 2.2 eV, compared to 3.4 eV).

Table 2.1 shows our calculated radiative lifetimes τ evaluated using $\frac{1}{\tau}=\frac{1}{2\pi m_e}\frac{e^2}{\varepsilon\varepsilon_0}\left(\frac{n}{c}\right)^3 f_{HL}\omega_{HL}{}^2$ (taken from reference 26), where $\frac{e^2}{\varepsilon\varepsilon_0}$ is the screened interaction of the exciton as evaluated in ref. 30 for $Si_{35}H_{36}$, c is the velocity of light, n the index of refraction (n=2.2 for our SRN samples), m_e the mass of the electron, ω_{HL} is the gap and f_{HL} is the HOMO-LUMO dipole oscillator strength. This oscillator strength depends on the symmetry and the degree of overlap of the orbitals, which in turn is sensitive to the details of the atomistic structure. Therefore, as we anticipate that the details of the atomistic structure of the nitrogen groups on the cluster surface may be altered in the presence of a SRN matrix, we only compare the order of magnitude of the radiative lifetimes with experiment. Structures (b), (d), (e) and (j) have large radiative lifetimes for their lowest transitions. In structure (d), the HOMO-LUMO transition is forbidden by symmetry and the lowest allowed transition is the HOMO to LUMO+1. For structures (b) and (e), the high atomic symmetry of the nitrogen groups is weakly broken by structural relaxations, such as the rotation of an N-H bond, yielding only a weak oscillator strength. For structure (j) the low oscillator strength and hence long radiative lifetime arises from the small overlap between the HOMO and LUMO, which are localized in different regions of the cluster. Structure (f) has the shortest lifetime, an order of magnitude lower than the

reference $Si_{35}H_{36}$ cluster and at least one order of magnitude lower than any other structure. We note that these radiative lifetimes have been calculated in the frozen lattice approximation (0 K calculations) and that phonon-assisted radiative recombination will lower the lifetimes. In addition to radiative recombination of carriers, we also expect some non-radiative carrier decay. Therefore the calculated radiative lifetime should be considered an upper bound to the measured lifetime.

By combining our first-principles simulations and experimental measurements we can constrain the range of structures responsible for photo-luminescence in SRN. Structures (f) and (j) with nitrogen bridged between two bonded Si atoms have the lowest gaps for the crystalline and amorphous structures respectively and are therefore closest to the measured gaps. If one also considers the radiative lifetime, the structure (f) is the only structure which exhibits both a short radiative lifetime and an onset of absorption consistent with our experimental results. The crystalline core of this structure is consistent with the observation of dark clusters in the inset of fig. 2.1 (c).

We have also calculated the structural Stokes shift between the onset of absorption and emission using the approach described in refs. 24 and 25. This structural Stokes shift is calculated by constraining the cluster in an excited triplet state and calculating the structural relaxation induced by this electronic excitation. The magnitude of the Stokes shift depends on the degree to which the nitrogen atoms on the surface of the clusters relax their geometry in this excited electronic state. In structures (b) and (e) the NH groups are relatively free to relax and the clusters exhibit large Stokes shifts between 1.5 and 2.0 eV. In structures (c) and (d) the nitrogen is constrained within the silicon network producing a

Stokes shift of only 0.2 eV, smaller than the Stokes shift of the reference $Si_{35}H_{36}$ cluster (1.0 eV). As the magnitude of Stokes shift is determined by the bonding configuration of the nitrogen atoms at the surface of the cluster, we anticipate that directly embedding the clusters in a SRN matrix is likely to strongly influence the magnitude of the Stokes shift.

2.1.5. Conclusion

In conclusion, we have studied the light emission in SRN films fabricated by PECVD deposition followed by low temperature (500~900°C) thermal annealing and we have demonstrated intense near-infrared emission with nanosecond recombination times. First-principles simulations show that Si clusters, terminated with nitrogen atoms exhibit a range of near-infrared absorption gaps. The calculated radiative lifetimes and Stokes shifts are sensitive to the atomic geometry of the nitrogen and structures with a Si-N-Si bridge show the closest agreement with our experimental measurements. The fast and efficient light emission from SRN systems can provide alternative routes towards the fabrication of optically active CMOS-devices.

2.1.6. References

[1] L. T. Canham, Appl. Phys. Lett. **57**, 1046 (1990).

[2] Z. H. Lu, D. J. Lockwood, J. M. Baribeau, Nature **378**, 258 (1995).

[3] K. D. Hirschman, L. Tsybeskov, S. P. Duttagupta, P. M. Fauchet, Nature **384**, 338 (1996).

[4] *Towards the first silicon laser,* NATO Advanced Studies Institute, Series 11, edited by L. Pavesi, S. Gaponenko and L. Dal Negro, Kluwer Academic, Dordrecht, vol 93 (2003).

[5] *Silicon Photonics,* edited by L. Pavesi, D. J. Lockwood, Springer-Verlag, Berlin (2004).

[6] M.V. Wolkin, J. Jorne, P. M. Fauchet, G. Allan, C. Delerue, Phys. Rev. Lett. **82**, 197

(1999).
[7] A. J. Williamson, J. C. Grossman, R. Q. Hood, A. Puzder, G. Galli, Phys. Rev. Lett. **89**, 196803 (2002).
[8] A. Puzder, A. J. Williamson, J. C. Grossman, G. Galli, J. Chem. Phys. **117**, 6721 (2002).
[9] E. Degoli, G. Cantele, E. Luppi, R. Magri, D. Ninno, O. Bisi, S. Ossicini, Phys. Rev. B. **69**, 155411 (2004).
[10] L. Pavesi, L. Dal Negro, C. Mazzoleni, G. Franzò, F. Priolo, Nature **408**, 440 (2000).
[11] L. Khriachtchev, M. Rasanen, S. Novikov, J. Sinkkonen, Appl. Phys. Lett. **79**, 1249 (2001).
[12] L. Dal Negro, M. Cazzanelli, L. Pavesi, S. Ossicini, D. Pacifici, G. Franzò, F. Priolo, F. Iacona, Appl. Phys. Lett. **82**, 4636 (2003).
[13] J. Ruan, P. M. Fauchet, L. Dal Negro, M. Cazzanelli, L. Pavesi, Appl. Phys. Lett. **83**, 5479 (2003).
[14] L. Dal Negro, M. Cazzanelli, B. Danese, L. Pavesi, F. Iacona, G. Franzò, F. Priolo, J. Appl. Phys. **96**, 5747 (2004).
[15] M. Cazzanelli, D. Kovalev, L. Dal Negro, Z. Gaurro, L. Pavesi, Phys. Rev. Lett. **93**, 207402 (2004).
[16] M. J. Chen, J. L. Yen, J. Y. Li, J. F. Chang, S. C. Tsai, C. S. Tsai, Appl. Phys. Lett. **84**, 2163 (2004).
[17] N. M. Park, C. J. Choi, T. Y. Seong, S. J. Park, Phys. Rev. Lett. **86**, 1355 (2001).
[18] T. Y. Kim, N. M. Park, K. H. Kim, G. Y. Sung, Y. W. Ok, T. Y. Seong, C. J. Choi, Appl. Phys. Lett. **85**, 5355 (2004).
[19] K. S. Cho, N. M. Park, T. Y. Kim, K. H. Kim, G. Y. Sung, J. H. Shin, Appl. Phys. Lett. **86**, 071909 (2005).
[20] X. D. Pi, O. H. Y. Zalloum, J. Wojcik, A. P. Knights, P. Mascher, A. D. W. Todd, P. J. Simpson, J. Appl. Phys. **97**, 096108 (2005).
[21] I. H. Campbell, P. M. Fauchet, Solid State Comm. **58**, 739 (1986).
[22] Y. Kanemitsu, H. Uto, Y. Masumoto, T. Matsumoto, T. Futagi, H. Mimura, Phys. Rev. B. **48**, 2827 (1993).
[23] P. Mishra, K. P. Jain, Phys. Rev. B. **64**, 073304 (2001).
[24] A. Puzder, A. J. Williamson, J. C. Grossman, G. Galli, J. Am. Chem. Soc. **125**, 2788 (2003).
[25] A. Franceschetti, S. T. Pantelides, Phys. Rev. B **68**, 033313 (2003).

[26] A. Yariv, *Quantum Electronics*, 3rd ed. (Wiley, New York, 1989)
[27]The GP[28] code was used for the structural relaxation and the ABINIT[29] code was used to evaluate gaps and oscillator strengths. All calculations use norm conserving, Troullier-Martins pseudopotentials and a plane-wave basis with a 70 Ry cutoff.
[28] F. Gygi, Lawrence Livermore National Laboratory
[29] The ABINIT code is a common project of the Université Catholique de Louvain, Corning Incorporated, and other contributors (URL http://www.abinit.org)
[30] A. Tsolakidis, D. Sanchez-Portal, R. M. Martin, Phys. Rev. B **66**, 235416 (2002).
[31] E. W. Draeger, J. C. Grossman, A. J. Williamson, G. Galli, Phys. Rev. Lett. **90**, 167402 (2003).

2.2. Light emission efficiency and dynamics in silicon-rich nitride films

Light-emitting Si-rich nitride films (SRN) were fabricated by Plasma Enhanced Chemical Vapor Deposition followed by thermal annealing and the SRN external quantum efficiency was measured. An efficiency of 7 % at room temperature was obtained and compared with the 4.5 % efficiency of optimized Si nanocrystals samples produced by sputtering of Si-rich oxide. The SRN light emission temperature dependence and recombination dynamics were also studied. Small emission thermal quenching from 4 K to 330 K with wavelength dependent, nanosecond recombination lifetime was observed. Light emission from SRN systems can provide alternative routes towards the fabrication of efficient optical CMOS-devices.

2.2.1. Introduction

Monolithic integration of optoelectronic materials atop the silicon electronics platform is of intense interest in intrachip, chip-to-chip, and chip-to-fiber-optic communications and networking. Progress towards these goals is curtailed by the lack of efficient light emission

from silicon. Photon emission from silicon originates from low-probability phonon-mediated transitions that compete unfavourably with fast non-radiative de-excitation paths, such as Auger and free carrier recombinations.

In view of these limitations, several strategies have been recently developed to engineer Si into a more efficient light-emitting material [1-5]. The approach of quantum confinement has led to a dramatic improvement of the light generation efficiency in Si nanostructures [4-7]. Emission efficiency up to ~ 4 % under optical pumping has been achieved in oxidized porous-Si [6-8] and sizable optical gain in Si-nanocrystals (Si-nc) nucleated from a Si-rich silicon oxide film (SRO) has been recently demonstrated by several groups [4, 9-13]. The presence of Si=O double bonds [14-17] at the surface of small Si-nc is believed to have a dramatic impact on the light emission properties of these systems. However, porous-Si and SRO-based systems are not suitable for the fabrication of stable and efficient electroluminescent devices due to the difficult electron injection in an oxide-based matrix, requiring high electric fields.

It is therefore necessary to investigate alternative CMOS-compatible approaches that can lead to intense light emission from nanostructured silicon systems that are also compatible with efficient and stable electrical excitation. An intriguing possibility is offered by the nucleation of Si clusters in dielectric hosts with smaller band-gaps than SiO_2. Visible and near-infrared light-emitting Si-nc embedded in silicon nitride matrices have been recently demonstrated [18, 19] and efficient visible electroluminescence has been reported [20, 21]. However, their emission mechanism is based on the quantum confinement in the Si-nc core itself with size dependency. This model can not explain the emission behavior of

our SRN material we observed in this work. With our work we argue that photoluminescence spectra from SRN material result from the combined effect of quantum confinement and interface state mediated recombination due to the formation of nanometer sized silicon clusters.

2.2.2. Fabrication and analysis

In this letter we report on a direct comparison of the formation parameters and external quantum efficiencies of Si-rich silicon nitride films (SRN) obtained by Plasma Enhanced Chemical Vapor Deposition (PECVD) and Si-rich oxide films (SRO) deposited by magnetron sputtering. In addition, by studying the temperature dependent light emission and recombination dynamics of SRN films we demonstrate that pure quantum confinement cannot explain the optical properties of our SRN samples.

The SRN samples were fabricated by PECVD using an Applied Materials Centura DxZ chamber and the SRO samples were fabricated by reactive magnetron sputtering deposition as described in detail elsewhere [19, 22]. All the samples have comparable thickness (~ 700 nm) and have been deposited on transparent fused silica substrates and annealed at different temperatures ranging from 500°C to 1250°C. Room temperature photoluminescence (PL) experiments were performed using a 488 nm Ar-ion pump laser and a single grating monochromator coupled to a nitrogen-cooled InGaAs phototube. External photoluminescence quantum efficiency (PLQE) measurements were performed using a calibrated integrating sphere setup as described in ref. 23, 24. This approach allows a direct PLQE measurement without the need of any assumption on the angular anisotropy

of the emission profiles, the scattering and absorbance properties of the investigated samples. Photoluminescence time decay measurements were performed using the 400 nm second harmonic line of a Ti:Sapphire laser (pulse width ~100 fs, repetition rate = 25 MHz, wavelength tuned to 800 nm) and a time-correlated single photon counting system with a time resolution of 50 ps under the collaboration with Prof. Edward Sargent group in Univ. of Toronto.

2.2.3. Experimental results and discussion

In fig. 2.3 (a1) we show the trends of the integrated PL intensity versus the SRN film refractive index (measured at 1.3 μm by prism coupling technique) and post deposition annealing temperature (Fig. 2.3 (a2)). We found that the best light emission performances of SRN films were obtained for samples with the highest Si content (a refractive index of approximately 2.24) after thermal annealing at 700°C for 10 min. Fig. 2.3 (b1) and (b2) show the light emission optimization trends versus the film refractive index and the annealing temperature (1 hour) for SRO films deposited by magnetron sputtering. The corresponding SRO film stoichiometry varies between 33 % at. Si and 53 % at. Si, as measured by Rutherford Back Scattering analysis [22]. In the SRO case we found that the integrated PL intensity is maximized for films with a refractive index of 1.7 (~ 38 % at. Si) and annealed at 1150°C for 1 hour. These trends result from a competitive interplay between Si clusters size, emission efficiencies and Si clusters density. Our data indicate that a major difference in the formation kinetics exists between SRN and SRO light-emitting systems. The optimum annealing time (1 hour) and temperature (1150°C) required to

maximize the Si-nc light emission in oxide systems are much larger than what is required for Si-nc embedded in Si-nitride hosts. This suggests that the Si-nc growth kinetics in an amorphous nitride environment results in the formation of small Si clusters at a faster rate and at a lower annealing temperature than the SRO case. Indeed, small size (1-2 nm)

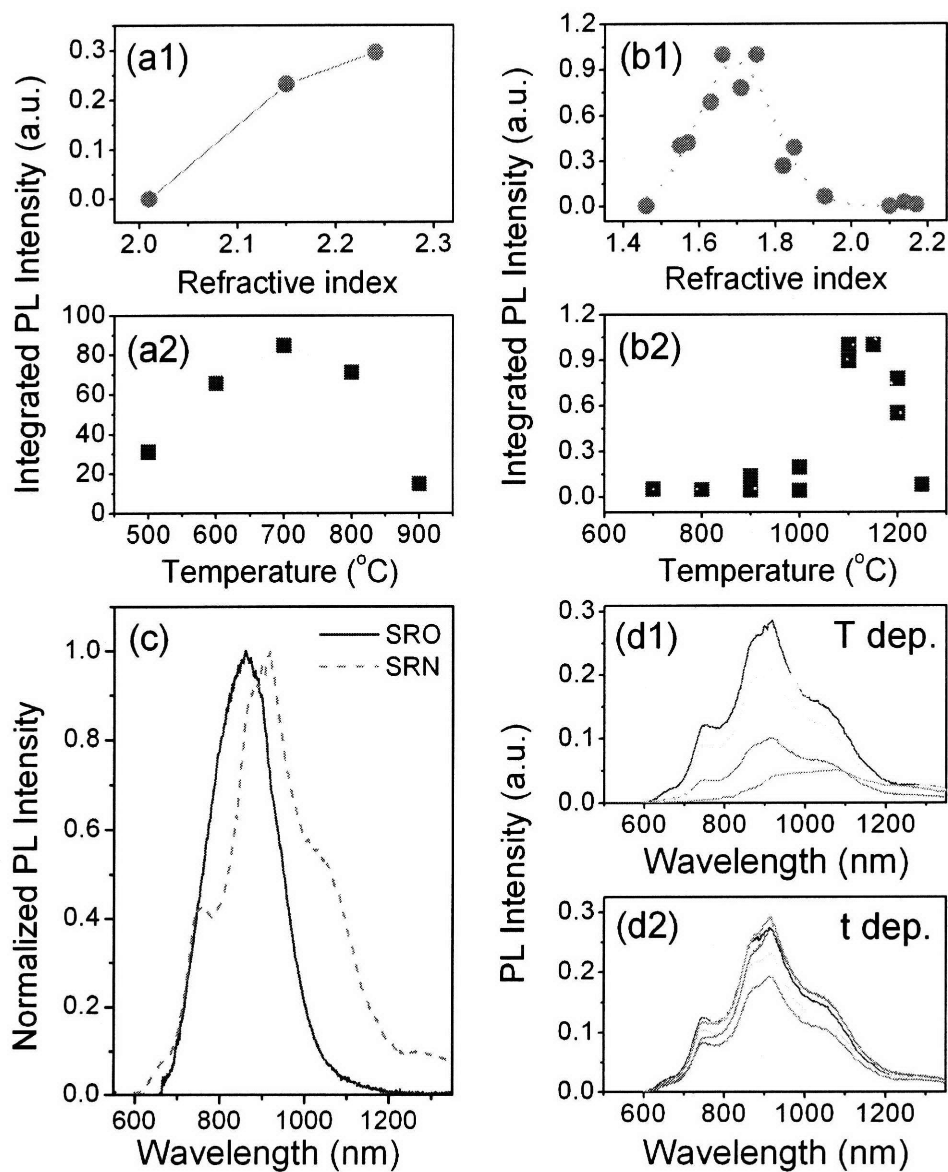

Figure 2.3 (a1) Integrated PL intensity versus refractive index for SRN films annealed at

700°C for 10 minutes. (a2) Integrated PL intensity versus annealing temperature for SRN films with n=2.24 refractive index and annealed for 10 minutes. (b1) Integrated PL intensity versus refractive index for SRO films annealed at 1100°C for 1 hour. (b2) Integrated PL intensity versus annealing temperature for SRO films with n=1.7 refractive index and annealed for 1 hour. (c) Normalized PL spectra of the optimized (n=1.7, annealed for 60 min. at 1100°C) SRO film (solid line) and the best emitting (n=2.24, annealed for 10 min. at 700°C) SRN film (dash line). Pump power 5 mW at 488 nm. The oscillations in the SRN emission spectrum are due to interference induced from finite sample thickness (700 nm). (d1) PL spectra of SRN films versus annealing temperatures for a fixed annealing time of 10 minutes. The sequence of PL intensities follows the trend of panel (a2) with the highest intensity at 700°C. (d2) PL spectra of SRN films versus annealing time for a fixed annealing temperature of 700°C. The annealing times are 1, 2, 5, 10, 20, and 60 minutes and the PL spectra show increasing peak intensity accordingly.

Si-nc's are formed in the amorphous nitride matrix as confirmed independently by cross section transmission electron microscopy analysis (Fig. 2.5, inset). Since the SRO integrated intensity decreases by increasing the SRO refractive index beyond a characteristic value (~ 1.7 for our choice of deposition parameters) as shown in fig. 2.3 (b1), we refer to this situation as supersaturation limited. This trend was not observed in the case of the SRN films, where within the set of deposition conditions that we investigated, the integrated emission monotonically increases by increasing the film refractive index (Fig. 2.3 (a1)).

In order to compare quantitatively the emission efficiency of SRO versus SRN light-emitting systems, we have measured the PLQE of the best emitting SRN film (n=2.24, 700°C, 10 min.) and the PLQE of the SRO sample with optimized emission characteristics (n=1.7, 1150°C, 1 hour).

Figure 2.3 (c) shows the normalized and almost overlapping room temperature

emission spectra of the SRO (solid line) and SRN (dash line) samples that we have compared. By direct PLQE measurements, performed as described in ref. 23-24, we have obtained a value of 7 % for the SRN film versus the 4.5 % PLQE of the optimized SRO sample under the collaboration with Prof. Edward Sargent group in Univ. of Toronto. We notice that these efficiency results are particularly interesting since we have compared the efficiency of a fully optimized (in terms of stoichiometry and annealing temperature) SRO film, as shown in fig. 2.3 (b1) and (b2), with the best emitting SRN sample whose stoichiometry (excess Si content) does not show a fully optimized trend (Fig. 2.3 (a1)).

Another important feature of light-emitting SRN films is that both the emission wavelength and emission lineshape are almost independent on the annealing temperature and annealing time, as shown in figure 2.3 (d1) and (d2) respectively. A very weak peak shift was also observed by changing the SRN stoichiometry in the range from 2.01 to 2.24 (not shown here), while the emission of the stoichiometric silicon nitride (n=2.01) is too weak to be detected. The lack of emission tuneability observed in our SRN systems strongly indicates that the origin of light emission is not determined by size-dependent quantum confinement effects.

In order to gain more insights on the light emitting mechanism of our Si-nc systems, we have performed temperature dependent and time resolved PL measurements. In fig. 2.4 we show the integrated PL of the SRN for temperatures ranging from 4 K to 330 K. We found that the SRN emission shows negligible temperature quenching (approximately a factor of 4) over the investigated temperature range. In addition, no appreciable emission lineshape modifications have been observed from 4 K to room temperature (Fig. 2.4, inset).

We notice that the temperature dependence of the PL that we have experimentally measured in SRN systems is different from the temperature behavior that is generally observed for Si-nc embedded in SiO_2 matrices [25] or for porous Si [26]. In oxygen passivated Si-nc systems, the PL temperature behavior has been accurately described within a model

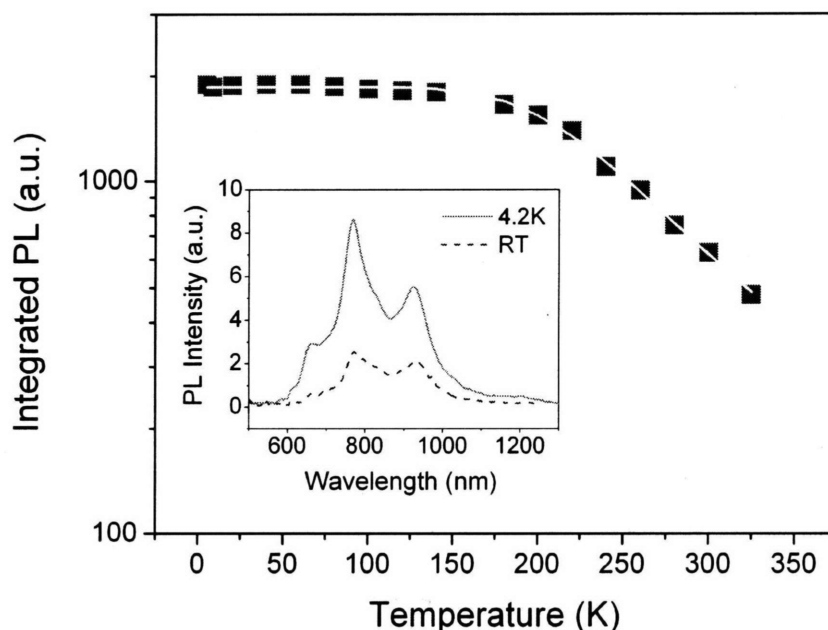

Figure 2.4. (squares) Integrated PL intensity versus temperature for the best emitting SRN sample (n=2.24, annealed for 10 minutes at 700°C). (solid line) Theoretical fitting curve according to the model of ref. 29; for the best fit we have used E_A=117 meV and β=184. (Inset) Room temperature (dash line) and 4.2 K (solid line) SRN emission spectra. The oscillations in the SRN emission spectra are due to interference induced from finite sample thickness (700 nm).

introduced by Calcott [27], that includes the splitting of the singlet-triplet excitonic states due to the exchange interaction in strongly confined silicon systems. According to this model, the total radiative recombination rate is determined by the detailed balance of the

temperature dependent occupation of the singlet and triplet excitonic excited states, separated by the size dependent electron-hole exchange energy. Since radiative transitions from the triplet state (in principle parity forbidden) are only weakly allowed by the mixing of the states symmetry due to spin-orbit coupling, the PL intensity of Si-nc decreases at low temperatures, where mainly the triplet state (at lower energy) is populated. On the other hand, since in the high temperatures regime the non-radiative phonon coupling becomes a dominant recombination channel, it has been found that the trend of the Si-nc PL versus temperature follows a bell-shape behavior typically peaked around 100 K [25]. On the contrary, the temperature-dependent PL behavior of our SRN samples (Fig. 2.4) cannot be explained within the Calcott model of quantum confined excitons. The PL data shown in fig. 2.4 can be accurately described by a simple phenomenological model based on thermal ionization from localized radiative traps [28], as similarly reported in ref. 29. According to this model, the temperature-dependent PL intensity at a given temperature $I_{PL}(T)$ can be expressed as: $I_{PL}(T) = I(0)\left[\frac{1}{1+\beta \exp(-\frac{E_A}{k_B T})}\right]$ where $I(0)$ is the PL intensity at the lowest measured temperature, β is a constant inversely proportional to the radiative rate of the system [28], and E_A is an activation barrier which surrounds the recombination center. Both β and E_A are phenomenological constants whose microscopic origin is associated with the detailed nature of the interface region between the amorphous Si nitride matrix and the Si-clusters. This model describes our data accurately with E_A=117 meV and β=184, in agreement with the results obtained in ref. 29. However, here we propose a different physical interpretation of the microscopic nature of the radiative localized state involved in

the photoluminescence process. Based on first-principles calculations of the optical properties of small size silicon clusters (1~2 nm) embedded in a silicon nitride matrix, we have demonstrated in the previous section that, in our SRN systems produced by PECVD, localized nitrogen states at the surface of Si-nc result in nanosecond relaxation times and large absorption/emission Stokes-shifts which are compatible with the experimental results [30, 31]. Therefore, the microscopic nature of the radiative nitrogen trap states responsible for light emission consists of strongly localized states introduced within the optical gap of small Si clusters by bridging nitrogen configurations at the Si-nc surface [30, 31].

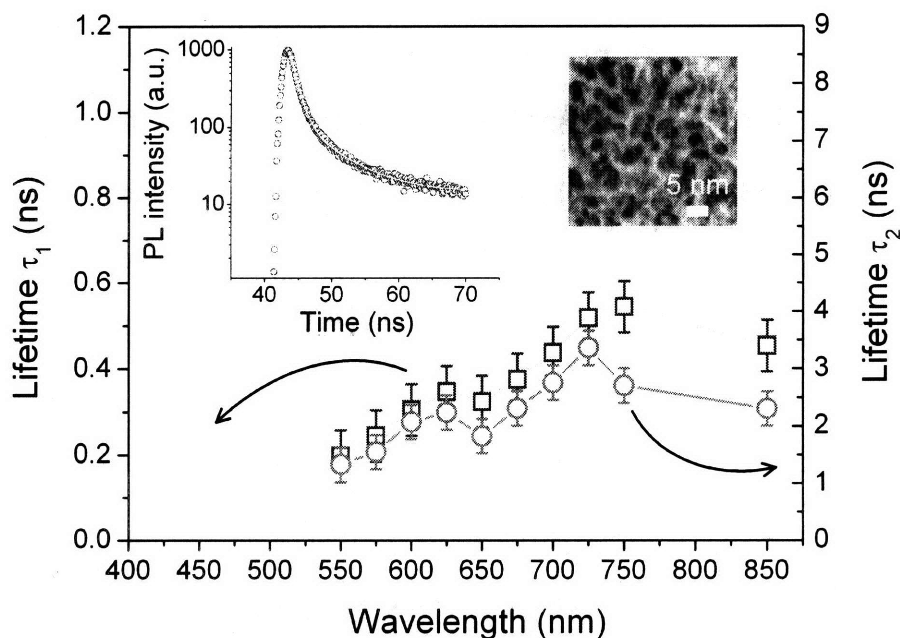

Figure 2.5. PL emission lifetime versus observation wavelength for the best emitting SRN sample (n=2.24, annealed for 10 minutes at 700°C). A typical decay curve (observed at 710 nm) is shown (left inset, open circles) together with a double exponential fit (left inset, solid line). Cross section TEM image of the best emitting SRN sample showing silicon nanocrystals as dark spots (right inset).

In fig. 2.5 we show the measured wavelength dependent PL lifetime of the best emitting SRN film. We found that the SRN lifetime can be described by a double exponential function with a resolution-limited sub-nanosecond fast decay component and a longer decay component that ranges between 1 and 5 ns, depending on the observation wavelength. According to our interpretation of the light emission mechanism, the fast sub-nanosecond PL decay component can be associated with a non-radiative exciton trapping time on the radiative nitrogen states while the longer (ns) decay results from the recombination (both radiative and non-radiative) of the trapped excitons.

In addition, we observe that, because of the lack of emission tuneability in our SRN system (Fig. 2.3 (d1), (d2)), the wavelength dispersion of the lifetime data shown in fig. 2.5 cannot result from nanocrystals size dispersion. On the contrary, it is associated with the various types of Si-N bonding groups (with different recombination lifetimes) that can passivate the interface between the Si clusters and the surrounding matrix [30, 31].

2.2.4. Conclusion

In conclusion, we have measured the PLQE of SRN and optimized SRO films fabricated by PECVD and magnetron sputtering, respectively, and we have demonstrated 7 % PLQE for SRN samples. In addition we have demonstrated small emission temperature quenching from 4 K to 330 K and nanosecond-fast, wavelength-dependent recombination dynamics. The lack of emission tuneability, the PL temperature behavior, and its emission dynamics suggest that the light emission originates from strongly localized radiative states

introduced by nitrogen groups that passivate the surface of small Si-nc's, rather than from the core of Si-nc's. The fast and efficient light emission from SRN systems can provide alternative routes towards the fabrication of optically active and electrically driven CMOS-devices.

2.2.5. References

[1] L. T. Canham, Appl. Phys. Lett. **57**, 1046 (1990).

[2] Z. H. Lu, D. J. Lockwood, J. M. Baribeau, Nature **378**, 258 (1995).

[3] K. D. Hirschman, L. Tsybeskov, S. P. Duttagupta, P. M. Fauchet, Nature **384**, 338 (1996).

[4] *Towards the first silicon laser,* NATO Advanced Studies Institute, Series 11, edited by L. Pavesi, S. Gaponenko and L. Dal Negro, Kluwer Academic, Dordrecht, vol. 93 (2003).

[5] *Silicon Photonics,* edited by L. Pavesi, D. J. Lockwood, Springer-Verlag, Berlin (2004).

[6] J. C. Vial, A. Bsiesy, F. Gaspard, R. Hèrino, M. Ligeon, F. Muller, R. Romestain, R. M. Macfarlane, Phys. Rev. B. **45**, 14171 (1992).

[7] B. Gelloz, T. Nakagawa, N. Koshida, Appl. Phys. Lett. **73**, 2021 (1998).

[8] B. Gelloz, Appl. Surf. Sci. **108**, 449 (1997).

[9] L. Pavesi, L. Dal Negro, C. Mazzoleni, G. Franzò, F. Priolo, Nature **408**, 440 (2000).

[10] L. Khriachtchev, M. Rasanen, S. Novikov, J. Sinkkonen, Appl. Phys. Lett. **79**, 1249 (2001).

[11] L. Dal Negro, M. Cazzanelli, L. Pavesi, S. Ossicini, D. Pacifici, G. Franzò, F. Priolo, F. Iacona, Appl. Phys. Lett. **82**, 4636 (2003).

[12] J. Ruan, P. M. Fauchet, L. Dal Negro, M. Cazzanelli, L. Pavesi, Appl. Phys. Lett. **83**, 5479 (2003).

[13] M. J. Chen, J. L. Yen, J. Y. Li, J. F. Chang, S. C. Tsai, C. S. Tsai, Appl. Phys. Lett. **84**, 2163 (2004).

[14] M.V. Wolkin, J. Jorne, P. M. Fauchet, G. Allan, C. Delerue, Phys. Rev. Lett. **82**, 197 (1999).

[15] A. J. Williamson, J. C. Grossman, R. Q. Hood, A. Puzder, G. Galli, Phys. Rev. Lett. **89**, 196803 (2002).

[16] A. Puzder, A. J. Williamson, J. C. Grossman, G. Galli, J. Chem. Phys. **117**, 6721 (2002).
[17] E. Degoli, G. Cantele, E. Luppi, R. Magri, D. Ninno, O. Bisi, S. Ossicini, Phys. Rev. B **69**, 155411 (2004).
[18] N. M. Park, C. J. Choi, T. Y. Seong, S. J. Park, Phys. Rev. Lett. **86**, 1355 (2001).
[19] L. Dal Negro, J. H. Yi, V. Nguyen, Y. Yi, J. Michel, L. C. Kimerling, Appl. Phys. Lett. **86**, 261905 (2005).
[20] T. Y. Kim, N. M. Park, K. H. Kim, G. Y. Sung, Y. W. Ok, T. Y. Seong, C. J. Choi, Appl. Phys. Lett. **85**, 5355 (2004).
[21] K. S. Cho, N. M. Park, T. Y. Kim, K. H. Kim, G. Y. Sung, J. H. Shin, Appl. Phys. Lett. **86**, 071909 (2005).
[22] M. Stolfi, L. Dal Negro, J. Michel, X. Duan, J. Le Blanc, J. Haavisto, L. C. Kimerling, Mat. Res. Soc. Symp. Proc. **832**, F.11.8.1 (2005).
[23] T.-W. F. Chang, A. Maria, P. W. Cyr, V. Sukhovatkin, L. Levina, and E. H. Sargent, Synthetic Metals **148**, 257 (2005).
[24] J. C. de Mello, H. F. Wittmann, R. H. Friend, Adv. Mater. **9**, 230 (1997).
[25] M. L. Brongersma, P. G. Kik, A. Polman, K. S. Min, Harry A. Atwater, Appl. Phys. Lett. **76**, 351 (2000).
[26] A. G. Cullis, L. T. Canham, P. D. J. Calcott, J. Appl. Phys. **82**, 909 (1997).
[27] P. D. J. Calcott, K. J. Nash, L. T. Canham, K. J. Kane, D. Brumhead, J. Phys: Condens. Matter. **5**, L91 (1993).
[28] J. I. Pankove, *Optical Processes in Semiconductors*, Dover Publications, NY (1971).
[29] S.V. Deshpande, E. Gulari, S.W. Brown, S.C. Rand, J. Appl. Phys. **77**, 6534 (1995).
[30] L. Dal Negro, J. H. Yi, L. C. Kimerling, S. Hamel, A. Williamson, G. Galli, Appl. Phys. Lett. **88**, 183103 (2006).
[31] L. Dal Negro, J. H. Yi, M. Hiltunen, J. Michel, L. C. Kimerling, S. Hamel, A. Williamson, G. Galli, T. W. F. Chang, V. Sukhovatkin, E. H. Sargent, J. Exper. Nanoscience **1**, 29 (2006).

Chapter 3. Emission enhancement from silicon rich nitride

In this chapter light enhancement phenomena from silicon rich nitride is presented and discussed, especially based on Thue-Morse one dimensional light emitting structure, aperiodic waveguide structure, and finally the thermal treatment by sequential annealing technique.

Aperiodic structures are deterministically generated structures with non-periodic refractive index modulation and represent an intermediate organization stage between periodic dielectric materials, namely photonic crystal structures, and random media. Aperiodic structures can form the band gaps caused by coherent multiple scattering of partial waves analogous to a periodic structures [1]. When refractive index contrast is high enough, omnidirectional band gap can be achieved [2, 3]. Disorder leads to the localized states with strong light dispersion, group velocity reduction, and spatial confinement of electromagnetic waves [4, 5]. Aperiodic dielectrics have the unique property of critically localized photon states that can dramatically enhance light-matter interaction. These states are related to the lack of translational symmetry and an unprecedented degree of structural complexity.

The investigation of aperiodic photonic structures represents an exciting opportunity in order to assess the full potential of this new class of dielectric materials, which eventually leads to optical devices of new conception. In particular, the combination of light emission and complex dielectrics can result in the demonstration of novel multifrequency optical devices based on critically localized light modes with strong field enhancement effects.

Previous works on aperiodic structure has been focused on the one dimensional multilayer dielectric stack as in the structure above. However, the system size with the number of the multilayers is limited by structural stability such as stress, crack and also by the interface irregularity and the thickness variation which increase with the number of multilayers. The thickness variation is critical for the optical properties including transmission spectra of aperiodic structures. In this chapter, we propose a novel concept of aperiodic waveguide structure what is more independent of these defective features. Fabrication issues are discussed based on the experimental results.

Enhancement of the light emission not only for the specific wavelengths but for the entire emission range can provide more advantages for many applications. To increase overall emission efficiency, the number of emission sources and/or emission efficiency of each emission source need to increase. Here we suggest a thermal treatment technique for silicon nanocrystal based light emitter to enhance the light emission by increasing the number of nanocrystal density. We also introduce the basic concept and the experimental results with detailed discussion.

3.1. One dimensional Thue-Morse aperiodic light emitting structure

Light-emitting Thue-Morse (T-M) multilayer structures of silicon rich nitride, SRN and SiO_2 have been fabricated in order to investigate the generation and transmission of light in strongly aperiodic deterministic dielectrics. Photoluminescence and optical transmission data experimentally demonstrate the presence of emission enhancement effects occurring at wavelengths corresponding to multiple T-M resonance states. A factor

of almost 6 in emission enhancement with respect to homogeneous SRN dielectrics has been experimentally measured, in good agreement with theoretical simulation based on transfer matrix simulations. The structural flexibility of T-M systems can provide alternative routes towards the fabrication of optically active multiwavelength photonic devices.

3.1.1. Introduction

Deterministic aperiodic systems represent a fascinating intermediate regime between quasiperiodic and disordered random structures [1–4]. The principal example of an aperiodic deterministic structure is given by the Thue-Morse (T-M) sequence [5], which is generated by two symbols, A and B. The sequence follows the simple inflation rule $\sigma_{T\text{-}M}$: A→AB, B→BA) [2,3], For example, the lower-order T-M strings are: S_0=A, S_1=AB, S_2=ABBA, S_3=ABBABAAB, etc. The T-M sequence has been extensively investigated in mathematical literature as the prototype of a substitutional aperiodic symbolic map with highly nontrivial properties [6–8]. A T-M string never repeats itself and, despite the lack of periodicity, it shows remarkable self-similar (multifractal) features [9, 10]. In particular, the singular continuous character of the T-M system's Fourier spectrum expresses a far richer complexity than the widely investigated quasiperiodic Fibonacci systems, whose Fourier spectrum contains self-similar Bragg peaks [1–4], One dimensional T-M aperiodic photonic structures can be generated by stacking together layers of two different dielectric materials, A and B, according to the inflation rule $\sigma_{T\text{-}M}$ [11]. As a result, the refractive index of one-dimensional T-M photonic structures shows an aperiodic spatial modulation on the length

scale of the light wavelength. An extensive theoretical literature recognized that in T-M photonic structures, despite the lack of global translational invariance, coherent multiple wave scattering gives rise to a self-similar hierarchy of pseudobandgap regions split by narrow transmission resonance states with field enhancement [1–4, 7–10, 12]. Even though the detailed mathematical nature of T-M states is still under debate, it has been recently clarified that T-M structures can sustain critical states; namely, extended multifractal wave functions with anomalous transport properties [13, 14]. Very recently, our group investigated experimentally the bandgap fractal scaling of Si/SiO_2 T-M photonic multilayers and demonstrated the occurrence of a large omnidirectional photonic bandgap [11]. However, despite the large interest in the passive T-M optical properties (transmission), light-emitting T-M structures have not been experimentally investigated so far.

In this chapter, we report on the experimental realization and study of light-emitting SRN/SiO_2 T-M structures up to 64 layers with emission enhancement at multiple resonances. The choice of a SRN-based material system is motivated by two key factors: its ability to produce efficient broadband light emission at room temperature (RT) [15, 16] and its high transparency in the visible range [15], allowing homogeneous optical pumping of complex multilayered structures.

3.1.2. Fabrication

The samples were fabricated on transparent fused silica substrates through plasma-enhanced chemical vapor deposition using an Applied Materials Centura DxZ chamber.

The silicon rich nitride layer is deposited using SiH_4 and N_2 as precursors while the oxide layers are deposited using SiH_4 and N_2O. The substrate temperature during deposition was 400°C. In order to maximize the effect of light scattering, the thickness $d_{A,B}$ of the two materials, SRN (layer A) and SiO_2 (layer B), has been chosen to satisfy the Bragg condition, $d_A n_A = d_B n_B = \lambda_0/4$, where n_A (2.23) and n_B (1.45) are the respective refractive indices and λ_0=1.65 μm. Optical transmission experiments were performed using a commercial Cary 5E double beam spectrophotometer coupled with a PbS detector (for the near infrared range) or a Hamamatsu photomultiplier tube (for the visible range). Room temperature photoluminescence experiments were performed using a 488 nm Ar pump laser and the radiation was collected by a single-grating monochromator coupled to a nitrogen cooled InGaAs phototube. In order to relate the light emission interference pattern with the normal incidence transmission spectra, all the samples were measured using a zero angle collection configuration, where the normal to the sample surface was aligned parallel to the collection axis.

3.1.3. Experimental results

In fig. 3.1 we show the measured (solid lines) and calculated (dotted lines) optical transmission spectra of two different T-M structures (with 32 and 64 layers, named TM32 and TM64, respectively). Fig. 3.1 (a) shows the transmission of TM32 where several photonic pseudogaps are connected through transmission bands and narrow

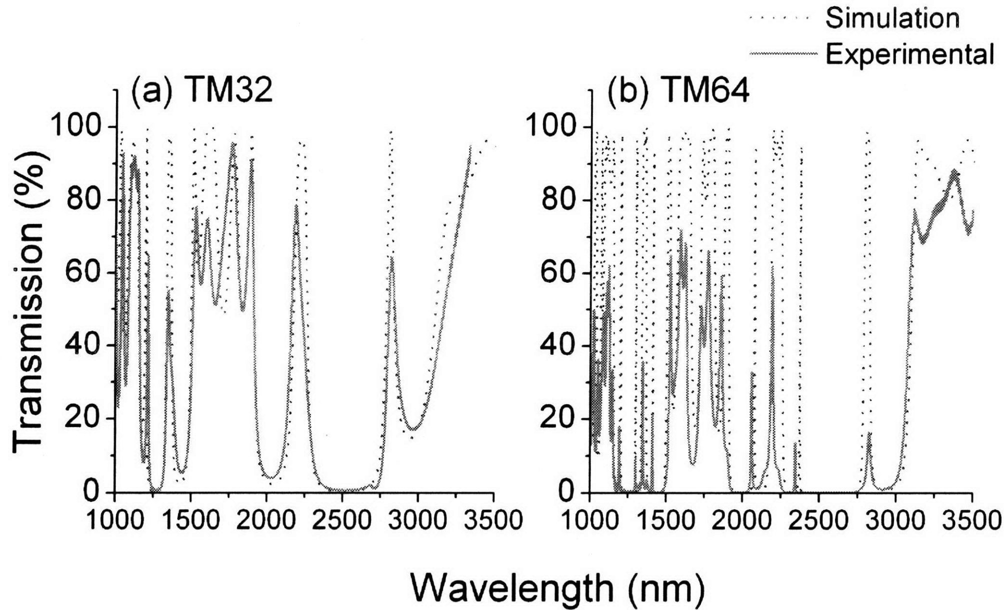

Figure 3.1 (a) Experimental (solid line) and calculated (dotted line) transmission for the 32 layer T-M structure (TM32). (b) Experimental (solid line) and calculated (dotted line) transmission for the 64 layer T-M structure (TM64). For all the simulations we have considered n_A=2.23 (SRN), n_B =1.45 (SiO_2). The thickness simulation parameters that yield the best fit to the experimental transmission data are d_A=198.9 nm and d_B=273 nm, which are approximately 6% thicker and 4% thinner than the targeted values defined by the Bragg condition at λ_0=1.65 μm.

band-edge states. The transmission of the TM64 sample is displayed in fig. 3.1 (b). As a typical signature of aperiodic systems, the complexity of the spectra depends strongly on the system size. In particular, we notice that new bandgap regions appear as a result of the TM32 transmission band splitting [3, 4, 10, 17]. The effect is clearly visible in fig. 3.1 (b) around 1300 and 2200 nm, where the wide transmission bands in the TM32 sample [Fig. 3.1 (a)) split into new gaps connected by narrower transmission states [Fig. 3.1 (b)]. The observed band-splitting

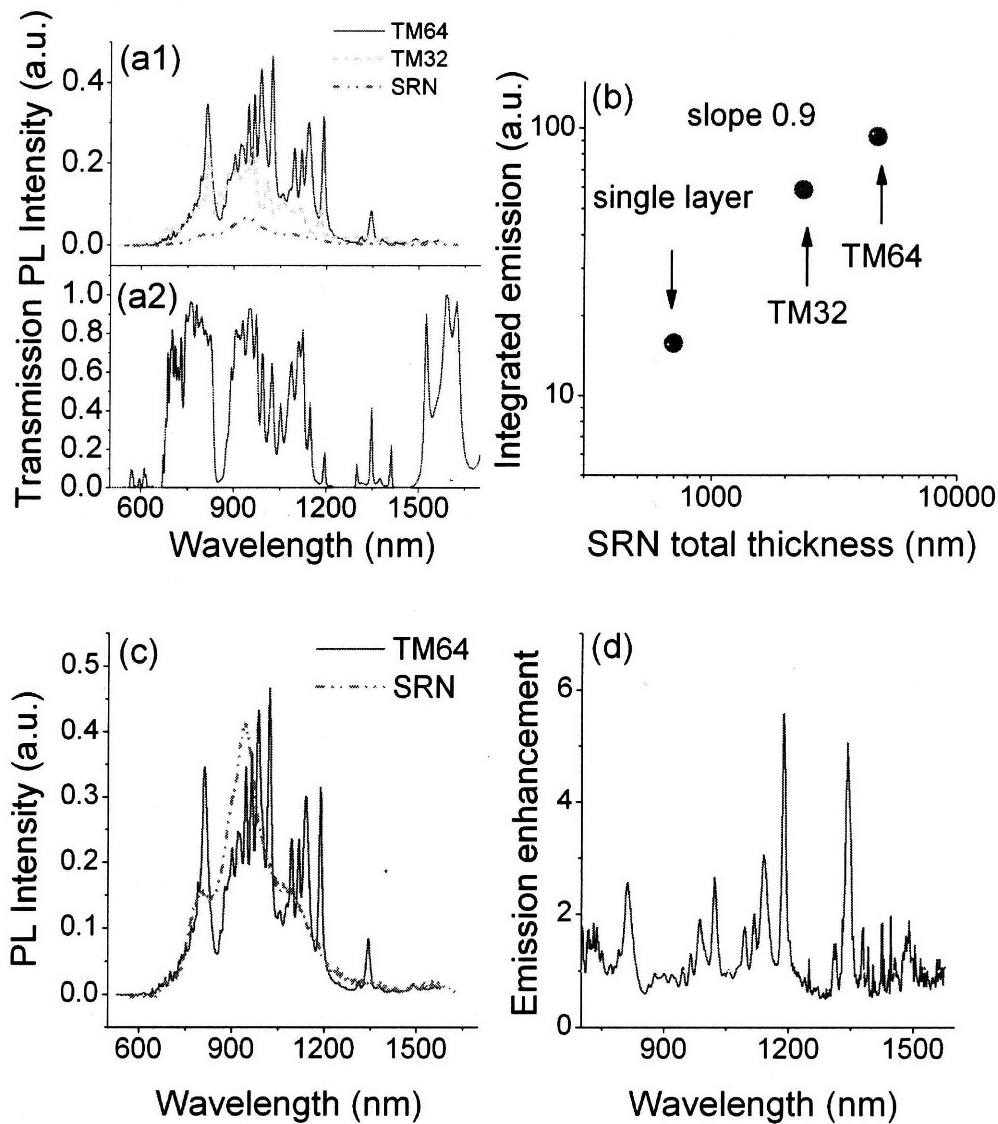

Figure 3.2 (a1) Room temperature PL intensity of TM64 sample (solid line), TM32 sample (dashed line), homogeneous SRN reference sample (dash-dotdot line). The excitation wavelength was 488 nm and the pump power was 10 mW. (a2) Experimental transmission spectrum for the 64 layer T-M structure. (b) Integral of the PL emission intensity (over the whole emission range shown at (a1) versus the total thickness of the light-emitting SRN

layers). The slope of the double logarithmic plot and the sample names are indicated. (c) Comparison of the TM64 emission spectrum and the homogeneous reference sample emission rescaled according to the SRN thickness ratio. (d) Experimentally derived wavelength spectrum of the optical emission enhancement in the TM64 sample.

behavior reflects the rich self-similar (multifractal) character of T-M structures [3, 4, 10]. In fig. 3.2 (a1), we show the RT emission spectrum of the TM64 (solid line) and TM32 (dash line) together with the emission of a reference homogeneous SRN sample (dash-dot-dot line). The TM64 transmission spectrum measured in the emission range is shown for comparison in fig. 3.2 (a2). The emission of the reference sample (a1, dashdot-dot) consists of a featureless wide band centered around 850 nm, consistent with data reported in the literature [15, 16]. On the contrary, when the SRN material is arranged to form a SRN /SiO_2 aperiodic T-M multilayer structure, its emission band is dramatically modified by the presence of the aperiodic environment and reflects the complexity of the associated T-M transmission spectrum [Fig. 3.2 (a2)]. In particular, narrow emission peaks appear in the emission spectrum of the TM64 sample and their position in wavelength matches the TM64 transmission spectrum [Figs. 3.1 (b) and 3.2 (a2)] within the broad SRN emission range. In order to assess the active role of the T-M structures by demonstrating emission enhancement effects at multiple resonant states, we studied the scaling behavior of the integral PL over the whole emission range in fig. 3.2 (a1). As shown in fig. 3.2 (b), the number of emitted photons (proportional to the integral of the PL emission) scales almost linearly with the thickness of the light-emitting SRN material embedded in the T-M structures. Therefore, rescaling the emission spectra of the samples according to their SRN thickness ratio allows one to derive experimentally the wavelength spectrum of T-M field

enhanced states. In particular, the rescaled reference sample and TM64 emission spectra are shown in fig. 3.2 (c). The ratio of the emission spectra shown in fig. 3.2 (c) yields the enhanced states wavelength spectrum due to the aperiodic T-M environment [Fig. 3.2 (d)]. In fig. 3.2 (d) we see that, for the TM64 structure, multiple states are enhanced by a factor of almost 6 with respect to the homogeneous SRN sample. If strong and recurrent scattering events occur, coherent feedback can eventually result in lasing. For lasing, closed loop path for light needs to be formed through recurrent scattering. Coherence length of a laser from the Thue-Morse structure, if achieved, is expected to be intermediate between random and periodic structures. Another interesting effect related to the significant field enhancement in TM64 structures has been observed through emission saturation measurements performed by comparing the pump-power-dependent emission of the TM64 and the reference sample for the same emission wavelengths.

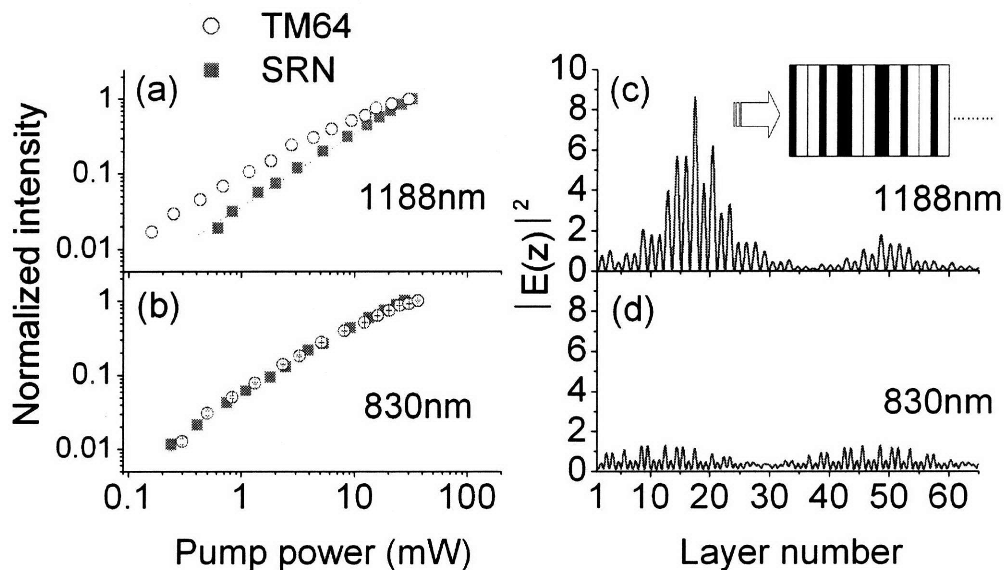

FIG. 3.3 (a) Room temperature PL intensity versus excitation pump power for the TM64 sample (open circles) and the homogeneous reference sample (black squares) collected at 1188 nm, corresponding to a critical T-M state. (b) Room temperature PL intensity versus excitation pump power for the TM64 sample (open circles) and the homogeneous reference sample (black squares) collected at 830 nm, corresponding to an extended T-M state. (c) One-dimensional (1D) transfer matrix calculation of the T-M state field intensity distribution at 1188 nm. The inset shows a sketch of the multilayer T-M structure with normalized plane waves entering from the left. (d) 1D transfer matrix calculation of the T-M state field intensity distribution at 830 nm.

As shown in fig. 3.3 (a), the emission behavior of the TM64 state with maximum emission enhancement at 1188 nm is significantly different with respect to the behavior of the homogeneous reference sample. Analogously to periodic photonic structures, the TM64 emission is strongly enhanced, in the low excitation regime, with respect to the emission of a reference sample. However, since at high pump powers the emission intensity saturates for both the samples at a common value uniquely determined by the number of emitting centers and their emission efficiency (the same for the TM64 and the reference sample since they are identically prepared), a change in the saturation trend for the two samples is expected. Therefore, when a localized TM64 state is excited, the strong field enhancement effect associated with the mode changes the trend of the pump power emission behavior with respect to the homogeneous dielectric [Fig. 3.3 (a)]. Consistently, the light emitted from extended T-M states with negligible field enhancement effects (i.e., at 830 nm) does not reveal a different saturation trend with respect to the homogeneous SRN sample [Fig. 3.3 (b)]. In order to account for the significant emission enhancement effects experimentally observed, we performed numerical one-dimensional simulations of the

electric field intensity distribution of the T-M states [18, 19]. It is known theoretically [3, 10] that in deterministic aperiodic systems, the wave functions are neither extended Bloch waves as in periodic systems [20, 21], nor exponentially localized states as in random materials [22, 23]. The notion of a critical wave function has been introduced to describe the rich behavior of critical states related to the complex multifractal character of aperiodic environments. In fig. 3.3 (c) we show the calculated field intensity for the T-M state that gives rise to the highest observed emission enhancement effect. The computed intensity profile consists of an extended envelope modulated by a richer fine structure of self-similar field fluctuations, in qualitative agreement with the standard picture of a critical state. On the contrary, the computation of the intensity profile corresponding to the 830 nm T-M state [Fig. 3.3 (d)] shows a negligible field enhancement effect, in agreement with the experimentally determined field enhancement spectrum shown in fig. 3.2 (d). We conclude that the excitation of T-M critical states is at the origin of the observed light-emission enhancement in T-M samples. Finally the localized character of these states is also reflected in the dramatic change of the angular emission profile of the T-M structure. Fig. 3.4 shows the strongly directional light emission observed for the T-M structures at different wavelengths corresponding to localized states with field enhancement. For the SRN homogeneous sample, an approximately Lambertian wide angle emission profile was observed since all the states are delocalized with negligible field enhancement.

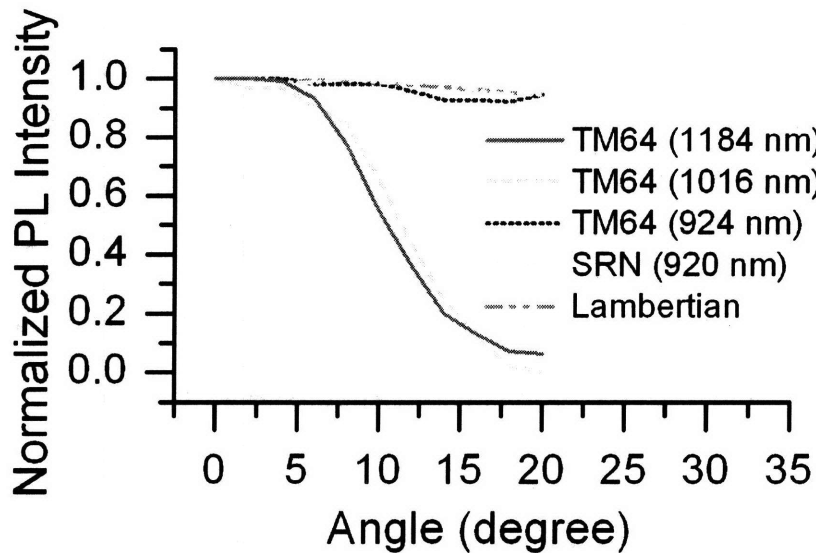

Figure 3.4. Angular profile of the normalized emitted intensity of T-M (64 layers) at different wavelengths indicated in the figure and for the reference homogeneous SRN sample.

3.1.4. Conclusion

In conclusion, we have reported on the experimental study of light-emitting SRN/SiO_2 Thue-Morse multilayer structures. We have shown significant light-emission enhancement effects for multiple resonance states and we have experimentally derived the wavelength spectrum of field enhanced states in a 64 layer thick T-M structure. A maximum emission enhancement by almost a factor of 6 with respect to a homogeneous light-emitting SRN sample has been observed along with a remarkably different emission saturation behavior. Strong directional light emission was observed for the localized states with field enhancement. Enhanced directionality is favorable characteristics for lasing efficiency. One-dimensional numerical simulations show qualitatively that the excitation of critical T-M wave functions is at the origin of the observed emission behavior. The demonstration of

broadband light-emitting T-M structures with multiple wavelength emission enhancement effects can provide an attractive route towards the fabrication of optically active devices for multiwavelength operation.

3.1.5. References

[1] M. Dulea, M. Johansson, R. Riklund, Phys. Rev. B **47**, 8547 (1993).

[2] M. Kolář, M. K. Ali, F. Nori, Phys. Rev. B **43**, 1034 (1991).

[3] N. Liu, Phys. Rev. B **55**, 3543 (1997).

[4] R. Pelster, V. Gasparian, G.. Nimtz, Phys. Rev. E **55**, 7645 (1997).

[5] M. Queffélec, *Substitution Dynamical Systems-Spectral Analysis, Lecture Notes in Mathematics,* vol. 1294 (Springer, Berlin, 1987).

[6] M. Morse, Trans. Am. Math. Soc. **22**, 84 (1921).

[7] X. Wang, U. Grimm, M. Schreiber, Phys. Rev. B **62**, 14020 (2000); S. Cheng, G. Jin, Phys. Rev. B, **65**, 134206-1 (2002).

[8] C. Godrèche, J. M. Luck, Phys. Rev. B **45**, 176 (1992).

[9] Sheng-Feng Cheng, Guo-Jun Jin, Phys. Rev. B **65**, 134206 (2002).

[10] C. S. Ryu, G. Y. Oh, M. H. Lee, Phys. Rev. B **46**, 5162 (1992).

[11] L. Dal Negro, M. Stolfi, Y. Yi, J. Michel, X. Duan, L. C. Kimerling, J.LeBlanc, J. Haavisto, Appl. Phys. Lett. **84**, 5186 (2004).

[12] P. E. deBrito, C. A. A. da Silva, N. H. Nazareno, Phys. Rev. B **51**, 6096 (1995).

[13] G. Gumbs, G. S. Dubey, A. Salman, B. S. Mahmoud, D. Huang, Phys. Rev. B **52**, 210 (1995).

[14] F. Iglói, L. Turban, H. Rieger, Phys. Rev. E **59**, 1465 (1999).

[15] S. V. Deshpande, E. Gulari, S.W. Brown, S. C. Rand, J. Appl. Phys. **77**, 6534 (1995).

[16] H. Kato, N. Kashio, Y. Ohki, K. Soo Seol, T. Noma, J. Appl. Phys. **93**, 239 (2003).

[17] J. M. Hollingworth, A. Vourdas, N. Backhouse, Phys. Rev. E **64**, 036611 (2001).

[18] A. Kavokin, G. Malpuech, A. Di Carlo, P. Lugli, F. Rossi, Phys. Rev. B **61**, 4413 (2000).

[19] L. Dal Negro, C. J. Oton, Z. Gaburro, L. Pavesi, P. Johnson, A. Lagendijk, M. Righini, L. Colocci, D. S. Wiersma, Phys. Rev. Lett. **90**, 5 (2003).

[20] E. Yablonovitch, Phys. Rev. Lett. **58**, 2059 (1987).

[21] J. D. Joannopoulos, P. R. Villeneuve, S. Fan, Nature **386**, 143 (1997).
[22] S. John, Phys. Rev. Lett. **53**, 2169 (1984).
[23] P. W. Anderson, Philos. Mag. **52**, 505 (1985).

3.2. Aperiodic waveguide structures

3.2.1. Introduction

The interesting features and advantages of the aperiodic structures were well described and discussed in the previous section. So far investigation of the aperiodic structure has been focused on the one dimensional multilayers. As revealed and discussed in the previous section, the increase of the system size leads to much richer states and accordingly more complex transmission states. However, the system size in multilayer structure is limited by structural instability of stress and crack and also by the interface irregularity and thickness variation which increase with the number of multilayers [1]. Here we introduce the novel concept and design of a CMOS-compatible, SRN-based waveguide structure that guide light due to the excitation of multiple resonant transmission states induced by the aperiodic dielectric environment.

3.2.2. Concept of aperiodic waveguide and discussion

In fig. 3.5 (a) and (b) we show the schematics of the aperiodic waveguide structure module that we have considered. Within this flexible module, we can easily change the aperiodic character of the guiding sub-units by simply considering different generation sequences. The number of the sub-units is not limited by the processing issues contrary to the one dimensional mutilayer case. We studied the light propagation in the aperiodic environments of Thue-Morse sequence [2]. The photonic structures that we have studied

are as follows: on top of an SiO_2 undercladding (10 μm thick) we have designed a Thue-Morse aperiodic sequence of SRN (n=2.2) and silicon oxynitride (SON) layers (n=1.7) with $3\lambda_0/4$ optical length and λ_0=1.55 μm. This corresponds to physical sub-unit length of d_{SRN}≅539 nm and d_{SON}≅704 nm respectively, when the effective refractive indices are considered. The reason for choosing length of the sub units to be three quarters instead of a quarter of wavelength comes from photolithography limitation. Illumination source of the photolithography has the wavelength of 365 nm. With this wavelength the resolution of the pattern is 450 nm, which means that the lengths of the sub units have to exceed this value. The device cross section is shown in fig. 3.5 (b). For these optimized design choice, the optical modes are perfectly matched for the different sub-units and the waveguide device can be easily fabricated using standard photolithography and etching steps. We have calculated the transmission spectrum of the aperiodic waveguide by using a commercially available three dimensional mode solver package based on mode matching techniques under the collaboration with M. Hiltunen, VTT Electronics [3, 4]. The optical transmission of the Thue-Morse waveguide with up to 256 SRN/SON sub-units is shown in fig. 3.5 (c). The waveguide transmission spectrum is very similar to the spectra of the strictly one dimensional system that we considered in fig. 3.1. However, for the waveguide structure, a bigger field enhancement effect and more enhanced transmission peaks can be achieved due to a much longer scattering length along the propagation axis. Sharp transmission peaks with high field enhancement as well as formation of the band gaps indicates the usefulness of the suggested structures for the application of selective filters, multifrequency optical cavities and sensors. The calculated electric field distribution in the waveguide structure is

shown in fig. 3.6 for two different T-M modes. In this specific example, a strongly localized mode (Fig. 3.6, (a)) yields a resonant transmission state at the wavelength (1390 nm) corresponding to a largely enhanced electric field (up to 80 times the incident field) in the structure. On the other hand, extended Thue-Morse states (with no field enhancement, 1550 nm) coexist in the structure (Fig. 3.6 (b)) and propagate through the waveguide without experiencing field enhancement effects. We emphasize that the aperiodic waveguide module introduced in fig. 3.5 can easily be generalized to study light-propagation in different aperiodic environments.

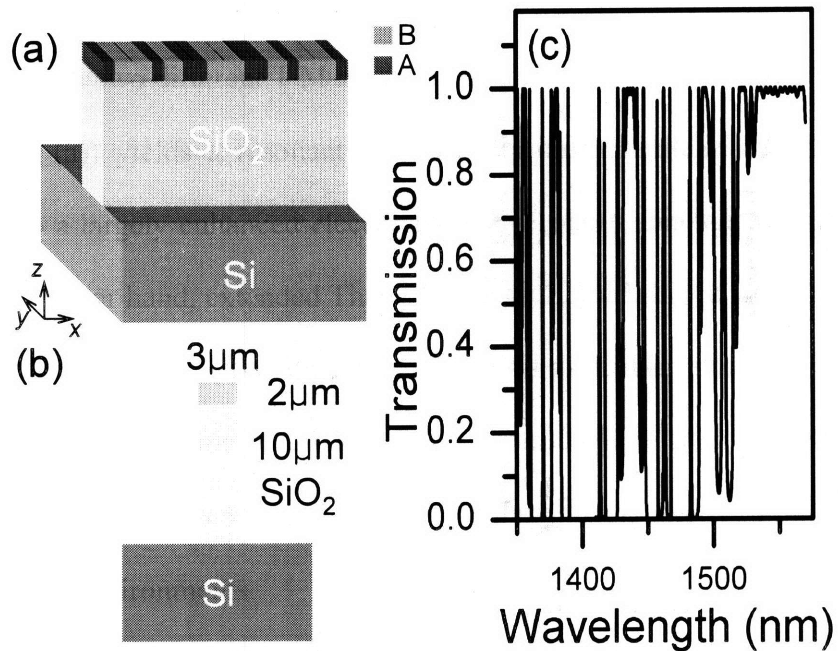

Figure 3.5 (a) Schematic diagram of a planar Thue-Morse aperiodic waveguide device. A and B represents different dielectric materials. For our simulations we have chosen A=SRN with n_A=2.2 and B=SON with n_B=1.7 (b) Cross section of the device (c) calculated transmission spectrum for the light that propagates through the aperiodic waveguide (Data courtesy: M. Hiltunen).

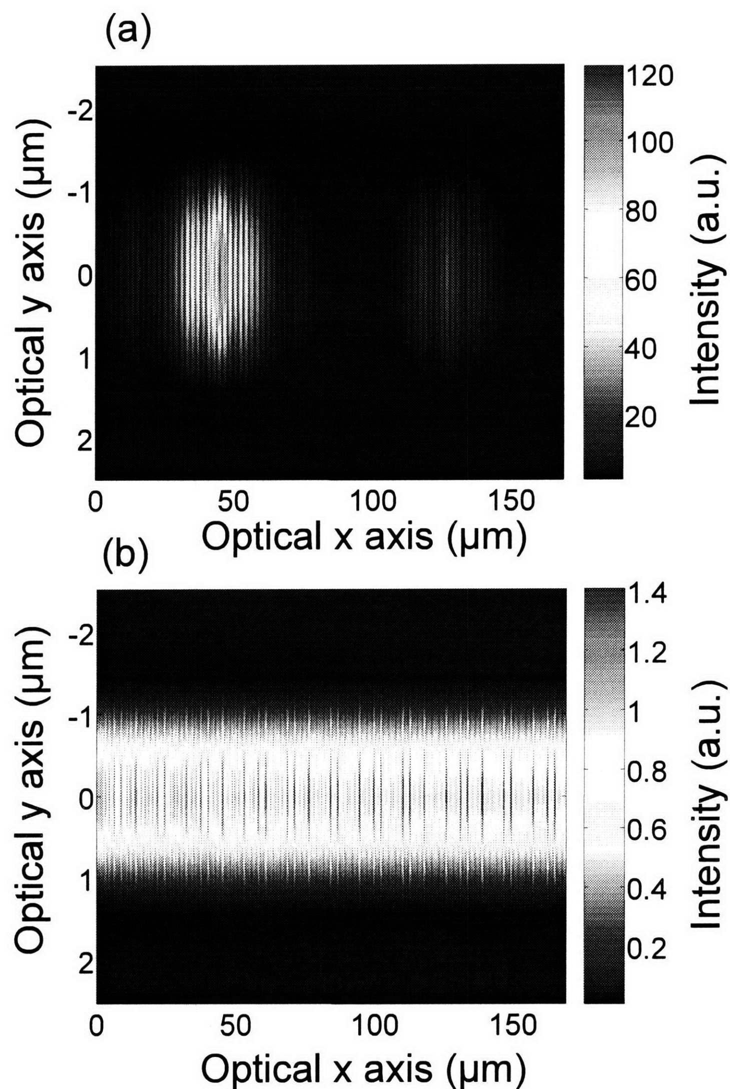

Figure 3.6 (a) Calculated electric field profile in the waveguide showing a localized T-M state at 1390 nm. (b) Calculated electric field profile in the horizontal plane of the waveguide showing an extended T-M state at 1550 nm (Data courtesy: M. Hiltunen).

3.2.3. Fabrication results and the related issues

We used SRN and SON as base materials and they are deposited by PECVD. The detailed process flow is described in fig. 3.7. We started with 3 or 10 µm oxide on Si wafers

or thermally oxidized Si wafers. 2 μm thick PECVD SRN was deposited on top and Thue-Morse sub-units were patterned by standard lithography and dry etching. The unit length of the sub-unit was described in the previous section. The large aspect ratio due to the height of 2 μm restricted the dry etching process in selecting the recipe. Very high selectivity between the mask and the SRN is preferred to main the shape of the sub-units. Therefore, we used oxide hard mask, not only the photoresist. This step is omitted in fig. 3.7 for simplicity. It also includes selective oxide and photoresist removal.

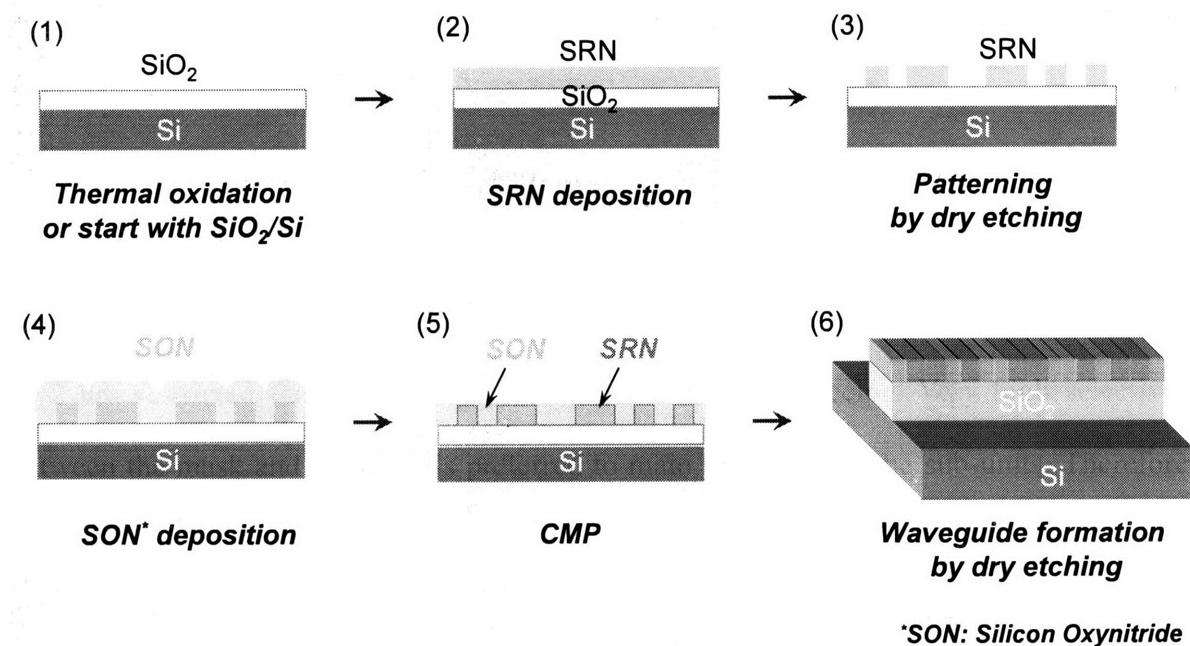

Figure 3.7. Detailed process flow for the fabrication of Thue-Morse waveguide structure.

Fig. 3.8 shows SEM images right after process step (3). We can clearly observe aperiodic features of the waveguide.

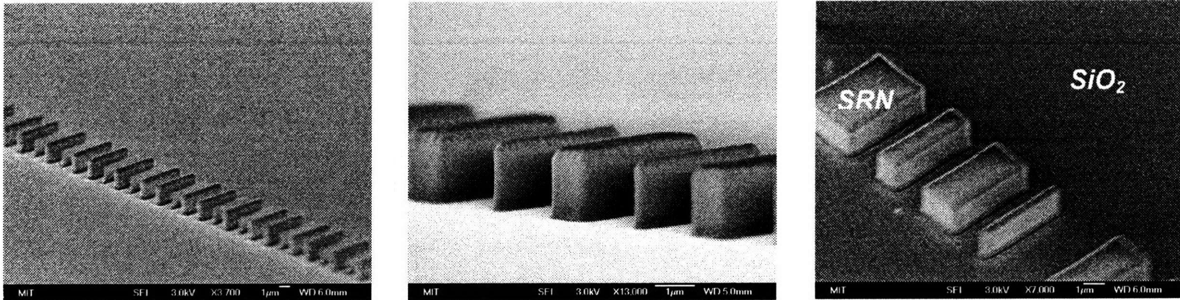

Figure 3.8. SEM images of Thue-Morse waveguide structure right after process step (3). All the small scale bars on the bottom indicate 1μm (Image courtesy: Dr. C. Hong).

Right after patterning process by dry etching (3) SON (n=1.7) was deposited to cover the whole area. Considering the following CMP planarization step, SON thickness was not 2μm, but 3μm. 1μm of SON will be removed during CMP process. With dummy SON wafer we checked polishing rate by CMP process. However, it was hard to predict that of the patterned samples even though they have large open area. Another dry etching process with waveguide pattern followed after CMP process to define the final waveguide structure. Even though it seems simple process, the detailed optimization of each process was delicate and challenging. Optical microscope images in fig. 3.9 show the final fabrication results after all the processes. Optical microscope was preferred to SEM here since it can show wider range of the area. In the images the darker features are SRN sub-units and long base waveguides. Some area shows left-over of SRN sub-units, but some other area shows no feature which means all the SRN sub-units in that area were torn away. It is suspected that the tear-away happened during the CMP process or SON etching process. However, it does not mean the limitation of the concept given here. It only needs to be optimized further with detailed care in each process step.

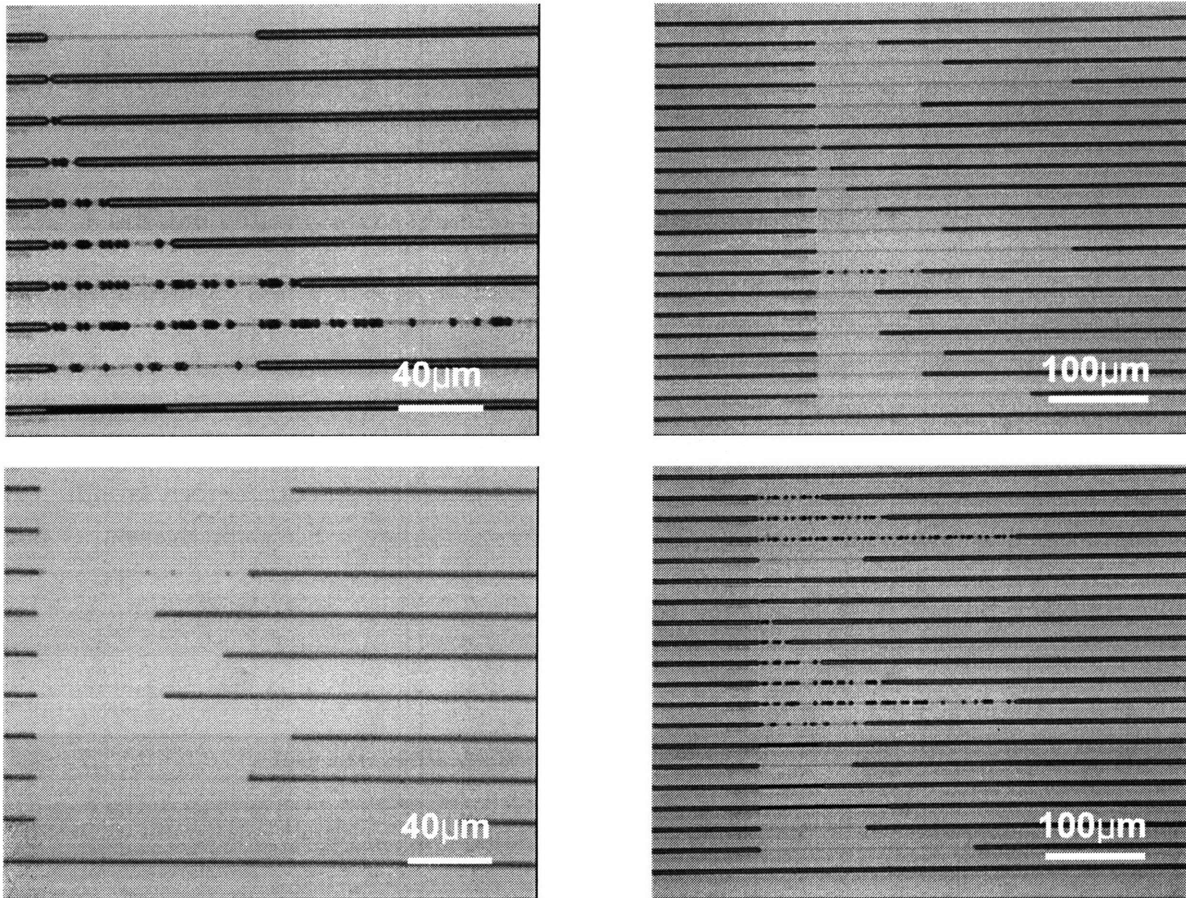

Figure 3.9. Optical microscope images after all the processes completed.

3.2.4. Conclusion

A novel concept of aperiodic waveguide structure was proposed and discussed the advantages of the structure. Thue-Morse waveguide structure with increased system size provided multiple localized states with the increased enhancement. However, due to limited processing capability, partially successful fabrication of the device structure was achieved. The proposed aperiodic waveguide structures can be applied for selective filters, multi-frequency optical cavities and sensors.

3.2.5. References

[1] W. Gellerman, M. Kohmoto, B. Sutherland and P.C. Taylor, Phys Rev. Lett. **72**, 633 (1994).

[2] M. Dulea, M. Johansson, R. Riklund, Phys. Rev. B. **45**, 105 (1992).

[3] A. Sudbo, Pure Appl. Opt. **2**, 211 (1993).

[4] The Photon Design *FimmWave* software was used for optimization of the modal overlap in the waveguide sub-units and the *FimmProp* framework code was used to simulate the mode propagation.

3.3. Sequential annealing technique for light enhancement

3.3.1. Introduction

Enhancing the light emission not only for the specific wavelengths but for the entire emission range requires increase in the number of emission sources and/or emission efficiency of each emission source. In this section we suggest a thermal treatment technique to enhance the light emission by increasing the number of silicon nanocrystal density. Since the independent control, especially increase, of the silicon nanocrystal density is significant issue in silicon nanocrystal based light emitters. We introduced background for the concept and interpretation of our experimental results.

3.3.2. Nucleation of the silicon nanocrystals

To understand nanocrystal formation mechanism the classical nucleation theory should be revisited [1-3]. Si nanocrystal forms from the precipitation with the annealing treatment at high temperature. There are two competing driving forces. The first one is

based on the volume free energy reduction $\Delta G_v(X_{Si}, T_A)$ where X_{Si} is the mole fraction of Si and T_A is the annealing temperature. This force increases with the increase of X_{Si} above the stoichiometric level and also with the increase of T_A. The second competing force is based on the interface energy, γ_{surf}, between the Si nanocrystal and the dielectric matrix. The total free energy change with these two energy contributions can be expressed with the following equation.

$$\Delta G_{tot} = -\frac{4\pi r^3}{3}\Delta G_v + 4\pi r^2 \gamma_{surf}$$

When annealing temperature is too low, driving force to form nanocrystals is not enough and no nanocrystal is formed. Above critical annealing temperature, the critical nucleation size r^* is a function of annealing temperature T: $r^* = A_c/(T_m - T)$. A_c is a constant determined by the molar enthalpy of nucleation at the melting point T_m, the interfacial energy per unit area, and the volume of a Si atom [4]. When the annealing temperature is high with a fixed Si content, driving force to form the Si nanocrystal is strong. Therefore, small number of large size nanocrystals form. When the annealing temperature is lower, we expect large number of small size nanocrystals.

3.3.3. Emission enhancement from Si nanocrystals

To enhance light emission from Si nanocrystals we should have a large density of nanocrystal which can emit light. With conventional annealing, when the annealing temperature is too high, we expect small number of large size nanocrystals. Having too

much large size nanocrystals, the material can not emit light due to lack of quantum confinement effect. On the contrary, when the annealing temperature is too low, nanocrystal formation is not possible. Therefore, having an intermediate annealing temperature is necessary for optimal light emission.

Based on the nucleation theory and the limited processing window we propose the novel concept of sequential annealing to enhance the light emission. The concept of sequential annealing is based on the independent control of the nucleation and growth. To achieve high density nucleation sites, the sample is annealed at low temperature first. However, these sites are below critical size for light emission. Therefore, we adopted a second stage of annealing at high temperature to grow them into large enough size. With the additional annealing step at high temperature we can expect large number of nanocrystals which also can emit light.

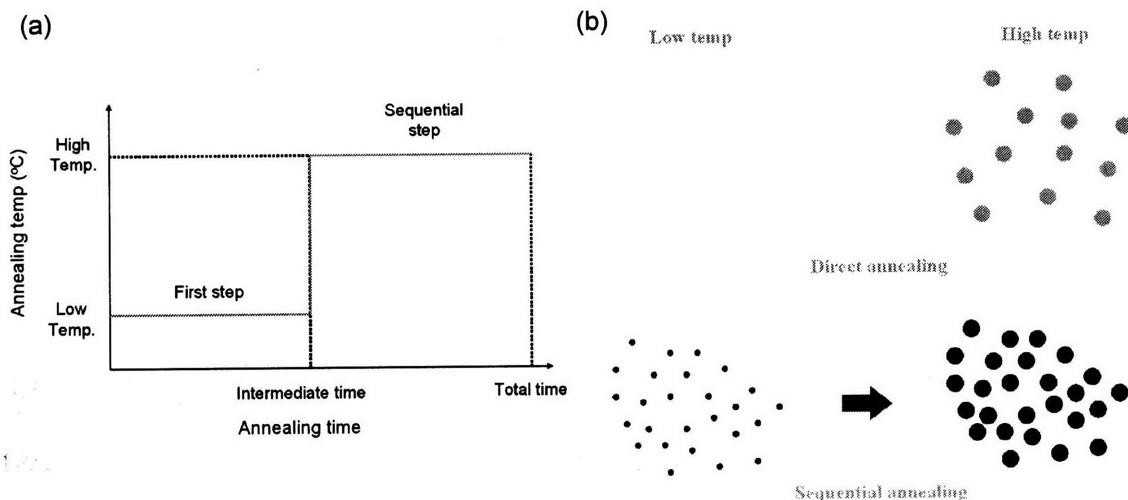

Figure 3.10 (a) Schematic diagram demonstrating the temperature profile with time for sequential annealing technique (b) Conceptual pictures for comparison between direct annealing and sequential annealing

As seen in fig. 3.10, annealing at low temperature is expected to induce many nucleation sites which then grow at higher temperature (Fig. 3.10 (a)) to appropriately sized nanocrystals (Fig. 3.10 (b)).

3.3.4. Experimental results and discussion

3.3.4.1. Concept of sequential annealing

For this experiment, we chose SRO rather than SRN since the SRN by PECVD has too small temperature window between the low temperature annealing step and the high temperature annealing step considering the fact that it was grown at 400°C and the optimal annealing temperature range is between 700~900°C. Therefore, we need to choose the first step of low temperature annealing at the temperature between 400°C and 700°C which is too much narrow. On the other hand, since SRO is grown by sputtering technique at room temperature and the optimal annealing temperature is around 1100°C (The detailed descriptions of the sputter system and processes are available in chapter 5), we can choose the first low temperature annealing step from a wider temperature range. To investigate the reason why the SRN films have much lower annealing temperature for silicon nanocrystal formation we performed the following experiments based on X. D. Pi *et al.* [4]. Multiple samples are prepared at varying annealing temperature and time. By plotting k_f value vs. $1/k_BT$ based on the relationship of $I=I_0+(I_{max}-I_0)\exp(-1/k_f t)$, where I, I_0, and I_{max} respectively are the PL intensity at time t, the PL intensity from the as-grown films, and the maximum PL intensity after long annealing times; and k_f is the formation rate of Si-nc's

with the assumption that the PL intensity is proportional to the concentration of Si-nc's, we could extract the formation energy of silicon nanocrystals, E_a, of 0.43±0.1 eV (Fig. 3.11). This value is much smaller than that of SRO at 1.4±0.5 eV [4]. Based on this analysis, lower annealing temperature is required for optimal photoluminescence in SRO.

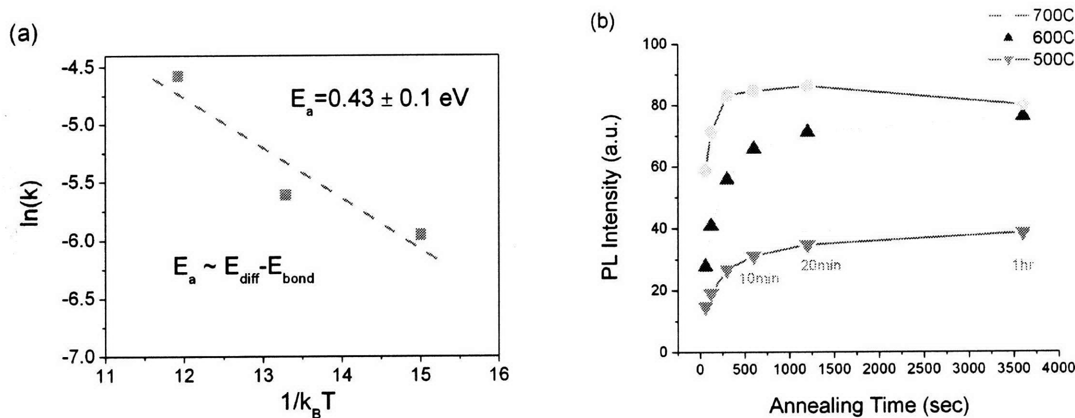

Figure 3.11 (a) Logarithmic plot of k_f vs. $1/k_BT$ to extract E_a, formation energy (b) Data set used for the experiments.

We selected the sample with the optimized silicon content with which strongest emission is expected. Detailed optimization process will be described in the following sections. Fig. 3.12 shows the photoluminescence spectra from the samples with direct annealing at 500°C for 45 min, at 1200°C for 15 min, and with the sequential annealing (500°C for 45 min + 1200°C for 15 min). With annealing at 500°C for 45 min there was no emission observed. It is obviously expected based on the previous argument regarding the size of the nanocrystals (Too much small size). Interestingly, the sequentially annealed sample produced stronger photoluminescence by 43% in peak intensity than the sample with normal annealing. Peak position is red shifted and the peak is broadened. It is well

known that the red shift in peak position is from the increase of the nanocrystal size and the broadening is from the wider distribution of the nanocrystal size [5].

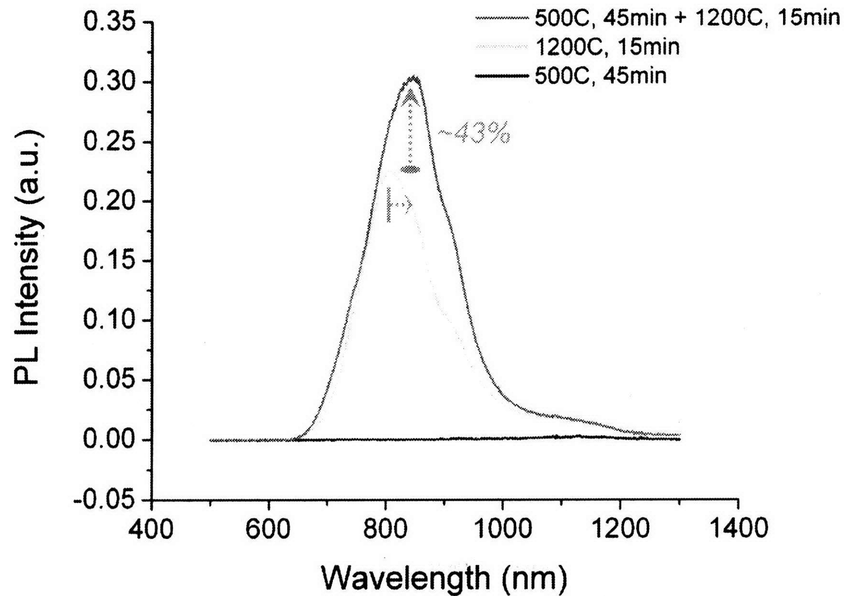

Figure 3.12. Photoluminescence spectra from the samples with annealing at 500°C for 45 min, at 1200°C for 15 min, and with the sequential annealing (500°C for 45 min + 1200°C for 15 min)

To investigate the effect further in detail regarding the annealing time we prepared the four samples with different combination of annealing time of the first step and the second step. (a) 1100°C, 60 min + 1200°C, 0 min, (b) 1100°C, 45 min + 1200°C, 15 min, (c) 1100°C, 30 min + 1200°C, 30 min, and (d) 1100°C, 0 min + 1200°C, 60 min. For easier understanding fig. 3.13 (a) will be helpful. Photoluminescence spectra from the samples in fig. 3.13 (b) revealed that sample with the annealing at 1100°C for 60 min clearly showed much lower intensity than those from other samples. Other samples showed similar

intensities. That is, with the additional first step annealing, similar photoluminescence intensity was achieved even with very short time (15 min) of second annealing (1200°C). Please note that photoluminescence intensity from the samples annealed at 1200°C for 60 min was similar to this sample.

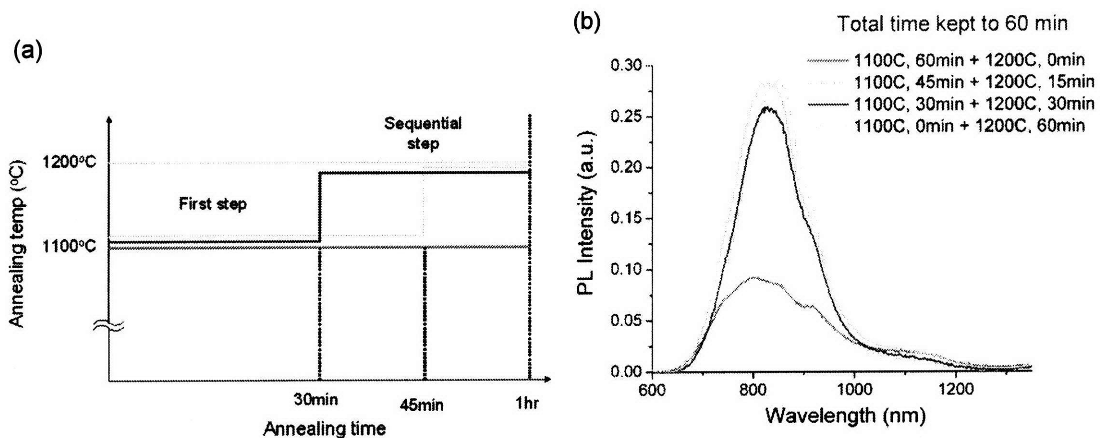

Figure 3.13 (a) Schematic diagram demonstrating the temperature control with time for the samples of (1) 1100°C, 60 min + 1200°C, 0 min, (2) 1100°C, 45 min + 1200°C, 15 min, (3) 1100°C, 30 min + 1200°C, 30 min, and (4) 1100°C, 0 min + 1200°C, 60 min (b) Corresponding the photoluminescence spectra

To investigate the effect of the annealing temperature in the first step we changed the temperature from 600°C to 1100°C and kept the temperature in the second step at 1200°C for all the samples. The annealing time for the first step was 45 minutes and that for the second step was 15 minutes. Fig. 3.14 (a) shows the process in detail with the schematic diagram of temperature profile. Photoluminescence results show interesting trend. First, all the sequentially annealed samples showed stronger emissions. More interestingly, as the temperature in the first step decreases, the final photoluminescence intensities increased.

We can note that the width of the photoluminescence spectrum was wider for the samples with lower annealing temperature in the first step. That means a wider distribution and higher density of silicon nanocrystals is expected.

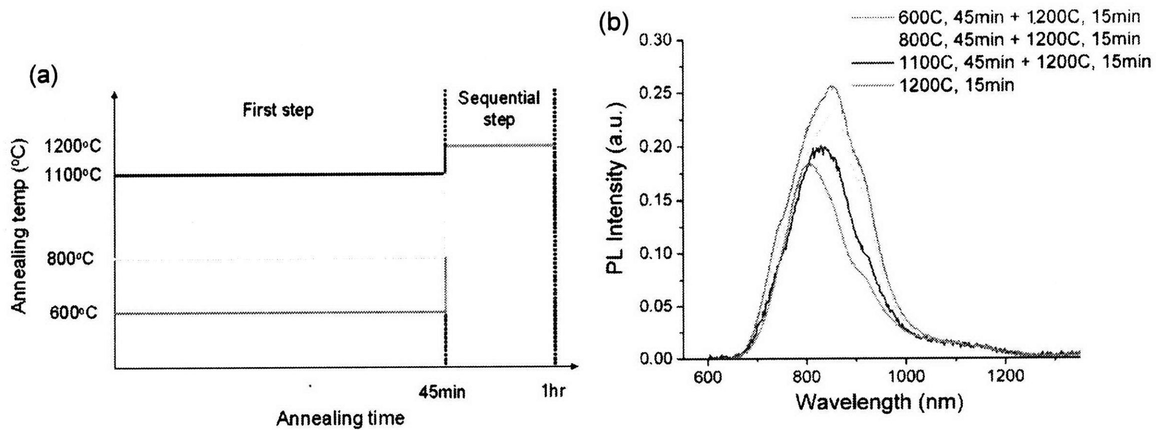

Figure 3.14 (a) Schematic diagram demonstrating the temperature control with time for the samples of (1) 600°C, 45 min + 1200°C, 15 min, (2) 800°C, 45 min + 1200°C, 15 min, (3) 1100°C, 45 min + 1200°C, 15 min, and (4) 1200°C, 15 min (b) Corresponding the photoluminescence spectra

3.3.4.2. Behavior with varied Si contents

We also compared samples with varied Si contents to investigate post sequentially annealing process. We used reactive sputtering technique to achieve silicon rich silicon oxide with controlling the oxygen content in the process gases. We fixed the rf power of the silicon target at 274 W and also the total flow rate of Ar and Ar+O_2 mixture gases at 20 sccm. With increasing the flow rate of the Ar+O_2 mixture gas, we expect decreasing refractive index to the lower limit of stoichiometric SiO_2. Fig. 3.15 shows the refractive indices with the change of Ar+O_2 flow rate and also corresponding growth rates.

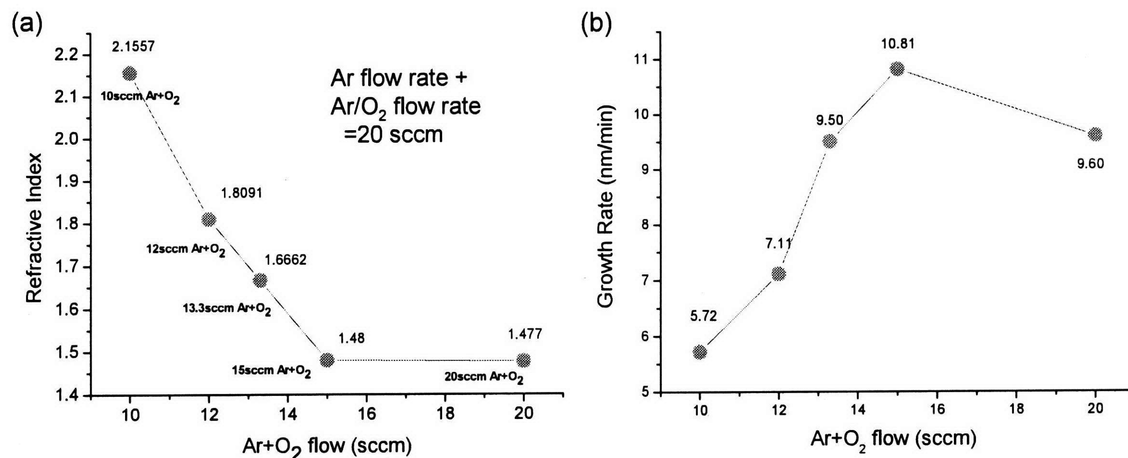

Figure 3.15. Refractive indices with the change of $Ar+O_2$ flow rate and also corresponding growth rates

For these samples we fixed annealing temperatures for the first and second steps at 500°C and 1200°C as in the case of fig. 3.12. Interestingly, we observed that the intensity increase due to sequential annealing with lower refractive index (Smaller Si content) film is larger up to by 50% (Fig. 3.16).

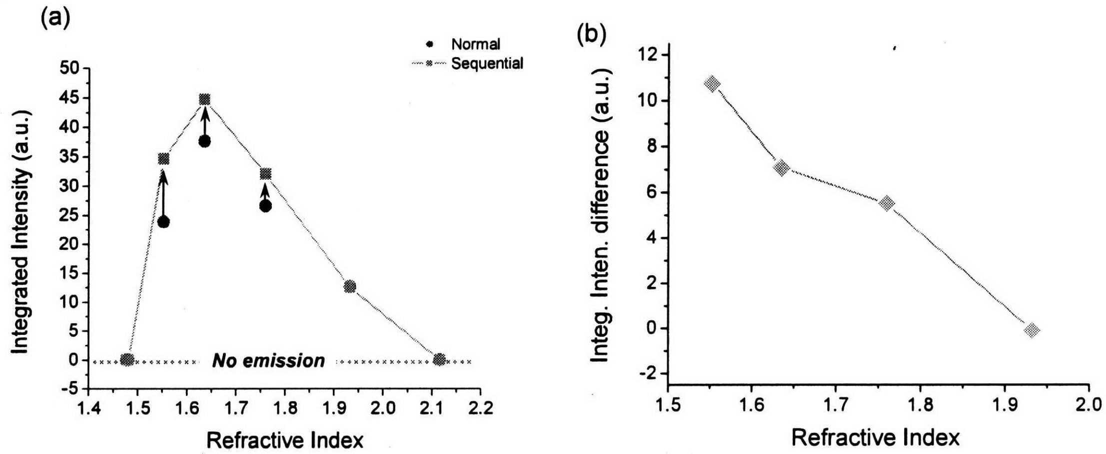

Figure 3.16 (a) Photoluminescence intensities for the normal annealing and sequential annealing of the samples with varied refractive indices. (b) Plot of the difference in photoluminescence intensities between the normal annealing and sequential annealing with varied refractive indices.

We also investigated the peak position change with refractive index for the normal annealing and sequential annealing cases. Fig. 3.17 (a) shows that peak positions generally increase with refractive index. As discussed in the previous section, with larger amount of silicon content, larger size of silicon nanocrystals form [5]. Therefore, longer wavelength is expected. However, if we focus on the sequential annealing case, it showed smaller peak shift than the normal annealing case. Based on the fig. 3.17 (b) we can explain the phenomenon with the easier nucleation and growth for the sequential annealing case. That is, when low Si content film is sequentially annealed, easier nucleation and growth leads not only to the increased Si-nc density, but also to the larger size of the Si nanocrystals. However, with high Si content, further growth to larger size can not contribute to longer wavelength since the nanocrystals with too large size can not contribute to light emission

due to lack of quantum confinement effect. Fig. 3.17 (b) will help the understanding of the phenomenon. The explanation is consistent with the case in fig. 3.14.

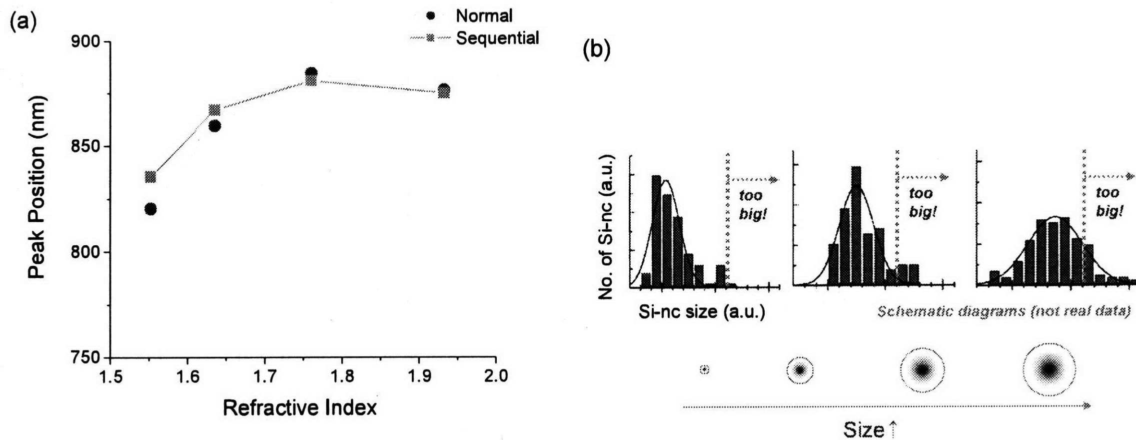

Figure 3.17 (a) Photoluminescence peak positions for the normal annealing and sequential annealing of samples with varied refractive indices. (b) Schematic diagrams showing the distribution of Si-nc size with refractive index. Si-nc size increases with refractive index.

3.3.5. Conclusion

For enhanced light emission from Si-nanocrystals, we proposed and demonstrated a novel concept of sequential annealing technique. Sequential annealing leads to the enhancement of light emission intensity up to by 40~50% compared to normal annealing technique. Sequential anneal with lower temperature in the first step leads to more enhancement. The samples with smaller Si content were affected more by sequential annealing.

By adopting sequential annealing we can improve light emission properties of silicon nanocrystal based material without utilizing complicated processes or elaborate system design. Further detailed investigation of sequential annealing technique based on the results

in this section will pave the way to a strongly emitting light source based on silicon nanocrystals.

3.3.6. References

[1] D. A. Porter and K. E. Easterling, *Phase Transformations in Metals and Alloys*, 2nd Edition, Chapman and Hall, London (1992).

[2] J. W. Christian, *The Theory of Transformations in Metals and Alloys Parts I and II*, 3rd Edition, Elsevier Science Ltd., Oxford (2002).

[3] R. W. Balluffi, S. M. Allen and W. C. Carter, *Kinetics of Materials*, 1st Edition, Wiley-Interscience (2005).

[4] X. D. Pi, O. H. Y. Zalloum, J. Wojcik, A. P. Knights, P. Maschera, A. D. W. Todd, and P. J. Simpson, J. Appl. Phys. **97**, 096108 (2005).

[5] F. Priolo, G. Franzo, D. Pacifici, V. Vinciguerra, F. Iacona, and A. Irrera, J. Appl. Phys. **89**, 264 (2001).

Chapter 4. Electrical properties and electroluminescence of SRN

4.1. Introduction

Highly efficient light emission has recently been achieved from the Si-based nanostructures in SiO_2 matrices [1] and also sizeable optical gain has been demonstrated [2]. Despite these significant results, porous Si and Si-nc's embedded in insulating SiO_2 matrices are not suitable for the fabrication of efficient, optically stable and fast electroluminescent devices due to the glass matrix and the slow exciton recombination lifetime (10~100 μs). Therefore, there is a need to investigate alternative CMOS-compatible approaches that can potentially lead to efficient light emission along with stable and efficient electrical injection. We successfully demonstrated strong emission from SRN with PLQE of 7% by optical pumping [3] in chapter 2. One of the strongest advantages of SRN material is superior electrical injection property due to much smaller barriers for electrons and holes from Si to silicon nitride as compared to SRO case. Therefore, a particularly attractive feature of SRN-based luminescent systems is the possibility to achieve efficient and stable electrical injection under low biasing voltages. Detailed values for electrical barriers of electrons and holes are provided, as well as the schematic energy band diagram as illustrated in fig. 4.1.

- Barrier at Si/SiO_2: 3.8/3.15 eV for h^+ & e^- (E_g (SiO_2)=8 eV)
- Barrier at Si/Si_3N_4: 1.5/2.0 eV for h^+ & e^- (E_g (Si_3N_4)=3.9~4.1 eV)

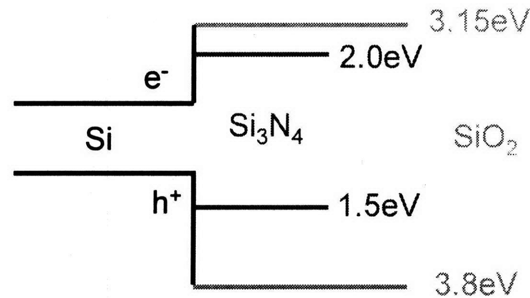

Figure 4.1. Energy band diagram of Si/Si_3N_4 junction and Si/SiO_2 junction for the comparison of the electrical barriers for electrons and holes.

Based on this characteristic, we expect that SRN has better electrical injection properties (higher current density at lower bias) than SRO. We are also interested in light emission phenomena based on electrical injection. Therefore, in this chapter we have fabricated light emitting devices and investigated electrical injection properties of SRN and the related electroluminescence behaviors.

4.2. Electrical injection improvement

To investigate electrical injection properties, a simple device structure was fabricated with SRN material grown by PECVD as in chapter 2. Detailed process parameters for SRN growth and thermal annealing can be found in chapter 2. First, gold metal was used as an electrode material to investigate current density level with applied voltage since we are not trying to observe light emission through the electrodes in this experiment. Au metal was deposited in an Argon gas atmosphere by a sputtering tool. Film thickness was controlled by sputtering time, pressure, and Ar flow. Thickness is 100 nm and process parameters were calibrated regularly to maintain thickness consistency. The optimal Au thickness was

determined based on the experiments where Au thickness was varied and the I-V stability and the current density levels were checked after fabrication. If the Au layer is too thin, some of the area was not fully covered and the current density was not stable, and furthermore it changes with the position we analyze. Conversely, if there is enough Au thickness, the whole area is fully covered at a low level of nonuniformity and the current density level is similar across many probe positions. However, too much increase of Au thickness only consumes expensive target. We decided around 100 nm is appropriate for our purpose. A simple aluminum shadow mask was used to pattern the Au electrode. That is, only a small designated area was open for Au deposition not to cover the sidewall of the sample. If the sidewall is covered with Au metal, it may lead to leakage path through the sidewall with Au. Current will not flow through SRN material itself, but through the Au on the sidewall. Annealing treatment was applied to induce Si-nc formation before Au deposition and the temperature was changed to alter Si-nc density in the matrix. Fig. 4.2 shows the experimental results from the I-V measurement [4].

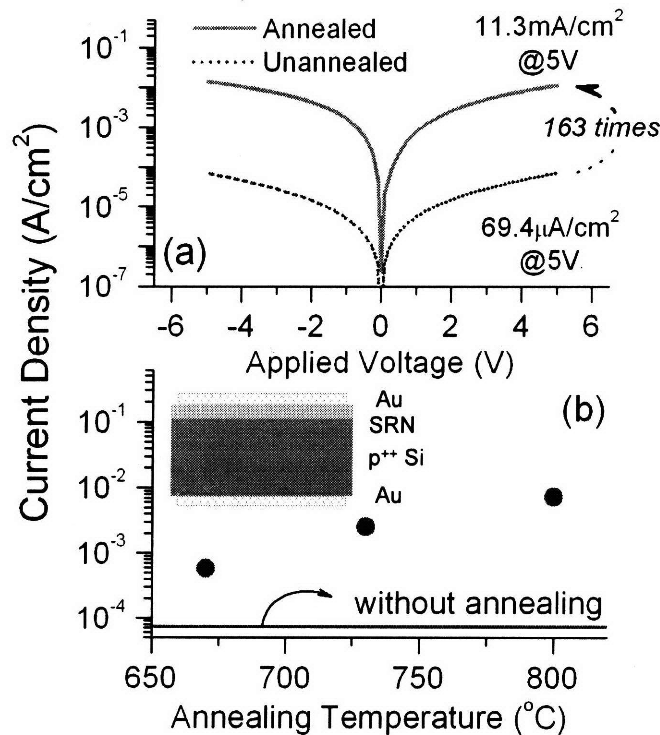

Figure 4.2 (a) Current density vs. applied voltage for the unannealed and annealed samples. Annealing was performed at 800°C for 10 min. in a nitrogen atmosphere. Strong enhancement could be observed. (b) Current density at the applied voltage of 5V with changing annealing temperature. Inlet shows the device structure used for this investigation.

From fig. 4.2 (a) it can be determined that the annealed sample showed much higher current density (11.3 mA/cm^2 at 5V) than that of the unannealed sample (69.4 μA/cm^2 at 5V). Annealing was performed at 800°C for 10 min. in a nitrogen atmosphere. More than a two order enhancement in current density was observed. To get the detailed trend we changed the annealing temperature from 680°C to 800°C (Fig. 4.2 (b)). First, compared to the unannealed case shown with solid line the current density was higher by more than 1 order (even for the annealed sample at 680°C). Second, current density increases with the increased annealing temperature.

Interestingly there is current flow even with the unannealed sample. This can be easily understood in the same way for the photoluminescence observation from the unannealed sample even though peak intensity was weak. This is basically the same situation considering that SRN growth by PECVD was done at 400°C and cooled down after growth. We can expect that *in situ* annealing happened during the process. That is, with some annealing effect, weak photoluminescence (not no emission) and small current flow (not no flow) could be observed.

To explain the observed phenomena of increased current density with annealing temperature we performed I-V characterization by changing the sample temperature during measurement. Please keep in mind that it is sample temperature, not annealing temperature. that was varied Conclusively we propose that the increased nanocluster density with increased annealing temperature is the reason for the observed behavior of increased current density.

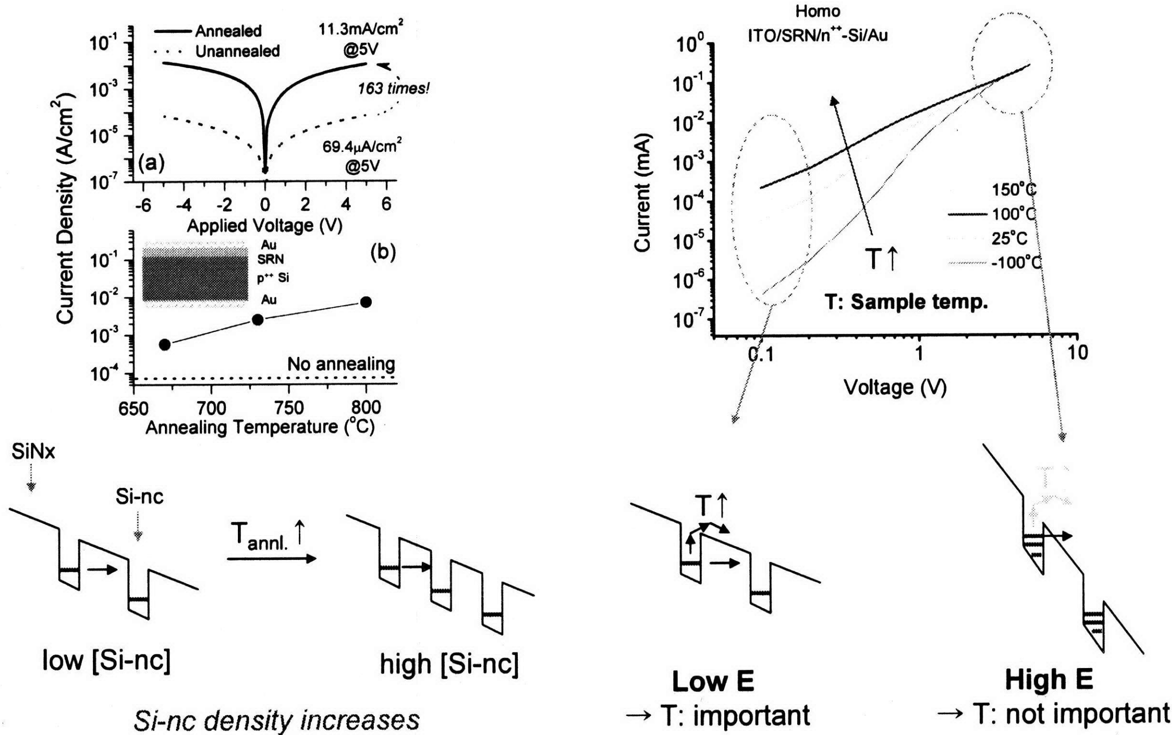

Figure 4.3. (Figure 4.2 was copied out here for clarity.) The figure on the right shows I-V characteristics with changing the sample temperature from -100°C to 150°C. On the bottom of each graph, an energy band diagram is shown to illustrate the conduction phenomenon for each case.

Increased current density can be explained by increased Si nanocluster density with annealing temperature. As in the diagram on the bottom left side of fig. 4.3, with increased Si-nc density the tunneling distance between the clusters becomes smaller. Therefore, we can expect a corresponding higher current density. This picture was confirmed by the I-V characteristics with the changed sample temperature as shown on the right side of the fig. 4.3. When the electric field is small, each well of Si-nc is filled in low level and the (triangular) barrier distance is long. Therefore, the thermal energy has an important role in

increasing the current. That is the reason why we observed the increased current density at low electric fields (low voltage with same sample thickness) with the increased sample temperature. However, when the electric field is large, each well is filled higher than the previous case, and the barrier distance is smaller due to tilting of the energy band diagram. In this case the contribution by thermal energy is very little. So, current levels are similar for the widely varied temperatures.

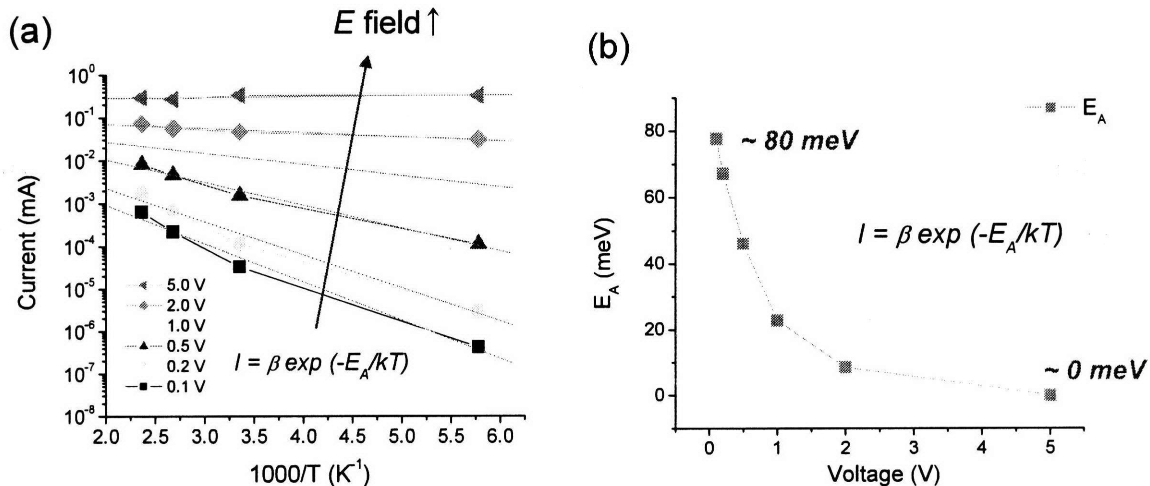

Figure 4.4 (a) Logarithmic plot of current versus inverse temperature with varied voltage. (b) Activation energy of the electrical barriers with varied voltage.

To investigate the electrical barriers in this model we plotted current logarithmically versus inverse temperature by varying applied voltage (proportional to electric field with fixed thickness). As the applied voltage increases, the slope of the fitted line becomes small which means the electrical barrier becomes small (Fig. 4.4 (a)). Data points could be fitted very well with exponential dependency on inverse temperature. From the fitting activation

energy, E_A, for the electrical barrier could be extracted and plotted in fig. 4.4 (b). The barrier is changed from 80 meV to almost 0 meV as the voltage is varied from 0.1V to 5V. When 0.1V is applied (with the barrier of 80 meV), temperature change from room temperature even to $100^{o}C$ results in strong enhancement of current, by nearly an order of magnitude. With the barrier of 0 meV, however, any dependency on temperature can not be observed.

Lastly, we want to emphasize that the current density level we observed in this investigation is much higher than that of SRO. Fig. 4.5 shows the current density level by varying the applied voltage to the SRO based device [5]. As we can compare, the current density level from 10^{-10} to 10^{-8} A/cm^2 was observed at 5V by changing the Si content from 39 at. % to 46 at. %. Considering the thickness of the SRO samples investigated here was 80 nm and that of our investigation was 700 nm and the current density level of our sample was ~10^{-2} A/cm^2 level, the range of current density level through SRO is far too low (approximately 6~8 orders lower even with smaller thickness of 80 nm). This comparison clearly demonstrates experimentally that SRN has superior electrical injection properties to SRO.

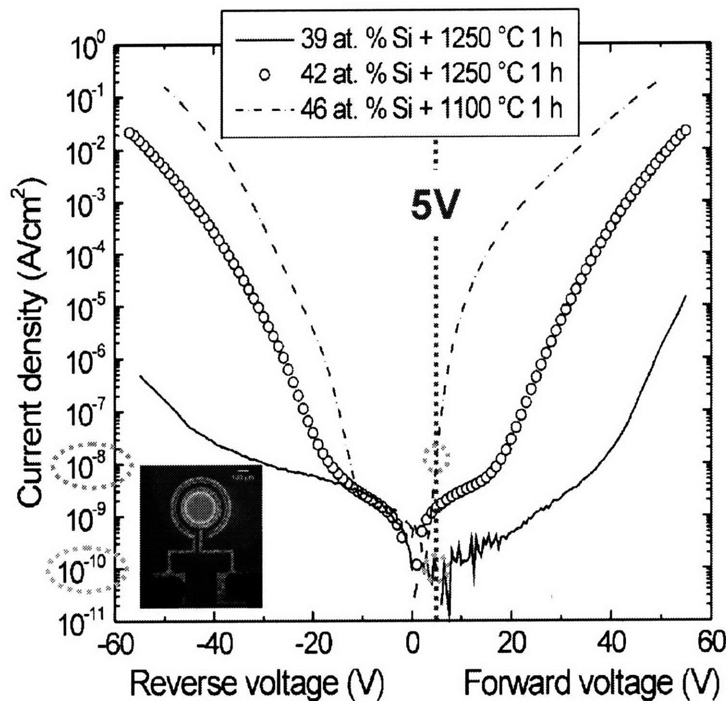

Figure 4.5. Current density with applied voltage for SRO samples with Si contents and annealing conditions shown in the figure. Considering the fact that the light emitting device with electroluminescence in the inlet was fabricated with the delicate silicon processing, we can figure out how high current density we could achieve from our SRN devices. With this observation we confirm that SRN material has superior electrical injection properties to SRO material [5].

4.3. Light emitting device and electroluminescence

Based on the electrical injection properties we observed in the previous section we fabricated a light emitting device with a transparent electrode such as ITO (Indium Tin Oxide). An ITO film was deposited by an rf sputtering tool in MIT MTL with an ITO target. Before the main deposition, a dummy run was processed to ensure a clean chamber condition. Base pressure was reached down to low 10^{-6} Torr. The same aluminum shadow mask used in the previous section was used in this experiment to open the electrode area

only in the center. Resistance was checked for the process confirmation with the ITO on glass sample. If the resistance value was not obtained in the expected range, process was not continued further with the main device and maintenance steps were taken care of. The 100 nm thickness was confirmed by ellipsometry. There is a tradeoff between transparency and conductivity with thickness increase. Figure 4.6 shows the schematic diagram of the device structure used for this investigation.

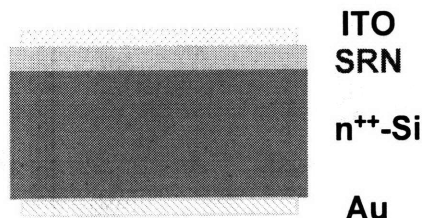

Figure 4.6. Schematic diagram of the device structure for light emission by electrical injection. ITO film was used as a top electrode and Au as a bottom electrode.

The deposited ITO film demonstrated a high transmission value (> 80%) for the wavelength range for which we are interested (600~1500 nm). Fig. 4.7 (a) shows the experimentally measured transmission data for the ITO films (100 nm, n=1.85) used for the light emitting devices. Various ITO samples from the separate depositions showed a similar level of transmissivity. We also compared photoluminescence spectra from SRN samples with and without ITO films on top. Fig. 4.7 (b) clearly demonstrates that the emission intensity and lineshape do not change significantly with ITO on top. Minor interference features in the photoluminescence spectrum arose with ITO.

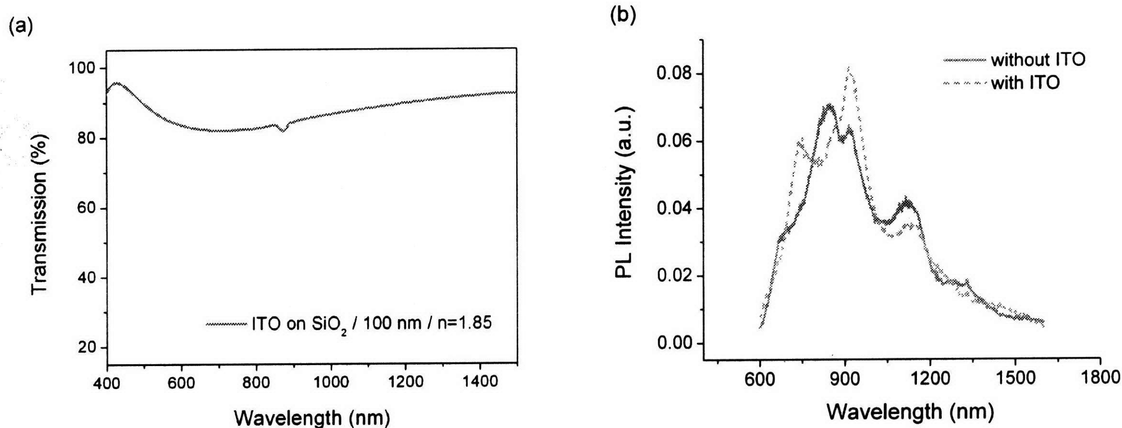

Figure 4.7 (a) Transmission data for the ITO film deposited for light emitting devices. (b) Photoluminescence spectra from the SRN samples with and without ITO films on top.

To investigate the importance of the injection scheme we prepared an ITO/SRN/p^+-Si/Au structure and an ITO/SRN/n^+-Si/Au structure. Fig. 4.8 shows the I-V characteristics from these device structures. With the ITO/SRN/p^+-Si/Au structure we observed almost linear I-V characteristics without diode-like behavior and we expect unipolar injection from this structure (Fig. 4.8 (a)). With the ITO/SRN/n^+-Si/Au structure we observed diode-like behavior and bipolar injection is expected (Fig. 4.8 (b)). Interestingly, no electroluminescence was observed from the unipolar injection case even though a wide range of voltage was applied. However, we could easily observe electroluminescence at the applied voltage of 5V in the bipolar injection case and fig. 4.9 shows the electroluminescence which is well overlapped with photoluminescence within the sensitivity range of the detector. We conclude that the bipolar injection scheme based on a ITO/SRN/n^+-Si/Au structure is required to observe electroluminescence from the thermally annealed SRN systems.

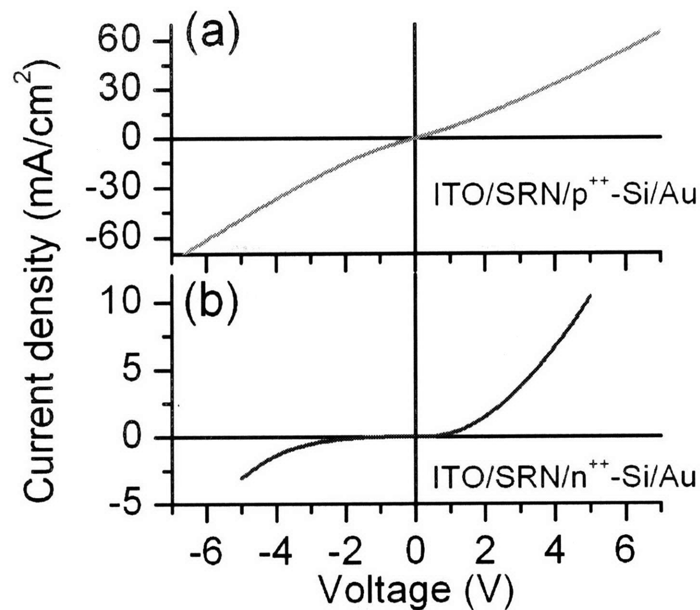

Figure 4.8 (a) I-V characteristic for the ITO/SRN/p^+-Si/Au sample and (b) for the ITO/SRN/n^+-Si/Au sample.

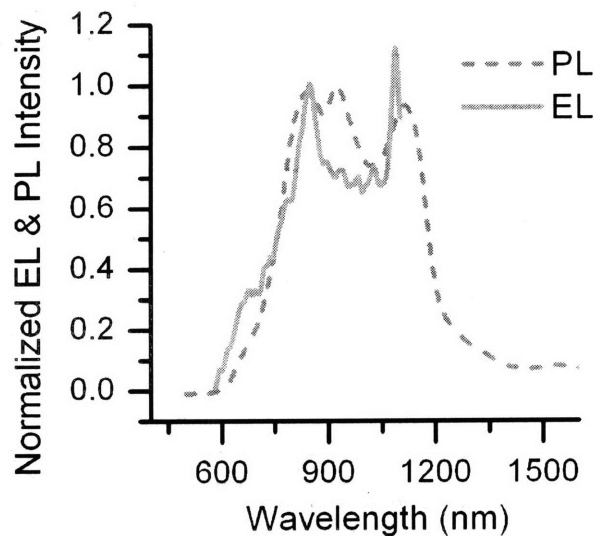

Figure 4.9. Electroluminescence and photoluminescence spectra normalized to provide better comparison.

4.4. Conclusion

In this section we investigated electrical properties of SRN material and observed electroluminescence phenomena. 6~8 orders higher current density was observed for SRN even with much thicker films (700 nm compared to 80 nm of SRO). Strong enhancement of current density level was observed with increased annealing temperature. Detailed experiments with varied sample temperatures demonstrated that the conduction mechanism is based on the increase of the Si-nc density. Thermal contribution was important for a low electric field, but not for a high electric field. To investigate light emitting devices, a transparent electrode like ITO was adopted as a top electrode. ITO/SRN/p^+-Si/Au structure for unipolar injection and ITO/SRN/n^+-Si/Au structure for bipolar injection were prepared to investigate the importance of the injection scheme. Only with an ITO/SRN/n^+-Si/Au structure could we observe diode-like I-V and electroluminescence well overlapped with photoluminescence. Demonstration of high current density and also electroluminescence at low applied voltage contributes substantially to the way for low voltage operating silicon-based light emitter and other related applications.

4.5. References.

[1] L. Pavesi and D. J. Lockwood, *Silicon Photonics*. Berlin, Germany: Springer-Verlag (2004).

[2] L. Pavesi, L. Dal Negro, C. Mazzoleni, G. Franzo′, and F. Priolo, Nature **408**, 440 (2000).

[3] L. Dal Negro, J. H. Yi, J. Michel, L. C. Kimerling, T.-W. F. Chang, V. Sukhovatkin, and E. H. Sargent, Appl. Phys. Lett. **88**, 233109 (2006).

[4] Luca Dal Negro, Jae Hyung Yi, Jurgen Michel, Lionel C. Kimerling, Sebastien Hamel,Andrew Williamson, and Giulia Galli, IEEE J. Select. Topics Quantum Electron. **12**,

1628 (2006).
[5] G. Franzò, A. Irrera, E. C. Moreira, M. Miritello, F. Iacona, D. Sanfilippo, G. Di Stefano, P. G. Fallica, and F. Priolo, Appl. Phys. A **74**, 1 (2002).

Chapter 5. Optical properties of Er:SRN

5.1. Introduction

SRN material has various advantages including high emission efficiency, good electrical injection properties, and low annealing temperature for nanocrystal formation with the CMOS compatibility maintained as SRO material. However, the emission wavelength range from our SRN material is around 700~1000 nm which is quite deviated from 1.54 μm, the most interested wavelength for telecommunication. Er incorporation into SRN material can be considered to obtain the emission wavelength of 1.54 μm which leads to the minimum transmission loss through optical fiber, also with good electrical injection characteristics. Sensitization role of Si-nc's in SRO could be utilized to excite Er more efficiently than direct optical excitation. However, Si-nc embedded in SiO_2 matrices are not suitable for the fabrication of reliable, optically efficient and stable electrically-driven light sources due to the insulating SiO_2 barriers and the slow exciton recombination lifetime (10-100 μs). Therefore, alternative Si-compatible (or CMOS compatible) approaches that can yield fast (ns), efficient and stable electrical excitation need to be investigated. An intriguing possibility would be the nucleation of Si nano-clusters in dielectric matrices with smaller bandgap than SiO_2 and more favorable electrical properties. Based on the situation we have investigated SRN material up to chapter 4, we investigate Er:SRN material optically and electrically from this chapter.

Optimization of Si content in Er:SRN material and also the investigation of the role of Si content is important even for the electrical device. The relationship between the SRN emission and Er emission from Er:SRN is also considered to understand the role of SRN

emission in energy transfer to Er atoms from SRN matrix.

Gain related investigation based on the key parameters such as sensitizer concentration, cross-section, Er concentration, etc has been pursued for better understanding of how these key parameters will affect the gain in the Er:SRN system. This investigation will also be helpful as supplementary information for the comparison when we consider the electrical excitation of Er.

Finally, energy transfer from SRN to PbS quantum dots has been investigated. Luminescence from colloidal quantum dots is very efficient and widely tuneable in wavelength. Coupling CMOS compatible but inefficiently light emitting silicon-based materials with highly efficient colloidal quantum dots would greatly enrich silicon's growing set of functionalities. Not only for the advantages of the SRN-PbS coupled system, this investigation can imply physics related with the energy transfer from Si resonator to Er:SRN which we may utilize in the coupled device structure.

5.2. Fabrication and analysis

Er-doped SRN films (Er:SRN) were fabricated by direct magnetron co-sputtering with Er, Si and Si_3N_4 targets using a Kurt J. Lesker Co. CMS 18 sputtering system (Fig. 5.1). SRN films were also deposited to investigate the relationship between SRN emission and Er emission from Er:SRN only with Si and Si_3N_4 targets. We could not utilize the PECVD machine which we used to grow SRN studied in chapter 2~4, since PECVD machine is a shared facility at MIT MTL to which we could not attach Er-based precursor line, even though we know that generally PECVD dielectrics give better optical and structural

properties with well-controlled microstructure. Base pressure of 1 x 10^{-7} ~ 1 x 10^{-8} Torr was achieved by cryo pump before the main deposition. The substrate was rotated at around 30 rpm during the deposition to achieve better uniformity and was not heated. All the samples have been deposited on transparent fused silica substrates or silicon substrates and annealed at different temperatures ranging from 300°C to 1100°C after sputter deposition.

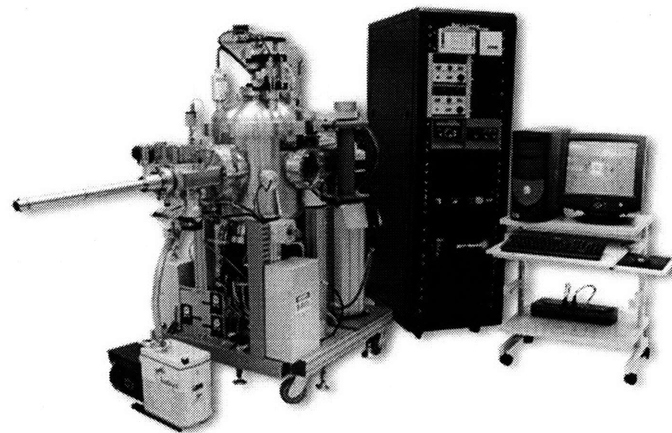

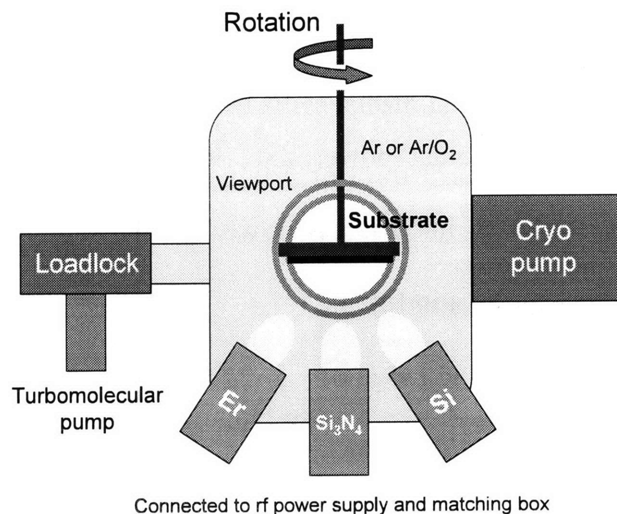

Figure 5.1. Direct magnetron co-sputtering system with three different targets attached purchased from Kurt J. Lesker Company and schematic diagram of the main chamber. Three targets can be used simultaneously. With turbomolecular pump and cryo pump we can pump the main chamber down to the base pressure of 10^{-8} Torr level.

Room temperature photoluminescence (PL) experiments were performed using 488 nm or 457 nm Ar pump laser and a liquid nitrogen cooled InGaAs photomultiplier tube. Oscilloscope combined with photomultiplier tube was used to get the rise and decay time of the luminescence.

5.2.1. Investigation on the process conditions

We investigated the process conditions for the Er:SRN growth by varying the deposition parameters including Si, Si_3N_4, Er target powers and Ar flow rate. The growth rate was determined mostly by the Si_3N_4 target power as shown in fig. 5.2 (a) since Si_3N_4 is the main matrix material. In this plot Er target power is fixed to 10 W, but there is some variation in Si target power between 10 and 200 W. However, the contribution to the growth rate from Si incorporation by varying Si target power is not significant as we can observe in fig. 5.2 (b). That is, change in Si_3N_4 target power led to dramatic change in growth rate, but change in Si target power only led to slight change in growth rate. Therefore, having some variation in Si target power for the plot in fig. 5.2 (a) does not diminish the significance of the plot in fig. 5.2 (a).

Variation of Ar flow rate in the range of 7.2~21.6 sccm did not affect the growth rate that much. Even though there were some insignificant increase and decrease, it was smaller than data fluctuation. Therefore, we did not focus on Ar flow as a process parameter since it only increases complexity in controlling parameters.

Increase of Si incorporation by increasing the Si target power led to increased refractive index as shown in fig. 5.3. Refractive index can be used as a relative measure of

the Si content in the nitride matrix if all other parameters are fixed (RBS analysis to determine the accurate content has been not available any more due to the termination of service by Harvard University). In the next section the detailed investigation of luminescence properties based on the process parameters including annealing conditions will be provided and discussed.

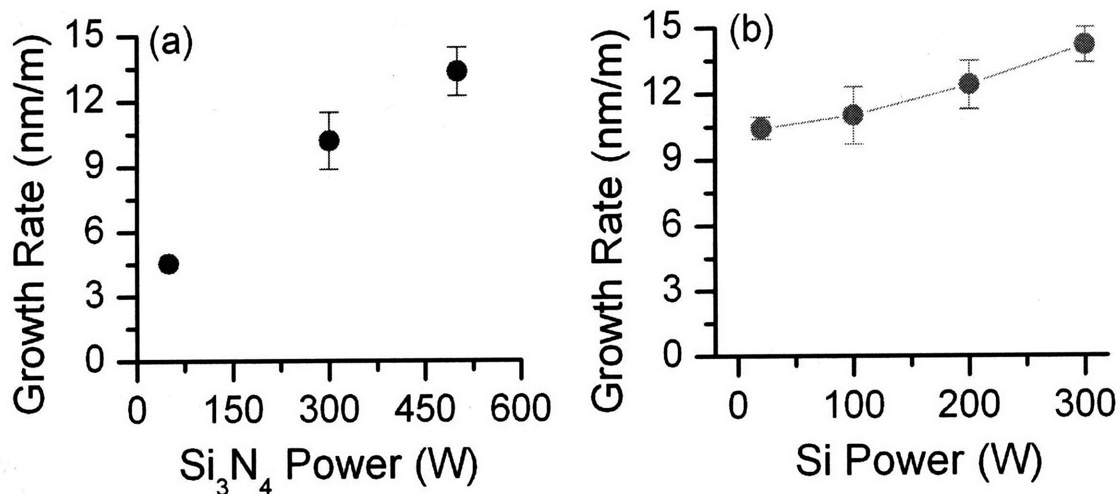

Figure 5.2 (a) Plot of the growth rate (nm/m) versus Si_3N_4 target power. Er target power is fixed to 10W, but there is some variation in Si target powers between 10 and 200 W. However, contribution from Si target power increase is not significant to change the general trend. (b) Plot of growth rate (nm/m) versus Si target power. Si_3N_4 and Er target powers are fixed to 500 W and 10 W, respectively.

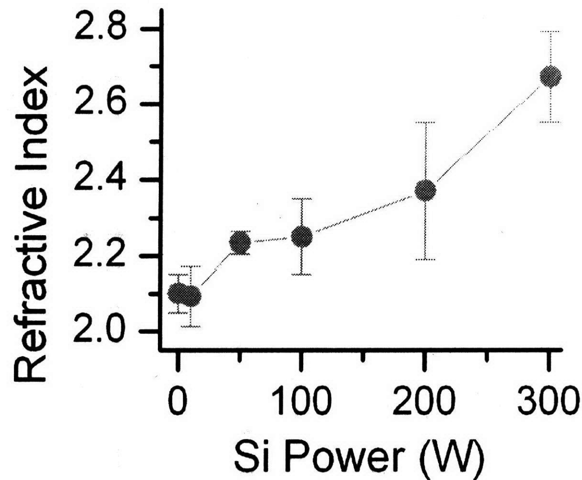

Figure 5.3. Plot of the refractive index versus Si target power. Si_3N_4 and Er target powers are fixed to 500 W and 10 W, respectively.

5.3. Optical properties of Er:SRN

5.3.1. Luminescence optimization

Er is one of the rare earth elements in the lanthanide group. Optical transitions in Er are parity-forbidden. However, if it is incorporated into a solid matrix, it usually becomes Er^{3+} ions. The Er^{3+} level splits up due to Stark effect and the matrix makes some transition allowed with odd character. With this modification we can observe luminescence from Er atoms in the solid matrix. Understanding the luminescence properties of Er in SRN matrix with variation of process parameters is interesting and important since the situation described above will be changed dramatically with process parameters.

First, the luminescence properties were investigated by varying the Si target power with the fixed Er and Si_3N_4 target power. As shown in fig. 5.4 (a), there was an optimal Si target power in the photoluminescence intensity at the wavelength of 1.54 μm. To investigate in the more systematic way we prepared more samples with varied ratio of

Si_3N_4 target power to Si target power. Also from the figure 5.4 (b) we could clearly observe that there is a certain optimal ratio of Si_3N_4 target power to Si target power for the best luminescence. That is, when there are too much Si contents in the matrix, the Er luminescence is totally quenched out. In addition, when we did not use Si target in preparing Er:SRN, the Er luminescence was much weaker than the Er:SRN sample with a certain optimal Si content. The detailed discussion on the role of Si content in Er sensitization is provided in the section 5.4.

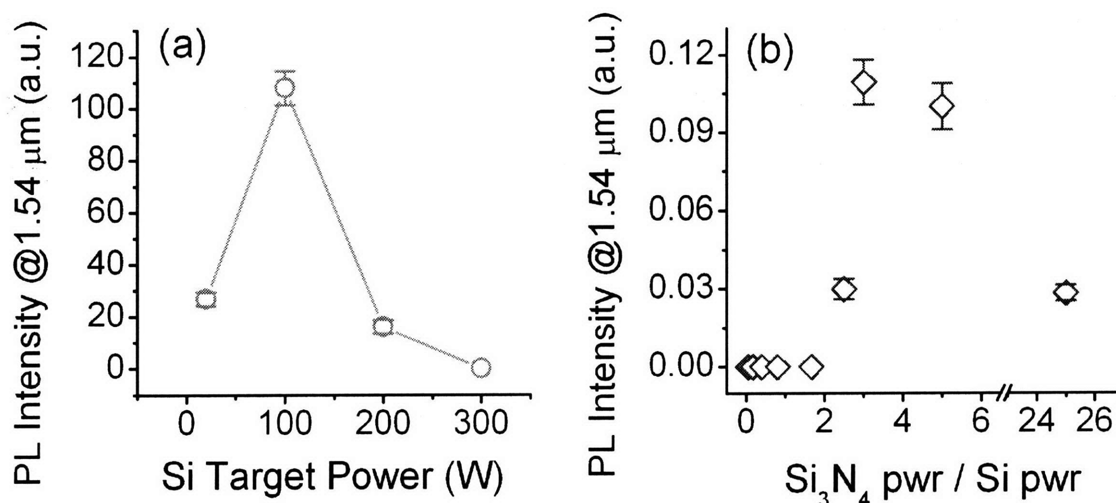

Figure 5.4 (a) Photoluminescence intensity at the wavelength of 1.54 μm with varying Si target power. (b) Photoluminescence intensity at the wavelength of 1.54 μm with the ratio of Si_3N_4 target power to Si target power for more systematic investigation.

To understand what the most important factors in annealing treatment are and why those factors are important in changing Er emission, we investigated several annealing conditions like annealing temperature and annealing atmosphere. With the varied annealing temperature there is certain optimal point for maximized Er emission intensity. Er

activation at high temperature is needed to get Er emission, but annealing at too high temperature usually causes emission quenching. Fig. 5.5 clearly demonstrates the trend.

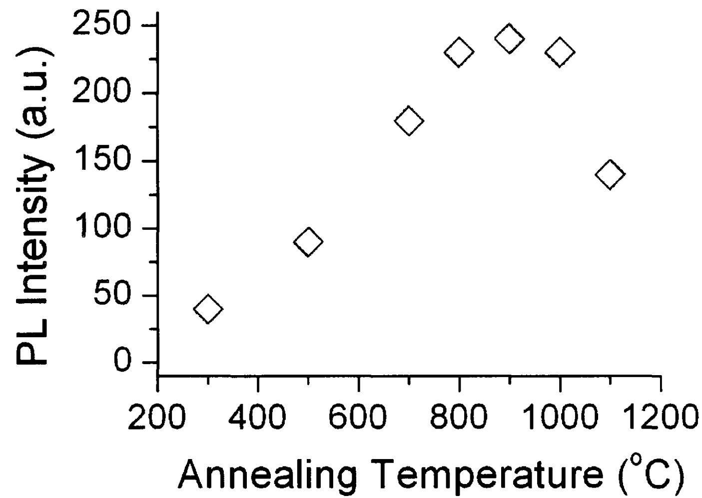

Figure 5.5. Photoluminescence peak intensity at the wavelength of 1.54 μm with the annealing temperature varied from 300°C to 1100°C.

To investigate the passivation role of the hydrogen for the defects quenching or reducing luminescence, annealing was performed at 300°C for 1 hour in forming gas atmosphere. The forming gas contains 5% hydrogen and 95% argon in composition. Defects are important in Er luminescence because they can serve as recombination centers for the photon-generated carriers and luminescence efficiency can be reduced accordingly. They can also provide nonradiative decay channels for the excited Er atoms and reduce the overall efficiency of Er luminescence. Annealing in hydrogen-containing gas atmosphere is known to enable the passivation of defects described above without changing the matrix itself dramatically. Effective passivation of defected silicon nanocrystals in SRO matrix was reported [1]. From our experimental results with annealing in forming gas there was

slight increase in emission intensity from the samples annealed in nitrogen gas in photoluminescence intensity as shown in fig. 5.6 (a). Defected sensitizers are expected to be passivated and, accordingly, Er luminescence from increased sensitization can be resulted. However, this slight increase in Er luminescence intensity was diminished as the Ar flow rate increases from 7.2 sccm to 21.6 sccm as shown in fig. 5.7. As a summary, fig. 5.7 (d) shows the trend with the varied Ar flow rate. The samples grown with the Ar flow rate of 21.6 sccm did not show any difference. If optically active Er atoms are isolated from the defected sensitizers, the overall luminescence will not be changed even with passivation of the defects. Basically the photoluminescence intensity at 1.54 μm decreases as Ar flow increases. This trend was stronger for the samples annealed in forming gas. Further detailed investigation is needed to determine the relationship between the isolation of optically active Er atoms and the Ar flow rate more clearly.

To investigate the role of hydrogen further we deposited Er:SRN films in forming gas atmosphere which was used in the annealing experiments above. From this approach we expect the *in situ* passivation will happen during the growth process. Even though annealing treatment in the forming gas with the sample grown in Ar gas atmosphere has some effect in increasing Er luminescence as in fig. 5.6 (a), there was little difference between the samples annealed in forming gas and nitrogen gas when it was grown in forming gas (Fig. 5.6 (b)). We expect that the extra heat treatment in forming gas after *in situ* growth in forming gas may have little additional effect in passivation. Comparing the relative intensities of the samples grown in Ar atmosphere and forming gas atmosphere, we could not observe any significant difference (Solid line in fig. 5.6 (a) vs. solid line in fig.

5.6 (b)). That is, *in situ* growth of Er:SRN in forming gas was not effective as expected.

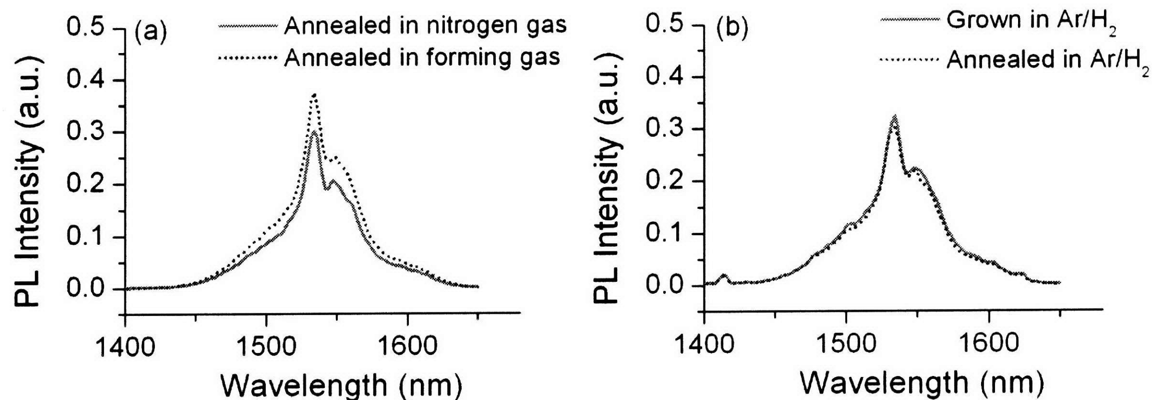

Figure 5.6 (a) Photoluminescence spectra from the optimized sample annealed in nitrogen gas (Solid line) and in forming gas (Dotted line). (b) Photoluminescence spectra from the sample grown in forming gas followed by the annealing in nitrogen gas (solid line) and the sample grown in forming gas followed by the annealing in forming gas (dotted line).

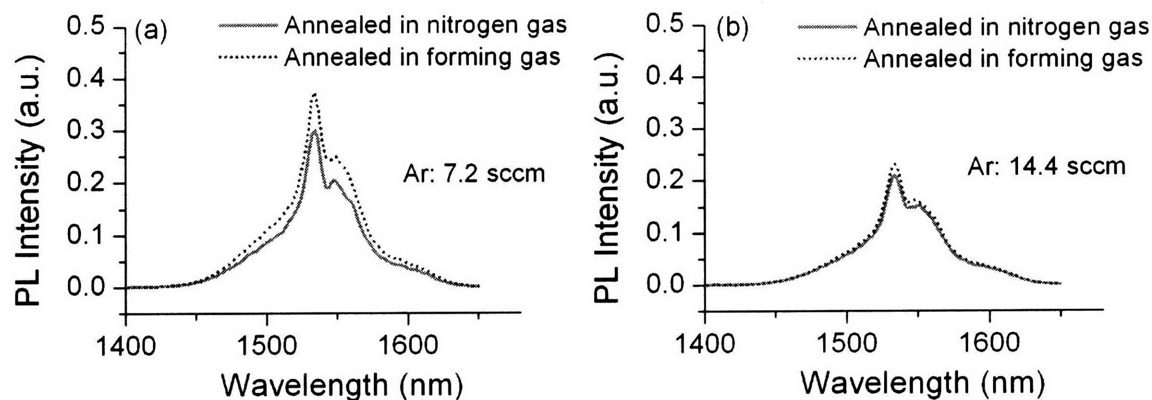

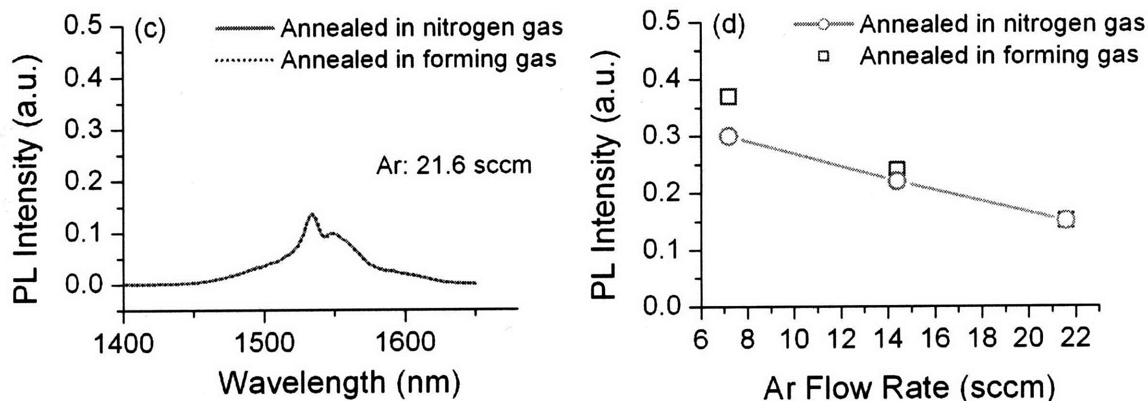

Figure 5.7 (a) Photoluminescence spectra from the sample with Ar flow of 7.2 sccm annealed in nitrogen gas and in forming gas. (b) Photoluminescence spectra from the sample with Ar flow of 14.4 sccm annealed in nitrogen gas and in forming gas. (c) Photoluminescence spectra from the sample with Ar flow of 21.6 sccm annealed in nitrogen gas and in forming gas. (d) Plot of the photoluminescence intensity at 1.54 μm with varying Ar flow rate for the samples annealed in nitrogen gas and in forming gas.

5.3.2. Non-resonant pumping, excitation cross section, and upconversion

The investigation of non-resonant pumping behavior is important to examine the role of sensitizers for Er excitation. Optical excitation cross section of Er indicates, for given pump photon flux, what the optical excitation rate of the Er atoms is. In addition, upconversion behavior is also important since it informs us, for a given pump power, how high the population in the excited state is available for optical gain. One of the dominant mechanisms for the non-radiative recombination in Er-doped material is the upconversion process.

Direct pumping (resonant pumping) can be done with 488 nm wavelength (resonant with the $^4F_{7/2}$ energy level of Er) and non-resonant pumping with 457 nm (not resonant with any Er energy level). If there is a strong difference in emission intensity when pumped at

488 nm and 457 nm or no intensity only by the pumping at 457 nm, it proves that Er was excited directly and sensitizing role by any agent was not provided. However, if there is some intensity from non-resonant pumping, sensitization process can be regarded to work. We clearly show in fig. 5.8 that the 1.54 μm Er emission can be efficiently excited also by pumping without the Er transitions resonance, using pumping wavelength of 457 nm where Er atoms are not absorbing (The optimized sample as in the previous section was used). The almost totally overlapping Er emission spectra obtained under resonant (488 nm) and non-resonant (457 nm) pumping conditions, directly prove that Er excitation in Er:SRN is completely mediated by the SRN dielectric matrix that efficiently transfer the excitation energy to the Er atoms. We can argue that non-resonant pumping of the Er atoms happens in our Er:SRN system. The origins of main and satellite peaks and of the wide tails of the spectra in fig. 5.8 are the Stark splitting of the first excited state and ground state in the host electric field (inlet in fig. 5.8) and also the homogeneous and inhomogeneous broadening. These two peaks are the only resolved Stark structures. Peak width is similar to that of typical Er:SRO samples [4]. We could also observe the non-resonant pumping phenomena from many other Er:SRN samples. Some cases show slightly different emission intensity due to the difference of SRN absorption coefficient between 457 nm and 488 nm, but the difference was not significant. Therefore, we can conclude that the Er atoms could be efficiently excited in SRN matrix under both resonant and non-resonant excitation. Er in stoichiometric silicon nitride (Si_3N_4) is expected to be excited only under resonant condition as Er in SiO_2 which is well known. Therefore, we wanted to confirm pumping of Er:Si_3N_4 only with resonant wavelength. However, we could not get the Er in

stoichiometric silicon nitride by our sputter with even using Si_3N_4 and Er targets only. Even in that case refractive index was 2.1 (Refractive index of stoichiometric silicon nitride is 2.0). That means it is also Er in silicon rich nitride. With this material we also could get Er pumped even at the non-resonant wavelength of 457 nm.

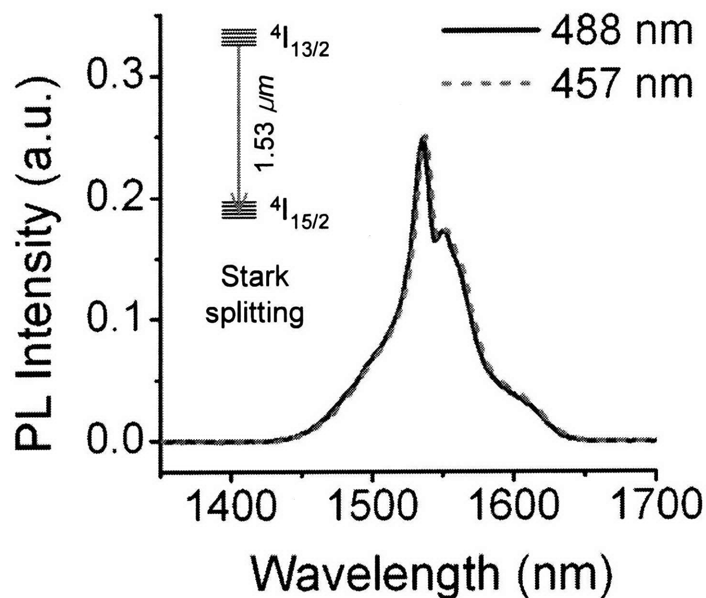

Figure 5.8. Photoluminescence spectra with resonant pumping (488 nm, solid) and non-resonant pumping (457 nm, dashed).

We performed time resolved photoluminescence to understand the dynamics of the emission process through an analysis of the emission lifetime and the excitation cross section. The optical excitation cross section is a measure of the probability that a photon will be absorbed leading to the excitation of an electron from the ground state to the excited state and subsequent relaxation to the ground state leading to the emission of a photon. For this analysis we consider the energy level diagram of the SRN sensitizer in fig. 5.9 where

the transitions between electronic states in the SRN sensitizers are represented by the excitation cross section, σ_{exc} and the emission lifetime, τ_{ba}, which represents the radiative and non-radiative lifetimes combined.

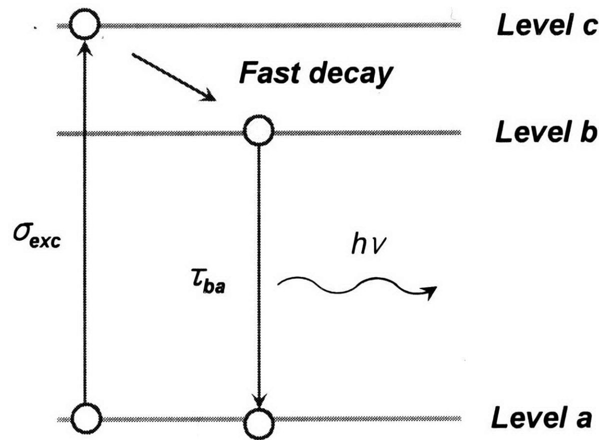

Figure 5.9. Schematic diagram of energy levels for the SRN sensitizer. Level a is the ground state, level b the excited state, and level c the representative high state from where fast decay to level b happens.

With a low photon flux non-radiative processes leading to saturation of the emission process can be ignored. Excitation processes happen in the linear excitation regime in this situation. In the regime the rise time of the PL spectrum measured by time resolved PL is related to the excitation cross section and the emission lifetime based on the following expression:

$$\frac{1}{\tau_{on}} = \sigma_{exc}\Phi_p + \frac{1}{\tau_{ba}}$$

where τ_{on} is the rise time of the PL spectrum and Φ_p is the pump-photon flux in units of 'number of photons/cm^{2}s'.

We measured the rise time by varying pump-photon fluxes with the observed wavelength of 1535 nm. The excitation cross section is measured from the slope of the inverse rise time versus pump-photon flux data while the inverse emission lifetime is obtained from the extrapolated intercept based on the equation given above as shown in fig. 5.10. Here the excitation cross section was measured to be $8.2x10^{-16}$ cm^2 and the lifetime was obtained to be 400 μs. Considering the direct optical excitation cross-section of Er is in the range of 10^{-21} cm^2, it is a significantly enhanced value. It implies that strong sensitization processes happen through SRN matrix. This value is even higher than the one usually obtained from SRO matrix (~ 10^{-16} cm^2). The sample was used with the optimized annealing process as in fig. 5.10 (b). We also obtained the lifetime of the same sample at a low pump photon flux by fitting the decay curve of the photoluminescence as shown in figure 5.11. The fitting result provided a value of 410±10 μs in good agreement with the value obtained from the fitting of the data from inverse rise time vs. pump-photon flux. Similar to the analysis for Er:SRN samples we also have measured the excitation cross section for SRN by PECVD. The excitation cross section value was measured to be $2.4x10^{-15}$ cm^2 and it was quite close to the value for Er:SRN we obtained above (~10^{-15} cm^2). This measured value is just for reference information since it is not that of SRN by sputter. We could not measure that of sputtered SRN directly since light emission from sputtered SRN is very little or quite weak. To measure excitation cross section value we need to change the pump photon flux in a wide range, but getting any signal at low pump photon flux was

extremely difficult.

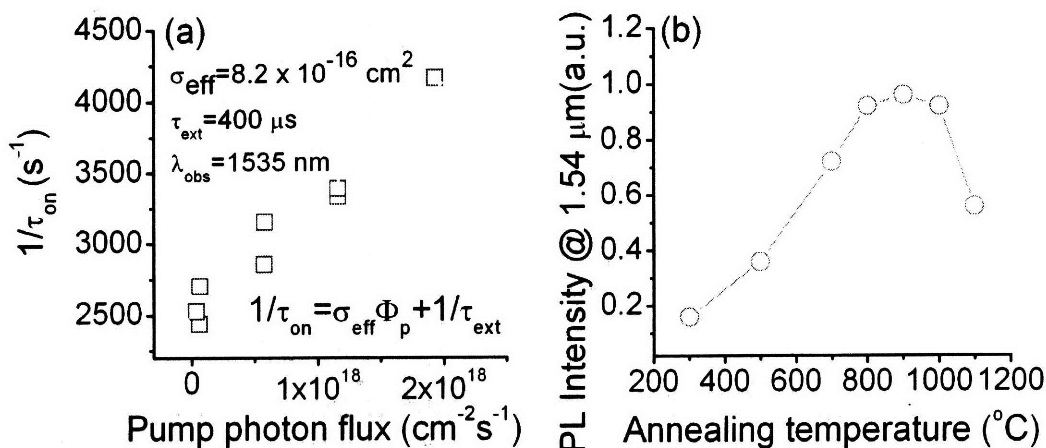

Figure 5.10 (a) Inverse rise time versus pump-photon flux for a Er:SRN sample with the detection wavelength set at 1535 nm (Open squares). The dash line is a linear fit to the data yielding an excitation cross section of 8.2x10^{-16} cm^2 and an emission lifetime of 400 μs. (b) Photoluminescence peak intensity (Open circles) with annealing temperature changed from 300°C to 1100°C.

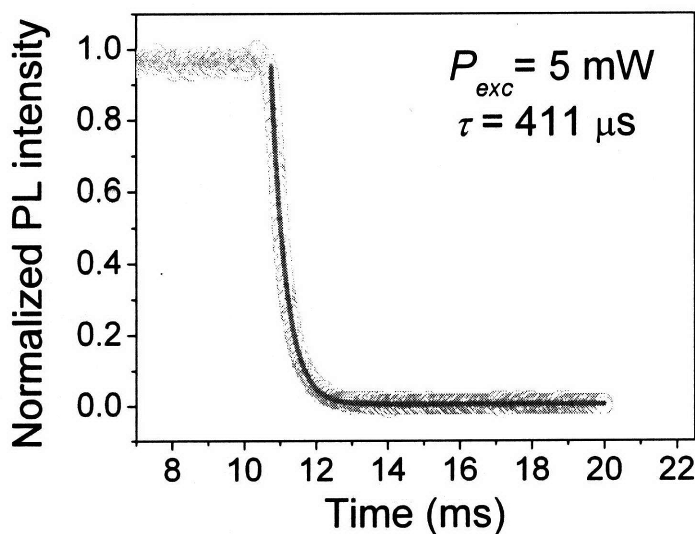

Figure 5.11. Photoluminescence decay for a Er:SRN sample with the detection wavelength

set at 1535 nm and a pump power of 5 mW (open circles). The solid line is an exponential decay fit to the data yielding an emission lifetime of 411 μs.

In addition, we investigated the cooperative upconversion phenomenon for the Er:SRN samples which is described in fig. 5.12. When two excited Er^{3+} ions are positioned proximately each other, one Er ion will transfer its energy to the other with promoting an electron to an excited energy level and de-exciting the electron in the first Er ion to the ground-state. The excited Er ion will typically emit from the $^4I_{11/2}$ level leading to 980 nm light emission. The process where two or more excited Er ions simultaneously transfer their energy to another excited Er ion is known as the cooperative upconversion process.

The upconversion process depends on the square of the population of the Er atoms in the excited-state. We can write the time dependent excited-state population of the Er based on the following equation.

$$\frac{dN_2}{dt} = \sigma N_1 \Phi_p - \tau N_2 - 2C_{UP} N_2{}^2$$

where N_1 is the ground-state population ($^4I_{15/2}$ level), N_2 is the excited-state population in the level of $^4I_{13/2}$, and C_{UP} is the upconversion coefficient (cm^3s^{-1}). This equation is helpful for understanding of the upconversion process in fig. 5.12. Here is the detailed explanation of the upconversion process. Two excited Er atoms in the level of $^4I_{13/2}$ end up with the non-radiative de-excitation of one Er atom (to $^4I_{15/2}$ state, 1.53 μm) and the radiative de-excitation of another Er atom (from $^4I_{11/2}$ state, 0.98 μm) after fast decay from $^4I_{9/2}$ state to $^4I_{11/2}$ state.

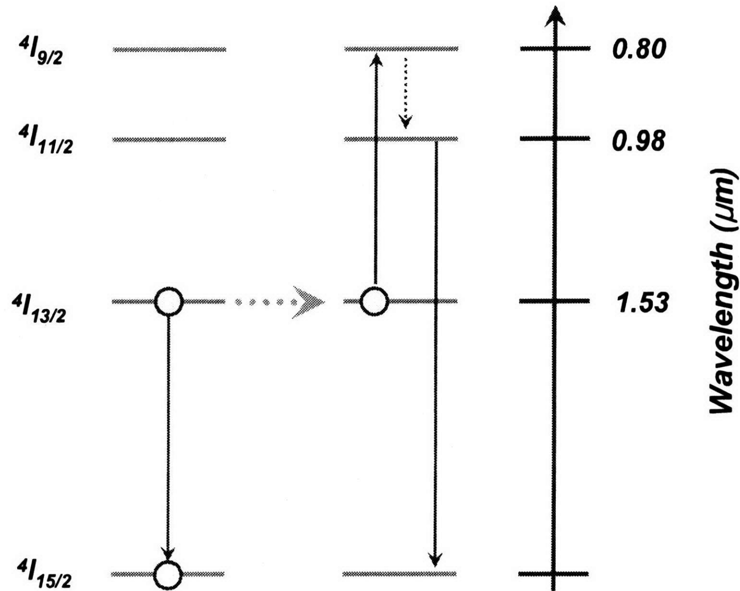

Figure 5.12. Schematic diagram of energy levels and processes for cooperative upconversion between nearest neighbor Er atoms, resulting in non-radiative de-excitation of one Er atom (to $^4I_{15/2}$ state, 1.53 μm) and the radiative de-excitation of another Er atom (from $^4I_{11/2}$ state, 0.98 μm).

In order to confirm that the cooperative upconversion is one of the most dominant de-excitation processes, without contributing to spontaneous emission and stimulated emission, we measured photoluminescence intensity with pump power at wavelengths of 1.53 μm and 0.98 μm as in the figure 5.13 (a). Photoluminescence peak at 1.53 μm implies the concentration of excited state ($^4I_{13/2}$) Er atoms, while photoluminescence peak at 0.98 μm corresponds to the second excited state population ($^4I_{11/2}$) of Er atoms, coming from the cooperative upconversion process, corresponding to a de-excitation of the atoms in the $^4I_{13/2}$ state by resonant energy transfer to excite the neighboring atom in the $^4I_{13/2}$ state to the $^4I_{9/2}$ state. The excited electrons in the $^4I_{9/2}$ level decays to $^4I_{11/2}$ rapidly as shown in fig. 5.6.

If we plot the photoluminescence intensities from $^4I_{13/2}\rightarrow{}^4I_{15/2}$ de-excitation (λ=1.53 μm) process vs. the intensities from $^4I_{11/2}\rightarrow{}^4I_{15/2}$ de-excitation (λ=0.98 μm) process at the same pump power, we can get the correlation plot [2] whose slope implies the power law process corresponding to the transitions from the level $^4I_{13/2}$ to the level $^4I_{11/2}$. Usually the slope of 2.0 in the correlation plot suggests the normal cooperative upconversion process. However, we observed the slope of 1.6 from the Er:SRN correlation plot (Fig. 5.13 (b) and (c)). That means the Er level based rate equation could not entirely represent the Er transition processes well enough. That is, there may be some additional energy transfer mechanisms involved in our Er:SRN material.

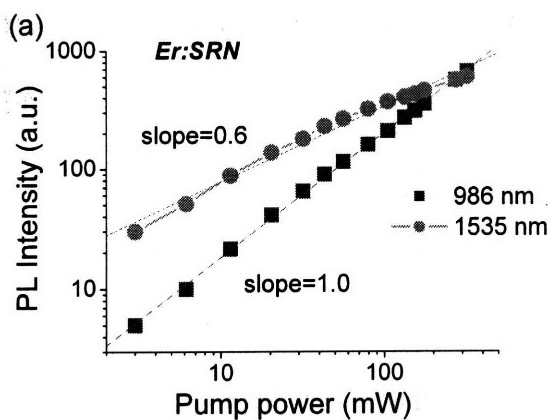

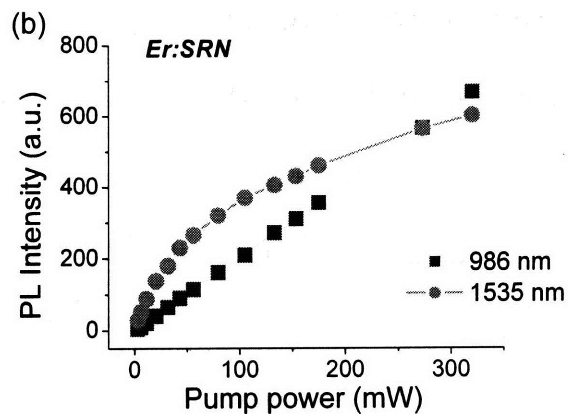

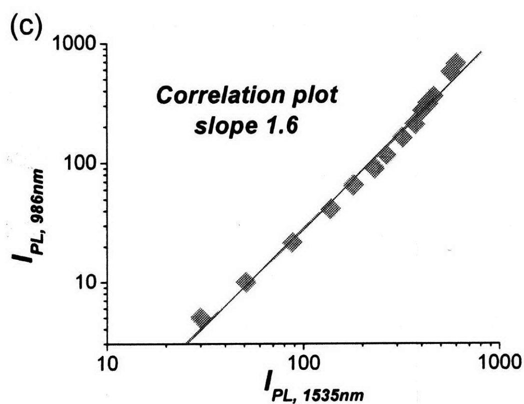

Figure 5.13 (a) PL peak intensity at λ=1535 nm versus λ=980 nm for Er:SRN. (b) Correlation plots identifying the upconversion process for Er:SRN in linear scale. (c) Correlation plots identifying the upconversion process for Er:SRN in log scale.

5.3.3. The relationship between SRN emission and Er emission

In the investigation of Er:SRO many researchers argued that Si-nc's are the sensitizers for Er excitation and many of their studies implied that Si-nc's have significant role in sensitizing Er atoms optically. With the larger excitation cross section of Si-nc by several orders than Er atom and the efficient energy transfer to Er atom, optical excitation of Er through the Si-nc sensitizers can be achieved much more efficiently than direct Er excitation. The typical mechanism used to explain energy transfer between Si-nc's and Er ions is Förster-Dexter non-radiative energy coupling with a transfer rate that is directly proportional to the donor (SRO) emission rate [3]. However, recent experimental data by many research groups imply that Si-nc's are not the only resource for Er sensitization. Some research groups argue that the dominant transfer mechanism is based on the nonradiative energy transfer from excitons in Si-nc's to Er ions located in silica environment [21,22]. However, some other groups argue more complex mechanism where energy is transferred first from excitons to centers at the Si/SiO_2 interface and/or to some defect states in SiO_2, and then transferred to Er ions [23]. As in Mike Stolfi's MIT Ph.D. thesis [4], our group also confirmed that light emitting Si-nc's in SRO matrix are not the only agents for Er sensitization. Stolfi and other colleagues have recently questioned the validity of this simple picture since only inefficient light emission (no appreciable SRO emission) can be obtained in the case of low temperature annealed samples (donors) without

the presence of Er atoms (acceptor) even though they observed strong Er emission from the Er:SRO with this SRO material [4, 5]. They have recently suggested that the efficient energy transfer observed for low temperature annealed Er:SRO materials can be assisted by non-radiative defect states within the SRO matrix bandgap [5]. He observed even stronger Er emission with the Er:SRO samples annealed at very low temperature like 600°C where there is no nanocrystal formation and the Er emission was also confirmed under the non-resonant pumping condition. Considering the results we should think the role and importance of Si-nc's in Er sensitization more carefully.

At that time even with our Er:SRN system we observed similar phenomena and shared our experimental results with Mike and other colleagues for better understanding of these phenomena. Fig. 5.14 (a) shows experimental data when the Er is incorporated into SRN and as a result the SRN emission is totally quenched out. The energy for light emission from SRN was not used to emit light, but was transferred and used to excite Er atoms. Therefore, we observe only Er emission from Er:SRN without observing any SRN emission. In majority of the Er:SRO studies this kind of experimental result is provided to prove energy transfer from the light emitting media (especially Si-nc's in Er:SRO system) to Er atoms.

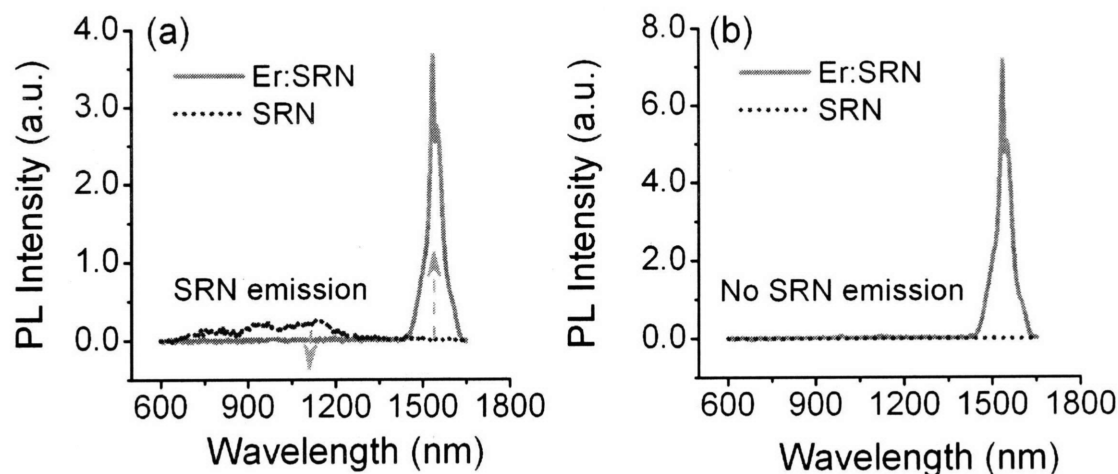

Figure 5.14 (a) Photoluminescence spectra from SRN and Er:SRN. In this case the growth condition of SRN was chosen to have light emission from SRN. (b) Photoluminescence spectra from SRN and Er:SRN. In this case the growth condition of SRN was chosen to have no light emission from SRN. Most of the cases correspond to this case.

However, from most of the samples we could get Er emission from Er:SRN where the SRN with no light emission was used. That is, even though there was no light emission from SRN, Er emission from Er:SRN was observed where we used the SRN having same growth condition with that of Er:SRN except Er target power. Sensitization of Er atom is not necessarily assisted by light emitting SRN, but can be assisted by non-emitting SRN. It indicates that the sensitization of Er is not always by Si-nc's, but can be achieved through SRN matrix (non-radiative silicon excess related defects). D. Kuritsyn *et al.* also observed sensitization of Er by the silicon excess related defects in Er:SRO system [24]. This is very important observation to question the role of silicon nanocrystals for the Er sensitization even in nitride matrix. Considering the combined results from Mike Stolfi and us, the optimization of parameters for silicon nanocrystal emission, such as the concentration and size of silicon nanocrystal, is not directly related to optimal Er emission. Control of the

matrix properties which are also directly related with Er sensitization is essential.

To understand how the sensitization of Er is affected by the SRN matrix, we varied Si contents in SRN matrix by varying the ratio between Si target power and Si_3N_4 target power. Detailed results and discussion are provided in the following section.

5.4. Er sensitization with varied Si content

From the previous section we learned that Er sensitization is not related mainly with SRN emission. That is, SRN emission is not a necessary condition for Er sensitization. To understand better how the Er sensitization is changed with Si content in SRN matrix, we prepared Er:SRN samples with varied Si target power and Si_3N_4 target power. All the samples here did not show any light emission from SRN itself when we prepared SRN samples with the same conditions (only without Er incorporation). Fig. 5.15 (a) shows photoluminescence spectra from the representative Er:SRN samples with the refractive index of 2.1, 2.2 and larger than 2.4. For easier understanding of the effect, only Er peak intensities of photoluminescence spectra were plotted by varying the ratio of Si target power to Si_3N_4 target power. Refractive index values were provided for the samples to give an idea how much Si is incorporated.

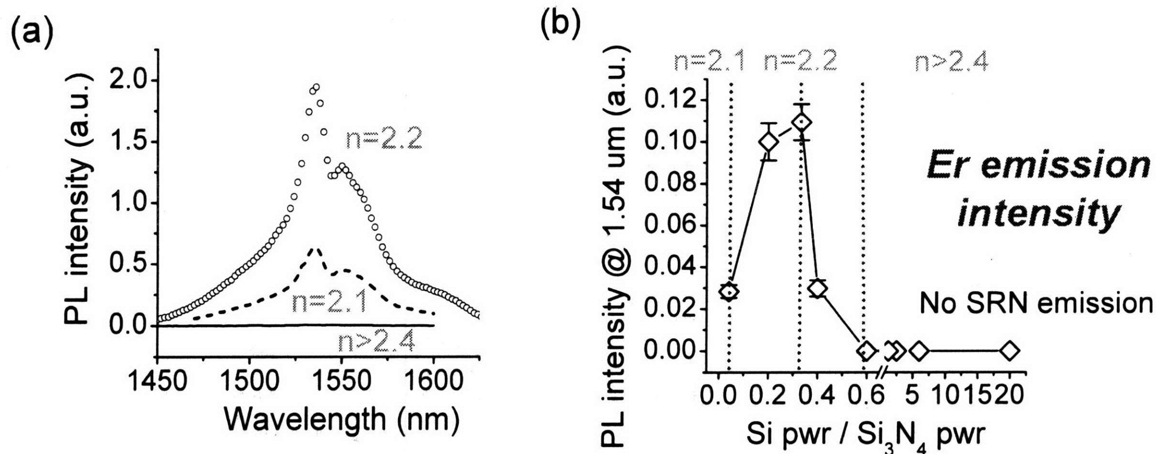

Figure 5.15 (a) Photoluminescence spectra from the representative Er:SRN samples with the refractive index of 2.1, 2.2 and larger than 2.4. (b) Er peak intensities of photoluminescence spectra vs. the ratio of Si target power to Si_3N_4 target power. Refractive index values were inserted to give an idea on how much Si is incorporated.

We can clearly observe in fig. 5.15. (b) that Er emission could be enhanced with Si incorporation up to certain level (n=2.2) but totally quenched out when Si content is high (n>2.4). The non-radiative silicon excess related defects are considered to be increased by Si incorporation and it leads to significant enhancement in Er sensitization effect up to certain point (n=2.2). Too much Si incorporation is expected to form conglomerates which can not contribute to Er sensitization effectively. Jessica Sandland in our group reported the experimental relationship between the 4K lifetime of Er doped samples (SiO_2, SiON, and Si_3N_4) and number of silicon dangling bonds in her Ph.D. thesis [25]. With increased number of silicon dangling bonds, 4K lifetime decreased significantly.

The variation of Si content in the Er:SRN significantly affects the electrical properties of the Er:SRN devices as well. Si incorporation into the insulating silicon nitride matrix can result in more conductive characteristics of the film. We will discuss the detailed results in

chapter 7 where we investigate electrical properties and electroluminescence phenomena of Er:SRN system.

5.5. Discussion on gain related parameters with optical pumping

SRN sensitizers including Si-nanocrystals or silicon related non-radiative states have a significant role in optical Er excitation since the direct excitation cross section of Er by optical pumping is very small ($\sim 10^{-21}$ cm^2). In this section we have investigated the key parameters such as Er concentration, excitation cross section of SRN sensitizers, coupling coefficient, upconversion coefficient, etc, to understand their contribution to gain from Er atoms. This investigation will be a meaningful fundamental for the comparison with the electrical excitation case and we can understand how the optical and electrical excitations of Er are so different. The results similar to the electrical excitation cases were omitted to avoid redundancy by just providing some comments on the parameters.

We built up rate equations based on the two level systems of SRN sensitizer and Er atom as we did in chapter 7 except the fact that excitation is by optical pumping. Fig. 5.10 shows the two level systems we consider here. Rate equation model usually provides information regarding the gain and the loss, coupling and excitation phenomena based on the behavior of carriers and photons with numerical (sometimes external) parameters. Without losing the advantage of simplicity it helps users understand numerical parameters which are used to describe the given system. Based on the work prof. Dal Negro proposed, two level equations were rebuilt for our SRN-Er system [6]. The model for SRO-Er system given in ref. 2 is a simplification of the model developed by Pacifici *et al.* [7] where the

second excited state of Si-nc's and the third through fifth excited states of Er ion were considered. Since these states have relatively short lifetime, their effect on the transition dynamics can be disregarded. That is, the most significant processes are the excitation through the energy transfer from the sensitizer and the processes related with the second excited state ($^4I_{13/2}$ level) of Er such as cooperative upconversion, etc. The rate equations and parameters we adopted here were given next to fig. 5.16. Due to the limited parameters experimentally measured, the values from the simulation results can not be relied and used. However, general trend from the parameters can be used to understand optical excitation of Er and to compare with electrical excitation. Compared to electrical excitation case, almost all the parameters contribute significantly or to some degree at least.

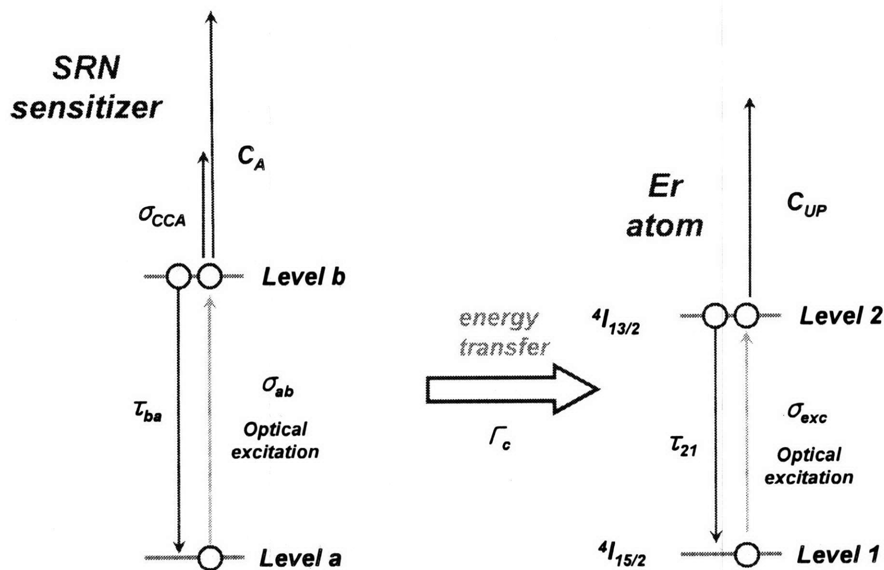

Figure 5.16. Two level systems for SRN sensitizers and Er atom with optical excitation.

$$\frac{dN_b}{dt} = \sigma_{ab}^{opt}\Phi_p N_a - \frac{N_b}{\tau_{ba}} - \Gamma_c N_b N_1 - 2C_A N_b^2$$

$$\frac{dN_2}{dt} = \sigma_{exc}^{opt}\Phi_p N_1 - \frac{N_2}{\tau_{21}} + \Gamma_c N_b N_1 - 2C_{UP} N_2^2$$

Table 5.1. Parameters and values used in the simulation for optical excitation of Er in SRN matrix.

Parameter	***Value***	***Notes***
[Er]	$5.0\text{x}10^{20}$ cm^{-3}	
[Sensitizer]	$6\text{x}10^{18}$ cm^{-3}	
Γ_c	$1.0\text{x}10^{-12}$ cm^{3}s^{-1}	SRN → Er coupling coefficient
σ_{exc}^{opt}	$1.0\text{x}10^{-21}$ cm^2	Er excitation cross section (Optical)
τ_{21}	0.5 ms	Er emission lifetime (measured)
σ_{ab}^{opt}	$1.0\text{x}10^{-15}$ cm^2	Excitation cross section of sensitizer
τ_{ba}	$1.0\text{x}10^{-6}$ sec	Sensitizer emission lifetime
C_A	$1.0\text{x}10^{-13}$ cm^{3}s^{-1}	Coefficient for Auger recombination in sensitizer
C_{UP}	$3.0\text{x}10^{-18}$ cm^{3}s^{-1}	Coefficient for cooperative upconversion in Er
σ_{Er}	$3.5\text{x}10^{-20}$ cm^2	Er emission cross section
α_{tot}	5 cm^{-1}	total loss

First, the trends with Er concentration and upconversion coefficient were similar to what were given in chapter 7. Higher pump photon flux is needed to achieve net gain for a higher Er concentration. However, the maximum gain achievable increases with Er

concentration. Maximum gain value does not change with upconversion coefficient changed. Threshold pump photon flux for the net gain decreases with lowering upconversion coefficient value. Detailed results with graphical presentation can be found in chapter 7. The simulation results are not repeated here to avoid redundancy.

However, effects of sensitizer density, excitation cross section of sensitizer, coupling coefficient were not negligible at all as in chapter 7. Here are the related simulation results and discussion on the effects of these parameters.

5.5.1. Effect of sensitizer density

Since the excitation cross section of sensitizer is much larger than that of Er atom itself in optical excitation case, excitation through sensitizer should be considered significant. Here we varied the sensitizer density from 1×10^{16} cm^{-3} to 1×10^{20} cm^{-3}. Fig 5.17 (a) shows the maximum gain value could not be varied with sensitizer density due to the relationship of $g=\sigma_{em}(N_2-N_1)$ for Er-coupled system. That is, the achievable maximum gain value is determined by the Er emission cross section, σ_{em}, multiplied by the population inversion at saturation, $\Delta N=(N_2-N_1)$. However, the threshold pump photon flux for the net gain could be reduced by more than 4 orders of magnitude. With higher sensitizer density Er excited states population could be reached to maximum value with much smaller pump photon flux as in fig. 5.17 (b). It is clearly from the excitation by the sensitizers which are excited first and then transfer energy to Er atoms (Fig. 5.17 (c)). Energy transfer to Er atom is known to be non-radiative process in sensitizer rather than radiative transition followed by reabsorption by Er atom [8, 9]. This process limits the excited state population in sensitizer

to enable the consequent excitation to be ready.

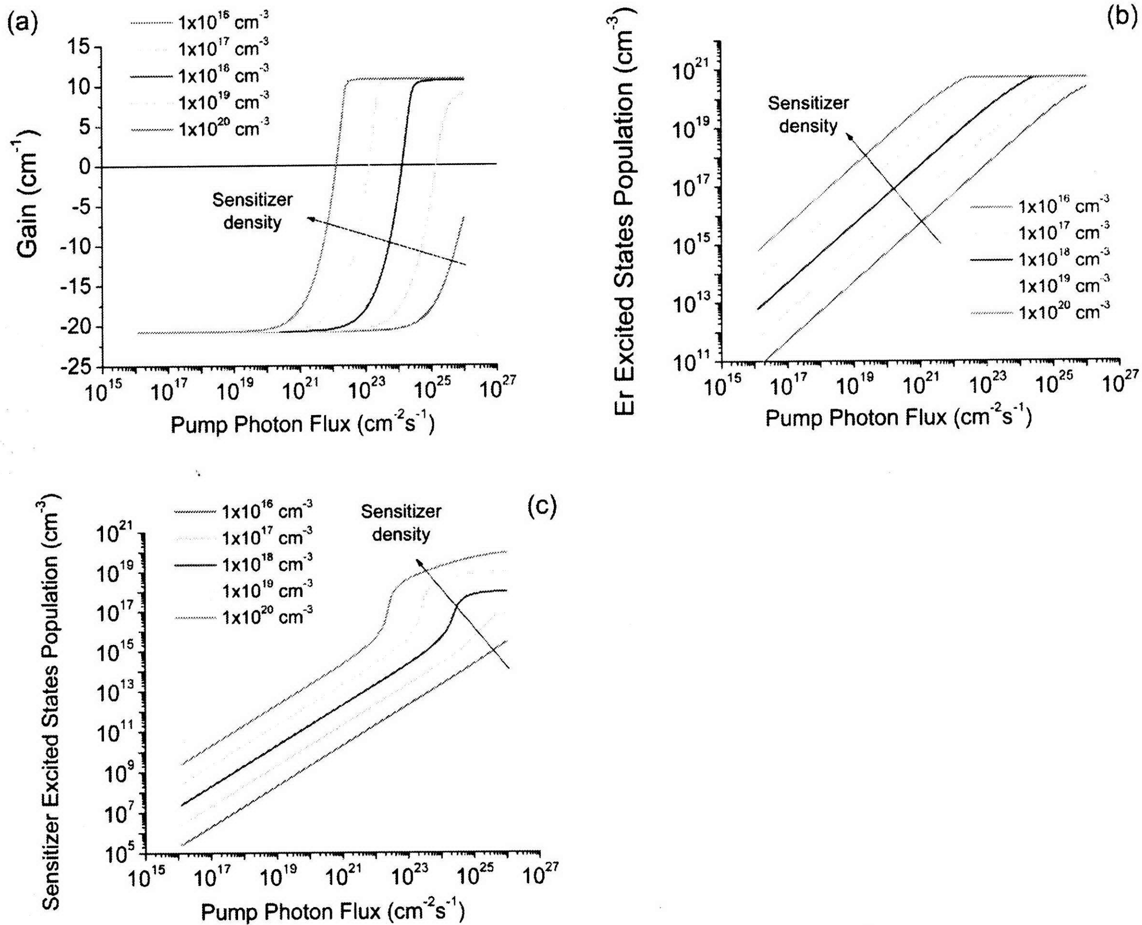

Figure 5.17 (a) Gain, (b) Er excited states population, and (c) Sensitizer excited states population with pump photon flux varied for sensitizer density of 1x10^{16} cm^{-3}, 1x10^{17} cm^{-3}, 1x10^{18} cm^{-3}, 1x10^{19} cm^{-3}, and 1x10^{20} cm^{-3}. All other parameters are fixed as in table 5.1.

5.5.2. Dependency on coupling coefficient

Coupling coefficient represents how strongly sensitizers and Er atoms are coupled. Therefore, higher coupling coefficient implies energy transfer from sensitizer to Er atom is stronger. It describes the coupling between the excited sensitizer level and the ground level

of Er. Interaction between these two levels is described by the product of the population of carriers in the levels. Energy coupling efficiency is high when the coupling coefficient and the excited state population of sensitizer are high.

When the sensitizer and Er atom are coupled extremely weakly with the coefficient of 1×10^{-16} cm^3s^{-1}, the maximum achievable gain and Er excited state population are quite low (net gain not achieved) even with a very high pump photon flux of 10^{26} $cm^{-2}s^{-1}$ (~ MW/mm^2 level in optical power density). Even with the coefficient of 1×10^{-15} cm^3s^{-1}, threshold pump photon flux for net gain jumps up to 10^{27} $cm^{-2}s^{-1}$ level, more than 4 orders of magnitude increase compared to the cases with efficient coupling ($>1\times10^{-13}$ cm^3s^{-1}), due to the ineffective sensitizer absorption and energy transfer. However, when the coefficient is equal to or higher than 1×10^{-13} cm^3s^{-1}, there was no big difference with further increase in coupling coefficient.

Sensitizers were depleted more and more at the same pump photon flux as the coupling coefficient becomes higher (Fig. 5.18 (c)) due to efficient transfer of energy to Er atoms.

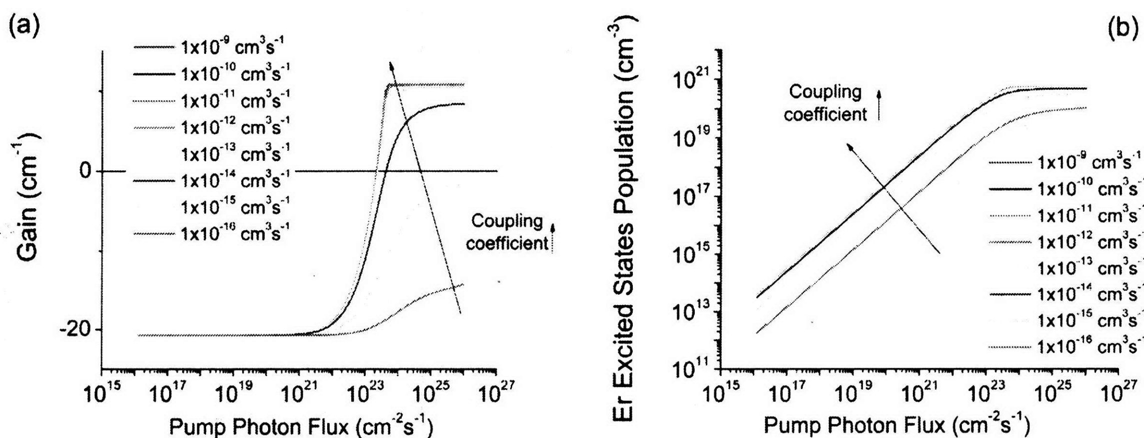

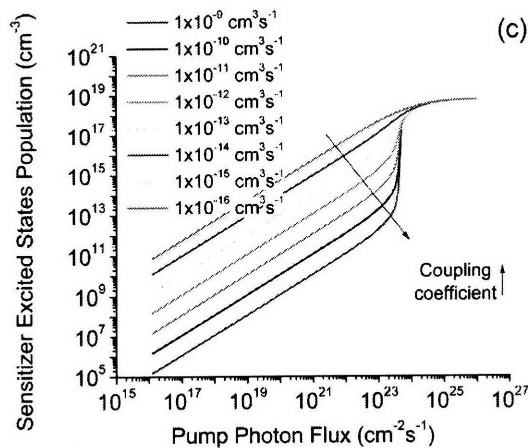

Figure 5.18 (a) Gain, (b) Er excited states population, and (c) Sensitizer excited states population with pump photon flux varied for coupling coefficient of $1\text{x}10^{-16}$ cm^{3}s^{-1}, $1\text{x}10^{-15}$ cm^{3}s^{-1}, $1\text{x}10^{-14}$ cm^{3}s^{-1}, $1\text{x}10^{-13}$ cm^{3}s^{-1}, $1\text{x}10^{-12}$ cm^{3}s^{-1}, $1\text{x}10^{-11}$ cm^{3}s^{-1}, $1\text{x}10^{-10}$ cm^{3}s^{-1}, and $1\text{x}10^{-9}$ cm^{3}s^{-1}. All other parameters are fixed as in table 5.1.

5.5.3. Effect of sensitizer excitation cross section

Since the excitation cross section of Er atom by optical pumping (~ 10^{-21} cm^2 level) is much smaller than that of sensitizer (by 5~6 orders), excitation through sensitizer can be highly effective. Therefore, change in excitation efficiency with varied excitation cross section of sensitizer will result in the overall change in Er excitation efficiency. Fig. 5.19 (a) demonstrates the maximum gain value can not be improved with increased excitation cross section of sensitizer. However, the threshold pump photon flux was strongly reduced as the excitation cross section was increased. This can be understood by the fact that much more sensitizers could be excited with lower pump photon flux as the excitation cross section increases (Fig. 5.19 (c)). These excited sensitizers effectively excite the Er atoms with much smaller pump photon flux (Fig. 5.19 (b)).

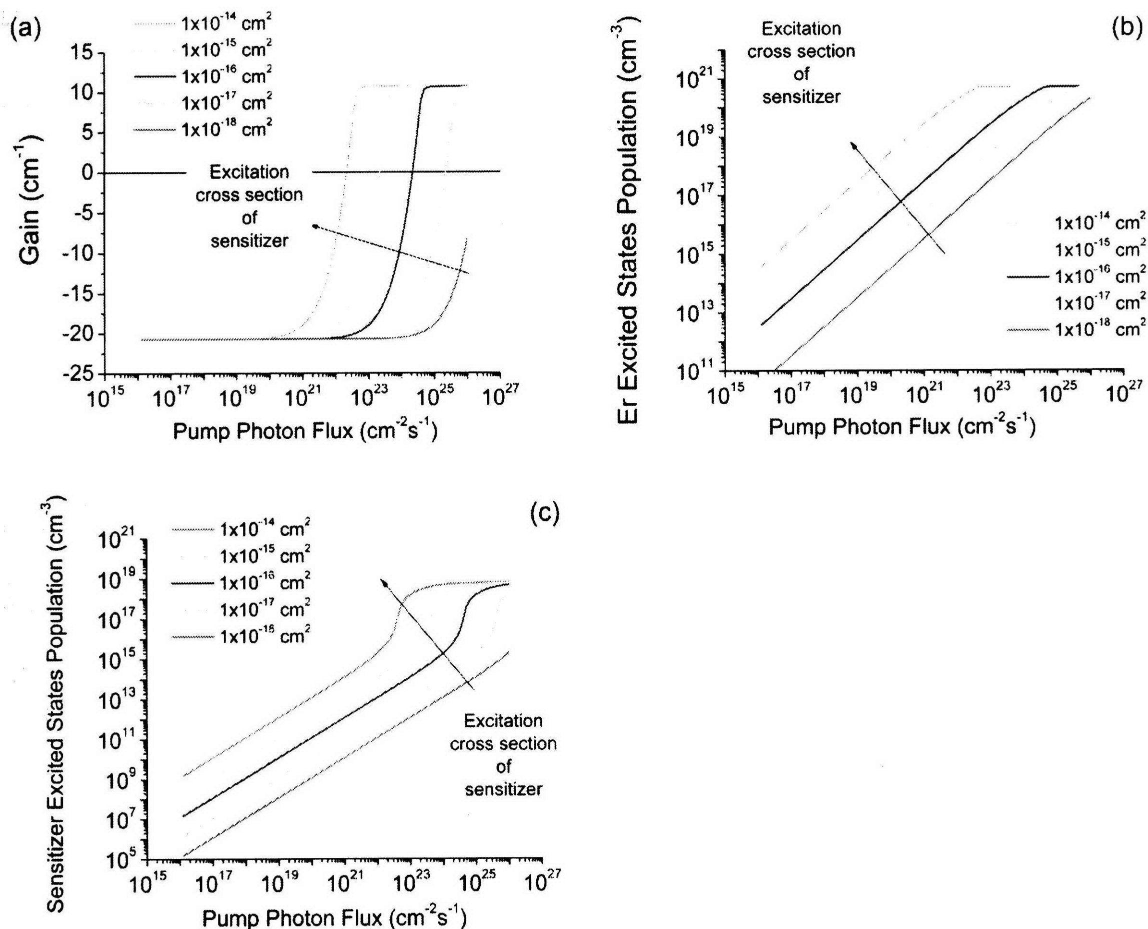

Figure 5.19 (a) Gain, (b) Er excited states population, and (c) Sensitizer excited states population with pump photon flux varied for sensitizer excitation cross section of 1x10^{-18} cm^2, 1x10^{-17} cm^2, 1x10^{-16} cm^2, 1x10^{-15} cm^2, and 1x10^{-14} cm^2. All other parameters are fixed as in table 5.1.

5.6. Energy transfer to lead sulphide (PbS) quantum dots

We learned that energy transfer phenomenon is very important in exciting the acceptor material (Er in the previous section) by sensitization. In addition to SRN (donor)-Er (acceptor), energy transfer phenomena from SRN to PbS quantum dots were investigated and we demonstrated non-radiative energy transfer at the room temperature. On top of SRN 5

monolayers of PbS quantum dots were spin-coated. Photoluminescence excitation analysis revealed the transfer efficiency of approximately 60±5%. This experimental demonstration provides promising possibility of utilizing highly efficient PbS quantum dots based on SRN material which is CMOS compatible.

5.6.1. Introduction

Silicon has been one of the strongest candidates for the integrated optics, modulator, switch, and laser [10-13]. However, silicon can not emit light efficiently due to its fundamental physical limitation. Even with silicon nanocrystal based approach the emission efficiency is quite lower than that of III-V or II-V compound semiconductor materials and the emission range is also limited to some of visible and infrared ranges. Colloidal quantum dots, however, can provide very high emission efficiency and also the wide tuneability between 0.4 μm and 4.0 μm [14] with easy processibility with CMOS compatible materials especially like SRN. If the energy transfer from SRN to colloidal quantum dots like PbS is achieved, it will enrich the range of silicon's application area greatly.

Energy transfer effect is based on dipole-to-dipole transfer which is quite well known in biology from long time ago, for example, photosynthesis and chromophore interaction, especially based on FRET (Förster Resonance Energy Transfer). However, it was introduced and used in the optoelectronics area quite recently [15]. Combination and emission through energy transfer under optical pumping of the colloidal quantum dots with inorganic semiconductor was demonstrated from III-V based quantum well structure only [16]. It is not obvious that the dipole-to-dipole coupling for energy transfer can work in the CMOS

compatible material combined with colloidal quantum dots.

In this section we demonstrated efficient energy transfer from CMOS compatible material to colloidal quantum dots emitting light. Especially we achieved energy transfer from infrared emitting SRN [17] material to PbS colloidal quantum dots [18]. The experimental results demonstrated here imply convenient strategy for the monolithic integration of solution-processible active optoelectronic materials on the electronics platform of CMOS silicon.

5.6.2. Materials preparation

We used colloidal PbS quantum dots synthesized by Dr. Tung-Wah F. Chang in Prof. Edward Sargent group in Univ. of Toronto with a collaboration effort. The following content is based on his description [19]. The oleate ligand is an 18-carbon-atom-long single chain terminated by a carboxylate group. The carboxylate group passivates the surface of the quantum dots and the carbon atom chain isolates the quantum dots from each other and makes them soluble in organic solvent. The length of the oleate ligand is approximately 2 nm. It has been shown previously that energy transfer efficiency increases monotonically as the length of the carbon atom chain decreases from 18 to 12, and to 8 [20]. In addition, replacing the end carboxylate group by an amine group has also been demonstrated to improve the transfer efficiency. In this work, we further decreased the carbon atom chain length of the ligand in order to increase the rate of energy transfer. Specifically, we replaced the oleate ligands with butylamine ligands. Each of the butylamine ligands has a 4-carbon-atom-long single chain terminated by an amine group. The length of the molecule was estimated to be

approximately 5 Å. A solution-based exchange procedure was adopted to replace the oleate ligands with the butylamine ligands. The donor material, SRN, was deposited on transparent fused silica substrates through Plasma Enhanced Chemical Vapor Deposition using an Applied Materials Centura DxZ chamber. SiH_4 and N_2 were used as precursors. The substrate temperature during the deposition was 400°C. The detailed description of the experimental procedures for the deposition and annealing is provided in chapter 2. Very thin layers of PbS quantum dots were deposited by spin-coating on the smooth surface of SRN films or quartz substrates. With the same acceleration, spinning speed and time, we observed from the transmittance measurement that very thin layers of PbS quantum dots have high reproducibility in thickness and uniformity. The thickness of each spin-coated film was obtained by measuring the depth of a scratch made on the PbS quantum dot film by adopting atomic force microscopy technique. The correlation of the transmittance with the thickness of the PbS quantum dot film could be established.

5.6.3. Experimental results and discussion

The large overlap of the SRN luminescence spectrum with the absorption spectrum of PbS quantum dots, as demonstrated in fig. 5.20, suggests a novel opportunity for energy coupling of these two promising optoelectronic materials.

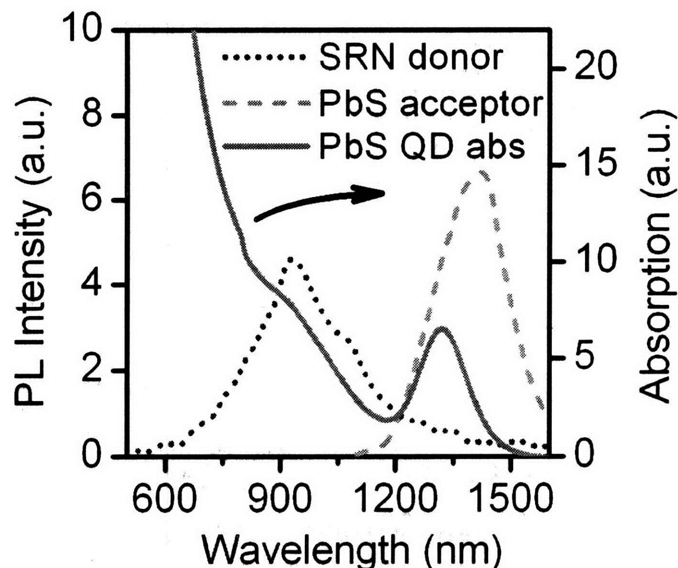

Figure 5.20. Absorption spectrum of PbS QD (solid line). Room temperature photoluminescence spectrum of 50 nm thick SRN (dot line) on quartz substrate and that of PbS QD on quartz substrate (dash line).

We have investigated energy transfer between SRN and PbS quantum dots by measuring photoluminescence excitation spectra (PLE) of three samples: the proximately-coupled donor-acceptor sample (Sample A), the acceptor-only reference sample (Sample B), and the donor-spacer-acceptor sample (Sample C), as shown in fig. 5.21.

In this study, the first excitonic peak of the PbS quantum dots is manifested on the absorption curve at 1300 nm (Fig. 5.20). The PbS quantum dots photoluminescence spectrum (Fig. 5.20, dash line) is Stokes-shifted to 1400 nm. These optical properties of the PbS quantum dots are given by dots with an average size of 5 nm, as shown in the electron micrograph in fig. 5.21. We produced the proximately-coupled donor-acceptor sample by spin-coating five monolayers of PbS QD's (about 25 nm film thickness) on 50 nm of SRN grown on a transparent quartz substrate. The reference sample was identical except that the

QD's were spin-cast onto a transparent quartz substrate. In the donor-spacer-acceptor structure, a 1 mm transparent quartz spacer was introduced between the PbS QD acceptor layer and the 50 nm SRN donor layer to prevent a short-range dipole coupling while still allowing radiative coupling.

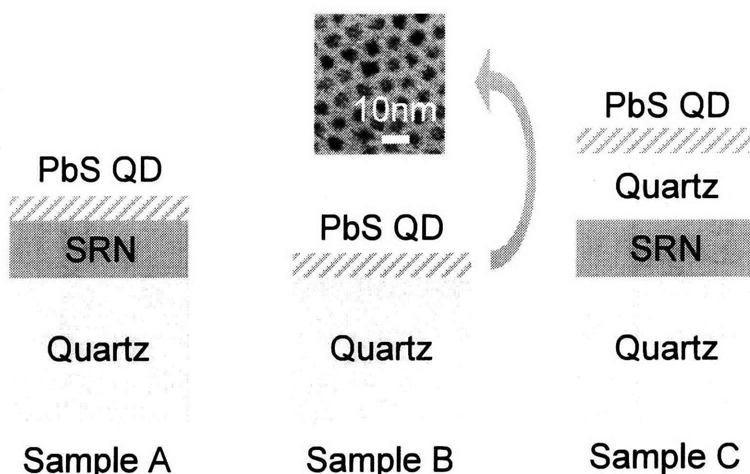

Figure 5.21. Structure of samples. (A) The proximately-coupled donor-acceptor sample. (B) The acceptor only reference sample. (C) The donor-spacer-acceptor sample. The inset shows a TEM image of the PbS QD's. Average diameter is about 5 nm.

In the PLE experiment (Fig. 5.22) the excitation wavelength was varied between 390 - 560 nm while the detection wavelength was fixed at the PbS QD emission peak. Photoluminescence excitation spectra of the samples along with the SRN absorption spectrum are shown in fig. 5.22. For excitation wavelengths longer than 500 nm where the SRN absorption is negligible, the PLE spectra overlap for all samples. This is the regime of direct PbS QD excitation alone, producing conventional photoluminescence. For excitation at wavelengths shorter than 500 nm, the photoluminescence of the proximately-coupled donor-acceptor sample rises significantly, while the reference sample and the donor-spacer-acceptor

sample overlap one another and do not rise. It is concluded that the factor-of-two luminescence enhancement of PbS QD's coupled to the SRN thin film donor is dominated by a short distance, non-radiative energy transfer process. The energy transfer efficiency at the room temperature at an excitation wavelength of 400nm is 60±5% from Dr. Tung-Wah F. Chang's calculation [19].

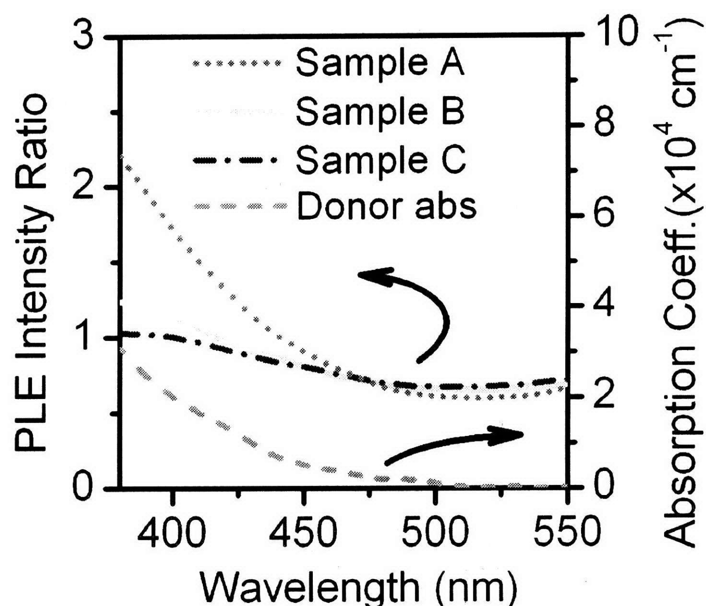

Figure 5.22. PLE trace of the acceptor-only reference sample (Sample B, solid line), the donor-spacer-acceptor sample (Sample C, dash-dot line), and the proximately-coupled donor-acceptor sample (Sample A, dot line). Absorption spectrum of 50 nm thick SRN (donor) on quartz substrate is also shown (dash line).

This finding points to the possibility of a convenient coupling and thus monolithic integration of solution-processible near-infrared-active optoelectronic materials on the electronics platform of CMOS silicon.

5.7. Conclusion

Optical properties of Er:SRN were investigated and energy sensitization from SRN to erbium ions was demonstrated with the optimization of annealing conditions and growth parameters. Annealing in forming gas was effective in enhancing Er luminescence slightly, but *in situ* growth in forming gas did not provide any difference. Annealing in forming gas with the sample grown in forming gas was not effective in enhancing Er luminescence. Very large excitation cross-section of $\sim 10^{-15}$ cm^2 level was obtained and the related non-resonant pumping issue was also discussed. Upconversion process which should be suppressed to achieve high population in the excited level was discussed based on the correlation plot. Strong dependence of the emission properties on Si content in Er:SRN was observed. Dependence of electrical properties on Si content will be provided and discussed in chapter 7. Er emission could be achieved even from the Er:SRN based on the SRN without SRN emission. Therefore, we learned that there are sensitizing agents not necessarily related with SRN emission.

Simulation results based on two level system with sensitizer and Er atom suggested that sensitizer density, coupling coefficient, and sensitizer excitation cross section are strongly contributive in changing the gain value and Er excited state population with pump photon flux even though these parameters do not contribute significantly in electrical excitation case as in chapter 7. However, the trends with Er concentration and upconversion coefficient were similar to what could be obtained in chapter 7.

We also have demonstrated energy transfer from SRN to colloidal PbS quantum dots. Detailed transfer mechanism was investigated and discussed. Energy transfer is dominated

by a short distance, non-radiative energy transfer process, not by emission and reabsorption process. This finding opens a convenient strategy for the monolithic integration of solution-processible active optoelectronic materials on the electronics platform of CMOS silicon.

5.8. References

[1] K. S. Min, K. V. Shcheglov, C. M. Yang, H. A. Atwater, M. L. Brongersma, and A. Polman, Appl. Phys. Lett. **69**, 2033 (1996).

[2] G. N. van den Hoven, E. Snoeks, A. Polman, C. van Dam, J. W. M van Uffelen, and M. K. Smit, J. Appl. Phys. **79**, 1258 (1996).

[3] T. Miyakawa and D. L. Dexter, Phys. Rev. B **1**, 2961 (1970).

[4] M. Stolfi, L. Dal Negro, J. Michel, X. Duan, J. LeBlanc, J. Haavisto, and L. C. Kimerling, Mater. Res. Soc. Symp. Proc. vol. 832 (2005). Mike Stolfi, Ph.D. Thesis, Massachusetts Institute of Technology (2006).

[5] L. Dal Negro, M. Stolfi, J. Michel, J. LeBlanc, J. Haavisto, and L. C. Kimerling, Appl. Phys. Lett. (in preparation).

[6] L. Dal Negro, "Rate equation modeling of energy coupling processes in Si nanocrystal – erbium systems," (unpublished).

[7] D. Pacifici, G. Franzo, F. Priolo, F. Iacona, and L. Dal Negro, Phys. Rev. B **67**, 245301 (2003).

[8] K. Imakita, M. Fujii, and S. Hayashi, Phys. Rev. B **71**, 193301 (2005).

[9] K. Watanabe, M. Fujii, and S. Hayashi, J. Appl. Phys. **90**, 4761 (2001).

[10] D. K. Armani, T. J. Kippenberg, S. M. Spillane, and K. J. Vahala, Nature **421**, 925 (2003).

[11] A. Liu, R. Jones, L. Liao, D. Samara-Rubio, D. Rubin, O. Cohen, R. Nicolaescu, and M. Paniccia, Nature **427**, 615 (2004).

[12] V. R. Almeida, C. A. Barrios, R. R. Panepucci, and M. Lipson, Nature **431**, 1081 (2004).

[13] H. Rong, A. Liu, R. Jones, O. Cohen, D. Hak, R. Nicolaescu, A. Fang, and M. Paniccia, Nature **433**, 292 (2005).

[14] E. H. Sargent, Adv. Mater. **17**, 515 (2005).

[15] S. Coe, W.-K. Woo, M. Bawendi, and V. Bulovic, Nature **420**, 800 (2002).

[16] M. Achermann, M. A. Petruska, S. Kos, D. L. Smith, D. D. Koleske, and V. I. Klimov, Nature **429**, 642 (2004).

[17] L. Dal Negro, J. H. Yi, L. C. Kimerling, S. Hamel, A. Williamson, and G. Galli, Appl. Phys. Lett. **88**, 183103 (2006).

[18] M. A. Hines, G. D. Scholes, Adv. Mater. **15**, 1844 (2003).

[19] Personal communication with Tung-Wah Frederick Chang, Vlad Sukhovatkin, and Edward Sargent.

[20] T.-W. F. Chang, S. Musikhin, L. Bakueva, L. Levina, M. A. Hines, P. W. Cyr and E. H. Sargent, Appl. Phys. Lett. **84**, 4295 (2004).

[21] P. G. Kik, M. L. Brongersma, and A. Polman, Appl. Phys. Lett. **76**, 2325 (2000).

[22] S-Y. Seo and J. Shin, Appl. Phys. Lett. **78**, 2709 (2000).

[23] C. E. Chryssou, A. J. Kenyon, T. S. Iwayama, C. W. Pitt, and D. E. Hole, Appl. Phys. Lett. **75**, 2011 (1999).

[24] D. Kuritsyn, A. Kozanecki, H. Przybylińska, and W. Jantsch, Phys. Stat. Sol. (c) **1**, 229 (2004).

[25] Jessica G. Sandland, "Sputtered Silicon Oxynitride for Microphotonics: A Materials Study", Ph.D. Thesis, Massachusetts Institute of Technology (2005).

Chapter 6. Si racetrack resonator

6.1. Introduction

Racetrack resonator (or ring resonator) is one of the important building blocks for photonics systems with complex functionality [1-5]. Its application area spans from WDM devices and optical modulators up to lasers. Resonator devices are appropriate for high index contrast photonics systems due to 1) short interaction distance between the ring and bus waveguides, 2) small bending radius, and 3) fast-decayed evanescent field from the waveguide. These features allow high performance photonic systems to be composed of small resonators with weak coupling.

In this chapter the design of a Si based racetrack resonator (and also ring resonator) structure was presented. The resonators were fabricated at MIT MTL by adopting LOCOS (Local Oxidation) process to couple our optimized Er:SRN material to the resonator structure. The resonance in the Si resonator structure can be transferred to Er:SRN materials on top. If the resonance coincides with the energy levels of Er atoms, lasing action is expected. The racetrack configuration was chosen instead of a ring structure since the resolution of the lithography tool at MIT MTL is limited. Since the minimum gap between the bus waveguide and ring waveguide is expected to be > 0.5 μm, increased coupling length was preferred to increase the chance of resonance. The ultimate goal of this project is to fabricate a functioning laser without replying on the facility outside of MIT.

6.2. Device design

6.2.1. Waveguide dimension for single mode

To determine the waveguide dimension for single mode we utilized Apollo simulation tools [6]. First we started with a Si core with the thickness of 0.26 μm (data from the available SOI wafers) and cladded the whole structure with a layer of SiO_2 as shown in fig. 6.1. By changing the width of the waveguide we calculated the effective refractive indices of both the fundamental mode and the second mode. Since the refractive index of the cladding layer is 1.46, if the effective refractive index of the second mode is less than this value we consider the waveguide supporting only a single mode. From the plot of the effective refractive index vs. waveguide width in fig. 6.2 we decided to use 0.7 μm as the waveguide width on the photomask because this dimension is close to the resolution limit of the photolithography tool at MIT MTL. The real dimension is expected to be smaller as a result of the thermal oxidation process based on our previous experience. The detailed results and control issue will be provided in the next section. We repeated the same approaches with Er:SRN cladding layer on top of the waveguide to ensure that the above dimension is safe enough for single mode operation and we also take into account that the sidewall angle can vary from 90° to 80° or even to smaller angles from oxidation process.

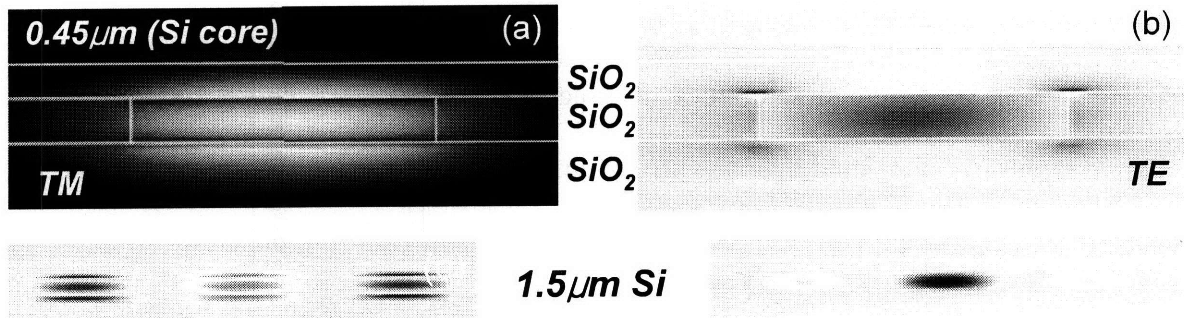

Figure 6.1. Representative optical mode profiles for TM and TE modes. (a) TM mode with the Si core width of 0.45 μm, (b) TE mode with the width of 0.45 μm, (c) TM mode with the width of 1.5 μm, and (d) TE mode with the width of 1.5 μm. We can clearly see that more than one mode can be supported with large dimension such as 1.5 μm.

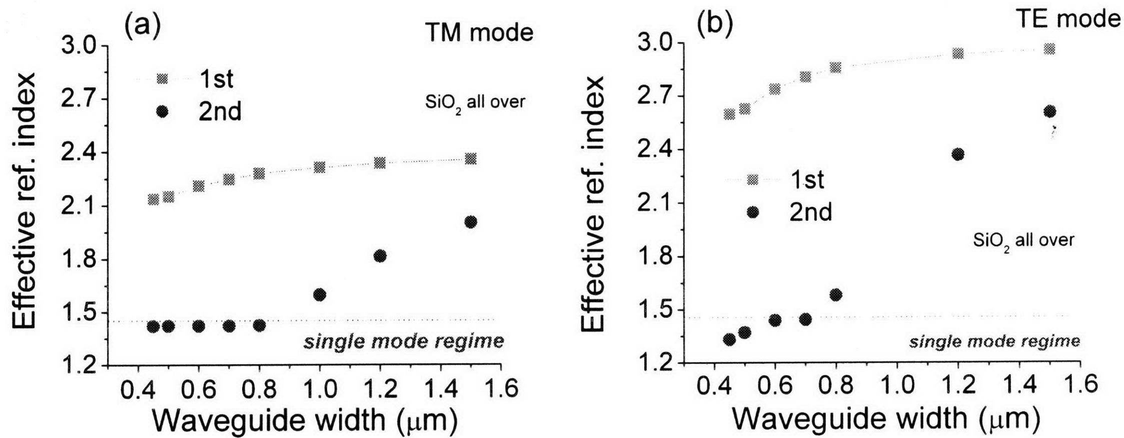

Figure 6.2. (a) Effective refractive index of the fundamental mode and second mode for TM and (b) TE modes by varying waveguide width. Refractive index of the cladding layer was inserted as guidance with dotted line.

6.2.2. Bending radius

Bending radius was varied to investigate the related loss. In the racetrack or ring resonator structure we have many components with 90° bending or 180° bending. Therefore it is needed to reduce the related loss to minimum. With the given dimension in section

6.2.1 we plotted bending loss as a function of bending radius. As shown in fig. 6.3 (a) the bending loss is predicted to saturate at the radius of 50 μm. We chose 100 μm as the bending radius for the bending parts in fig. 6.3 (b). This radius was used also in the paperclip structures. We will discuss the loss measurement from the paperclip structure in detail later. In short, bending loss associated with the chosen dimension was negligible.

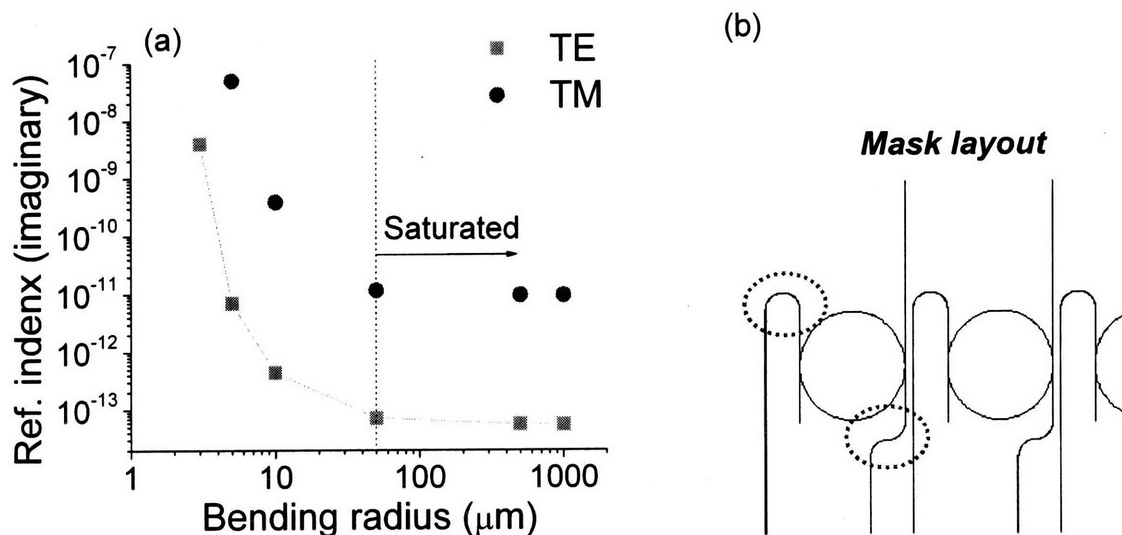

Figure 6.3 (a) Bending loss with bending radius for TE and TM modes. (b) Part of the device where bending component was used in common.

6.2.3. Coupling length

Due to the limited resolution in the available equipment at MTL, we can not expect to have narrow gap such as 0.1~0.3 μm between bus and ring waveguides. As a result, a ring structure is not enough to expect coupling phenomenon. Therefore, we considered a racetrack configuration. Coupling length, or coupled section length, was varied to maximize coupling factor. As in the fig. 6.4 coupling factor increases with increasing

coupling length. However, it is true within the half period of the coupling. As in the fig. 6.5 coupling is maximized periodically. Therefore just having a long coupling length does not guarantee good coupling. TE mode needs much longer coupling length than TM mode as shown in fig. 6.5. We varied the gap between bus waveguide and racetrack waveguides from 0.4 to 0.8 μm and selected an optimal coupling length for each gap and gave some small variation around the value chosen by considering the process tolerance and also the case with Er:SRN on top. The device structures from the mask layout are shown in fig. 6.6.

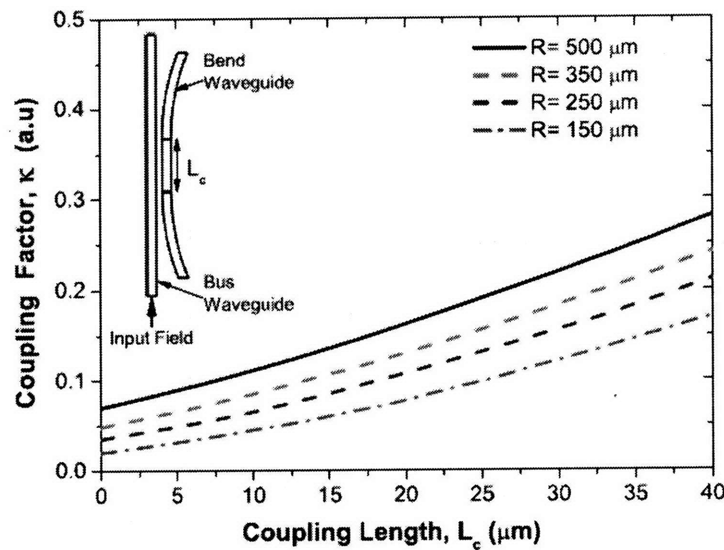

Figure 6.4. Numerically calculated coupling factors as a function of straight coupling length for different radii. Inset shows the device layout [7].

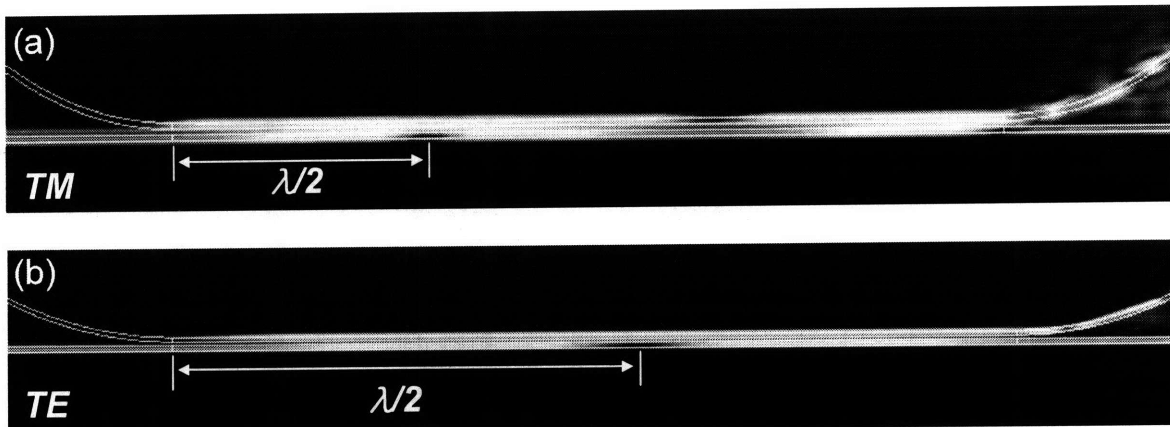

Figure 6.5 (a) Simulation results of coupling behavior with the racetrack structure with the gap of 0.6 μm and the coupling length of 30 μm for TM mode. (b) Coupling behavior with the racetrack structure with the gap of 0.5 μm and the coupling length of 50 μm for TE mode.

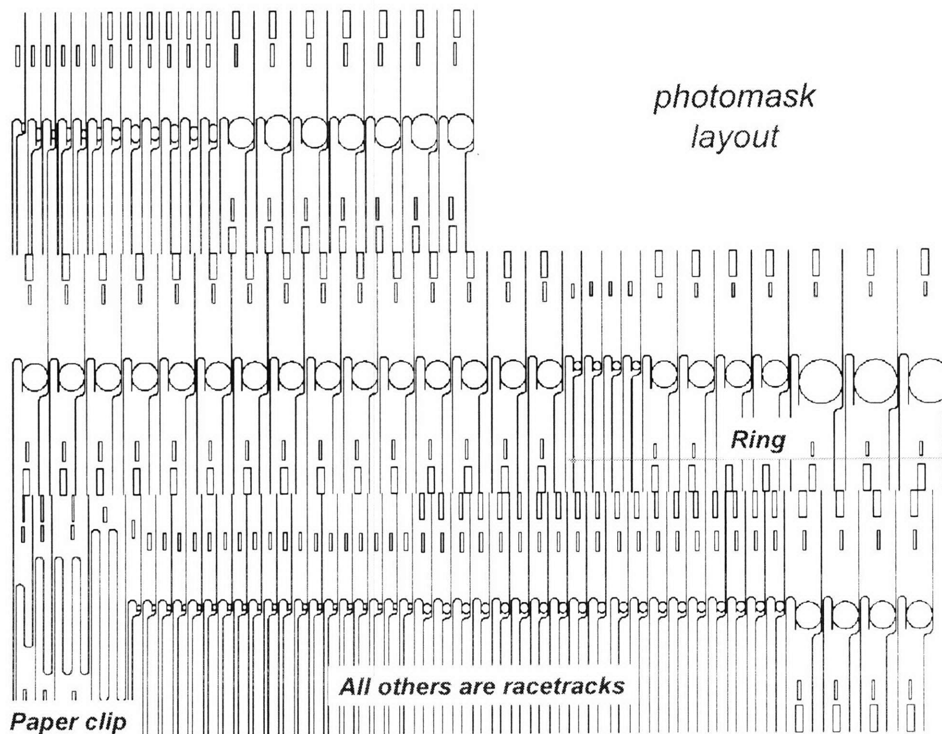

Figure 6.6. Device structures included in the mask layout with the same dimension in the photomask.

6.2.4. Resonance

Racetrack resonator (or ring resonator) operates based on the resonance phenomena. Resonance phenomena happen when the optical path length of the racetrack (or ring) is an integer number of wavelength in the track (or ring) as in the equation below.

$$m\left(\frac{\lambda_0}{n_{eff}}\right) = 2\pi R \quad \text{or} \quad 2\pi R + 2L$$

where R is the radius of the ring or the round part of the racetrack, L is the coupling length, λ_0 is the free space wavelength of resonant light, m is an integer indicating the resonator mode number, and n_{eff} is the effective index of the ring

When the resonance condition is satisfied as in the equation above, the circulating field in the ring or racetrack will interfere with the in-coming field from the bus waveguide constructively and the power will increase. The power coupling out of the ring also increases as the power in the ring increases. When the coupling happens, a phase shift of $\pi/2$ occurs simultaneously. As a result, coupling-in and coupling-out will lead to π shift. Finally it can interfere with the field in the bus waveguide destructively. If the dimensions of the racetrack (or ring) and the gap are properly designed, incoming field and the original field can be annihilated out. However, when the resonance condition is not met, no interference between racetrack (or ring) will happen and the original field will not change. More detailed information can be obtained in Prof. H. Haus' textbook [8].

6.2.5. Quality factor

Quality factor, Q, is important in the resonator since it is defined as the accumulated energy over the dissipated energy per each circulation in the ring (or racetrack). The following equation represents the situation.

$$Q \equiv \frac{\omega_0 \tau}{2} \cong \frac{\lambda_0}{\Delta\lambda}$$

where ω_0 and λ_0 are the resonance frequency and wavelength respectively, τ is the characteristic time constant of the resonator and $1/\tau$ is the damping rate of the field in the resonator. Quality factor value can be obtained from the transmission data by dividing the resonance wavelength divided by the FWHM width of the dip. High Q value of the device suggests an efficient build up of energy inside the ring. In that case the damping rate should be small. That is, the field in the racetrack (or ring) should travel long enough.

6.3. Fabrication process and related issues

As shown in fig. 6.7, on the Si wafer or SOI wafer we deposited a 150 nm thick silicon nitride film in the CVD reactor, "Vertical Thermal Reactor" and patterned it with photolithography and dry etching in CF_4 chemistry. A silicon nitride mask was used to prevent oxidation underneath the mask pattern and this area defines the region for waveguides. From literature and SALVACO simulations as in fig. 6.8 we found that more than 150 nm of silicon nitride thickness is enough for this purpose. We will discuss this

issue again later for better control of the waveguide shape. Thermal oxidation followed for waveguide formation with the expected dimension depending on oxidation time and waveguide measurements can be obtained at this step for preliminary measurement. Loss related issues from the waveguide measurements will be discussed later in detail in section 6.4. After removing silicon nitride and oxide respectively with hot phosphoric acid (at 165°C) and BOE or diluted HF, wet treatment can be used to smooth the side walls or the sharp corners of the waveguides to achieve a reduced loss value. Finally oxide can be deposited for reliable loss measurement. Not only oxide can be used for reliable loss measurements, but Er:SRN can be also deposited on top of waveguide. Other active materials like Er silicate or Er,Yb-silicate can be deposited as alternatives.

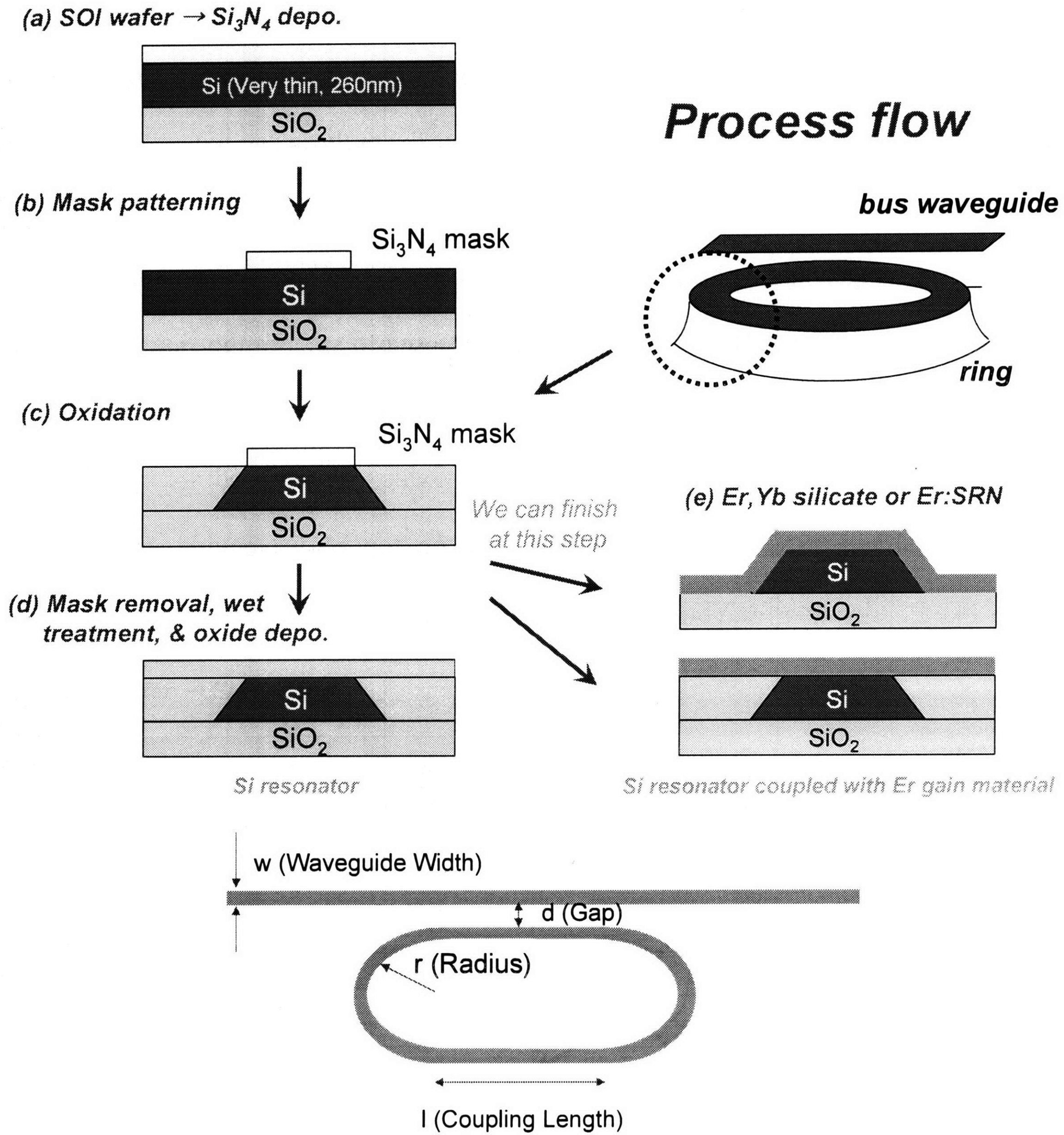

Figure 6.7. Detailed process flow of LOCOS Si resonator (Top) and schematic diagram of the final structure (Bottom).

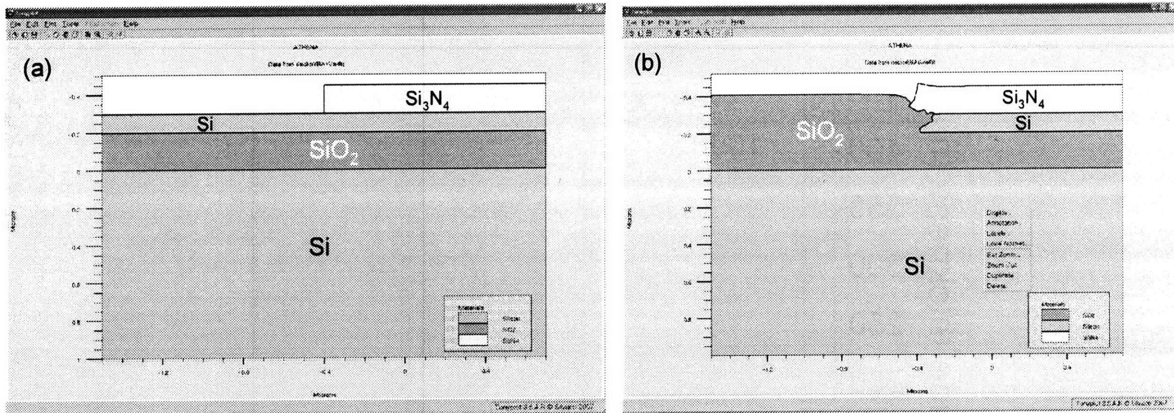

Figure 6.8. Salvaco simulation for thermal oxidation process with silicon nitride on top. (a) original structure. (b) structure after oxidation. From the top, silicon nitride (Cyan), silicon (Orange), silicon oxide (Sky blue), and silicon again (Orange).

6.3.1. Thermal oxidation

By controlling the thermal oxidation time we can control the oxide thickness and as a result Si waveguide width on SOI wafer can be also controlled. We used regular Si wafer first without using SOI wafer to test and optimize the thermal oxidation process since it is expensive. With wet oxidation at 1000°C, we were able to control the thickness reproducibly as in fig. 6.9.

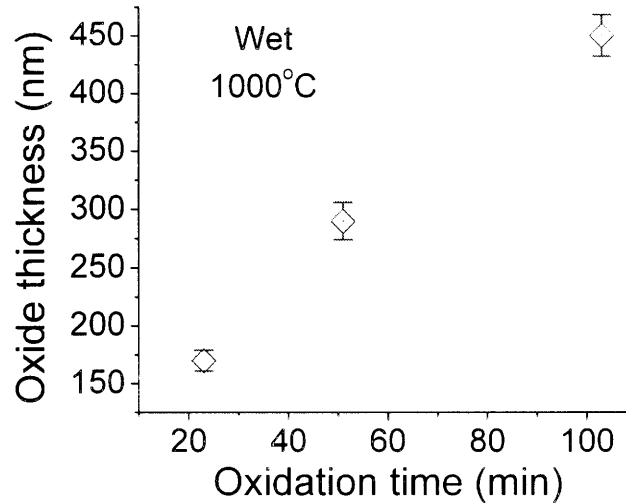

Figure 6.9. Oxide thickness with oxidation time in wet atmosphere at 1000°C.

6.3.2. Gap narrowing with thermal oxidation

With the process optimization by using Si wafers rather than SOI wafers we investigated how the gap narrowing varied for the various gap dimensions. As shown in fig. 6.10 gaps between the bus waveguide and racetrack waveguides were varied from 0.5 μm to 0.7 μm (designed dimensions in photomask). From the experimental result the gaps between nitride patterns were varied from 0.59 μm to 0.78 μm. Based on the experimental data for the gap narrowing under the nitride pattern as shown in fig. 6,11, the gaps between Si and Si waveguides were from 0.5 μm to 0.7 μm for the shortest distance and 0.7 μm to 0.9 μm for the longest distance. As you can see in the upper right picture of figure 6.10, the waveguide cross section is not rectangular, but somewhat trapezoidal with round sidewalls. The narrowest width and the widest width are different (470 nm vs. 910 nm as in the given picture). Therefore, distance between Si and Si waveguide is different depending on which

point we select. The MIT MTL facility of Nikkon stepper NSR-2005i9 has the resolution limit of 0.7 μm for the positive features and 0.5 μm for the gaps with the usual condition and 0.4 μm patterns could not be defined reliably. However, with the narrowing by oxidation we could get a smaller dimension in waveguide width than the resolution limit.

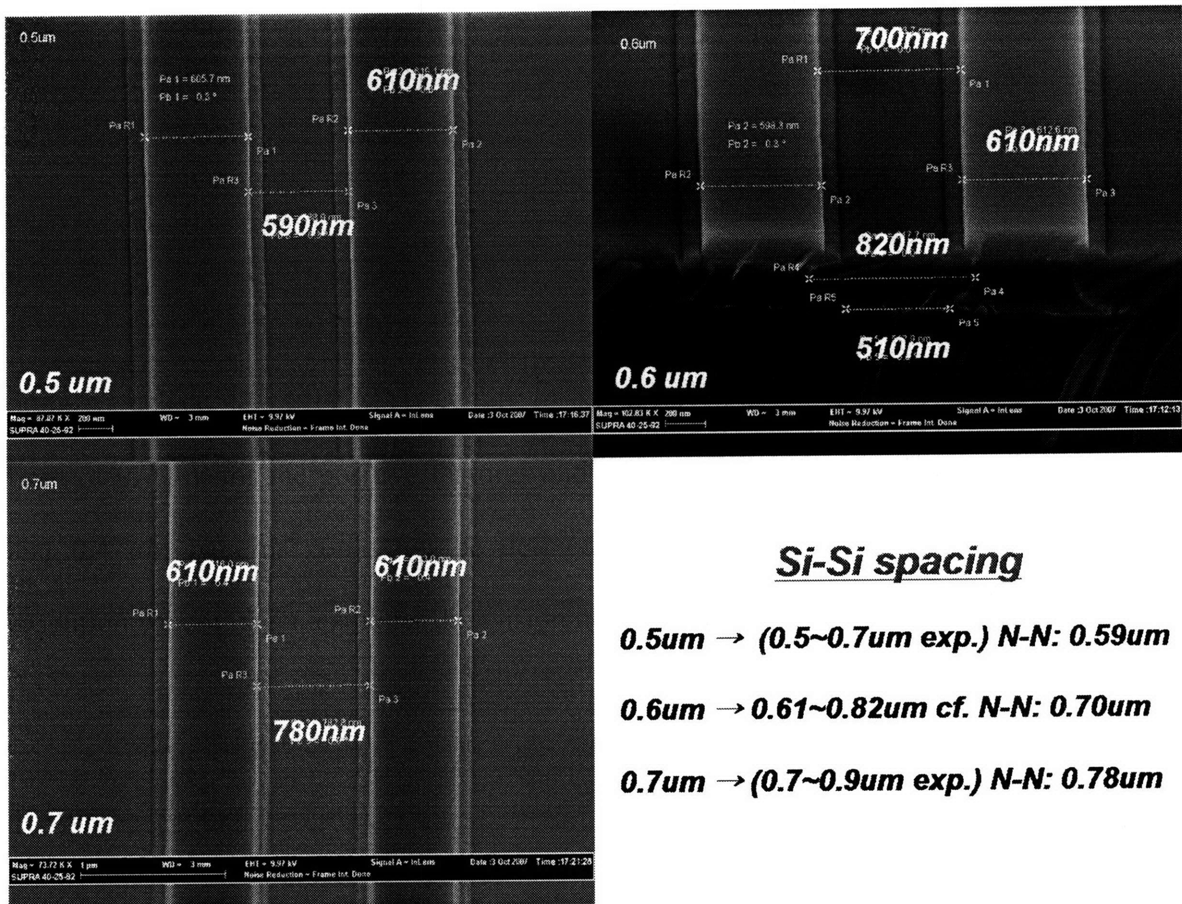

Figure 6.10. Bus waveguide and racetrack waveguide showing the gaps with varied gap dimensions from 0.5 μm to 0.7 μm.

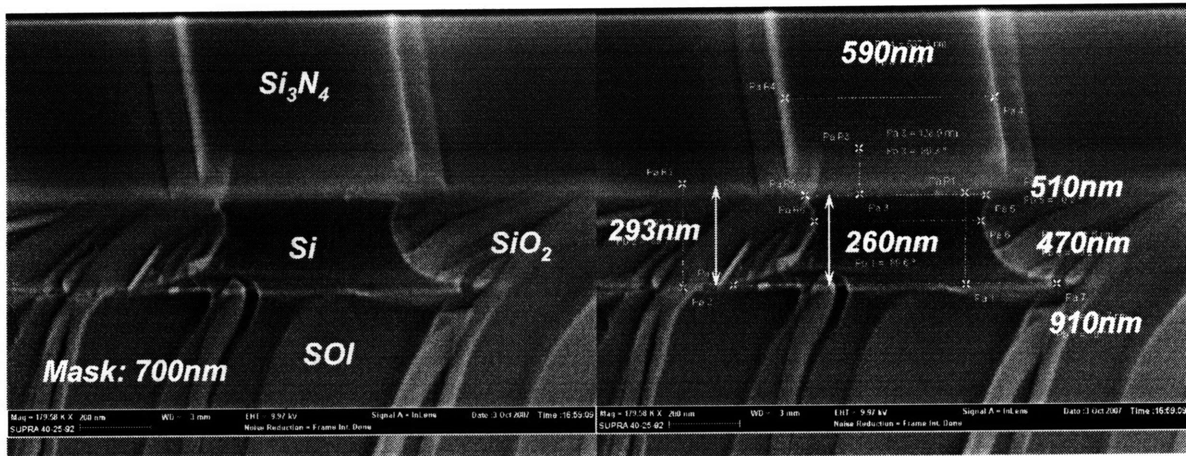

Figure 6.11. Cross sectional SEM showing SOI waveguide with detailed dimension. Rough surface was from poor cleaving in sample preparation, not intrinsic property of the structure and materials here.

6.3.3. Nitride and oxide removal

Waveguide structure right after thermal oxidation for waveguide formation was optically analyzed and the loss value obtained was somewhat large, ~ 8.0 dB/cm. The detailed measurement results and discussion will be provided later in section 6.4. VTR nitride can be the source of the loss due to the formation of the N-H bonds or silicon nanocrystals [9]. Considering the wavelength range we are interested the presence of silicon nanocrystals can be regarded as inhomogeneities which can potentially scatter light. In situ nanocrystal formation is possible due to the high growth temperature of the nitride by VTR reactor (775°C). Therefore, nitride was removed for the piecewise samples with hot phosphoric acid at 165°C (Etch rate of ~ 4 nm/min). However, piecewise samples are hard to be rinsed cleanly enough after wet etching without showering function in our facility. As shown in fig. 6.12 and 6.13, phosphoric acid residues could not be removed even with rinsing. Oxide was also removed with BOE solution (Etch rate of ~ 100 nm/min)

for Er:SRN deposition on top. Fig. 6.12 and 6.13 show the removal of oxide layers. Phosphoric acid residues still can not be observed even with oxide removal. From this rough surface we can not expect coupling from Si resonator to Er:SRN gain material due to the large loss. For a clean removal of nitride, full wafer process with strong shower should be adopted as an alternative approach considering the sticky characteristics of phosphoric acid. Fig. 6.14 and 6.15 show Si and SOI waveguides after hot phosphoric etching and rinsing with strong shower capability followed by BOE etching and rinsing. You can clearly see that there is no phosphoric acid residue left and also the sidewalls of the waveguides are very smooth.

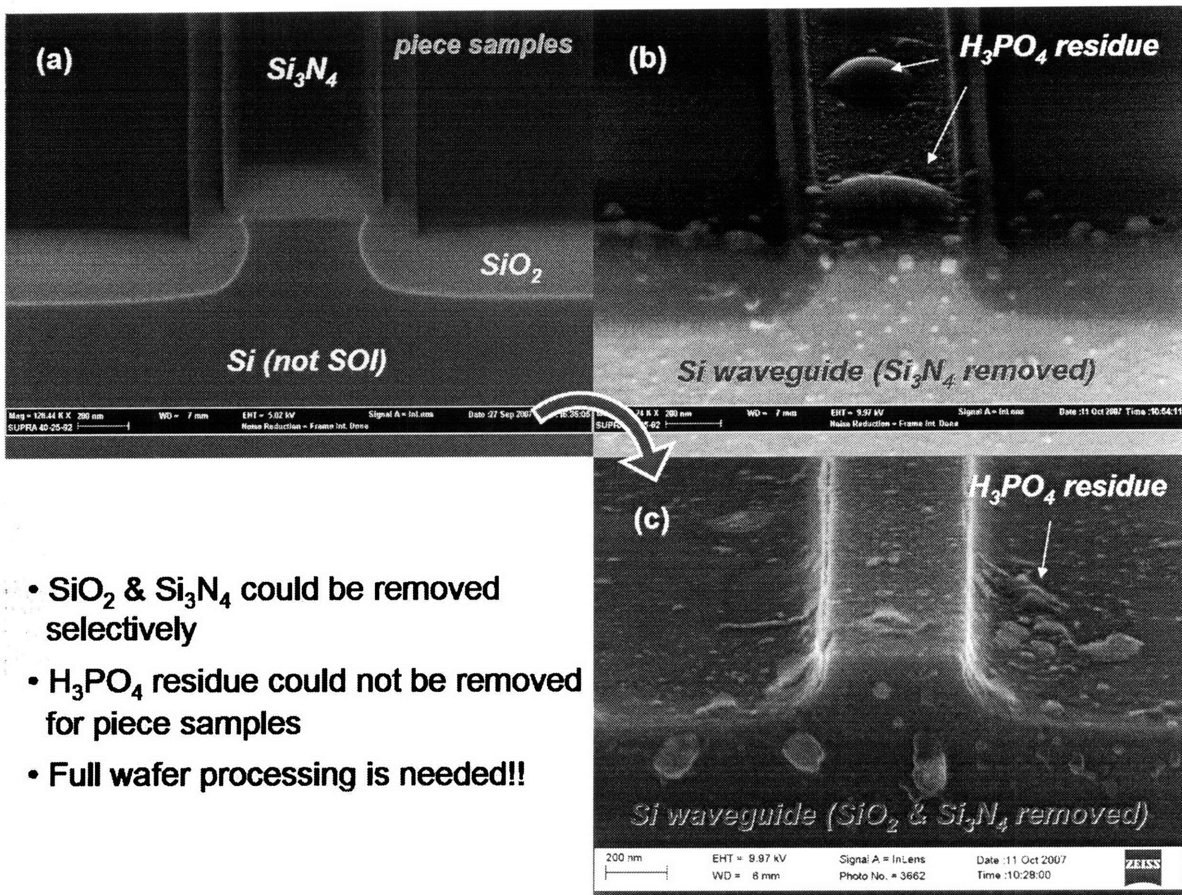

Figure 6.12. Si waveguides (a) right after oxidation with nitride pattern, (b) with the nitride pattern removed, (c) with the nitride and oxide layers removed

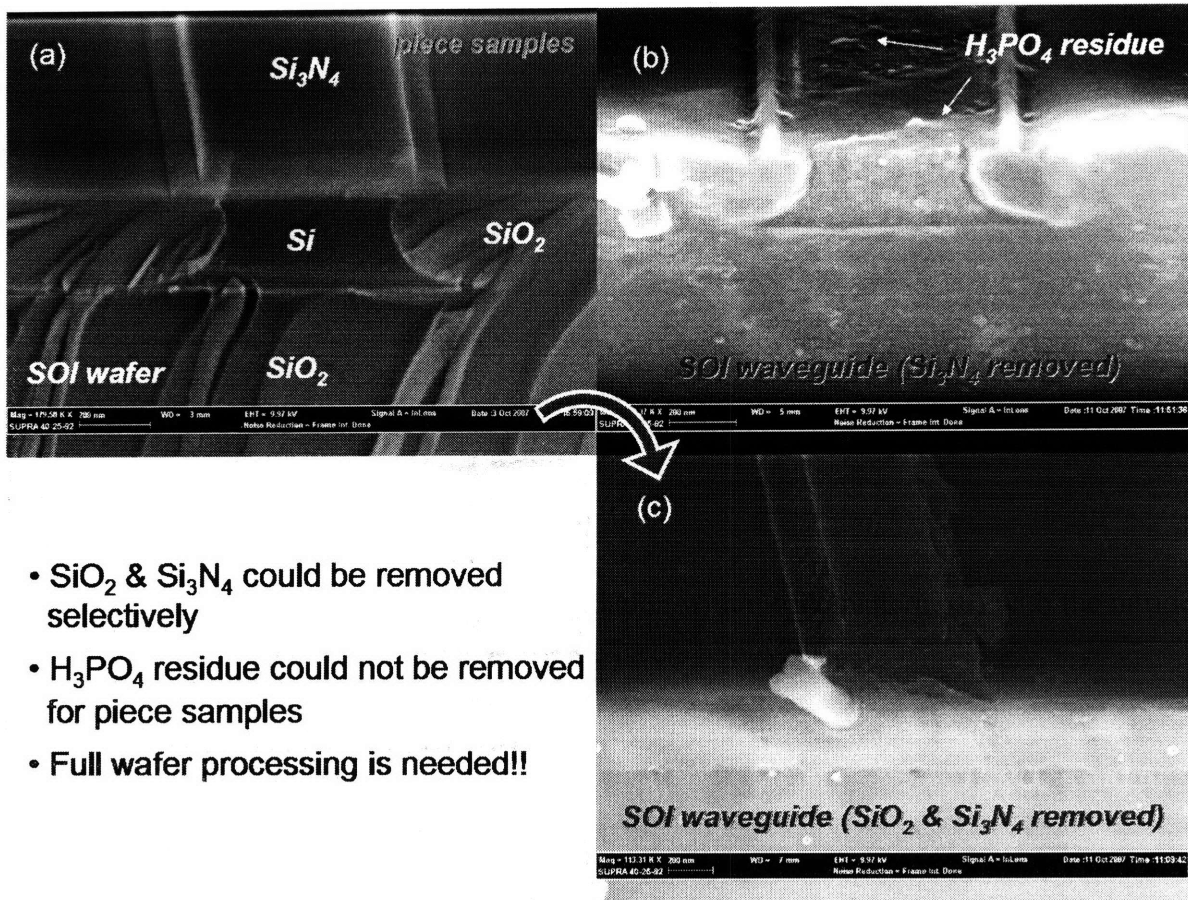

Figure 6.13. SOI waveguides (a) right after oxidation with nitride pattern, (b) with the nitride pattern removed, (c) with the nitride and oxide layers removed

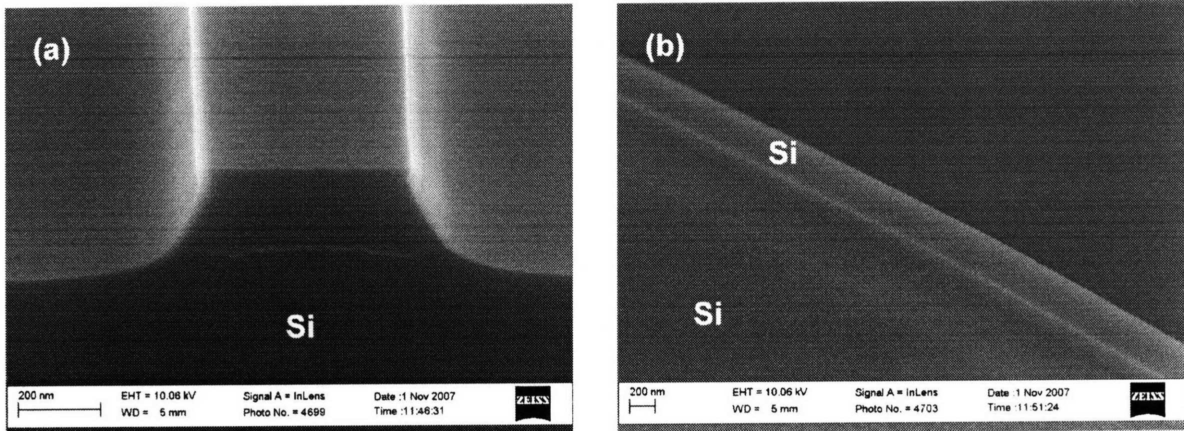

Figure 6.14 (a) Cross section of silicon waveguide after removal of nitride and oxide. (b) Slanted view from the side to show clean surface and also smooth side wall of the waveguide.

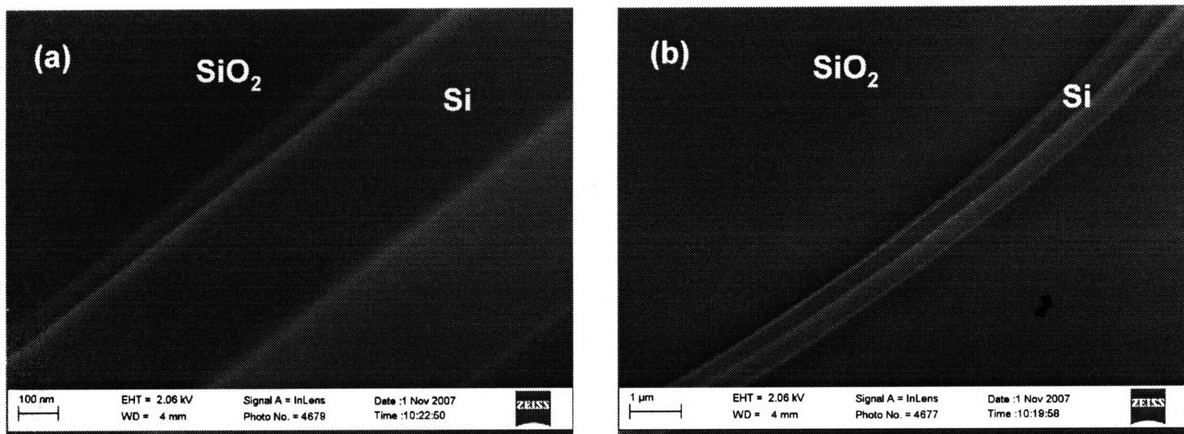

Figure 6.15 (a) Close up of SOI waveguide after removal of nitride and oxide. (b) Slanted view from the side to show clean surface and also smooth side wall of the waveguide. Clean contrast of the silicon waveguide to SiO_2 layer differentiates the picture in fig. 14 (b) where all the features and the surface are silicon without any contrast.

6.3.4. Wet treatment for smoothening

Sharp corners of the waveguides can be source of additional losses considering the mode profile in the cross section of the waveguide. Therefore smoothening process of the sharp corners was necessary. In Daniel Sparacin's MIT doctoral thesis the repeated RCA

treatment was effective in reducing sidewall roughness of Si waveguide from the dry etching process and the waveguide loss accordingly [9]. Therefore, this method was adopted to remove the sharp corner features. However, the sharp corners could not be removed even after repeated wet treatments. The wet treatment is believed to be effective in smoothing out the very small features (10~100 Å range, striation from dry etching process) of the sidewall. However, our sharp corners have the radius of ~ 10-30 nm range. Therefore, these large features could not be smoothed out with the wet etching process.

The sidewalls of the LOCOS waveguide were smooth from the beginning even before the wet treatment because they were made by thermal oxidation. The wet treatment was not effective in further reducing the loss of the waveguides. The detailed results will be discussed in section 6.4.

To achieve smooth and round corners of the waveguides, thinner nitride mask which leads to larger bird beak can be considered.

6.3.5. Oxide deposition and selective removal

3 μm PECVD oxide was deposited for reliable optical measurement since exposure of the uncladded waveguide to the moisture in air will affect the loss values in unreliable ways. Fig. 6.16 (a) and 6.17 (a) show SEM cross-sections of the Si and SOI waveguides with 3 μm oxide on top. These waveguides were not successful in terms of loss value (~8 dB/cm) since nitride removal was not complete due to unexpected reasons such as shorter etching time. Oxide layer was removed before depositing Er:SRN gain material on waveguide with BOE and HF respectively by controlling etching time without removing underneath oxide

of SOI. As shown in fig. 6.16 (b) it was easy to remove oxide selectively from Si waveguides. However, leaving SOI waveguide by controlling etching time in BOE was quite challenging. Our waveguide was removed away since the oxide underneath the waveguide was also over-etched (Fig. 6.17 (b)).

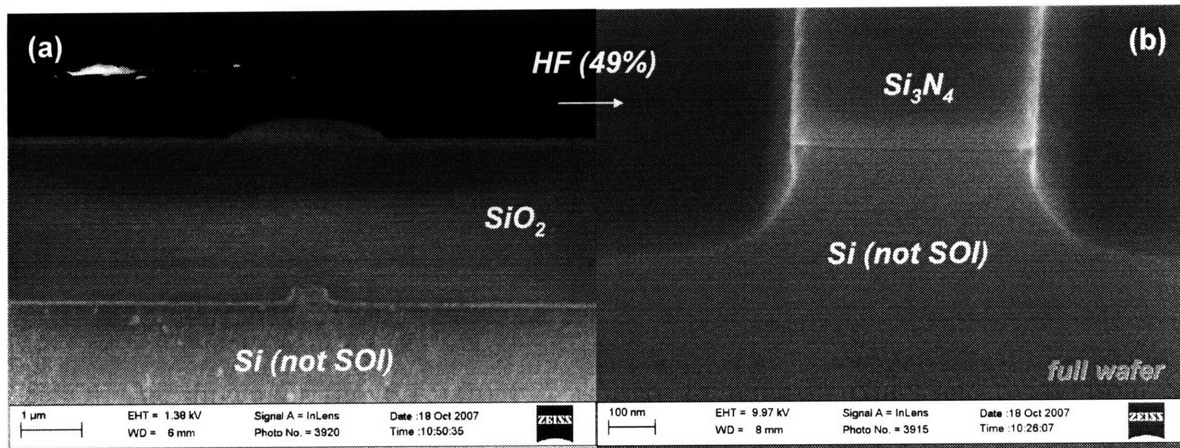

Figure 6.16. (a) Si waveguide with oxide cladding, (b) Oxide cladding was removed by HF.

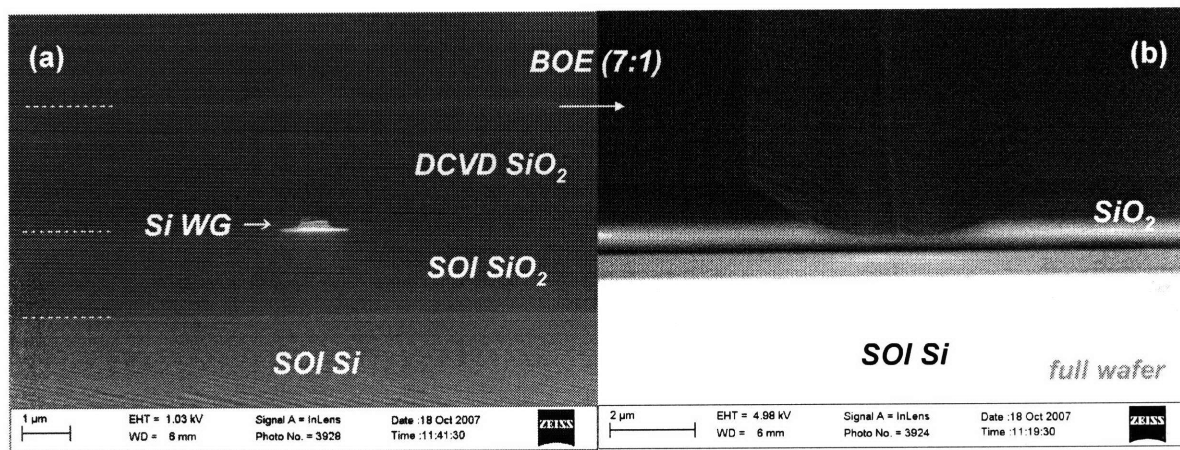

Figure 6.17. (a) SOI waveguide with oxide cladding, (b) Oxide cladding was removed by BOE, but Si waveguide was also removed due to over-etching.

6.3.6. Er:SRN deposition

Er:SRN layer was deposited on SOI waveguide in order to observe gain behavior from the combined resonator device. After removing nitride completely with hot phosphoric acid, oxide was also removed with BOE in controlled time (It was possible because it is thin to be removed in controlled time). Without any cladding layer left the Er:SRN layer of 200 nm thickness was deposited by sputtering. Sputter condition was chosen from the optimized PL conditions as stated in chapter 5. Fig. 6.18 shows a successfully fabricated device. After annealing with the optimal condition (900°C, 10 min) PL from the sample was confirmed as shown in fig. 6.19 (Solid red line). Er emission was as strong as from the Er:SRN layer on Si wafer (Dotted blue line).

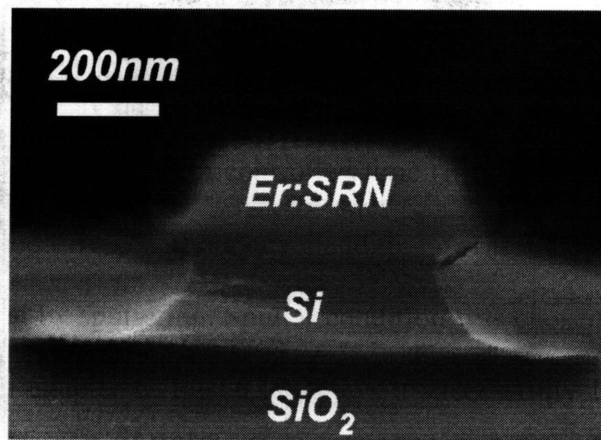

Figure 6.18. SOI waveguide with Er:SRN deposited on top. Scale bar represents 100 nm.

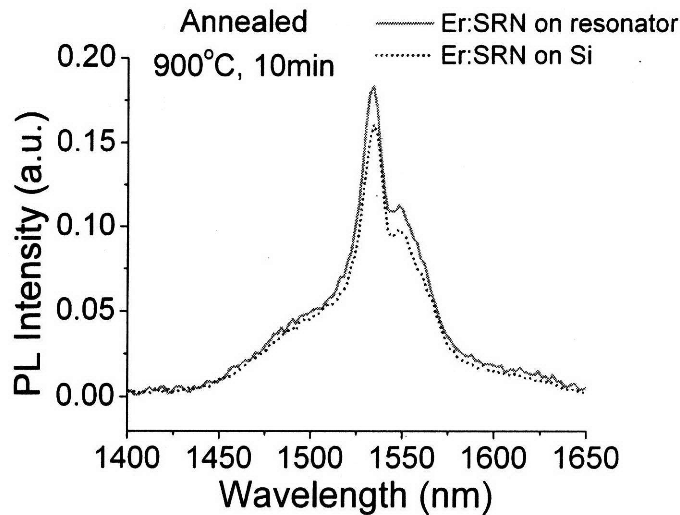

Figure 6.19. Photoluminescence spectrum from Er:SRN on SOI waveguide (Solid red line). Dotted blue line shows photoluminescence spectrum from Er:SRN on Si wafer.

6.4. Optical measurement

For the transmission spectrum measurement we used Newport-JDS system which is composed of a Newport Auto-alignment Station and a JDS Uniphase Swept Wavelength System (SWS). This system has fiber in and fiber out features. Newport Auto-alignment Station has two towers with in-fiber and out-fiber with the controllability in x-axis, y-axis, z-axis, and angle. With the freedom in four control parameters we can align the laser, the waveguide, and the detector accurately. After observing the light through the waveguide by a CCD camera, coarse alignment can be made by maximizing the light intensity by putting the input fiber near the waveguide. Output fiber can be aligned by maximizing the power through the output fiber in the power meter. This maximization can be done automatically with a precision of ±50 nm in x, y, and z directions. The lens, the CCD camera, and the optical microscope are not included in the fig. 6.22.

After proper alignment we shift the system from Newport Auto-alignment unit to JDS

Uniphase Swept Wavelength unit for transmission measurement. This unit is composed of a tunable laser, a polarization controller, and detectors. The spectral range of this unit covers the entire C band (1520 ~ 1570 nm) and L band (1570 ~ 1630 nm). Maximum and minimum data do not always correspond to TE and TM modes in general. It is true only for a simple waveguide structure.

After obtaining the transmission spectrum we can shift back to Newport Auto-alignment unit for another measurement. With the powerful automatic alignment function we can move to another waveguide and align in very short time. Therefore, measuring many devices in short time is possible unless the facet conditions are not good due to poor polishing or cleaving. However, some samples with too high loss can not be observed by the CCD camera when we align the system with waveguide even coarsely. If we can not see any light in the CCD, getting reasonable power level for fine alignment is not possible. In that case it is very hard to determine the loss value from our measurement system.

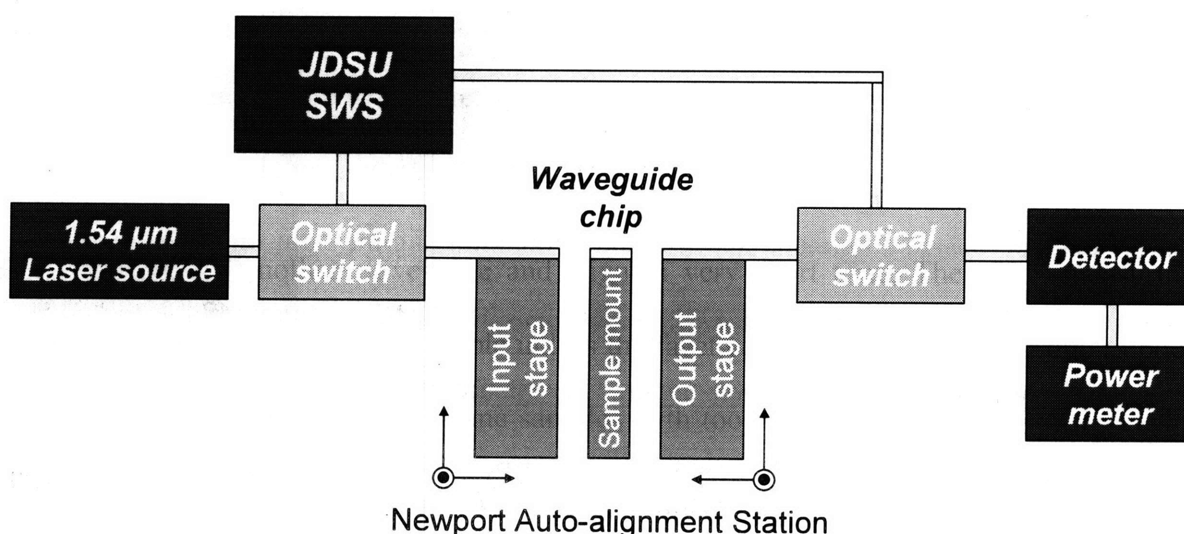

Figure 6.22. Schema of the Newport-JDS waveguide measurement system.

6.4.1. Loss measurement

The paperclip approach is one such design that avoids the detriments of traditional cutback. As seen in fig. 6.6, the arrangement of paperclip-shaped waveguides with identical cross-sections enables measurement of different length waveguides without the need to destructively reduce the size of the sample. The addition of two 180° bends allow the waveguides to have different lengths while maintaining identical input and output facet spacing. Maintaining a constant input to output port spacing facilitates easier sample preparation and reduces the alignment time among waveguide measurements. Additional loss that may arise from the waveguide bends is constant for each waveguide and does not affect the transmission loss value since the cutback is a relative measurement.

As shown in fig. 6.23 (a) and (b) loss value was 7.9 dB/cm when there are nitride and oxide cladding layers. Similar value was obtained with the waveguide in section 6.3.5 since there were nitride layers on top of Si waveguide for both of the cases. However, after removing nitride and oxide layers, loss value was lowered down to 2.5 dB/cm (Fig. 6.24). Considering that there is no cladding layer (which means additional loss from the moisture or other stuff in the air can be resulted in), this value can be lowered further with a reliable upper cladding layer like oxide.

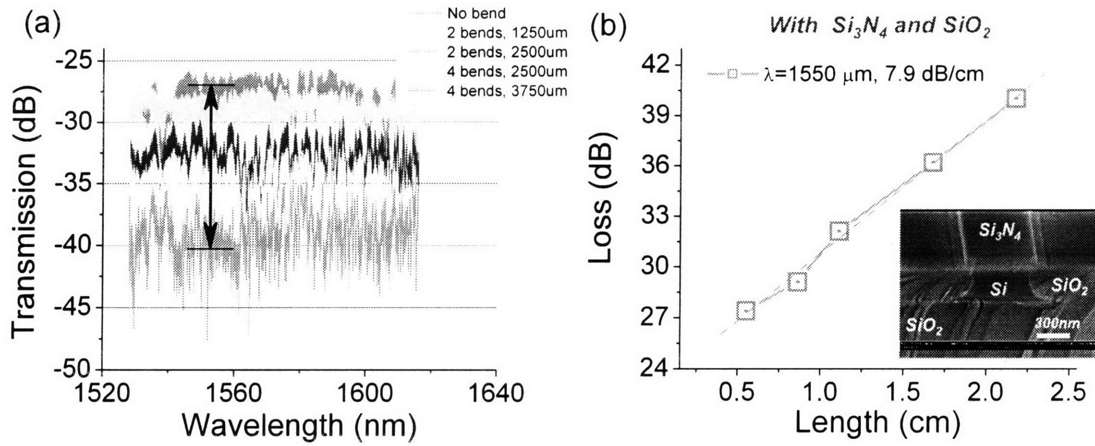

Figure 6.23 (a) Transmission data with paper clip structures for LOCOS Si waveguide with Si_3N_4 and SiO_2. Black arrow is added for clear presentation of the range of the loss values (b) Plot of loss versus length from the data given in (a). Inset shows the cross-section of the waveguide structure.

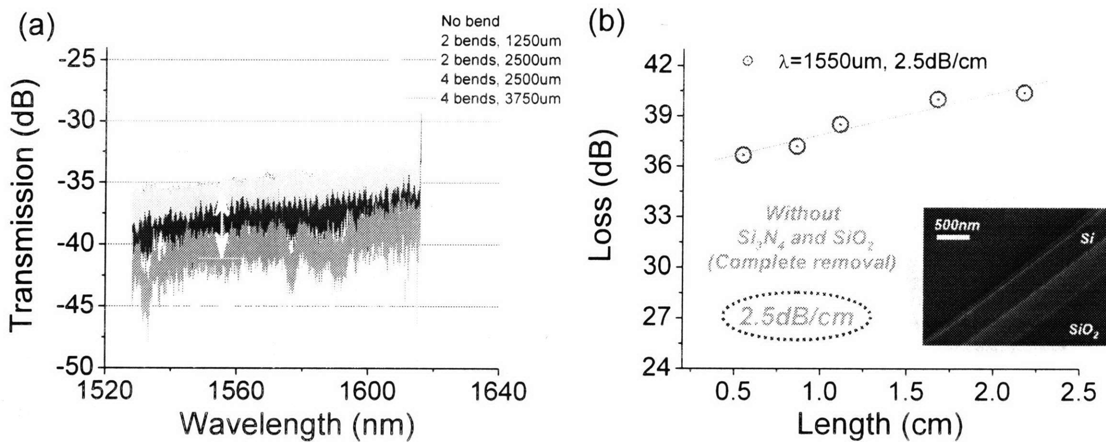

Figure 6.24 (a) Transmission data with paper clip structures for LOCOS Si waveguide without Si_3N_4 and SiO_2. White arrow is added for clear presentation of the range of the loss values (b) Plot of loss versus length from the data given in (a).

6.4.2. Observation of resonance

With racetrack structure resonance phenomena were observed. As shown in fig. 6.25

sharp dips with an even spacing were observed and the calculated FSR (Free Spectral Range) quite corresponds to the measured values.

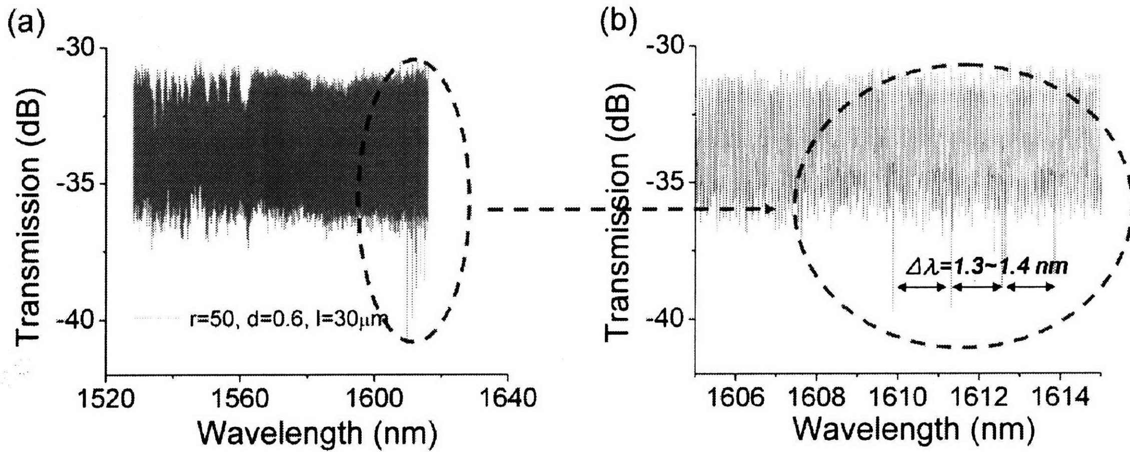

Figure 6.25 (a) Transmission data for the Si racetrack structure with the radius of 50um, the gap of 0.6 μm, and the coupling length of 30 μm. (b) Zoom-up of (a) for the wavelength range where resonance behavior observed.

Quality factor (Q) is also obtained from one of the sharp dips, on the order of 10^5.

$$FSR = \Delta\lambda = \frac{\lambda_0^{\ 2}}{2nL} = \frac{\lambda_0^{\ 2}}{2n \times 2\pi R} = \frac{(1612.5nm)^2}{2 \times 3 \times 2\pi \times 50\mu m} = 1.38nm$$

$$Q = \frac{\lambda_0}{\Delta\lambda} = \frac{1609.88nm}{2.92 \times 10^{-3}\,nm} = 5.5 \times 10^5$$

However, the fact that there are resonance dips only at long wavelength longer than around 1600nm is not understood. Therefore, we performed simulation with the exact shape of the waveguide as in the SEM images. Simulation results implied that single mode condition could not be sustained at short wavelength (< 1600 nm), but with the wavelength longer than 1600 nm, single mode operation was possible. Multimode in the waveguide leads to interference among the modes and resonance phenomenon is unlikely. To get more reliable

results we deposited 3 μm oxide on top and obtained transmission data. Figure 6.26 (a) shows the transmission data for the racetrack device with 50 μm radius, 0.7 μm gap, and 200 μm coupling length. We can clearly see the dips due to resonance in wider range. Some of the resonance dips were zoomed in for Lorentzian fitting to get Q values. We could get Q values of low to high 10^4. Fig. 6.26 (b) and (c) shows some of the representative dips of resonance.

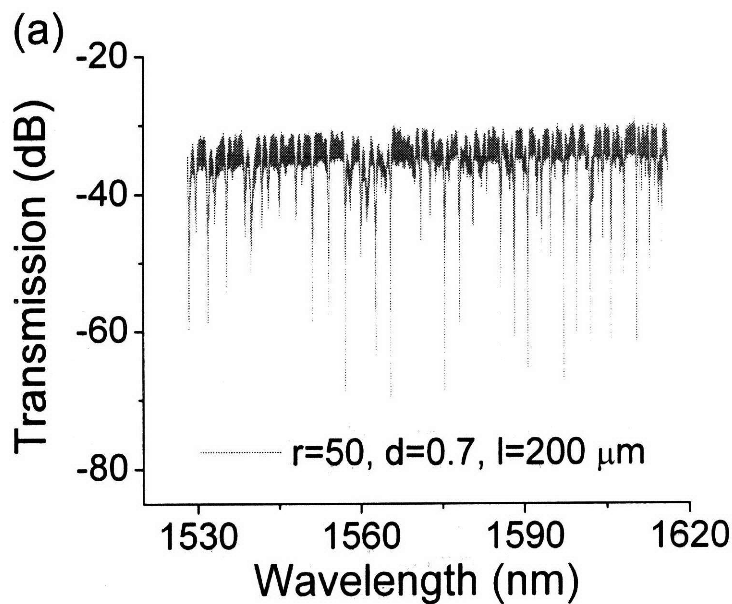

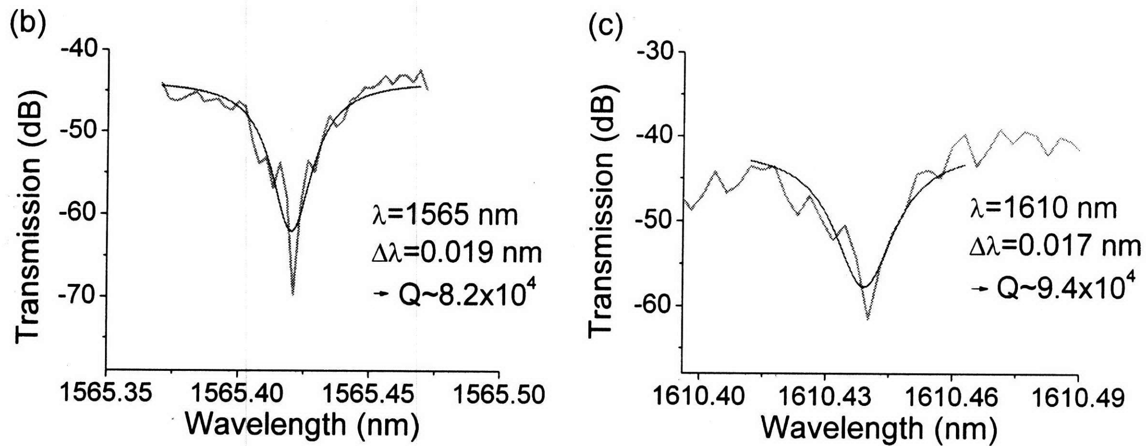

Figure 6.26 (a) Transmission data for the Si racetrack resonator with the dimensions of 50 μm radius, 0.7 μm gap, and 200 μm coupling length. (b) Close-up of the dip around 1565 nm (Q~8.2×10^4) and (c) 1610 nm (Q~9.4×10^4).

Further confirmation on the resonance behavior is needed for a better understanding of the phenomena and the improvement of the device performance.

6.4.3. Gain measurement

Gain measurement was performed with Er:SRN on SOI resonator structure by the collaboration with Lehigh university. With their 1480 nm laser source we expect Er to be pumped without absorption of the pump light by Si waveguide.

From the observation overall loss with Er:SRN on top is too high and, therefore, even with the Si waveguide of loss of 2.5 dB/cm no light was observed from bended waveguide which was consistent to the previous observation from the high loss waveguide samples. The conservative estimation of the loss from the dips in transmission spectrum is over 20 dB/cm which is way too large considering the gain level we can achieve from our Er:SRN based on the basic material parameters used in the chapter 5. We suspect that the overall

quality of the sputtered Er:SRN film, the interface between Si waveguide and Er:SRN film, the surface of Er:SRN affected the loss adversely [8]. From our previous member's experience (Sajan Saini's MIT Ph.D. Thesis), we learned that materials loss of sputtered nitride is measured to be larger than 20 dB/cm using a prism coupler set-up [10]. This result is quite consistent with the estimation above. However, several members (Sajan Saini and Jessica Sandland) observed 0.7~2 dB/cm from the sputtered SiON (from cosputtering and reactive sputtering) [10,11]. Intrinsic material loss is affected by many factors such as bond vibrations (e.g. absorption by N-H bond, Si-H bond, etc), absorption by dangling bonds, and film irregularities. To achieve much smaller loss from Er:SRN we need to consider other deposition tools like PECVD with which microstructural issues such as columnar structure and large volume of voids can be avoided. Alternatively we may investigate Er doped silicon rich oxynitride as candidate material.

6.5. Conclusion

From the loss measurement it was revealed that nitride was detrimental in causing extra loss. It is expected to be caused by the N-H bonds. Without the lossy nitride cladding layer the overall loss value could be lowered down from 8 dB/cm to 2.5 dB/cm. Further improvement can be expected under a better smoothening process. This process includes, but is not limited to, wet treatment to smoothen the upper corners of the waveguides. Lower corners can be smoothened out by etching the underneath oxide a little bit further down and then treating with wet chemicals discussed in section of 6.3.4. Ridge waveguide can be also considered as an alternative to avoid this issue of sharpness at the bottom corners. By

having shorter oxidation time a ridge waveguide structure can be fabricated and it can be expected to provide a better coupling even with large gaps between the bus and ring waveguides.

Gain measurement was performed with the sample of Er:SRN on Si resonator structure with 1480 nm pumping source. However, due to large loss from the sputtered Er:SRN, the measurement was not completed successfully. Therefore, achieving the Er:SRN gain material with low loss is a prerequisite for further investigation on the gain related phenomena.

6.6. References

[1] T. Barwicz, M.A. Popovic, P.T. Rakich, M.R. Watts, H.A. Haus, E.P. Ippen, and H.I. Smith, Opt. Exp. **12**, 1437 (2004).

[2] B. E. Little, S. T. Chu, H. A. Haus, J. Foresi, and J.-P. Laine, J. IEEE J. of Lightwave Tech. **15**, 998 (1997).

[3] C.K. Madsen, G. Lenz, A.J. Bruce, M.A. Capuzzo, L.T. Gomez, T.N. Nielsen, and I. Brener, Opt. Lett. **24**, 1555 (1999).

[4] S. J. Choi, Z. Peng, Q. Yang, S. J. Choi, and P. D. Dapkus, IEEE Photonics Tech. Lett. **16**, 356 (2004).

[5] V. R. Almeida, C. A. Barrios, R. R. Panepucci, and M. Lipson, Nature **43**, 1081 (2004).

[6] Apollo software (Apollo Photonic Software Suite) was used for the device simulation in this chapter. It is a commencial design tool for photonic integrated circuits (PICs), and based on Object Oriented Design Flow (OODF).

[7] I. Kiyat, A. Aydinli, and N. Dagli, Opt. Exp. **13**, 1900 (2005).

[8] H. A. Haus, *Waves and Fields in Optoelectronics,* Prentice-Hall, NJ (1984).

[9] Daniel K. Sparacin, “Process and Design Techniques for Low Loss Integrated Silicon Photonics”, Ph.D. Thesis, Massachusetts Institute of Technology (2006).

[10] Sajan Saisi, “Gain Efficient Waveguide Optical Amplifiers for Si Microphotonics”, Ph.D. Thesis, Massachusetts Institute of Technology (2004).

[11] Jessica G. Sandland, “Sputtered Silicon Oxynitride for Microphotonics: A Materials Study”, Ph.D. Thesis, Massachusetts Institute of Technology (2005).

Chapter 7. Optical and electrical excitation of Er

7.1. Introduction

To achieve light emitting device with Er based dielectric material as an active layer, Er should be able to be excited electrically. Thus, the understanding of the related phenomena is required at this moment. We fabricated light emitting devices with the Er:SRN active layers prepared with the optimized process conditions in chapter 5. Electrical properties have been investigated by varying the stoichiometry of the Er:SRN emitting layer. Detailed comparison with optical excitation of Er was provided and discussed for better understanding and fabrication of the Er:SRN based electrical devices. The role of Si-nc's in optical and electrical excitation of Er was discussed also for this purpose. The gain related issues based on simulation with rate equations was investigated to find out what criteria have to meet in order to achieve the electrically injected Si-based laser device.

7.2. Electrical properties of Er:SRN

We fabricated Er:SRN based light emitting device by varying stoichiometry to investigate the electrical properties. The device structure is given in fig. 7.1. The detailed process conditions and parameters for the electrodes were described in chapters 4 and 5.

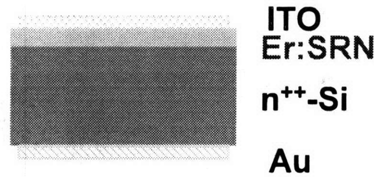

Figure 7.1. Schematic diagram of the Er:SRN light emitting device.

As shown in chapter 5, Si content strongly affected the Er sensitization role of SRN matrix and changed the Er emission intensity accordingly. When we varied Si content in the Er:SRN layer, I-V characteristics were changed dramatically as in fig. 7.2. When we have too much silicon in Er:SRN, we have almost linear I-V characteristics with high current density due to reduced insulating property with the increased silicon content (Magenta line in fig. 7.2 (b)). However, from the Er:SRN grown only with Er and Si_3N_4 targets, we could not get any current injection since it was too much insulating (Not shown here). Intermediate Si contents resulted in diode-like behaviors and also the current levels between the two extreme cases mentioned above. Therefore, controlling the Si content properly is significantly essential to achieve high current density level to inject many carriers and also diode behavior for the injection of electron and hole [1, 2]. With intensive optimization processes including growth conditions of Ar flow and target power for Si, Er, and Si_3N_4, we could achieve reasonably high current density level (~ mA/cm^2) and strong photoluminescence intensity similar to that of the optimized Er:SRO as in fig. 7.3 (Si_3N_4 power: 500W, Si: 100W, Er: 10W, Ar flow: 7.2 sccm, annealed at 900°C for 10 min) [3].

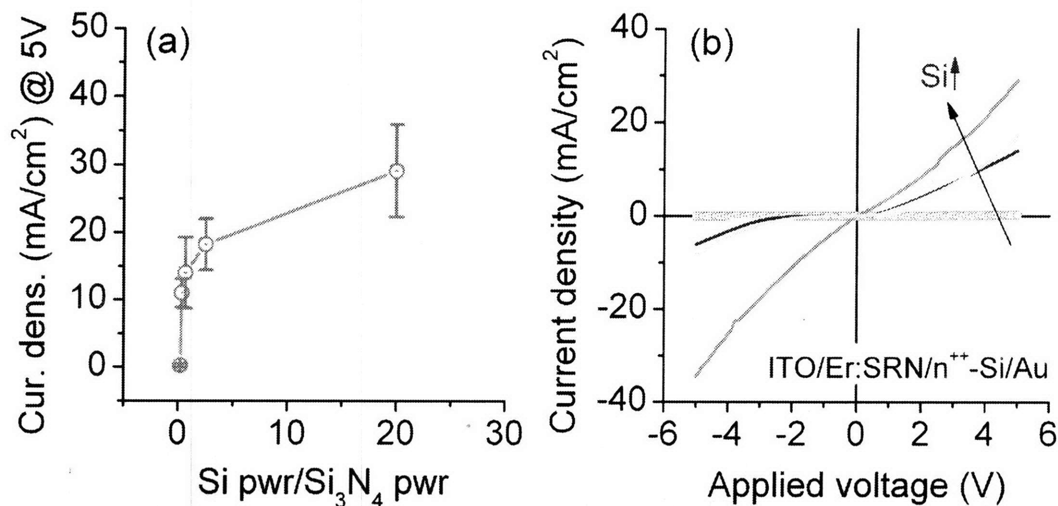

Figure 7.2 (a) Current density at 5V of the Er:SRN devices with varied Si content. The detailed information on Si content can be found in chapter 5. (b) I-V characteristics of the corresponding Er:SRN devices. We can clearly observe the increased current density with the Si content.

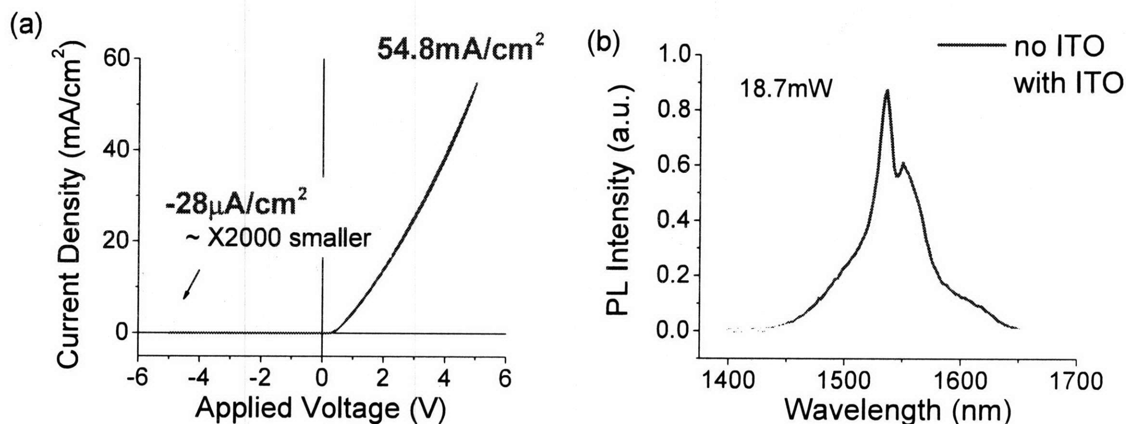

Figure 7.3 (a) I-V characteristics of the optimized Er:SRN device. (b) Photoluminescence from the same sample with and without ITO electrode.

7.3. Electrically injected light emitting device and electroluminescence

With the optimized Er:SRN devices described in section 7.2, we investigated

electroluminescent properties. Fig. 7.4 (a) shows the electroluminescence set up for EL image with the CCD camera and fig. 7.4 (b) the set up for EL spectrum with spectrophotometer. Set up is equipped with probe tips, sample stage, power supply, current meter, CCD camera, and photospectrometer. We used the same photospectrometer which was used for photoluminescence study.

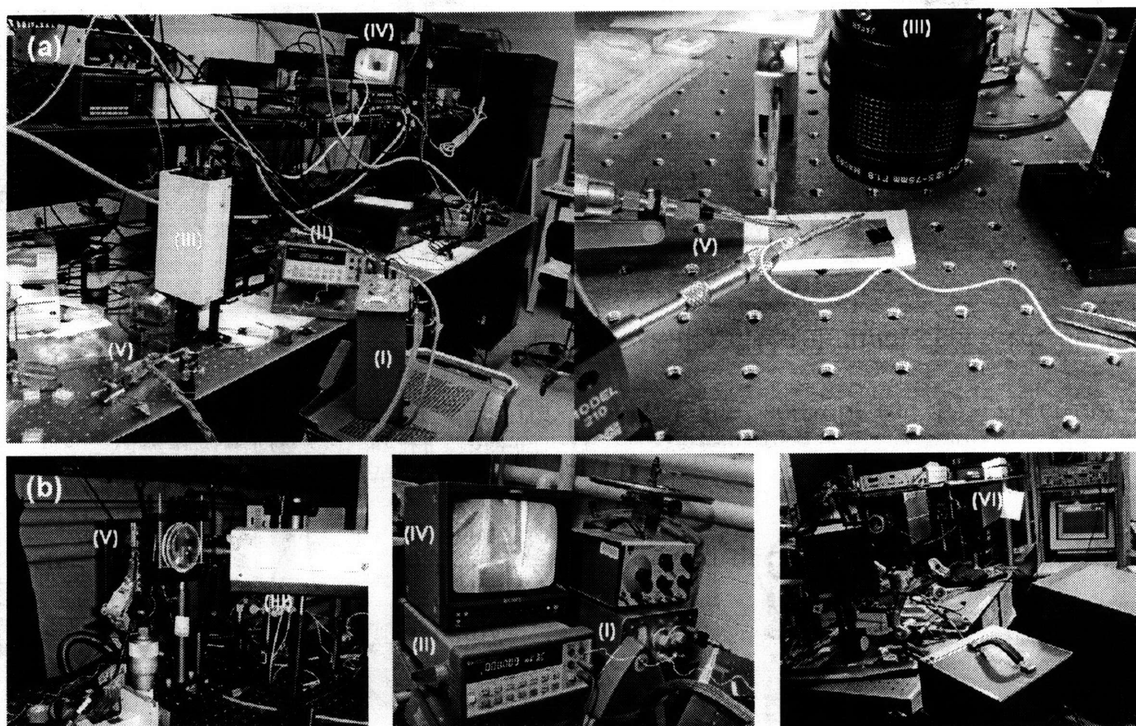

Figure 7.4 (a) Electroluminescence set up for EL image: Power supply (I), Multimeter (II), CCD Camera (III), Monitor (IV), and Probe tips (V). (b) Electroluminescence set up for spectrum: Power supply (I), Multimeter (II), CCD Camera (III), Monitor (IV), Probe tips (V), and Photomultiplier (VI).

When we applied low voltage less than 30 V, we could not get any light emission. However, when it reached 30 V we observed light emission through CCD camera as shown in fig. 7.5 (c). We also obtained electroluminescence spectra with photospectrometer at the

other side of the set up as in fig. 7.5 (b). Even though we used the samples grown with the same condition except the total thickness of Er:SRN layers, we obtained totally different electroluminescent spectra.

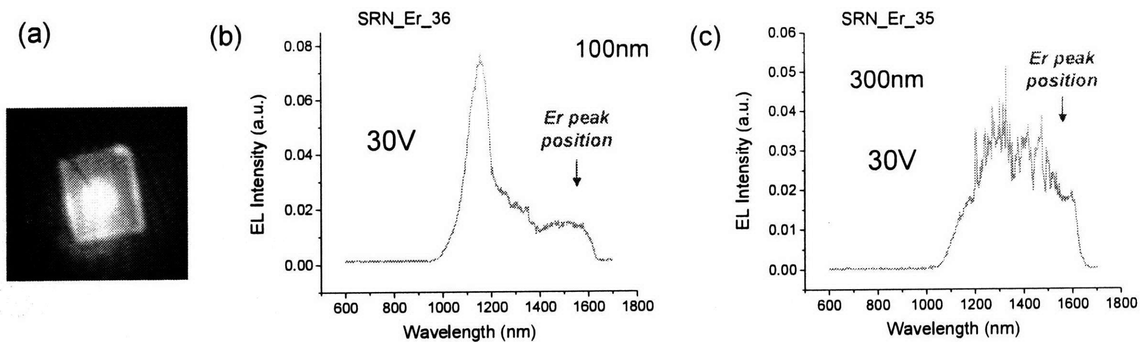

Figure 7.5 (a) Electroluminescence spectrum from the optimized Er:SRN with thickness of 100 nm (b) of 300 nm (c) light emission from the sample taken by CCD camera

From the electroluminescence spectra we observed Si emission, defect-related emission without Er emission at 1.54 μm. Why is the electrical excitation of Er so difficult compared to optical excitation of Er as in chapter 5 even though we optimized I-V characteristics and photoluminescence simultaneously? In the following section 7.4 we provided the detailed comparison between optical and electrical excitation of Er and the discussion of the difference.

7.4. Detailed comparison and analysis of optical and electrical excitation of Er

Before discussing the difference of the two excitation schemes in detail, let's remind ourselves on the optical excitation mechanism which is somewhat well known. When the Er atoms are excited directly by optical pumping, the pump wavelength should be resonant

with the atomic levels of Er as in the fig. 5.6. In this case the effective excitation cross section of luminescence at a pumping wavelength of 488 nm is very small, ~ 10^{-21} cm^2 level (Table 7.1). However, when there are energy sensitizers such as Si-nc's or defects in the dielectric matrix, the situation is changed significantly. As in fig. 7.6, excitation of Er^{3+} ion is generated by energy transfer from e-h pairs which are excited in the Si-nc by optical pumping: the overall efficiency of luminescence at 1.535 μm through direct absorption in the Si-nc is given by an effective excitation cross section σ_{exc} of Er^{3+} ion. The excitation cross section value for the Er in SRO (Si-nc embedded SiO_2) is around five orders higher (~ 10^{-16} cm^2) than that of direct excitation (Table 7.1). That is, Si-nc's are helpful in exciting the Er atoms optically. On the contrary it should be noted that effective excitation cross section value of the electroluminescence for direct excitation of Er in SiO_2 is very high (~ 10^{-14} cm^2). This information is helpful for the discussion of excitation efficiency in the following paragraphs.

Table 7.1. Cross section values for the Er in SiO_2, Er in Si, and Er in SRO (Si-nc embedded SiO_2) [4~8].

		Er in SiO_2 (cm^2)	Er in Si (cm^2)	Er in Si-nc (cm^2)
Effective excitation cross section of luminescence at a pumping wavelength of 488 nm		$1\text{-}8 \times 10^{-21}$	3×10^{-15}	$1.1\text{-}0.7 \times 10^{-16}$
Effective excitation cross section of electroluminescence	σ_{exc}	1×10^{-14} (from other ref.)	4×10^{-14}	1×10^{-14} by impact ionization
Emission cross section at 1.535 μm	σ_{em}	6×10^{-21}		2×10^{-19}
Absorption cross section at 1.535 μm	σ_{abs}	4×10^{-21}	2×10^{-20}	8×10^{-20}

"Si-nc's helpful!"
(Optical exc.)
Electrical excitation
is efficient!

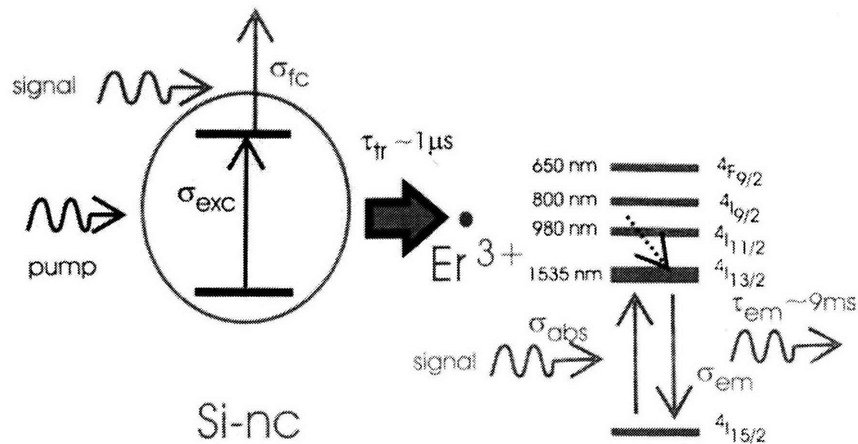

Figure 7.6. Schematic diagram of the excitation process of Er^{3+} ions via a Si-nc, with the main related cross sections. On the left, the main internal energy levels of the Er^{3+} are shown [9].

To find out the main reason why electrical excitation of Er is so different from optical excitation we can look into the efficiency equation closely. Based on the following equation of photoluminescence intensity we see that $\sigma\tau$ value should be large to get high efficiency. Considering that lifetime τ only changes a little (or just an order at maximum, from msec to hundreds of μsec range) by incorporating Si-nc into the SRN but σ changes by more than several orders (from 10^{-21} cm^2 to 10^{-15} cm^2, for example), efficiency change is mostly determined by the change of σ.

$$PL = PL_{\max} \frac{\sigma\tau\phi}{\sigma\tau\phi + 1}$$

Therefore, when there are sensitizers like Si-nc's in SRN, luminescence efficiency can be much higher than the case of direct Er excitation. These processes of optical excitation are

described in detail in fig. 7.7.

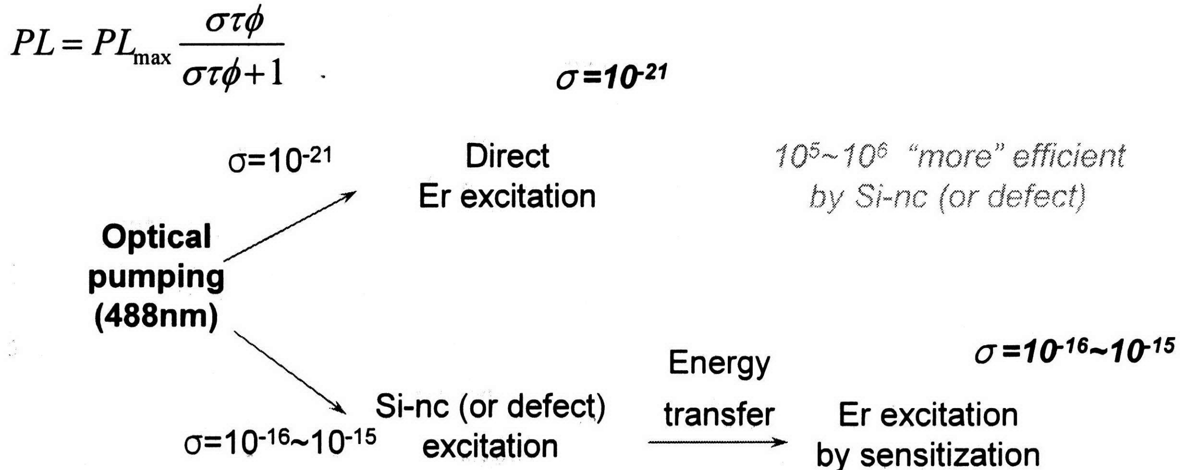

Figure 7.7. Schematic diagram of optical excitation processes of Er in dielectric matrix.

Contrary to the optical excitation of Er, the direct excitation cross-section of Er is very large (10^{-14} cm^2). This leads to extremely different situation for the Er excitation mechanism. When there are Si-nc's or defects, this value becomes smaller or approaches to zero (because the excitation of Er is not possible if the carriers are captured by defects). Therefore, overall efficiency inevitably becomes low. Especially, if the defects kill the injected carriers, Er excitation is not possible. Presence of Si-nc's or defects which are helpful in sensitizing the Er atoms in optical excitation case is detrimental to electrical excitation. The detailed processes are described in fig. 7.8. When there are silicon

nanocrystals in the matrix, direct tunneling between the nanocrystals increase. Therefore, energy of hot electron decreases to low value to contribute to Er excitation and also the interaction with Er atoms will decrease. Trapped electrons in silicon nanocrystals repulse incoming electrons by Coulomb force with large cross section and it leads to smaller average energy of the incoming electrons and also to the lower Er excitation cross section.

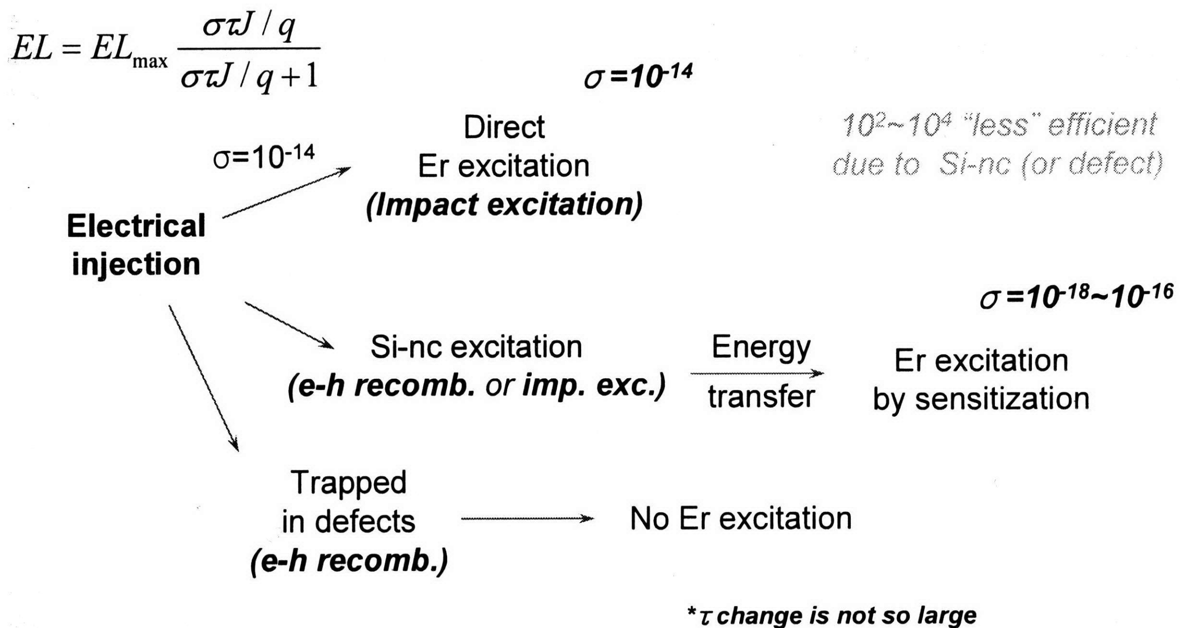

Figure 7.8. Schematic diagram of electrical excitation processes of Er.

As a summary, fig. 7.9 shows the optical and electrical excitation processes of Er altogether for easier and detailed comparison. We can clearly see and compare the main difference of two excitation processes. That is, the direct excitation cross-section values for electrical excitation and optical excitation are so different (10^{-14} vs. 10^{-21} cm^2). The direct

optical excitation cross-section is much smaller than that with Si-nc's (or defects) serving as energy sensitizers by 5~6 orders. For electrical excitation case, however, the direct excitation itself is much efficient based on the very large excitation cross-section of 10^{-14} cm^2. When there are Si-nc's or defects, excitation cross-section values become much smaller by 2~4 orders. Furthermore, with defects in the matrix, if the injected carriers can be annihilated at these sites, Er excitation is not possible. Conclusively Si-nc's or defects in the dielectric matrix are very helpful for Er sensitization in optical excitation. However, they are not helpful in electrical excitation case in increasing efficiency. At this moment readers may question why the direct electrical excitation itself of Er atoms is so efficient compared to that of optical excitation? First, wide distribution of hot electrons in their energy spectra considerably improves the excitation efficiency compared to narrow distribution of photons in monochromatic laser [10]. Electrons with higher energy than certain Er atomic level can excite the Er atoms. One electron can excite many Er atoms with multiple impacts if it has very high energy. Second, momentum of electrons is larger than that of photons, and thus electrons excite vibrational transitions of the luminescent Er more efficiently. It would lead to larger oscillator strengths [11, 12]. Even when optical pumping wavelength is matching with one of the Er atomic levels, photon can not excite vibrational transitions efficiently because of much smaller momentum compared to electron.

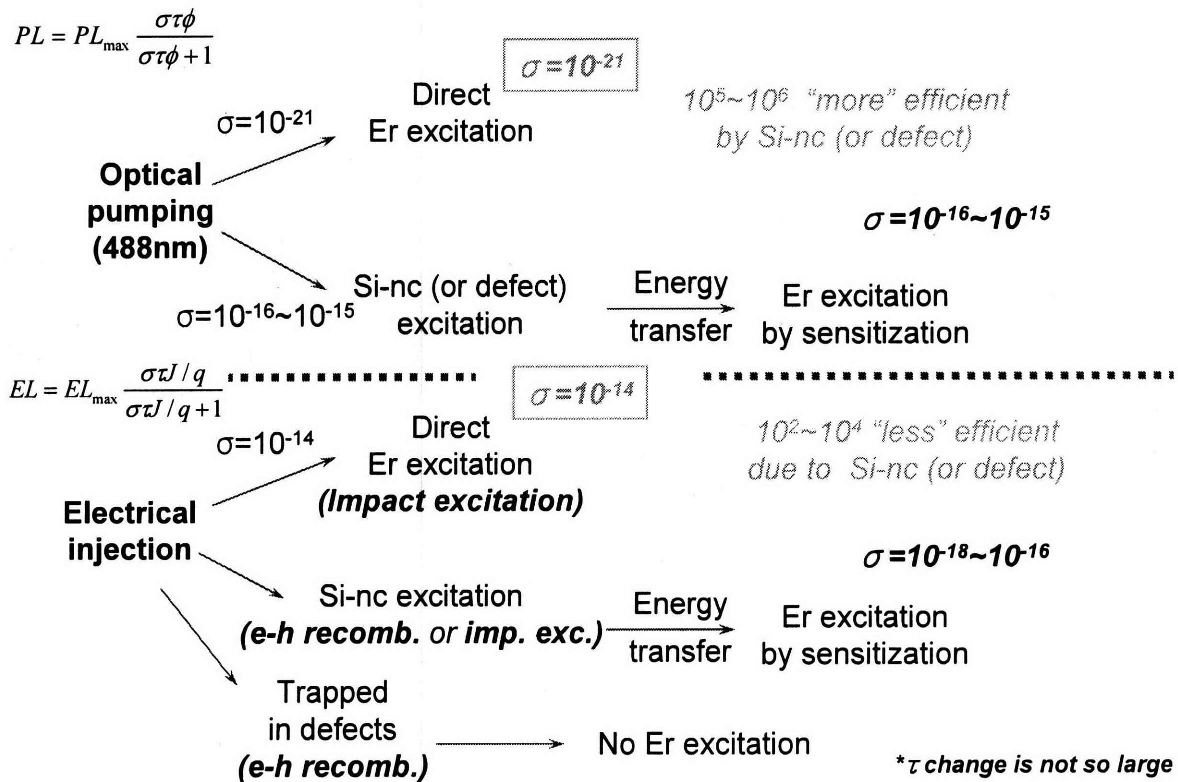

Figure 7.9. Detailed summary of optical and electrical excitation processes of Er.

Discussion in this section is significantly essential in realization of the electrically injected Er based light emitting devices since we now know that those processes should be regarded in totally different ways.

7.5. Alternative approach for Er excitation by electrical injection

Since Er excitation by electrical injection was not achieved from our device structure given in section 7.1 (We only observed electroluminescence from silicon or defects) and we figured out that utilization of impact excitation (direct excitation of Er) would be better for electrical Er excitation, we considered the following structure in fig. 7.10 for improvement.

With increased energy of electrons by acceleration layer we expect Er atoms to be excited by impact excitation.

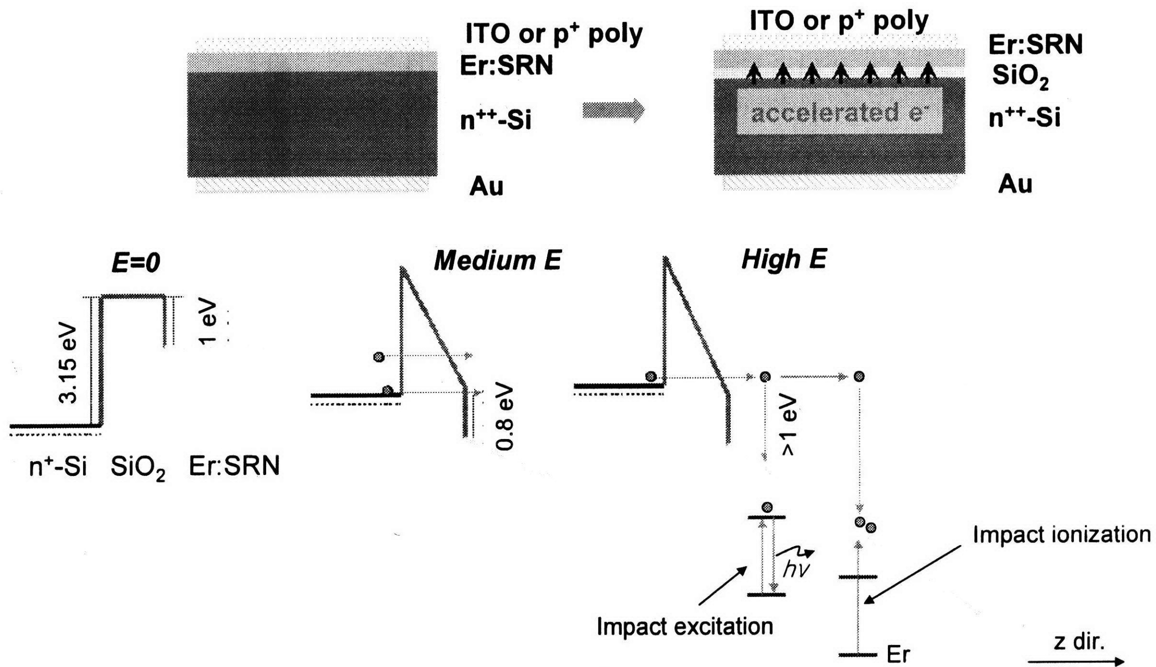

Figure 7.10. Suggested acceleration structure to utilize impact excitation of Er. This structure contains SiO_2 acceleration layer to make electron to be accelerated to have high enough energy to excite Er atoms. The top left schematic diagram shows the old structure and the top right diagram shows new structure. The energy band diagrams on the bottom show how energy band changes when the applied electric field increases.

We calculated number of hot electrons for the kinetic energy in z direction with the thickness of acceleration layers varied. The z direction here is along the vertical direction of the device. Total kinetic energy is equal to or larger than the kinetic energy in z direction. We learned that larger kinetic energy can be achieved with thicker acceleration layer. However, as in right figures in fig. 7.11, current density levels are smaller for thicker

acceleration layers at certain voltage. The voltage here is additional voltage needed only for acceleration layer. Therefore, the total voltage to be applied to the device is expected to be higher.

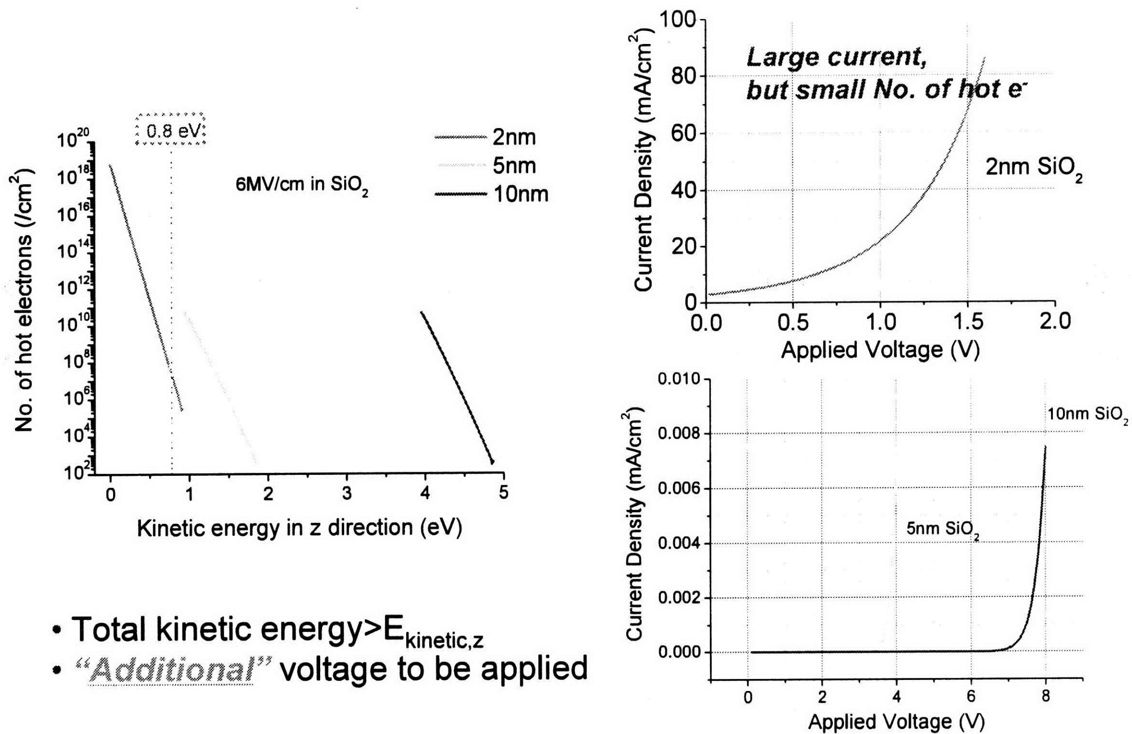

Figure 7.11. Number of hot electrons with the certain kinetic energy in z direction by varying acceleration layer thickness. Current density vs. applied voltage for varied acceleration layer thickness (2, 5, and 10 nm)

Based on the calculation we fabricated acceleration device with the thermal oxide thickness of 2, 5, and 10 nm (Device structure as in fig. 7.10) and also the device without oxide layer for parallel comparison. However, we could not obtain the current levels with oxide thickness which was expected to show a certain trend with thickness (The thicker, the

lower). Current levels were quite random rather than in trend. We strongly suspected the sputtering process of the Er:SRN might have damaged the thermal oxide below because the rf power is so high (500 W) and physical ion bombardment can damage underlying oxide layer, oxide here. Although we prepared more samples with the oxide thickness of 20, 50, and 100 nm expecting the damaged layer thickness is constant for all the samples so that the remaining oxide thickness contributes as effective oxide thickness showing a clear trend in current level vs. oxide thickness, we could not observe clear trend with oxide thickness, with these samples, either. To confirm the trend of the current level with oxide thickness we prepared Au/SiO_2 (varied thickness)/n^+ Si structures with the oxide thicknesses of 0, 2, 5, 10, 20, and 100 nm. Fig. 7.12 shows the current level at the applied voltage of 5 V and we could clearly observe the current levels are reasonably in trend.

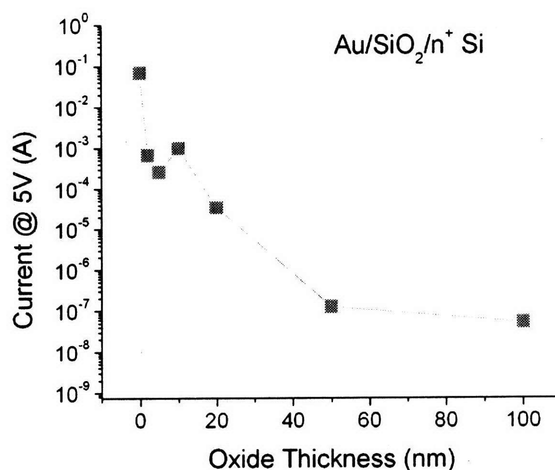

Figure 7.12. Current at the applied voltage of 5 V with the oxide thickness of 0, 2, 5, 10, 20, and 100 nm. The device structure used here is Au/SiO_2 (varied thickness)/n^+ Si.

Based on the experimental results, damage of the oxide layer by sputtering of Er:SRN

should be avoided. Changing the growth condition of Er:SRN is not an option here because we want to adopt the Er:SRN layer with the conditions optimized so far. We suggest to invert the structure to have the oxide layer on top of the sputtered Er:SRN layer (Fig. 7.13) to avoid damage of oxide layer during sputtering process of Er:SRN. However, for this structure we can not use (high quality) thermal oxide because oxidation needs the Si below. Therefore obtaining the high quality oxide with other process is a prerequisite. We have investigated the sputtered oxide and PECVD oxide for this purpose. However, sputtered oxide and PECVD oxide did not provide reasonably good trend of current levels as thermal oxide did as in fig. 7.12. Therefore, we could not fabricate the acceleration device structure successfully which works with effective acceleration function. From some of the devices fabricated above so far, we could observe electroluminescence spectra similar to those in fig. 7.5. That is, spectra without Er peak, but with many other peaks related with defects. It is obviously expected because acceleration layer could not work effectively and, therefore, the devices were virtually without acceleration layer. However, we believe the electrical Er excitation can be done with acceleration scheme if 1) mild growth condition of Er:SRN by other growth method and 2) the inverted structure of the high quality oxide on Er:SRN are available.

Original structure

Alternative structure

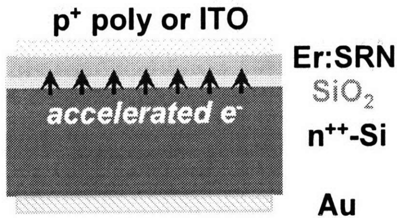

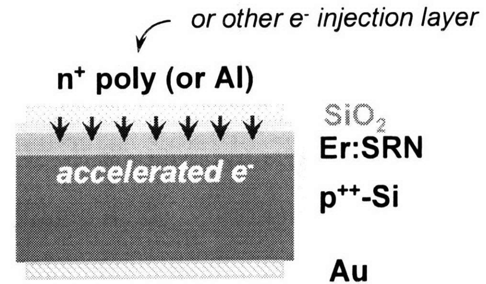

Figure 7.13. Original acceleration structure and alternative structure with inverted sequence.

7.6. Discussion on gain related parameters with electrical pumping

Compared to gain related phenomena with optical pumping (see section 5.5), gain related phenomena with electrical pumping should be regarded in different way since the excitation mechanism is totally different as discussed in section 7.4.

We built up rate equations based on the two level system of SRN sensitizer and Er atom as we did in chapter 5 except the fact that excitation is by electrical pumping. Fig. 7.14 shows the two level systems we consider here. This two level system can represent many level systems well enough with simplified calculation [13] since the most significant processes are the excitation through the energy transfer from the sensitizer and the processes related with the second excited state ($^4I_{13/2}$ level) of Er such as cooperative upconversion, excitation through energy transfer from sensitizer, etc. The rate equations we adopted here are also given next to fig. 7.14.

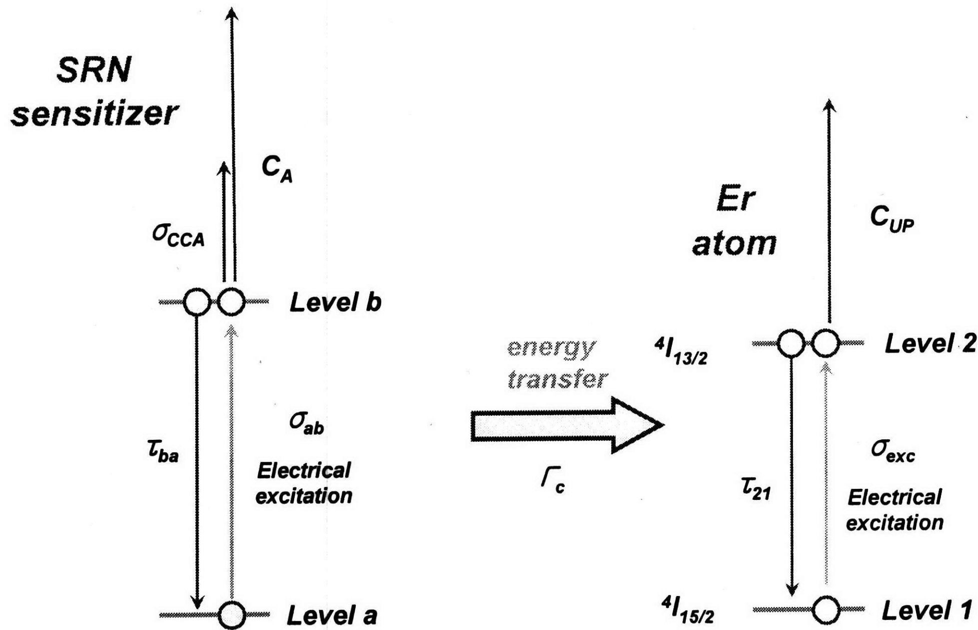

Figure 7.14. Two level systems for SRN sensitizers and Er atom.

$$\frac{dN_b}{dt} = \sigma_{ab}^{elec}\Phi_p N_a - \frac{N_b}{\tau_{ba}} - \Gamma_c N_b N_1 - 2C_A N_b^2$$

$$\frac{dN_2}{dt} = \sigma_{exc}^{elec}\Phi_p N_1 - \frac{N_2}{\tau_{21}} + \Gamma_c N_b N_1 - 2C_{UP} N_2^2$$

Table 7.1. Parameters and values used in the simulation for electrical excitation of Er in SRN matrix.

Parameter	***Value***	***Notes***
[Er]	5.0x10^{20} cm^{-3}	
[Sensitizer]	6x10^{18} cm^{-3}	
Γ_c	1.0x10^{-12} cm^{3}s^{-1}	SRN → Er coupling coefficient
σ_{exc}^{elec}	1.0x10^{-14} cm^2	Er excitation cross section (Electrical)
τ_{21}	0.5 ms	Er emission lifetime (measured)

σ_{ab}^{elec}	$1.0\text{x}10^{-18}$ cm^2	Excitation cross section of sensitizer
τ_{ba}	$1.0\text{x}10^{-6}$ sec	Sensitizer emission lifetime
C_A	$1.0\text{x}10^{-13}$ cm^{3}s^{-1}	Coefficient for Auger recombination in sensitizer
C_{UP}	$3.0\text{x}10^{-18}$ cm^{3}s^{-1}	Coefficient for cooperative upconversion in Er
σ_{Er}	$3.5\text{x}10^{-20}$ cm^2	Er emission cross section
α_{tot}	5 cm^{-1}	total loss

The parameters given above are representative values and they were varied in our simulations. Some are experimental values, but others are based on assumptions. However, in a later simulation we will demonstrate that many of the parameters above do not affect the final result significantly. Therefore, it is not necessary to have experimental values for all simulation parameters.

This simulation was performed not in order to obtain exact values. The aim of this simulation was to examine the general trend in the parameters, find out how much those parameters contribute to gain by electrical excitation, and to compare the trend with optical excitation that was discussed in chapter 5.

7.6.1. Effect of loss

Loss values were varied to see how large a current density would be needed to overcome loss to achieve net gain. Fig. 7.15 (a) shows that net gain is possible even with a loss of 10 cm^{-1}. However, gain value was smaller when the loss is larger. Furthermore, the threshold current density for net gain increases with loss value. Fig. 7.15 (b) clearly shows how much increase in current density is needed with increased loss value.

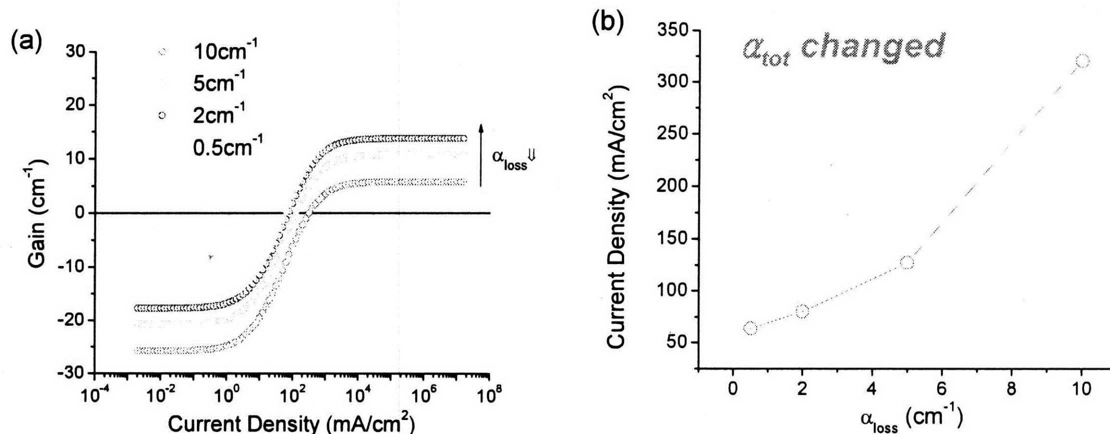

Figure 7.15 (a) Gain vs. current density (b) Threshold current density for net gain with varied loss values of 0.5, 2, 5, and 10 cm^{-1}

Clearly high current density is needed to overcome large loss value. It should be noted that this current density values are quite high, considering the assumption that ideal injection of the carriers took place without any leakage. As the current density level with an acceleration structure was on the order of ~μA/cm^2, this level of current density is not easy to achieve using an acceleration structure.

7.6.2. Dependence on Er concentration

We wanted to see how high gain we can achieve with the increased Er concentration and how much current density we need to pump up the increased number of Er atoms. The representative experimental Er concentration in Er:SRN we could get from our experiment was mid 10^{20} cm^{-3}, which is not the concentration of optically active Er. This value is considered the hypothetical upper limit for the optically active Er atoms. When we

increased Er concentration, we needed higher current density to get all the Er atoms excited (Fig. 7.16 (a)).

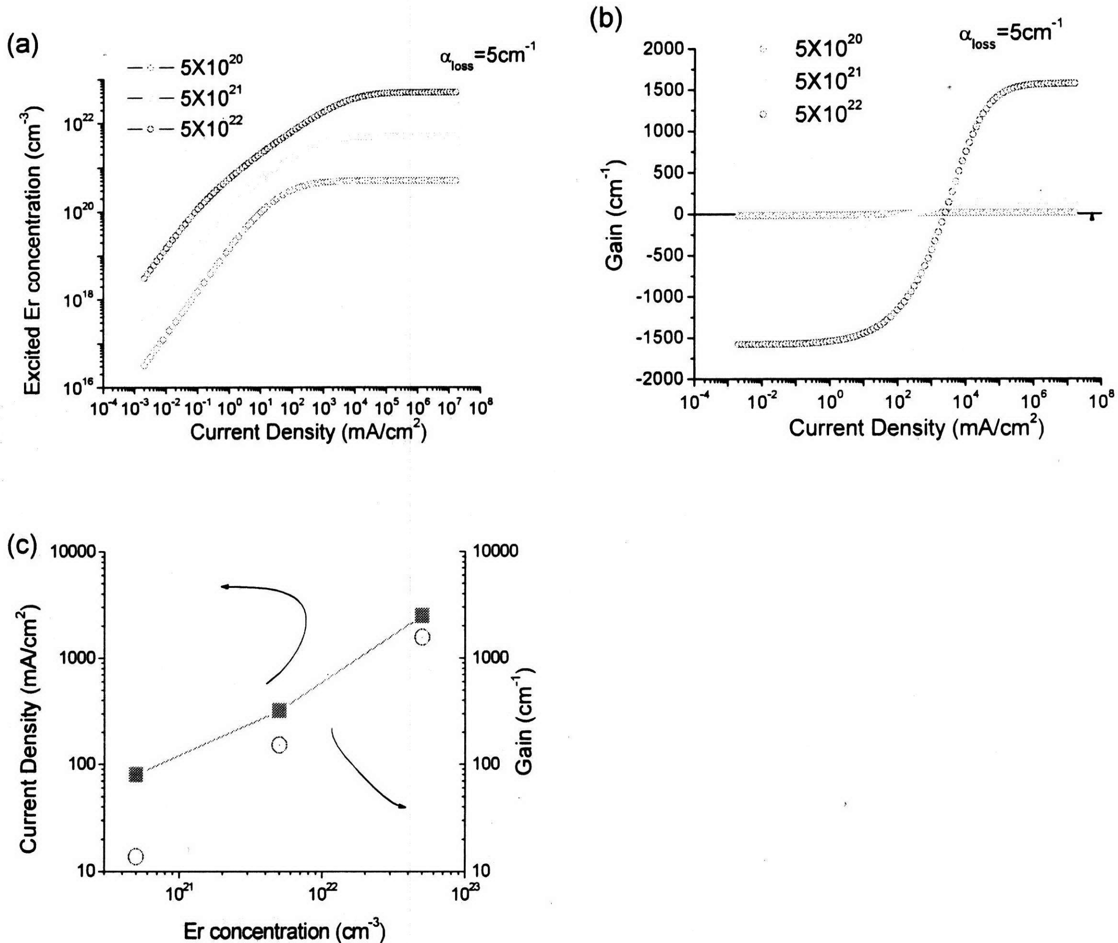

Figure 7.16 (a) Excited Er concentration and (b) gain with current density varied for Er concentration of $5x10^{20}$ cm^{-3}, $5x10^{21}$ cm^{-3}, and $5x10^{22}$ cm^{-3} (c) Threshold current density for net gain and the maximum gain value achieved with Er concentration varied.

Fig. 7.16 (b) more clearly shows higher current density is needed to achieve net gain for higher Er concentration. However, the maximum gain achievable increases with Er

concentration. The whole situation was summarized in fig. 7.16 (c). Although the fact that higher gain value is achievable with higher Er concentration is promising, the current density level (~ A/cm^2) needed was so large considering the leakage behavior of nitride matrix. To overcome large loss value of the matrix we may need high Er concentration of 10^{21} or 10^{22} cm^{-3}. Further investigation is needed to achieve high Er concentration in silicon nitride matrix or to find out alternative Er doped materials affording high Er concentration is possible.

7.6.3. Importance of upconversion coefficient

If upconversion coefficient is high, it's very hard to keep the excited Er level high. As we can see in fig. 7.17 (a), making the excited Er level high with high upconversion coefficient is difficult. Therefore, higher current density is needed. More importantly, as in fig. 7.17 (b), maximum gain value did not change with upconversion coefficient changed. Threshold current density for net gain decreased with lowering upconversion coefficient value. However, it did not decrease without limit. It saturated to a certain value. Fig. 7.17 (c) clearly shows the situation of saturation. The saturated value is at the level of tens of mA/cm^2 level. From this result, it can be inferred that, even if some material with very low upconversion coefficient can be found, the current density level has to be high enough. Therefore, injection property is still important.

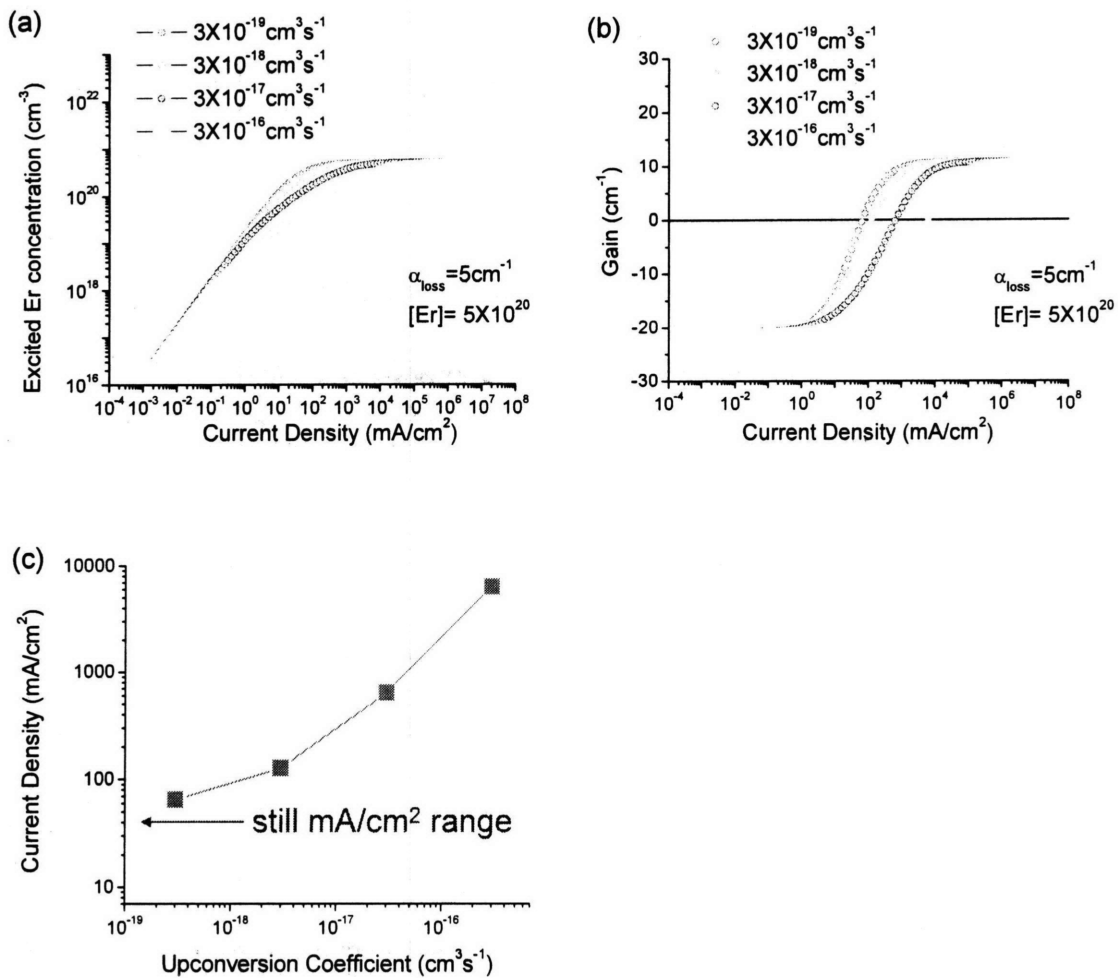

Figure 7.17 (a) Excited Er concentration and (b) gain with current density for the upconversion coefficient of $3x10^{-19}$ cm^3s^{-1}, $3x10^{-18}$ cm^3s^{-1}, $3x10^{-17}$ cm^3s^{-1}, and $3x10^{-16}$ cm^3s^{-1} (c) Threshold current density for net gain with the upconversion coefficient varied.

7.6.4. Effect of coupling

The coupling coefficient represents the amount of energy transfer from SRN matrix to Er atoms. That is, it shows the contribution from the SRN matrix including Si-nc's or Si related states which can work as Er sensitizers. However, fig. 7.18 shows there is no change in excited Er concentration and gain at all even when coupling coefficient was varied in a

wide range. This is easily understandable as Er excitation by direct impact excitation is efficient enough with a cross section value of 10^{-14} cm^2. Therefore, even a strong coupling between sensitizer and Er atom does not have any appreciable effect due to poor sensitizer excitation efficiency with much lower excitation cross section. Furthermore, if there are defects that annihilate injected carriers, sensitizer excitation efficiency becomes even lower. This was the main difference from optical excitation where direct Er excitation was inefficient with a cross section value of 10^{-21} cm^2 [14]. Conclusively, contribution from the sensitizers in SRN matrix can not be regarded as being significant. On the contrary, in chapter 5, we observed that optical excitation resulted in a strong change in maximum achievable gain, excited states population of Er atoms, and excited states population of sensitizers with coupling coefficient due to the efficient excitation of the sensitizer followed by transfer of energy to Er atoms.

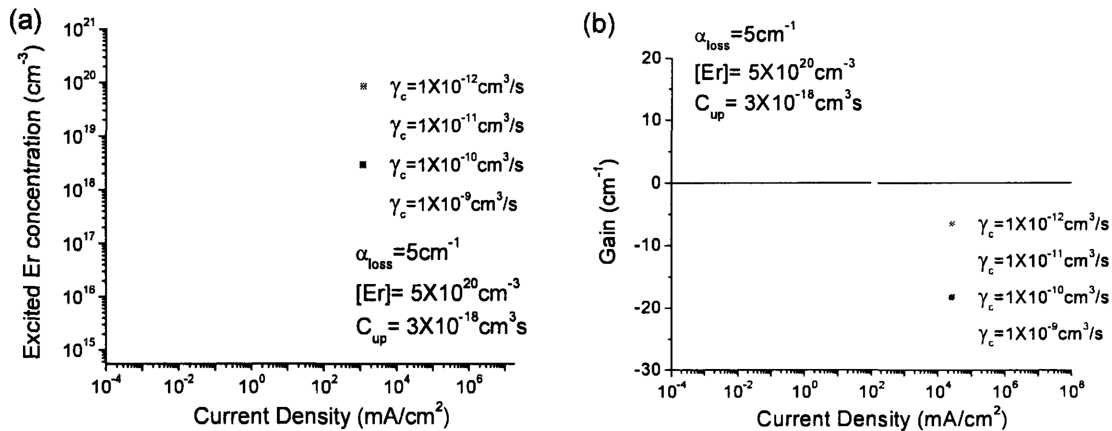

Figure 7.18 (a) Excited Er concentration and (b) gain with current density changed for coupling coefficient of 1×10^{-12} cm^{3}s^{-1}, 1×10^{-11} cm^{3}s^{-1}, 1×10^{-10} cm^{3}s^{-1}, and 1×10^{-9} cm^{3}s^{-1}. All the curves are overlapped to one curve.

We also could not observe any contribution from the SRN sensitizer by varying the sensitizer density. While the sensitizer density value was varied from $1x10^{16}$ cm^{-3} to $1x10^{20}$ cm^{-3}, the final simulation results have not changed. That is, Er excited states population and the threshold current density for net gain have not changed with the increase of the sensitizer density. It is easily understandable from the fact that the direct excitation of Er by electrical pumping is highly efficient. Therefore, contribution by energy transfer from sensitizers can be regarded to be minor. However, as discussed in section 5.5.3, the direct optical excitation cross section of Er is on the order ot ~ 10^{-21} cm^2 which is approximately 5~6 orders smaller than that of the sensitizer. Therefore, contribution to Er excitation from optically pumped sensitizer in Er excitation is significantly large by energy transfer processes (Refer to section 5.5.1 for detailed information regarding the effect of sensitizer density.).

7.6.5. Excitation cross section

Importance of excitation cross section was investigated. As we can see in fig. 7.19 (a), large decrease in the current density to achieve maximum excited Er concentration was observed as excitation cross section value increased from $1x10^{-16}$ cm^2 to $1x10^{-13}$ cm^2. Accordingly the threshold current density needed to achieve net gain increases as the excitation cross section value decreases. However, the achievable maximum gain was not changed with excitation cross section values increased. Based on the result, it is considered to be important to have high cross section value to achieve low threshold current density. Fig. 7.19 (c) clearly shows how large current density is needed to achieve net gain when the

excitation cross section is small, for example, $1x10^{-16}$ cm^2.

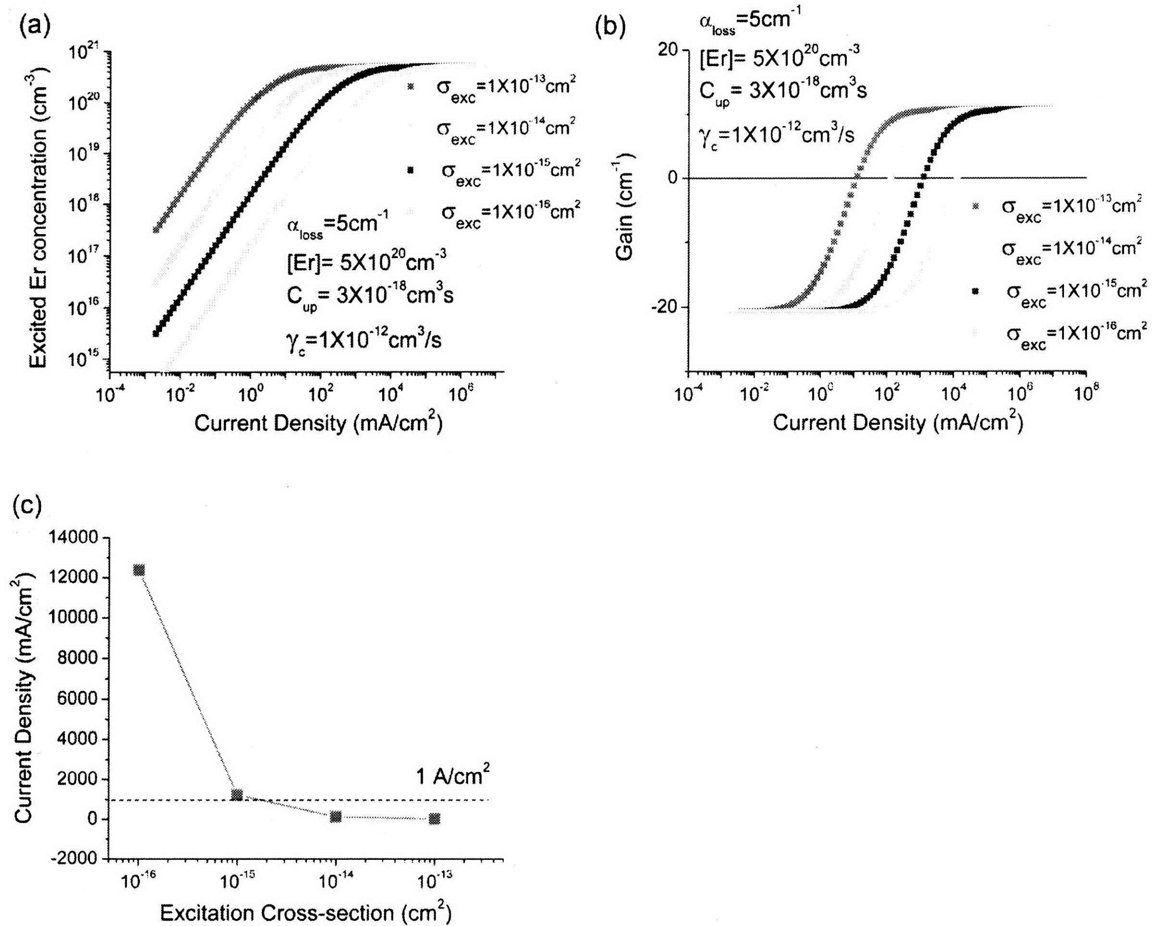

Figure 7.19 (a) Excited Er concentration and (b) gain with current density changed for excitation cross section of $1x10^{-16}$ cm^2, $1x10^{-15}$ cm^2, $1x10^{-14}$ cm^2, and $1x10^{-13}$ cm^2. (c) Threshold current density for net gain with excitation cross section varied.

However, the dependency of the current density on the excitation cross section of sensitizer was negligible. While the excitation cross section value was varied from $1x10^{-16}$ cm^2 to $1x10^{-20}$ cm^2, the final result did not change. This follows from the fact that direct

excitation of Er by electrical pumping is more efficient with a much larger excitation cross section ($1x10^{-14}$ cm^2). In comparison, direct excitation cross section of Er is ~ 10^{-21} cm^2 when optically excited. Therefore, the contribution from the sensitizer in optical Er excitation is strong as shown in section 5.5.3. These investigations clearly suggest that the relationship between excitation cross sections of Er atom and sensitizer is essential in Er excitation mechanism.

In conclusion, we investigated various key parameters important for gain from Er atoms in SRN matrix based on rate equations. From these investigations, we have gained an understanding of the role and importance of each parameter inachieving gain. Having a small loss value is important in order to achieve net gain with small current density. With increased Er concentration we could achieve high net gain, but the current density necessary for such high net gain was also increased dramatically. Having a small upconversion coefficient is important in order to achieve net gain with small current density. However, having small upconversion coefficient does not change the maximum net gain and the minimum level of threshold current density was still high (> tens of mA/cm^2 level). Coupling from the SRN sensitizer to Er atoms is not significant. We could not see any variation of gain and threshold current density even when the coupling coefficient was varied in a large range (3 orders of magnitude). It is because direct Er excitation in electrical injection is much more efficient than the excitation by sensitizers with much smaller excitation cross section. Finally, excitation cross section is of high importance in reducing the threshold current density for net gain. However, interestingly enough the maximum achievable gain value does not change with excitation cross section. Considering

the current density level revealed in the simulation results, the acceleration device structure may not be useful in achieving net gain even though it will be useful in getting electroluminescence from Er:SRN materials.

7.7. Conclusion

To investigate the electrical properties and electroluminescence from the Er:SRN we fabricated light emitting devices. I-V characteristics was dramatically changed with Si content in Er:SRN layer. From the process optimization we achieved strong PL and good I-V with diode behavior. However, from electroluminescence study we only observed Si related peak and defect related peaks without any Er peak from many different samples tried. To explain the phenomena and to find out methods to improve we discussed and compared difference of optical and electrical excitation of Er in detail. The main difference, conclusively, comes from the large difference of direct excitation cross section of Er. In optical excitation of Er the excitation cross section becomes much higher (5~6 orders) with sensitizers in the matrix. However, electrical excitation shows totally different behavior because the excitation cross section for direct impact excitation is already huge (~ 10^{-14} cm^2). When there are defects in the matrix, the injected carriers can be captured and killed without contributing to the excitation of Er atoms. With sensitizers involved in the process, the excitation cross section becomes smaller. Therefore, sensitizers are not helpful in the case of electrical excitation of Er.

To utilize impact excitation we fabricated acceleration structure with thermal oxide as an acceleration layer. However, due to process issues thermal oxide was damaged and could

not contribute as acceleration layer. Experiments to confirm the current level with oxide thickness were done. It was revealed that the deposition of Er:SRN on top of oxide caused the problem. Therefore, the inverted structure having the oxide layer on top of Er:SRN active layer was suggested for future work.

Various key parameters related with gain in Er:SRN material system were investigated based on rate equations with two levels for SRN sensitizer and Er atom. There are following significant deliverables.

(1) With increased loss, higher current density is needed to achieve net gain. (2) With increased Er concentration, higher gain value could be achieved, but higher current density was needed for net gain. (3) With decreased upconversion coefficient we got lower threshold current density for net gain. However, the current density level required was still at the level of tens of mA/cm^2. Maximum gain value was not changed with upconversion coefficient. (4) Coupling coefficient was not important at all in threshold current density and gain value because the direct excitation cross section is already large and coupling from the sensitizers can not contribute further. (5) Threshold current density for net gain was changed dramatically with excitation cross section values. High cross section was needed for small threshold current density. However, maximum achievable gain value was not changed with excitation cross section. (6) Sensitizer density and excitation cross section of sensitizer did not contribute significantly compared to optical excitation case.

The trend of gain values and threshold current densities for gain are important facts that could be discovered from these investigations. A high current density level of more than mA/cm^2 is a conservative estimate of what is needed for net gain. Considering, in

addition, the fact that no leakage current had been assumed in these calculations, it is quite a challenging requirement to be met.

7.8. References

[1] Jae Hyung Yi, Luca Dal Negro, Jurgen Michel, and Lionel C. Kimerling, Materials Research Society, The 2006 Spring Meeting, Apr. 17, 2006, San Francisco, CA, USA.

[2] J. H. Yi, L. Dal Negro, J. Michel, and L.C. Kimerling, Materials Research Society, The 2005 Fall Meeting, Nov. 28, 2005, Boston, MA, USA.

[3] L. Dal Negro, J. H. Yi, M. Stolfi, J. Michel, J. Le Blanc, J. Haavisto, and L. C. Kimerling, 2005 IEEE IEDM (International Electron Devices Meeting) Technical Digest, 40.1.1 (2005).

[4] F. Priolo, G. Franzo , D. Pacifici, V. Vinciguerra, F. Iacona, and A. Irrera, J. Appl. Phys. **89**, 264 (2001).

[5] A. J. Kenyon, C. E. Chryssou, C. W. Pitt, T. Shimizu-Iwayama, and D. E. Hole, J. Appl. Phys. **91**, 367 (2002).

[6] F. Iacona, D. Pacifici, A. Irrera, M. Miritello, G. Franzo, F. Priolo, D. Sanfilippo, G. Di Stefano, and P. G. Fallica, Appl. Phys. Lett. **81**, 3242 (2002).

[7] Hak-Seung Han, Se-Young Seo, Jung H. Shin, and Namkyoo Park, Appl. Phys. Lett. **81**, 3720 (2002).

[8] P. G. Kik and A. Polman, J. Appl. Phys. **91**, 534 (2002).

[9] L. Pavesi, Materials Today, Jan. 2005, p.18.

[10] D. Kuritsyn, A. Kozanecki, H. Przybyliska, and W. Jantsch, Appl. Phys. Lett. **83**, 4160 (2003).

[11] P. W. Atkins, *Physical Chemistry*, Oxford University Press, New York (1990), 4th ed., Sec. 17.2.

[12] M. Blasse and B. C. Grabmaier, *Luminescent Materials,* Springer, Berlin (1994), Sec. 2.1.

[13] L. Dal Negro, "Rate equation modeling of energy coupling processes in Si nanocrystal – erbium systems," (unpublished).

[14] P.C. Becker, N.A. Olsson, and J.R. Simpson, *Erbium-Doped Fiber Amplifiers Fundamentals and Technology*, Academic Press, San Diego (1999).

Chapter 8. Conclusion and future work

In this section I will conclude the thesis by summarizing what has been investigated and discussed and also by suggesting the essential factors to be considered for electrically injected silicon based laser devices based on the experimental results and discussion so far. Additional work will be needed to clarify and confirm the research direction suggested and discussed here.

8.1. Conclusion

Basically, light emitting materials of SRN and Er:SRN have been investigated and incorporated into resonator structures (Thue-Morse structure for SRN and Si racetrack resonator structure for Er:SRN). To investigate electrical properties and electroluminescence properties we also fabricated light emitting devices with SRN and Er:SRN as active materials. Finally, detailed comparison and discussion on the difference between optical and electrical excitation processes of Er was provided. In addition, in this chapter the important factors for electrically injected silicon based laser devices will be suggested and shared based on work completed so far.

The following is a more detailed summary of the completed work.

First, I investigated optical properties of SRN grown by PECVD and determined that light emission comes from localized states in the Si-nc's and confirmed with the first

principles simulation. The presence of Si-nc's was also confirmed experimentally by TEM and micro-Raman, showing similar sizes for both methods. A PLQE (Photoluminescence Quantum Efficiency) of 7% was demonstrated.

Second, this light emitting SRN by PECVD was incorporated into a photonic resonator structure based on the Thue-Morse complex sequence. With T-M 32 and T-M 64 structures we could observe many high Q states from the transmission spectrum measurement. The light emitting Thue-Morse complex photonic structure demonstrated the enhanced light emission by up to a factor of 6 in photoluminescence spectra. This is the first fabrication and demonstration ever of the light emitting Thue-Morse photonic structure. Thue-Morse waveguide structure was proposed and fabrication based on CMOS process was tried to increase system size without being restricted by physical limitations such as film stress, interface irregularities, etc with increased film thickness. A sequential annealing technique was proposed as a novel approach to enhance the luminescence from silicon nanocrystal based light emitting materials and light enhancement was demonstrated experimentally.

Third, a light emitting device was fabricated with SRN as an active layer and high current density of tens of mA/cm^2 was observed which is much higher than that of an SRO system (6~8 orders). Significantly enhanced current density was achieved with an increased annealing temperature. The related phenomenon was explained and supported experimentally based on tunneling between Si-nc's. Electroluminescence was observed

only from the ITO/SRN/n^+-Si/Au structure (for bipolar injection) and it was well overlapped with photoluminescence. However, with the ITO/SRN/p^+-Si/Au structure (for unipolar injection) we could not observe any electroluminescence.

Fourth, we moved further into Er:SRN material to get light emission at 1.54 μm by co-sputtering technique with Si, Er, and Si_3N_4 targets used altogether. We confirmed energy transfer from SRN matrix to Er atoms with non-resonant pumping and high excitation cross-section of ~ 10^{-15} cm^2 was obtained. Strong Er emission was possible not only from the Er:SRN with the SRN matrix having SRN emission, but also from the Er:SRN with the SRN matrix without SRN emission. Therefore, we learned that light emitting SRN is not necessarily the energy sensitizer. A SRN matrix without emission can also contribute to Er sensitization. Variation of Si content in the SRN matrix strongly affected Er sensitization. Finally, energy transfer from SRN to PbS quantum dots has been investigated. Energy transfer is dominated by a short distance, non-radiative energy transfer process, not by an emission and reabsorption process. Coupling CMOS compatible but inefficiently light emitting silicon-based materials with highly efficient colloidal quantum dots would greatly enrich silicon's growing set of functionalities.

Fifth, Er:SRN was coupled with Si racetrack resonator structure fabricated by the LOCOS process. With the LOCOS process we could get a very smooth sidewall and the waveguide width could be controlled by varying oxidation time. A low loss value of 2.5 dB/cm was achieved by removing the nitride and oxide layers completely. Q factor values

of mid 10^4 ~ mid 10^5 from the resonance peaks were demonstrated with the SOI resonator structure. The optimized Er:SRN was deposited on top of the resonator to observe coupling behavior and luminescence from Er was confirmed from the device. However, due to high loss of the sputtered Er:SRN material, resonance phenomena could not be observed from the coupled devices.

Sixth, light emitting devices were fabricated to investigate electrical properties and to observe electroluminescence from Er:SRN. With varied Si content in Er:SRN, the I-V characteristics were changed dramatically in shape and current density at fixed applied bias. With the optimized process conditions we could get strong photoluminescence comparable to Er:SRO system and good diode behavior at the same time. However, we only observed Si peak and other defect related peaks from electroluminescence spectra of Er:SRN. We compared and discussed in detail why optical and electrical excitation processes of Er are so different. The main difference came from the fact that the direct excitation cross section values of Er atoms are different by more than 6~7 orders (The electrical one is much higher.). In addition, based on the rate equations of two level systems for SRN sensitizer and Er atom, many key parameters such as total loss, upconversion coefficient, coupling coefficient, etc. were simulated to see how much these parameters are important in achieving net gain in our Er:SRN system and to have approximate and conservative estimation on how high current density level is needed. The effects of these parameters in optical excitation of Er were also compared in detail. Completely different behaviors could be observed for the parameters such as sensitizer density, coupling coefficient, and

sensitizer excitation cross section.

Finally, I suggested the significant factors to be considered for electrically injected silicon based laser devices in the next section.

8.2. Important factors

Here I want to share and suggest the important factors for electrically injected silicon based laser devices which include, but are not limited to, the following factors.

1. We want to adopt the Er incorporated material system, especially CMOS compatible material, to utilize the Er atoms for light emission at the wavelength of 1.54 μm.

2. Electrical excitation of Er is entirely different from optical excitation as discussed in chapter 7. The role of sensitizers to excite Er electrically which worked favorably for enhancing efficiency in optical pumping is in doubt. Direct Er excitation in electrical injection is preferred due to high excitation cross section unless Si-nc's (or some other equivalent agents) serve as excellent sensitizers with larger or similar excitation cross section and fast transfer rate.

3. The current density level to achieve net gain with the key parameters varied as in chapter 7 is quite high (higher than ~ tens of mA/cm^2 level) even though this level was

calculated in a conservative way. Considering the fact that the simulation results were based on the condition of no leakage current, this current density level seems to be not easily achieved with the limited CMOS compatible material candidates. Therefore, finding out certain CMOS compatible materials incorporated with Er atoms which allow high current density without large leakage current is the most urgent task.

4. Free carrier absorption is a very important phenomenon which must be looked at carefully, and should be suppressed to the minimum level to achieve net gain. Usually the injected free carriers will absorb photons. If the free carrier absorption is very strong when the carriers are injected into the active layer at high concentration, achieving population inversion will be difficult. Light that is emitted, or comes from outside source, will not be amplified in that case to contribute to lasing because the rate of stimulated emission is far below that of free carrier absorption. Therefore, we may need to consider separating the injection layer from the emission layer if we can not find out a material candidate with low free carrier absorption intrinsically. That is, one layer serves as the host for the e-h recombination and the energy from the recombination can be transferred to the emission layer where only light emission (with amplification by stimulated emission) will happen. To achieve net gain from the emission layer we need to have a high energy transfer rate faster than the emission rate. Therefore, finding a material candidate with a very low free carrier absorption or achieving a device structure avoiding free carrier absorption issue is essential.

8.3. Future work

For a better understanding of our materials and the new materials with the characteristics described above, and also for further improvements, I propose the following experiments and studies to be pursued in the future.

1. The material candidate for Er excitation with high current density without large electrical leakage, that is, probably with low concentration in defects contributing to leakage can be investigated. High Er concentration for higher gain with less upconversion for easier population inversion is preferred. For example, Er silicate is known to have a high concentration of optically active Er and a small interaction of excited Er^{3+} ions due to large distance between the nearest Er^{3+} ions in the neighbor. It also has very small temperature quenching and high optical transition probabilities due to low symmetry sites of Er^{3+} ions in the matrix. The upconversion coefficient acquired experimentally so far is smaller than Er in other dielectrics and there is still some room for further improvement since it is at an early stage of investigation. Yb,Er silicate can be also considered as a candidate based on the fact that incorporation of Yb can provide higher excitation cross section and also suppress the upconversion problem. However, electrical injection properties are not well investigated yet even with their significance. Large excitation cross-section in electrical injection is important in selecting a material candidate considering the dependency on threshold current density for net gain as illustrated in chapter 7.

2. To utilize the separation of the injection layer from the emission layer, an electrical injection mechanism into the injection layer should be investigated in detail by focusing on

the energy by the recombination and also its dynamics. The energy transfer phenomena should be considered carefully to achieve population inversion in the emission layer containing Er atoms. That is, the energy transfer including transfer rate and back transfer phenomena should be investigated in detail to utilize energy transfer and to suppress free carrier absorption at the same time.

3. Coupling of the Er gain layer into the resonator structure for electrical injection should be designed carefully and investigated further since the electrical injection followed by coupling into the Er gain layer is more restricted by many factors such as carrier injection and their recombination dynamics, energy transfer from the injected carriers, etc. than the optical pumping case. Considering the large loss of the Er:SRN by sputtering technique in coupling with Si resonator structure in chapter 7, SRN by PECVD or other CVD technique for better material quality followed by Er implantation can be considered as an alternative option. Er doped silicon oxynitride can be also investigated considering the low material loss of oxynitride.

4. Up to this moment we have not considered the electrical contact issues seriously yet. However, to inject the electrons and holes into the active layer with high carrier concentration for population inversion, low contact resistance level should be achieved for the small contact area (Small area is preferred to achieve high current density with reasonable current level).

5. Er excitation by impact excitation can not be the ultimate and practical solution considering the lifespan of the device. That is, the active layer containing Er atoms will be worn out due to repeated impact excitation by the electrons (rarely by holes) with high energy. Hot electron excitation presents issues of efficiency and reliability that may mitigate against it as an EL device principle for lasers.

Even though an electrically injected Si laser could not be achieved from the study in this thesis, I hope the results and ideas can contribute to achieving the ultimate goal of this field.